NASA
Technical
Paper
3374

November 1993

Leading-Edge Vortex-System Details Obtained on F-106B Aircraft Using a Rotating Vapor Screen and Surface Techniques

John E. Lamar,
Jay Brandon,
Kathryn Stacy,
Thomas D. Johnson, Jr.,
Kurt Severance,
and Brooks A. Childers

NASA

NASA Technical Paper 3374

1993

Leading-Edge Vortex-System Details Obtained on F-106B Aircraft Using a Rotating Vapor Screen and Surface Techniques

John E. Lamar,
Jay Brandon,
and Kathryn Stacy
Langley Research Center
Hampton, Virginia

Thomas D. Johnson, Jr.
Lockheed Engineering & Sciences Company
Hampton, Virginia

Kurt Severance
and Brooks A. Childers
Langley Research Center
Hampton, Virginia

NASA
National Aeronautics and Space Administration
Office of Management
Scientific and Technical Information Program

Page intentionally left blank

Page intentionally left blank

Contents

Summary 1

Introduction 1

Symbols and Abbreviations 2

Description of Aircraft, Vapor-Screen Systems, and Flight-Test Experiment 3

- Aircraft 3
- Vapor-Screen Systems 3
- Flight-Test Experiment 3

Image Data Development 4

- General 4
- Flight Vapor Screen 4
- Incorporation of Previous Flight Vapor-Screen Images 6

Discussion of Flight Results 6

- Vortex-System Origination 6
- 3-D Vortex Systems 7
- Effects of Angle of Attack and Reynolds Number on Vortex Systems 7
  - Surface Tracks 7
    - General 7
    - Results 7
    - Error assessment 8
  - As a Function of Φ 8
    - 2-D Images 9
    - Distance to the leading edge 9
- Comparisons 10
  - Surface Pressures 10
  - Surface Oil-Flow Patterns 12
    - At $\alpha = 13°$ 12
    - At $\alpha = 15°$ 12
    - At $\alpha = 17°$ 13
    - At $\alpha = 19°$ 14
  - Wind-Tunnel Results 15
  - Previous (1985) Results 16

Conclusions 16

Appendix A—Flight Research Systems and Operational Procedures 19

Appendix B—Description and Features of Computer Process for Image Analysis . . 31

Appendix C—Photogrammetric Reconstruction of Light-Sheet Images 42

Appendix D—Description of Wind-Tunnel Test and Vapor-Screen Systems 48

References 51

Tables 52

Figures 54

Video Supplement Sequences and Mail-In Card 157

Summary

A flight research experiment involving the use of a rotating vapor screen was conducted at NASA Langley Research Center on an F-106B aircraft. The experiment was initiated in order to better document the events leading to the occurrence of multiple primary vortices found unexpectedly during a previous flight test on this 60° delta-wing airplane. Digital enhancement, photogrammetry, and computer graphics techniques have been used to determine the origination of the vortex system and the multiple vortices, to spatially locate the wing vortex cores, and to define the vortex tracks over the wing. From the 3-D display of these results with a Silicon Graphics IRIS workstation, the surface pressure measurements, the oil-flow patterns, a related wind-tunnel test, and a previous flight experiment, a number of conclusions have been reached. Chief among them is that seemingly small distortions in wing leading-edge geometry could well be the cause of the multiple vortices observed. In conjunction with the formation of these vortices, there is an apparent change in the vortex from the leading-edge separation-bubble type to the more classical off-surface type with increasing angle of attack. Moreover, the vortex-system envelope becomes reflexive toward the leading edge. Downstream of this occurrence that system moves inboard and another vortex forms.

Increasing altitude causes the Reynolds number to decrease and large-scale, organized flow separation to begin on the wing at the lower test angles of attack. This separation reduces the number of vortex systems present by reducing the influence of the leading-edge distortions and causes the outermost vortex system to be more inboard. Conversely, increasing the Reynolds number, through either an altitude or a Mach number change, generally delays or suppresses large-scale separation.

The sparsely obtained pressure data do not indicate, except at one test condition, the influence of more than one primary vortex, even though more than one was observed and reported. A correlation study, based on vortex-core tracks and surface pressures, shows good agreement between the number and location of vortices and the suction pressure peaks for this test condition as well as for two other conditions dominated by a single vortex.

Limited results obtained from the method of identifying the reattachment point which uses out-of-phase pressure ports do produce results that are fairly consistent with those obtained from the vapor-screen images, both in number of vortices identified and in relative location. However, this method does not appear to have the same versatility in flight as the vapor-screen image technique and requires a dense placement of pressure ports in the vicinity of reattachment in order to properly identify its occurrence.

The surface oil flow on the wing is complex at angles of attack of 13° to 19° because of the existence of vortex systems both inboard and outboard of the wing slot. In a comparison of the reattachment point locations determined from the oil flow and those from the vapor-screen images inboard of the slot, the overall agreement in both number of vortices detected and their placement is generally good.

The effect of Reynolds number for high-altitude flight and that for wind-tunnel tests is similar over the forward portion of the wing, where only a single vortex system is generated for $\alpha \geq 14.8°$. Hence, vortex-system locations determined in the wind tunnel can give a reasonably good estimate of flight values for angles of attack from 16° to 20°, even on a cambered wing having a small leading-edge radius. Valid comparisons over the aft part of the wing were not possible because of insufficient in-flight vapor-screen coverage.

The Flow Analysis Software Toolkit (FAST), written to display computational fluid dynamics (CFD) results on IRIS workstations, can be used to display experimental flight vapor-screen images, vortex-system characteristics, and surface oil-flow patterns as well. Further extensions and applications to allow direct comparisons between experimental and CFD results appear likely.

Introduction

The vapor-screen technique—composed of seeding, illuminating, and image recording systems—has been applied in-flight by researchers from both the former U.S.S.R. and the U.S.A. The Soviet application was to a research aircraft with an ogee wing in the late 1970's (ref. 1), and the American (NASA) application was to an F-106B with a 60° delta wing in 1985 (refs. 2 to 4). Though the elements of each of the three systems differed for the two aircraft, both had a single, fixed illuminating plane—positioned perpendicular to the wing upper surface—and yielded important visual results. In particular for the F-106B, the recorded video images, both basic versions and digitally enhanced versions, showed the existence of multiple primary (i.e., corotating) vortices on the left wing. This is an unexpected phenomenon at the reported angles of attack. Corotating vortices have been reported as streamwise vortices at low angles of attack and supersonic speeds on flat and cambered

models (ref. 5) and on aircraft in flight under loaded conditions (ref. 6). However, it is not clear that these references document the same phenomenon as that under investigation. The enhanced set of images from reference 4 were examined in order to obtain the spatial location of the wing vortex-system core (designated "the outermost vortex") as a function of angle of attack, Reynolds number, and Mach number. This reference reported these results for a variety of seeding-probe locations and light-sheet widths. The vortex shape, size, and core location were all determined to be sensitive to flight and vapor-screen parameters.

As useful as the vapor-screen technique was in uncovering this unexpected phenomenon in the F-106B flight test, it could only provide limited spatial information about the vortex system. This limitation resulted because all visual data were confined to a fixed plane. To overcome this deficiency, a follow-on flight test was planned in which the light-sheet source was relocated to the top of the fuselage (see fig. 1); where it would produce a sheet perpendicular to the wing upper surface which has fore-and-aft rotation (ref. 7). With this hardware change and the addition of a side video camera, the aircraft was reflown in 1991, specifically (1) to determine the origination of the vortex system and the multiple vortices, (2) to establish the vortex-system core locations in space, and (3) to document the tracks across most of the wing upper surface. In order to improve the quality of the recorded images, the experience of the previous flight test, coupled with preliminary tests of this flight experiment, led to the seeding-probe location and light-sheet width used here. This paper reports the basic enhanced images, relocated from the camera image plane to 3-D space by photogrammetry, and the ensuing analysis made possible with computer graphics. (The procedures for accomplishing this analysis, along with 3-D video animations of the completed process and information about how the flight data were collected, are all shown in a video supplement to the written paper.) To facilitate further understanding of the vapor-screen images, surface oil-flow photographs and pressure distributions are also examined. In addition, comparisons are made with relevant wind-tunnel vapor-screen images to look for large Reynolds number effects.

Appendix A details the flight research systems and operational procedures. Appendix B provides the description and features of the image data procedures. Appendix C explains the photogrammetric reconstruction of light-sheet images. Finally, appendix D gives the description of the associated wind-tunnel test and its vapor-screen systems.

Symbols and Abbreviations

AIS	Aircraft Instrumentation (data) System
BL	butt line on aircraft, in. (see fig. 1)
$C_{p,u}$	upper-surface static-pressure coefficient
$\bar{c}$	reference wing chord, 23.75 ft
c_r	theoretical root chord for F-106B, 35.63 ft
FAST	Flow Analysis Software Toolkit
FS	fuselage station on aircraft, in. (see fig. 1)
F/S	flight/serial
g	acceleration due to gravity
h	altitude, ft
KIAS	knots indicated airspeed
LE	leading edge
l	inboard distance to vortex core from wing leading edge for vortex system along light-sheet footprint, in. (see fig. 30)
M_∞	free-stream Mach number
p	free-stream static pressure, lb/ft^2
R_n	Reynolds number, $1.2583\bar{c}pM_\infty[(T + 198.72)/T^2]10^6$ (based on ref. 8, eq. I.3.8-(1))
r	inboard distance to vortex reattachment point from wing leading edge for vortex system along light-sheet footprint, in. (see fig. 30)
sps	samples per second
T	absolute temperature, °R
TE	trailing edge
VCG	video character generator
WL	waterline on aircraft, in. (see fig. 1)
x/c_r	fractional distance along the theoretical root chord, positive aft
z	vertical distance to vortex core above upper surface, in. (see fig. 56)
2-D	two-dimensional
3-D	three-dimensional
α	angle of attack, deg
κ, ϕ, ω	Euler angles for camera orientation, deg (see fig. C4)

Φ light-sheet position angle, measured counterclockwise from fuselage nose as viewed from above, deg (see fig. 2)

Description of Aircraft, Vapor-Screen Systems, and Flight-Test Experiment

Aircraft

The F-106B aircraft is a two-place supersonic all-weather interceptor. It has an area-ruled fuselage, has a 60° delta-like wing of aspect ratio 2.20 (based on a theoretical span of 39.16 ft and root chord of 35.63 ft), and uses elevons instead of a conventional aileron-elevator arrangement, as shown in figure 1. The aircraft wing is based on a modified NACA 0004-65 airfoil (streamwise) coupled with conic-like camber from the leading edge to 80 percent of the local semispan. Specified thickness-to-chord ratios for this wing section are 3.89 percent at the aircraft centerline and 3.47 percent at 82 percent of the semispan, with the corresponding streamwise leading-edge radii of 0.717 in. and 0.113 in. These radii correspond to radius-to-chord ratios of 0.17 and 0.13 percent. (Values of the thickness-to-chord ratio and the leading-edge radius-to-chord ratio at other spanwise locations are not documented.) Figure 1 also shows the wing leading-edge region to be composed of many pieces and to have a slot. Some of these pieces, called access straps, bridge leading-edge access areas between major segments located ahead of the no. 1 spar. The slot acts as a boundary-layer fence to laterally constrain the flow. In addition, the aircraft was extensively instrumented to measure and record onboard parameters associated with the vapor-screen system, the aircraft motion, surface static pressures, and the surrounding environment. (See appendix A for details.)

The left wing was used for both the vapor-screen visualization technique and the oil-flow visualization technique. In order to improve the visual contrast of the recorded images, that wing was painted flat black. (The right wing was painted for symmetry.) Figure 1 shows vapor-screen reference lines on the left wing (white lines painted on the aircraft), which were located where the light sheet crossed the upper surface at $\Phi = 43°$, 63°, 93°, 108°, 123°, and 130°. Figure 2 shows the left-wing slot beginning at $\Phi = 103°$ and the approximate wing regions over which the seeding and light-sheet systems were effective. Note that the lateral extent of the seeded flow was inboard of the slot. The right wing was reserved for surface pressure measurements, and figure 3(a) shows the locations and designations for the 30 active static-pressure ports contained within the 4 belt sets (2 to 5) used in this test. Figure 3(b) displays the relationship between the ports and the left-wing light-sheet angles reflected about the centerline.

Vapor-Screen Systems

In this flight test the vapor-screen technique involved the use of systems that were conceptually the same as those for the 1985 test: propylene glycol vapor for seeding, mercury-arc light sheet for flow-field illuminating, and video system for image recording. Figure 4 shows the vapor-screen hardware associated with the previous F-106B application, and reference 3 provides a description. However, there are specific changes that were made in order to accomplish the objectives of the current test. Some of the hardware changes can be seen by comparing figures 1 and 4. Additional information about the detailed changes made in each system is provided in appendix A.

Flight-Test Experiment

The flight-test experiment, composed of both $1g$ maneuvers and loaded maneuvers, was conducted so as to obtain as much vapor-screen image data as possible on each of five night flights. Sometimes data were even taken while flying to and from the test area at an altitude of approximately 15 000 ft in order to speed up the rate of image accumulation. The test parameters were angle of attack α, free-stream Mach number M_∞, Reynolds number R_n, and load factor. Table I provides their serial-averaged values for each flight/serial. Variations of R_n with α were accomplished by flying a subsonic $1g$ deceleration maneuver at constant altitudes of about 15 000, 25 000, and 35 000 ft with α ranging from 13° to 22°. There are two causes for the R_n variation associated with this maneuver: (1) the decrease in atmospheric density with increasing altitude and (2) the speed reduction required in order to maintain $1g$ flight while increasing α. The ranges of M_∞ and R_n were 0.26 to 0.54 and 22.6×10^6 to 39.1×10^6, respectively, and are given in groups I, II, and III in table I. (The flight/serials of group V in table I have been included solely for the purpose of providing alternate or reference values.)

The loaded maneuvers were flown at transonic speeds with load factors of $1.6g$ to $3.9g$ and are denoted as group IV in table I. Because of the limited thrust of this aircraft, it was impossible to sustain a constant altitude throughout a given maneuver. Consequently, the test conditions were achieved during a spiral descent. (During the 1985 tests the

afterburner was used to perform these maneuvers, but it was not employed for the current test so that the contrast with ambient conditions could be enhanced.) The ranges of M_∞ and α covered herein were about 0.7 to 0.8 and 15° to 19°, respectively. For all maneuvers, the best vapor-screen contrast was obtained by flying at night with the aircraft position lights off, the Moon down, and away from ground-based lights. Angle-of-attack variation during data taking was about ±0.5°. Additional information about the flight-test operational procedures is contained in appendix A and in sequence 1 of the video supplement.

Image Data Development

General

There are four different sets of relevant visual data important to this paper: (1) the vapor-screen images from the current flights, (2) the vapor-screen images from the 1985 flights, (3) the surface oil-flow flight photographs, and (4) the wind-tunnel vapor-screen images. Except for the surface oil-flow results, all images needed some amount of image processing in order for the basic visual image data to be developed into a form that could provide quantifiable information for the vortex systems present. Details of the 2-D and 3-D image-processing procedures used herein are given in appendix B. Implicit in the 3-D procedures are the photogrammetric techniques described in appendix C for reconstructing 3-D locations from light-sheet images.

This section describes how the procedures of appendix B were utilized to enhance the two sets of flight vapor-screen data. The use of these procedures for the wind-tunnel vapor-screen images is covered in the section entitled "Wind-Tunnel Results."

The video supplement to this paper shows the use of these data development procedures, and sequences from it are cited herein in order to assist the interested reader. In particular, sequence 2 of the video supplement provides an animated overview of many of the key elements associated with the processing of the flight visual data. Figure 5 was taken from that sequence and shows a representative set of individual vortex-system images from the top and side cameras projected onto the 3-D numerical surface geometry of the F-106B (including pertinent wing features).[1] Determined core and reattachment lines have been added for completeness, and details associated with their determination are given next.

Flight Vapor Screen

Upon review of the videotapes for each flight/serial, specific single images from the top and side cameras were selected from each light-sheet sweep at an interval of approximately 1 sec for later digitization. These images were not time averaged because of two factors. The first is associated with the unreliability of the video characters displayed on the monitor (and recorded) for the angle of attack α and the light-sheet position angle Φ. This was especially true for Φ, as the displayed value often lagged the actual angle. The second factor is that the Aircraft Instrumentation (data) System (AIS) was only on during brief periods of the light-sheet operation, primarily during the actual sweep itself. Therefore, in order for these flight parameters to be known as accurately as possible for a given image, the AIS had to be interrogated at the appropriate time. The AIS time was also displayed on the monitor (and recorded) through the use of another character generator. Sample results of digitized top- and side-camera vapor-screen images along with reference views of the wing upper surface are shown in figure 6. Each of these 2-D images was composed of 512 by 480 picture elements, or pixels. (The digitization process can be seen in sequence 3 of the video supplement.)

After the digitization was completed, each flight/serial image was examined to select the "core location" and "reattachment point" using the **Extractor** procedure, as described in appendix B. (It is also shown in sequence 4 of the video supplement.) The core was located by first identifying in the 2-D image the region of the flow which contained the vortex systems, as evidenced by the light reflecting off condensed seeding particles. Reference 4 notes that unlike water, condensed propylene glycol vapor does not tend to revaporize inside the core, even with the decreasing pressure and rising temperature. This lack of revaporization results in a concentration of particles in the core region which causes high reflectivity, or backscatter.[2] This concentration of particles in

[1] Thanks to Brent L. Bates of ViGYAN, Inc., for providing this surface geometry.

[2] Light scattering from dielectric spheres of the size used in this experiment is governed by Mie scattering theory. The scattered radiation patterns are dependent on the ratio of illumination wavelength to particle size. The patterns are complex and have many lobes. However, all have the same general trend of a maximum forward scatter, a lower maximum backscatter, and a minimum near-side scatter. As the light sheet rotates, the intensity of scattered light viewed by the fixed cameras changes in a highly nonlinear fashion. The top camera always sees backscattered

the core region is especially germane when the resulting leading-edge vortex system originates from a nonsharp edge on a cambered wing. Therefore, image pixels satisfying the requirements of being inside the vortex envelope and having high gray-level values (corresponding to bright intensities) were used to compute a weighted gray-level centroid.[3] The result is a single pixel location for each vortex core.[4] Because of the highly reflective light-sheet footprint, software was written to circumscribe a region of the vortex envelope from which the core location would be computed. Contamination of the result with surface reflections was avoided by careful control of this region. As a practical matter, the region was generally a set distance above the wing upper surface. Exceptions occurred at the lower angles of attack because of the vortex systems lying quite near the surface. When more than one vortex was observed to be present as a separate and distinct system or was indicated by an unexpected bulge in the vortex envelope, the process was repeated for each portion of the image. Within the defined region only those pixels which satisfied a specified brightness criterion were used in the centroid computation.

This same software can also be used to locate the off-surface most inboard edge (inner extent) of the vortex envelope as a function of light-sheet position angle by circumscribing a small region at the inboard extreme. The locations determined in this manner are important in-and-of themselves to assess vortex-system movement. (See ref. 4.) Moreover, if they are projected to the wing upper surface, a track of the inboard extreme can be established. An alternative method of establishing this track is first to project the inner extent of the envelope to the surface and then do the small-region circumscription there. This alternative method was used with the software to arrive at a surface location that should be slightly outboard (qualitatively) of the reattachment point, as deduced from figure 7 (from refs. 9 and 10). The lateral difference between these two locations can be traced to the different stream surfaces giving rise to them. That is, the reattachment point is associated with the surface just outside of the vortex-core envelope, whereas the envelope represents the extent of entrained stream surfaces. Since the quantitative difference is not known, a *hypothesis is made in this paper that the distance between these locations is small.* Hence, the surface location of the inner extent of the envelope can be used as an *approximation* of the reattachment point. Hereafter, the resulting points and lines from this approximation are referred to as reattachment for reporting, presentation, and comparison purposes.

It is not possible to assess the error associated with this hypothesis from the flight data. However, a proper assessment could be made from a subsonic wind-tunnel test of a delta-wing model, provided it produced sufficient upper-surface pressure, oil-flow, and vapor-screen data.

There is another level of approximation inherent in using a vapor-screen result to estimate a surface-flow property—the possibility the off-surface flow is nonunique, because it is being seeded by a single vapor source, versus the uniqueness associated with the surface flow. Reference 4 shows examples of this off-surface nonuniqueness. The probe location chosen for this test gave a good representation of the vortex flow for this F-106B aircraft during the 1985 flight experiment. (See appendix A for additional details.)

Another source of error associated with this technique is the manner in which the projection is done, that is, *visual projection* using interactive computer graphics, as shown by the dashed lines in figure 8. In particular, the projections were vertically downward for the top camera and approximately horizontal for the side camera from the innermost portion of the digitally enhanced vortex system to the forward-most part of the light-sheet intersection with the wing upper surface. (The intersection is called the light-sheet footprint and is identified in the figure by the hatched region.) This process was repeated for each vortex in the image. An observation can be made from figure 8 about the results of this process for the top-camera images; namely, there is likely to be an inboard bias for $\Phi > 90°$. This bias is quantified subsequently.

Even with all these potential sources of error, this technique still provides a rational basis for estimating the reattachment location in those situations where standard techniques are not available. Comparisons with oil-flow results are presented in an attempt to gauge the reliability of this technique.

A Flow Analysis Software Toolkit (FAST, ref. 11) script, described in appendix B, was used to facilitate

light. However, for the side camera, as the light sheet is rotated from 40° to 70° the scattering changes from forward scattered to slightly backscattered because of the change in viewing angle. This change in scattering could have some influence on the subsequent results of the core location determinations, as well as on any interpretation of their movement, because for $\Phi < 70°$ there is an inboard bias and for $\Phi > 70°$ the bias is toward the leading edge.

[3] Note that the terms *vortex core* and *centroid* are used here interchangeably. It is understood, of course, that not all centroids of seeded flow regions are vortex cores, but all cores are centroids.

[4] Even if the core is void of seed particles, this technique would still properly locate the core, because the centroid of a bright ring of reflective particles is just its center.

(1) the 3-D display of both camera vortex images, (2) their core locations and associated reattachment points, and (3) the surface F-106B wing geometry on a Silicon Graphics IRIS workstation. (Sequence 5 of the video supplement shows this process.) When all this visual information was examined together for each flight/serial, some points from the field of view of one camera overlapped the field of the other camera. Consequently, when clarity of data presentation is an issue, the side-camera results are generally deleted. This amounts to basically restricting the side-camera data and images to $40° \leq \Phi \leq 70°$. (In keeping with the preceding, the top-camera results are, in general, restricted to $70° \leq \Phi \leq 125°$. See appendix A for additional discussion of these camera viewing restrictions and fig. A2 for illustration of the effective regions.) This examination with both cameras also highlighted, on occasion, a mismatch of the two sets of reattachment lines. Figure 9 shows two flight/serial examples, one for which there is disagreement (fig. 9(a)) and one for which there is little disagreement (fig. 9(b)). The most likely cause of the disagreement was that the top- and side-camera images being used were taken at different times—on the average about 24 sec apart. This difference translates into slightly altered test conditions (primarily an angle-of-attack variation of about 1°) and vortex-system characteristics. A secondary reason could be the particular application of the 2-D **Extractor** procedure to determine points of interest.

Incorporation of Previous Flight Vapor-Screen Images

Selected enhanced vapor-screen images from reference 4 are put in a framework such that they can be compared with the current flight images. A new technique, described in appendix B, was developed to map these images into 3-D for viewing on an IRIS workstation using FAST. The user can directly compare the 1985 vapor-screen images with the 1991 images for the same or an alternative angle of attack. (Sequence 6 of the video supplement shows this process.)

Discussion of Flight Results

This section examines what has been learned from the vapor-screen images in terms of vortex-system origination, core location, and surface track. Because of the unsteadiness of the vortex flow, the varying amounts of vapor entrained, the variation of angle of attack during a flight/serial, and the limited number of discrete light-sheet position angles at which the vapor-screen images were digitized, the resulting core locations should not be expected to vary smoothly. This lack of smooth variation is also true for the surface track results for both the cores and the reattachment points.

Also included for completeness are comparisons with flight surface pressure measurements and oil-flow results, with wind-tunnel vapor-screen images, and with previous flight images. These comparisons are used respectively to clarify the relationship between off- and on-surface phenomena, to determine Reynolds number effects, and to resolve an angle-of-attack effect. In order that data comparisons may be better understood, figure 3(b) has been included to help provide a geometric link between pertinent vapor-screen systems and pressure-measuring locations.

Vortex-System Origination

For some of the lower angles of attack ($\alpha \leq 15°$) the vortex systems were so small and close to the front part of the wing that it was difficult to distinguish them from the light reflections on the upper surface using the side camera. It was only in the aft portion of the wing that the vortex systems were clearly visible from this camera location. Because this was a region where the top camera already had a better view, there are flight/serials for which only the top-camera images and the corresponding core and reattachment lines are shown.

Figure 10 shows three models that could lead to the formation of multiple vortices on this wing. Figure 10(a) is taken from reference 12 and was based on the fixed-light-sheet information available with the 1985 flight experiment, while figures 10(b) and 10(c) are new and are based on the current test. The elements of the latter two models are those of a vortex forming along the leading edge and then being shed aft over the wing, followed by another and more outboard vortex system forming and being shed aft, and so forth. The model in figure 10(b) is supported by examining the enhanced side-camera images from F/S 91-13/11 ($\alpha = 13.9°$) and F/S 91-16/11 ($\alpha = 17.8°$) shown in figures 11 and 12. (See figs. 6 and 8 for orientation.) Figure 11 shows that with increasing light-sheet angle the core, or bright centroid, moves from being outboard to inboard within the vortex envelope. This movement could be construed as the vortex system changing from a leading-edge separation bubble type to the more classical off-surface type.[5] Moreover, the vortex

[5] According to reference 13, which was developed from supersonic flow data, the F-106B wing, with its conic-like camber,

envelope develops a reflexive region near the leading edge. As the centroid moves inboard, the reflex becomes more accentuated toward the leading edge (see fig. 11), and this accentuation leads to a thinning of the vortex system. Hence, an open space develops between the outboard edge of the formed vortex and the leading edge. Outboard of this open-space region a second vortex system emerges for $\Phi \geq 64.1°$, as shown in figure 12. Hence, multiple vortex-system origination is tied in with the inboard shift of the core at the lower angles of attack and a related envelope change. These changes could be caused by a phenomenon associated with a vortex-sheet tearing process (refs. 14 and 15), either fluid dynamic or brought about by some aspect of the aircraft geometry. (Figs. 11 and 12 were determined with the **Enhancer** procedure of appendix B, and a sample session of this procedure is given in sequence 7 of the video supplement.)

Thus, the elements associated with multiple vortex origination have been identified, but the exact cause has not.

3-D Vortex Systems

Some examples of vortex systems in 3-D space above a surface representation of the left wing for $\alpha = 13.9°$ to $22.5°$ at $h \approx 25\,000$ ft are shown in figures 13 to 16. These figures, based on 3-D projections of the 2-D image-plane data, show all pertinent features of the wing and the flow features of vortex systems. The vortex cores and reattachment lines are highlighted in red (with yellow asterisks) and black (with white asterisks), respectively. Note that the core lines can be seen to penetrate the images at the bright centroids. However, the reattachment lines, which should be on the surface, may be slightly below it. The fact that they are not always on the surface indicates a combination of two errors, namely, (1) the accuracy with which the reattachment point can be determined in the 2-D image plane using the visual projection scheme described previously and (2) the inaccuracy in the resectioning-determined parameters, as discussed in appendix C. Another problem is the difficulty in resolving the vortex-system features sufficiently from the images at the lower angles of attack. This may result in a wrong vortex assignment being made. The likelihood of this error occurring increases when the "correct" vortex system is not completely visible or discernible in the image. The middle region of figure 13 illustrates this difficulty.

These figures are instructive and useful for animation studies. However, this representation is not as easily quantifiable as the method of surface tracks (projection of these curves onto the surface). Also, comparative studies with other flight/serial data are better done if the results are presented in terms of the distance from the leading edge along a light-sheet ray.

Effects of Angle of Attack and Reynolds Number on Vortex Systems

Surface Tracks

This section presents and describes vapor-screen-determined quantitative and qualitative data as functions of the test parameters.

General. Figures 17 to 22 present the vortex-system core and reattachment-point surface tracks for various angles of attack graphed onto the plan view of the left wing. Most figures contain results from both the top camera and the side camera, and they cover most of the wing. Sometimes only top-camera results are used because the side camera could not distinguish the vortex system. This leads to tracks that do not extend as far forward. Two other features of the tracks should be noted. The first is that the vortex systems cannot be resolved in the trailing-edge region because of the inability of the current setup of vapor-screen systems to illuminate and record events there. The second is that some tracks suddenly shift outboard after starting inboard, or vice versa. This behavior is unusual and is most likely associated with four sources of error: (1) change in light scattering, as viewed by the side camera, from forward scattered to slightly backscattered (see section entitled "Flight Vapor Screen"); (2) nonuniform particle entrainment and hence reflection; (3) variations from the nominal angle of attack; and (4) the unsteady nature of the vortex system.

Results. Increasing angle of attack at a nominal altitude generally reduces the number of vortex

should produce the transition from leading-edge separation bubble to classical vortex type near $\alpha = 10°$ at $M_\infty = 0.4$. The supporting numbers are contained in table II for a representative deflection of 22° normal to the leading edge (11.42° streamwise). Because these numbers are based on conical flow, there will only be a single number per condition and no longitudinal dependence, a feature that is uncharacteristic of subsonic results. Hence, the current data can be expected to show some variability from the reference results, in terms of both vortex flow type and nondimensional spanwise location at a given angle of attack, as a function of either light-sheet angle or longitudinal position. Lastly, note that table II predicts classical vortex flow to be present for $\alpha \geq 10°$, whereas in the current test the vortex systems did not become visible until $\alpha \approx 13°$. The higher α's required here are most likely associated with two factors: the inexact transition boundary at this low value of M_∞ and the round, not sharp, leading edge of the F-106B aircraft.

systems from as many as three to one, and there is an overall inboard vortex movement. (See figs. 17 to 19.) Given the fact that multiple primary vortices were known to exist on this wing, these results are not surprising. However, the results at an altitude of 15 000 ft (fig. 17) are particularly interesting in that the first vortices to appear are more inboard than those seen before at the lower α's. With increasing α the number of discernible systems grows to three, and these encompass more of the wing. Above $\alpha = 16.9°$, the number of systems begins to decrease until a single system is evident for $\alpha \geq 20.2°$. These results are consistent with the delay in significant separation associated with flights at higher Reynolds numbers. In particular, the R_n's associated with the lower altitude flights range from 39.1×10^6 at the lowest α to 27.5×10^6 at the highest.

All these results have been superimposed on a plan view sketch of the left wing with its elevon, wing slot, and five leading-edge access straps outlined. In many of these figures the additional vortex systems seem to either point to one of the straps or be influenced by it in some way. Thus one likely source of the multiple vortices observed in flight is the disturbance associated with these access straps. Note from figure 2 that there is a strap near $\Phi = 70°$.

Figure 20 shows the effect of increasing the load factor on the vortex systems for $\alpha \approx 14.8°$. However, in order to increase the load factor from one flight/serial to another, it is necessary to increase Mach number and, consequently, Reynolds number. Therefore, the results do not have a single cause. The effect of increasing M_∞ is to move the vortex system inboard (ref. 4), and the effect of increasing R_n is to delay or suppress separation. The general result noted from these figures is that the number of discernible vortex systems increases because of the increase in R_n from 29.2×10^6 to 57.3×10^6. This R_n increase delays large-scale separation and promotes multiple smaller vortices. The exception is at $2.5g$ (F/S 91-15/11), where only a single system is present. The reason for this occurrence is unclear. Lastly, as a general rule, the aeroelasticity effects associated with increasing load factor should be small because of the "rigidity" of this wing.

Figure 21 shows the effect of increasing angle of attack on the vortex systems at a nominal $2.6g$. The general result is that as α increases from 14.8° to 18.6° and the Reynolds number decreases from 45.7×10^6 to 35.6×10^6, the number of systems increases to two. With the unexpected result for F/S 91-15/11 just discussed, other generalizations are difficult to make, except to note that there is some tendency for the vortex systems to move inboard with increasing α. Considering only the results for $\alpha = 16.8°$ and 18.6°, there is a correct trend for the vortex systems to merge at the higher α and lower R_n.

Figure 22 shows the effect of increasing angle of attack on the vortex systems at a nominal $3.7g$. As α increases from 14.8° to 19.4° and the Reynolds number decreases from 57.3×10^6 to 46.6×10^6, the number of systems changes from three to one. As just discussed for figure 21, this is the correct trend for both conditions.

Error assessment. To help assess some of the errors identified, a repeatability check for the top camera was done by comparing the data of F/S 91-15/10 for $\alpha = 21.9°$ with those of F/S 91-15/09 for $\alpha = 21.7°$. The results are shown in figures 23(a) and 23(b). The general agreement for both the vortex-core surface tracks and the reattachment-point surface tracks is quite good, with maximum local lateral errors of 11 and 7 in., respectively. Figure 23(c) shows the distances to these vortex features from the local leading edge along the light-sheet footprint as a function of light-sheet position angle for both data sets. The distances are denoted as l for the core and r for the reattachment. Overall, good agreement is noted between the sets for l and r, with a maximum local error of 9 and 7 in., respectively. (Appendix C points out that with respect to the aircraft, the numbers reported in this paper have a worst case error estimated to be under 3 in.)

Furthermore, in order to assess the impact of projection technique on the location of reattachment points, they were redetermined for F/S 91-15/10. For $\Phi \leq 90°$ the interactive computer graphics techniques of vertical projection or perpendicular-to-surface projection, an alternative, yielded essentially the same results. So in this Φ range, the reattachment points were just redetermined using vertical projection, and the r results are recorded in table III. The table shows that the repeatability is very good, with the differences in r being very small (a maximum of 0.26 in.). For $\Phi > 90°$ the two techniques had been observed to yield different results, so repeatability in this range is not the issue, and the differences reported in table III are as large as 8.08 in. (i.e., more outboard, as indicated by smaller numbers). Note that for this α, the reattachment point above $\Phi \approx 120°$ is too far inboard to be determined with either projection technique.

As a Function of Φ

Figures 24 to 29 present effects of angle of attack and Reynolds number on the enhanced 2-D

top-camera images as a function of nominal light-sheet position. The first, or outermost, core location and reattachment line as a function of α also appear in figure 30 as distances from the local leading-edge along a light-sheet ray for the $1g$ flight. Core locations only are shown in figures 31 to 33 in order to establish the effects of α and R_n under loaded conditions.

2-D images. Figures 24 to 29 show the growth and change of character of the vortex systems at three different nominal light-sheet position angles for each of the different altitudes and load factors. (Note that many images on these figures retain a portion of the image identification box.) Among the more interesting changes is the reduction in the number of vortices brought about by merging or coalescing. Also noteworthy is that vortex breakdown, or burst, has not been specifically identified from any of the images obtained with this test. At $\Phi \geq 103°$ one is able to see the influence of the slot vortex on the seeded inner vortex system in that it may move abruptly inboard and no longer be connected to the leading edge. Figure 27 shows an inboard shift of the largest system at all values of Φ for $\alpha = 14.8°$ because of the increase in load factor and Reynolds number produced by the increasing Mach number. Figures 28 and 29 generally show the expected vortex system inboard movement and growth at high load factors with increasing α and Φ. The most interesting result is that of figure 29 for $\alpha = 14.8°$. In particular, for $\Phi \approx 70°$ and 87.5° there are three distinct and unusual vortex systems that merge into a single vortex by $\Phi \approx 111°$. Alternately, one could say that at this α there is only a single overall vortex system, but it has three distinct vortical parts for $\Phi \leq 87.5°$.

Distance to the leading edge. Figures 30(a) and 30(b) show generally similar effects of altitude on core and reattachment point distance to the local leading edge for the various light-sheet angles over the angle-of-attack range for $1g$ flight. Except for the results for $\Phi = 70°$ and 120°, the general trend of l and r is to be displaced inboard over the middle α range with increasing altitude. The altitude increase is associated with a lower Reynolds number set, as shown in table I. The inboard movement is reasonable because of flow separation and vortex merging occurring at the smaller α's for the lower R_n set. This effect of lower R_n results in the outermost vortex system tending to be a single vortex at a moderate α. Further, the system is likely to be larger and to have its core and reattachment locations more inboard. Conversely, for the highest R_n set (lowest altitude group) a delay occurs in the separation process leading to vortex formation. Consequently, to maintain a fixed value of l or r as altitude decreases, α must increase.

For $\Phi = 70°$ reattachment distance follows the general trend but core distance does not. The cause for this is shown in figures 19(b) to 19(i), in which the core, near the access strap associated with FS 410, does not move much with increasing angle of attack. This lack of appreciable core movement for $\alpha \geq 17.7°$ may be the direct influence of the strap on the local flow. (See fig. 2.) If so, then the core is more sensitive to such an influence than is the reattachment point. This sensitivity to change is shown in figure 11, where for $\alpha = 13.9°$, small increases in Φ near 65° cause noticeable inboard movement for the core but not for the reattachment point.

For $\Phi = 120°$ the general trend only holds for the two highest altitudes. It is unclear why the results associated with the 15 000-ft altitude should be at or slightly inboard of those at the 25 000-ft altitude. However, the outward movement of the core and the reattachment point for the lower angles of attack and higher light-sheet angles at the 15 000-ft altitude is explainable. At the lower α's there are multiple vortices present over the middle of the wing, and the first one is quite far from the leading edge, as shown in figures 17(a) and 17(b). With increasing α the first vortex system occurs nearer the edge, then moves inboard in the conventional manner.

Figure 31 shows the effects of Reynolds number and load factor (both dependent on Mach number) on core distance from the leading edge for $\alpha \approx 14.8°$ to be almost identical over the range of light-sheet angles. Because R_n is the dominant fluid parameter in this figure, the aeroelastic effects associated with the load factor are small and the curves deviate only slightly from the R_n curves. Figure 31 is based on the information presented in figure 20, and the discussion associated with that figure points out that the results associated with $2.5g$ are not in line with the others. If they are discounted here (plotted but not considered in the analysis), then there is a trend for the core to move toward the leading edge based on the $3.9g$ results for $\Phi = 70°$, 100°, and 110°. This is also true for $\Phi = 90°$, for which no $3.9g$ results are graphed.

Figures 32 and 33 show the variation of core distance with angle of attack and Reynolds number at a nominal altitude of 35 000 ft and $2.6g$ and a nominal altitude of 30 000 ft and $3.7g$, respectively. These figures are based on the data shown in figures 21 and 22; hence, the trends of core distance with α presented here are consistent with the previous results. In figure 32, for $\Phi = 80°$ and 90°, where three values of l are available, the core moves first toward the leading

edge then away with increasing α. At $\Phi = 100°$ there are only two values available, but they also show the outward movement of the core at the lower values of α. For these maneuvers, R_n and α are inversely related, and the l curves reflect this behavior. (See table I.) For figure 33, the basic data set (fig. 22) has fewer points, but they apply over a greater range of Φ than in figure 32. Therefore, the l variations with α (and R_n) at $\Phi = 70°$, 90°, and 110° appear to be linear because each curve is composed of only two points. As with figure 32, the variation of l with α is inverse to the variation of l with R_n.

Comparisons

Surface Pressures

As previously described, figure 3(a) shows the placement of the 30 active static-pressure ports contained in four sets of belts on the right wing. Before the data are discussed, there are some general observations that need to be made.

1. In $1g$ steady flight, the aircraft exhibited a low-frequency pitch oscillation of about 0.4 Hz. This can be seen in figure 34 from a typical (F/S 91-15/06) time-history plot of angle of attack with its attendant variation of about $\pm 0.5°$. Because of these variations, similar oscillations are to be expected in the static-pressure data. (The higher frequency oscillations shown in this figure are most likely associated with angle-of-attack-vane dynamics.)
2. During flight 91-15 one of the edge fairings on belt-set 2 came loose. (Details on pressure belts are given in appendix A.) Subsequent analysis showed the results for only the first tube in that belt set to be erroneous. The fairing was repaired before the next flight, so only one flight does not contain a value for the first pressure port of belt-set 2 (C2S01).
3. Because of the volume and noise characteristics of the pressure signals, these data were smoothed with the following techniques. The data, which were recorded at a rate of 20 samples per second (sps), were time averaged by pairs to 10 data points per second for figures containing time-history plots. Other plots, in which specific flight conditions are given, were averaged over the duration of the maneuver usually associated with a sweep of the light sheet at a constant angle of attack.

A specific analysis technique based on wind-tunnel experiments, given in the appendix of reference 16, was utilized to help understand these flight data. It is first explained and then its use herein is outlined.

An aspect of pressure data that is useful in explaining separated flow conditions is the phasing of the data with respect to angle of attack. Figure 35, from reference 17 and based on reference 16, shows the variation of upper-surface static-pressure coefficient with α for a single port along a wing chord developing a single primary vortex during a wind-tunnel test. The inset sketches represent the position of the separated vortical flow and the associated reattachment points with respect to the port. At angles of attack below 6° in this example, the flow in the port region is dominated by attached flow, so the pressure curve is somewhat linear. This condition can be characterized by saying that the change in $C_{p,u}$ is in phase with α. For $\alpha \approx 6°$ the local flow near the port comes under the influence of the additional downwash associated with the vortex as the reattachment point approaches the port. This influence causes the pressure to become more positive and leads to a change in the relationship between $C_{p,u}$ and α to out of phase. Subsequent increases in α beyond about 7° cause the vortex to move closer to the port with the attendant lower pressures and makes the $C_{p,u}$ change to in phase with α again. This condition continues until the vortex core lies over the port at the minimum $C_{p,u}$. Therefore, by examining the individual port $C_{p,u}$ variations with α for a wing developing vortical flow, one can gain insight into what is happening off the surface. In particular, one can obtain the reattachment-point locations. (For $\alpha > 9.5°$, $C_{p,u}$ takes on more positive values, indicative of the passage of the primary-vortex core beyond the port. Since our purpose is in establishing the α at which the reattachment occurs at a particular port, the latter α range is not emphasized.) The shape of a corresponding curve for a flow with multiple primary vortices is unknown.

Attempts at developing a similar (single vortex) curve from the current flight data required the selection of discrete time segments for small ranges of angle of attack so that the full range of the test would be covered. However, when these ranges were plotted together, this technique proved unsatisfactory, as severe mismatches in the data occurred.

Although this attempt to directly duplicate the wind-tunnel result with flight data was unsuccessful, an alternative approach to locating the vortex-system reattachment points on the wing, based on the principles of figure 35, was carried out with the flight-pressure data. (There is likely to be some difficulty in making a direct application of these principles, since there is no corresponding figure for multiple

primary vortices.) The approach followed was to directly compare pressure-port time-history plots with corresponding angle-of-attack plots in order to identify those ports for which $C_{p,u}$ is in or out of phase with α. Figure 36 shows both effects. All the data on the left are in phase and follow the small α perturbations around a mean value of 9°. On the right, most ports are in phase while others (e.g., C3S02, C3S03, C3S04, C4S01, and C4S05) are out of phase for $\alpha \approx 14°$.[6] Because of the large camber on this wing, the in-phase $C_{p,u}$ variations near $\alpha \approx 9°$ are associated with attached flow, whereas near $\alpha \approx 14°$ vortical flow is present in the vicinity of the ports and leads to the assertion that the cited ports have vortex reattachment occurring there. Similar out-of-phase relationships exist for pressure ports C3S01, C3S02, C4S01, C4S02, and C4S03 at $\alpha \approx 17°$ in figure 37 over at least a portion of the time-history plot.

For both figure 36 and figure 37 the pressure data associated with the aft region of the wing (belt-set 5) are more difficult to interpret because the signals have a higher frequency content. When these data were graphed, the flow was determined to be basically in phase except at a few ports, and those were out of phase for only a small portion of the time-history plot (about 2 sec). Hence, no out-of-phase response is reported for this region of the wing.

Figures 38 and 39 provide examples of reattachment points identified from the time-history pressure plots, which are denoted here by filled symbols. (Note that there is only a single reattachment line associated with a region having adjacent out-of-phase pressure ports. This results from the realization that there is some expected movement of the reattachment point with varying α, and the reattachment point for a given port is not just definable in terms of a single α but rather over a small range of α, as shown in figure 35.) The results may be ambiguous because of the sparseness of the pressure ports available, but they do look appropriate. These figures also contain reattachment lines determined from the left-wing vapor-screen images for the same flight/serial. (See table I and fig. 18.) The results of both figures show that each technique identifies, where possible, the same number of reattachment lines per figure and that those obtained from the vapor-screen images are generally inboard of the pressure ones. There are two likely reasons for the relative positions. The first is associated—and consistent—with the vertical-projection technique used to locate the reattachment points from the top-camera vapor-screen images. The second reason pertains to figure 38. The reattachment points from the images are for $\alpha \approx 15°$, while those associated with the pressures are for $\alpha \approx 14°$. Therefore, the reattachment points from the images are more inboard. Figure 38 also shows a third reattachment line from the images, and it occurs in a region where there were no pressure ports. Hence, where both techniques provide indications of reattachment points occurring, the agreement between them is fairly consistent. However, the vapor-screen image technique shows reattachment point locations that are not indicated by the out-of-phase method.

Figures 40 to 42 present pressure data for the $1g$ deceleration-maneuver flight/serials averaged over the duration of the serial. These three figures, one for each of the nominal altitudes, are ordered by increasing altitude and contain data from all flight/serials grouped in ascending order of angle of attack. (See table I.) Based on these figures, developed from a sparse arrangement of ports, vortex-flow onset as a function of altitude can be inferred from the pressure data. To find the point at which this occurs, one looks for the fundamental vortical-flow characteristic pressure signature of *a suction peak surrounded by recompression.* This occurs away from the leading edge, on an upper surface with no rapid curvature changes (e.g., flaps). At an altitude of approximately 15 000 ft the peak is first noted at $\alpha = 15.8°$ and for $h \approx 25\,000$ ft the peak is first noted at $\alpha = 14.9°$. In both instances this occurs on belt-set 4. At $h \approx 35\,000$ ft vortex onset is already present at the two middle belt sets for $\alpha = 13.9°$. The early onset of vortical flow at the higher altitudes is a Reynolds number effect associated with this wing having a round leading edge. After vortex onset all data sets show a spreading of vortex activity with increasing α, primarily in the forward portion of the wing. On the whole, these results are somewhat typical of a round-edged wing developing vortical flow. Note that these pressure figures, based on a sparse spacing of ports, do not indicate the influence of more than one primary vortex, even though more than one is observed and reported herein. An exception appears to exist because of an unexpected inboard pressure peak on belt-set 3 for $\alpha = 14.9°$. (See fig. 41.) This exception is taken up next.

Figures 43(a) ($\alpha = 14.9°$), 43(b) ($\alpha = 17.0°$), and 43(c) ($\alpha = 18.8°$) are used to compare surface pressures with vortex-core tracks at 25 000 ft. Figure 43(a) shows good correlation over the middle part of the wing between the core tracks and the pressure peaks, including the second peak of belt-set 3.

[6] Note that the average value of α for the 10-sec record of the pressure plots can be different than the serial-averaged value used for the vapor-screen image value recorded in table I.

(Note that in order to compare these two different kinds of results, the pressure-port locations associated with the peak surface pressures must be used.) Figures 43(b) and 43(c) also show reasonably good correlation between the two data sets, and the agreement extends more forward on the wing. This second finding is associated with the core of this dominant, single-vortex system becoming determinable at the more forward positions on the wing at the higher α's.

Figures 44 to 46 present pressure data for the loaded (transonic) maneuver flight/serials averaged over the first part of the serial. Figure 44 shows that for a nominal $\alpha = 14.8°$ the primary effect is due to the Mach number, which causes the vortex system to flatten. Evidence of this flattening is the peak suction values occurring over a wider section of the wing for the middle two belt sets. Also, the vortex system appears on the forward portion of the wing at a lower α than it does for the $1g$ maneuver. Figures 45 and 46 present the effects of increasing α at elevated nominal load factors of 2.6 and 3.7. These two figures indicate the changes in pressure coefficient that occur with increasing α look basically like those at $1g$.

Surface Oil-Flow Patterns

Surface oil-flow studies were conducted at $\alpha = 13°$, $15°$, $17°$, and $19°$ with the flight-test technique described in appendix A. Prominent features in surface oil-flow data are streak lines, separation lines, reattachment lines, and shock locations. Streak lines are fundamental as they indicate the airflow limit line direction over the surface of the wing. Converging streak lines along with oil pooling are called separation lines. Diverging streak lines are known as reattachment lines (see fig. 7) and sudden sharp turns in the streak lines are associated with shock locations. No shocks were present at the low speeds for which these oil-flow studies were conducted. The results from these studies are discussed in order of increasing angle of attack.

At $\alpha = 13°$. A photograph of the oil-flow patterns at $\alpha = 13°$ is shown in figure 47(a). These data were obtained at 190 KIAS ($M_\infty = 0.31$) from a chase aircraft. Several flow features are evident in the oil-flow patterns. Lines of oil pooling can be seen originating near the leading edge and proceeding in a nearly streamwise direction over the wing. Additionally, streak lines of oil are present which show a more spanwise direction of flow on the wing surface. Finally, oil pooling near the tip of the wing indicates separated flow in that region. Most of the wing-surface flow is attached, as indicated by the gently curving streak lines that emanate from the leading-edge region and then turn aft and slightly outboard as they move downstream. A sketch based on the surface oil-flow features is shown in figure 47(b). The streamwise pooling of oil indicates the influence of vortices that are shed from the small surface discontinuities between leading-edge segments and from the leading-edge slot. Outboard of the leading-edge slot a well-organized vortex is formed. A reattachment line of this vortex is evident beginning at the forward edge of leading-edge segment 5 and extending to the wing-tip segment and is illustrated in the sketch.

The surface oil-flow features can be compared with vapor-screen estimates of reattachment line and vortex-core positions shown in figure 17(a). Two streamwise vortices were observed during the vapor-screen flight tests. The camera field of view and light-sheet coverage during the vapor-screen flight tests were such that the most inboard vortex, indicated by the separation line in figure 47(b), was not visible. Additionally, because of the probe location, vapor seeding of the flow was not possible outboard of the wing leading-edge slot; therefore no vapor-flow data are available for the outboard portion of the wing. Within these limitations, the number of vortices present above the wing is consistent between the two data sets, as is the spanwise location of the outboard vortices; however, the locations do differ for the inboard vortices.

At $\alpha = 15°$. A photograph of the oil-flow patterns at $\alpha \approx 15°$ is shown in figure 48(a). These data were obtained at 175 KIAS ($M_\infty = 0.29$) from a chase aircraft. The oil patterns indicate the presence of vortical flow along the entire length of the wing leading edge. Superimposed on the primary vortical structure are streamwise paths of several shed vortices. A sketch of the flow features is shown in figure 48(b). Inboard of the wing leading-edge slot, there is evidence of three vortex systems on the wing surface. (See fig. 10(c).)

The first identified vortex system is deduced from a flow reattachment line evident in the oil pattern for a short distance near the fuselage and wing apex. The secondary separation line of this vortex, indicated by pooling of oil, is located just inboard of the location at which the leading-edge segments attach to the wing. Near the forward section of leading-edge segment 2, the leading-edge vortex tears from the feeding sheet and is shed downstream.

A second vortex is identified by a reattachment line outboard of the first shed vortex. The secondary separation line corresponding to the second vortex is apparently inboard of the wing leading-edge segments. This second vortex tears away from the

leading-edge feeding sheet near the forward portion of segment 3 and is shed downstream.

The third vortex is identified outboard of the second vortex by the secondary separation line, which continues spanwise parallel to the wing leading edge. (See fig. 7.) The slot in the wing appears to displace the secondary separation line outboard near the slot in a discontinuous fashion. Aft of the slot, the vortex trails nearly streamwise. For each of the trailing vortices, it is interesting to note that when the vortex is shed downstream, the secondary separation line of that vortex results in oil pooling on the wing; however, the characteristic herring-bone pattern generally associated with secondary vortex systems in oil-flow studies is not evident in the photographs. This result is not unexpected in that the secondary vortex flows are generally much weaker and smaller than the primary vortex flows. In addition, the secondary flow may be absorbed by the adjacent downstream vortex, which has a flow reattachment near the secondary separation line of the preceding vortex.

Outboard of the wing leading-edge slot, a strong vortex system develops consisting of at least two additional vortices. Immediately outboard of the slot, oil pooling indicates a vortex that emanates from the slot and is shed downstream. Farther outboard, near the wing-tip segment, streak lines show extensive spanwise flow that culminates at a secondary separation line for the final (most outboard) vortex.

The oil-flow features can be compared with vapor-screen estimates of reattachment line and core locations from figure 17(c). Qualitatively the data show good agreement with the three vortex systems visible inboard of the wing leading-edge slot. The two outboard vortices show reasonable agreement in their position on the wing. The inboard vortex, however, appears considerably farther outboard in the vapor-screen data than is observed from the surface oil-flow patterns.

At $\alpha = 17°$. A photograph of the oil-flow patterns at $\alpha = 17°$ is shown in figure 49(a). These data were obtained at 160 KIAS ($M_\infty = 0.25$) from a chase aircraft. The oil patterns reveal the presence of a clearly defined multiple-vortex system. A sketch of the surface features is shown in figure 49(b). Inboard of the wing leading-edge slot there are three vortex systems observable on the wing surface. The secondary separation lines are discernible in the oil-flow photograph and are illustrated in the sketch. A reattachment line of the vortex nearest the wing apex is seen near the wing-fuselage juncture. (This line was most clearly seen in in-flight video images from a camera located on the inlet, not shown here.) The vortex is displaced inboard and another vortex is formed, beginning near the end of the first leading-edge segment. The influence of the first vortex can be seen progressing over the wing in a nearly streamwise direction. The secondary vortex separation line for the second observed vortex from the wing apex stays near the wing-leading-edge attachment joint through the length of segment 2. At the access strap between segments 2 and 3, the secondary reattachment line curves toward the leading edge, an indication of a perturbation in the vortex feeding sheet.

A third vortex develops midway on segment 3. The secondary separation line is seen near the leading edge, and it grows until it intersects the leading-edge slot. A reattachment line for the third vortex occurs very near the secondary separation line of the second vortex. The third vortex cuts off the second vortex from the feeding sheet, and the second vortex progresses nearly streamwise over the wing. The reattachment line for the second vortex can be seen in the oil-flow pattern and is evident in the in-flight video images. The third vortex gets displaced inboard and cut off from the leading-edge feeding sheet by the flow through the leading-edge slot. The secondary separation line for the third vortex initially moves streamwise aft of the slot. Near the wing tip, the separation line rapidly moves outboard, an indication of rapid growth, and perhaps bursting, of the vortex.

Aft of the wing slot, in segment 4, a reattachment line is seen along with another secondary separation line and indicates the presence of a fourth vortex system. In segment 5, a fifth vortex system is inferred as the result of yet another secondary separation line. The third, fourth, and fifth vortex systems apparently merge into one large system near the wing tip.

The oil-flow features can be compared with vapor-screen estimates of reattachment line and core locations. The core and reattachment locations shown in figure 17(e) indicate good qualitative agreement with the oil-flow patterns. Figure 49(c) shows a superposition of the vapor-screen- and oil-flow-derived flow features on the wing. The figure shows that the vapor-screen core locations are identified between the oil-flow reattachment and separation line locations for the two outboard vortices visible in the vapor-screen data. As previously discussed, the vapor-screen images do not show any features outboard of the wing slot because the seeding material did not extend beyond the slot. The third vortex (near BL 120 in fig. 49(c)) shows good agreement between the two data sets, with the reattachment lines being nearly coincident. The second (middle) vortex also shows

good agreement; however, the vapor-screen estimates of the reattachment line are outboard of the location observed in the oil-flow patterns. The first vortex (most inboard) is not seen in the vapor-screen data until aft of FS 450. Even though surface oil-flow patterns did not persist aft of approximately FS 450 for the inboard vortex because oil was not applied to this area of the wing, the vapor-screen estimates lie outboard of where the oil-flow patterns would indicate. This apparent difference may be because the light sheet did not extend to the surface of the wing in this area. Therefore the entire vortex was not illuminated, and this lack of illumination may lead to a bias in the derived reattachment and core location measurements from the video images.

A technique was developed to map video images onto the wing-surface geometry for analysis (appendix C), and it is illustrated in sequence 8 of the video supplement. This technique allowed direct comparisons of oil-flow data with vapor-screen images and data derived from the off-surface flow visualization such as vortex reattachment lines and core locations. Figure 50 shows an example of this technique applied to the current data comparing oil-flow patterns with the vapor-screen-derived vortex core and reattachment lines. The video image is not aligned precisely on the surface, as indicated by the slight mismatch in position of the painted lines on the wing and their representation on the wing geometry model. This mismatch was due to an inadvertent repositioning of the top camera on the airplane between the vapor-screen flight and the oil-flow flight-test series. The figure shows the field of view of the top camera on the wing surface. Good agreement between the oil-flow and vapor-screen data sets is shown, as discussed previously. This technique can be a very powerful tool in analyzing complex flow fields because it allows several visualization techniques to be combined into a single presentation format that can be viewed at any angle with computer graphics.

At $\alpha = 19°$. A photograph of the oil-flow patterns at $\alpha = 19°$ is shown in figure 51(a). These data were obtained at 150 KIAS ($M_\infty = 0.24$) from a chase aircraft. The oil patterns indicate flow similar to that at $\alpha = 17°$; however, the influence of the shed vortices on the surface flow is much weaker. This weaker influence indicates a more diffuse vortex system, or one that is higher off the surface of the wing, than that at $\alpha = 17°$. A sketch of the surface features is shown in figure 51(b). Beginning at the wing apex, the secondary separation line remains close to the point where the leading-edge segments attach to the wing. Near the aft edge of the first segment, a pooling of oil streams aft and indicates a shed vortex trailing streamwise down the wing. Farther down the wing leading edge the separation line shifts outboard on segment 2. A second streamwise pooling of oil emanates from this point and indicates a second trailing vortex. Analysis of the streak lines shows that these two vortices have much less influence on the surface flow than the similar systems at $\alpha = 17°$. Additionally, the vortex formed near the wing apex appears to have merged with the second vortex or may have dissipated (i.e., burst or lay well off the surface) forward of FS 450. Another difference between these two data sets is the more forward location of the second streamwise trailing separation line at $\alpha = 19°$.

Strong vortical flow is observed in the surface oil-flow patterns beginning at the aft part of segment 2, and this flow continues to the leading-edge slot. The very clearly defined secondary separation line near the wing leading edge and the typical herringbone pattern of the vortical flow scrubbing the wing surface can be seen. This vortex rapidly grows as it moves aft and becomes cut off from the leading edge by the flow through the leading-edge slot, similar to the effects at $\alpha = 17°$. The flow field aft of the slot again shows the formation of a new vortex beginning on segment 5, and the flow near the wing tip merges into that vortex.

The oil-flow features can be compared with the vapor-screen estimates of reattachment line and vortex-core locations shown in figure 17(g). The vapor-screen images show two vortex systems inboard of the slot. This finding is in good agreement with the oil-flow results. The oil-flow results show three systems; however, the vortex nearest the apex is very weak and probably merges with the second vortex far forward on the wing. The combined vortex system is observed in the vapor-screen images only between FS 470 and 490. This may be due to the weakness of the vortex, which could result in little seeding material entering into the flow. The second vortex in the vapor-screen data is first evident near FS 370 and extends to FS 550. This vortex corresponds to the strong vortex seen in the oil-flow patterns that formed beginning at leading-edge segment 2. The vapor-screen-derived location of the reattachment line of this vortex is inboard of the location indicated by oil-flow results.

Figures 51(c) and 51(d) are used to compare the surface tracks of the vortex system from the vapor-screen images with those from the oil-flow data at $\alpha \approx 19°$. The dominant-vortex reattachment lines are in good agreement near FS 490 and BL 100, and the core track is well positioned with respect to the streak lines, although it is outboard of the closest

secondary separation line. The surface streak lines do not indicate the presence of the inboard vortex determined from the images.

Based on the reattachment line comparisons between these two techniques at four test α's, the conclusion can be made that the use of vertical projection in determining the top-camera vapor-screen result is reasonable.

Wind-Tunnel Results

The **Enhancer** procedure of appendix B was employed to produce smoothed, contrast-stretched, color-contoured vapor-screen images overlaid onto the wind-tunnel model image at the appropriate longitudinal stations for $\alpha = 10°$ to 20°. These images are used herein for two purposes. The first is to gain a quantitative understanding of the effects of significantly different Reynolds numbers and seeding material on the vapor-screen images. The second is that qualitative flow observations can be made outboard of the wing slot in terms of the entire off-surface flow field above the wing because the water vapor is not inserted into the flow at just one location (as in flight) but rather seeds the entire flow around the model. (The wind-tunnel test was conducted in the NASA Ames 6- by 6-Foot Transonic/Supersonic Wind Tunnel on a 5-percent-scale F-106 model with water vapor used as the seeding material. The wind-tunnel model had a smooth wing; i.e., no access straps were modeled. Additional details of the test are provided in appendix D.)

For $M_\infty > 1$, or even at $M_\infty = 0.9$, the images show little or no water vapor present inside the vortex-system envelopes, as discussed in reference 18 and confirmed by the present wind-tunnel test. Hence, only the vapor-screen images for $M_\infty = 0.6$ are employed herein for comparison with the flight results. In particular, visual data from three (of the seven) longitudinal vapor-screen locations ($x/c_r = 0.5$, 0.6, and 0.9) are presented. Although data from other locations are available, these three are shown because the associated images have better contrast with the background. Figure 52 shows these locations relative to the light-sheet position angles of the aircraft.

Figures 53 to 55 show the individual wind-tunnel vapor-screen images arranged by vapor-screen location for $\alpha = 10°$ to 20°. These figures show (1) the progressively increasing size of the primary vortex system with increasing α at each location, (2) a well-defined core region, (3) the formation of another primary leading-edge vortex in the aft region (brought about by the aerodynamic-fence effect associated with the wing slot) and its subsequent merging with the forward primary system, (4) a juncture vortex, and (5) occasionally a high shear layer. These results differ from the flight results primarily in the number of vortex systems observed inboard of the slot at low α. The differences are most likely attributed to the presence of the access straps on the aircraft, which were not a part of the model.

Figure 56 shows the equivalent full-scale distance of the vortex-system characteristics, determined by scaling the exposed semispan of the model for each image to the airplane value and accurate to about ±4 in. (The scaling was necessary because no grid images were recorded by the video system, though grid images were recorded using a still camera from a slightly different viewing location, as shown in fig. D2.) These scaled measurements show a general inboard movement of the reattachment point (r) and small upward movement of the core (z) with increasing angle of attack. They also show that the lateral location of the core (l) is essentially independent of α for $x/c_r = 0.5$ and 0.9 above $\alpha = 14°$. Only at $x/c_r = 0.6$ does the core have the usual inboard movement with increasing α. (Note that for this x/c_r value and $\alpha = 10°$ the lateral features of the vortex were resolvable but not its core height.) It is interesting to note that at $x/c_r = 0.5$, even with the presence of a high shear layer, any restriction in core movement appears to be lateral and not vertical. At $x/c_r = 0.9$ the slot-generated, leading-edge vortex apparently restrains the more forward and inboard primary vortex system in such a way as to cause the only visible core to not move inboard or vertically with α.

An exact comparison between the vapor-screen results from the wind tunnel and from flight is not possible since there is no one-to-one correlation of light-sheet location between the two experiments. However, with the help of figure 52 a rough association can be established. In particular, the nominal flight values of $\Phi = 80°$, 100°, and 125° (±3°) can be loosely associated with $x/c_r = 0.5$, 0.6, and 0.9. Figure 57 presents comparative results (for a predominantly single-vortex system) based on this association and the effect of Reynolds number changing by a factor of about 15 (average at $h \approx 35\,000$ ft is $R_n = 26.1 \times 10^6$). This figure shows that over the forward portion of the wing, where the two light sheets roughly coincide, the two sets of core lateral location and reattachment point have similar trends with varying α, and even the magnitudes are close for α near 18°. This agreement is remarkable when one considers the entirely different manner by which

each data set was developed from the visual images and the subtle differences in geometry (i.e., smooth wing for the wind-tunnel model versus built-up wing for flight). Figure 57 also shows the R_n effects to be small over the forward part of the wing for $\alpha \geq 14.8°$. This is because the aircraft only has a single vortex reported there. Hence, vortex-system locations determined in the wind tunnel give a reasonably good estimate of the flight values for $\alpha = 16°$ to 20° even on a cambered wing having a small leading-edge radius. Furthermore, it is important to note that this single vortex is not significantly influenced by the presence of the flight access straps as reflected by the good agreement between the two sets of data.

Over the aft portion of the wing, significant differences exist because of the poorer agreement between the regions of the wing covered by the flight and wind-tunnel light-sheet locations. That the flight values are more inboard should not be surprising because the distance from the leading edge is being measured along a sweptback ray rather than along a perpendicular ray (relative to the aircraft or model centerline).

As to the effects of the seeding material (characteristics) on the results, as discussed in the section entitled "Flight Vapor Screen," it is interesting to note that there were dark cores occasionally observed in the wind-tunnel images, but none were found in flight images.

Previous (1985) Results

The initial intent of this comparison was to see how well the fixed-light-sheet results, obtained previously (ref. 4), were matched by the current data set. Figure 58 shows the positional relationship that exists between the two sets of light-sheet locations. Figure 59 presents the orientation of the images in the light sheets on the surface left-wing geometry. The previous results are presented in a grid plane on the left and the current results are given on the right for $\Phi \approx 110°$. (In order to obtain the most favorable image comparisons, Φ varied with α.) Figure 60 provides a direct comparison between the two enhanced-image data sets using the zoom capability of the IRIS workstation at four different nominal angles of attack and $h \approx 25\,000$ ft. (Previous results are those from fig. 24 of ref. 4. These are the best comparable images.) It is clear from the four parts of figure 60 that at the same nominal α, (1) the present images are larger, (2) the core, shown by the red line, is higher than those from the previous test, and (3) these vortex characteristics differ in a consistent manner. The conclusion drawn from these findings is that the α values reported in reference 4 are higher than those in the present test for the same vortex conditions.

In order to understand how this is possible, it is helpful to know that the aircraft attitude is measured through calibrated angle-of-attack and angle-of-sideslip vanes mounted on a nose boom. At any given attitude each vane seeks a position that yields an unloaded condition, or zero-lift angle. The results of these positions for different test attitudes then form the basis of the calibration. Since the vanes are lifting surfaces, any change in their mean-camber surface shapes will change their zero-lift angles. Warpage due to moisture retention is one way that the vanes may change shape. Vanes constructed of balsa wood are subject to warpage due to moisture retention and were used in the 1985 test. To circumvent this, the vanes used in the current test were made of metal. These α results should be better than the previous ones.

The angle-of-attack difference highlighted by figure 60 leads to the question of whether it is constant or variable over the α range. To address this question, present test images for nominally smaller values of α were compared with previous images for other α values to try and obtain a match of at least core height and location. Figure 61 presents the best matches for $\alpha = 18.8°$, 17.0°, 14.9°, and 13.9°. For $\alpha = 18.8°$ and 17.0° (figs. 61(a) and 61(b)), the error appears to be about 4°. However, for $\alpha = 14.9°$ (figs. 61(c) and 61(d)) the error is between 2° and 3°. (Note that perfect agreement is not achieved with either data set in that the cores from the 1991 data are outboard of the 1985 cores in fig. 61(c) and conversely inboard in fig. 61(d).) For $\alpha = 13.9°$ (fig. 61(e)) the difference is also less than 3°. Thus, there appears to be two error ranges, about 2.5° for lower α's and about 4° for the higher ones. Based on this comparison, it is noted that good agreement exists in the number of vortices present in the images at "truly comparable" α's.

Conclusions

A flight research experiment was conducted on the F-106B aircraft in which a rotating vapor screen and surface techniques were used to study the vortical flow and to gain insight into the origination of the multiple primary wing vortex systems determined previously. The results of this study and comparisons with the results from a previous flight test and a related wind-tunnel test are as follows:

1. The origin of the multiple vortices has been connected with the movement of the vortex core from outboard to inboard within the vortex envelope.

This movement could be construed as the vortex system changing from leading-edge separation bubble type to the more classical off-surface type. As the core moves inboard, the envelope develops a reflex near the leading edge which leads to an open space developing between the outboard edge of the formed vortex and the leading edge. Outboard of this open-space region a second vortex system emerges. Hence, multiple-vortex-system origination is tied in with the inboard shift of the core at the lower angles of attack and a related envelope change. These changes could be caused by a phenomenon associated with a vortex-sheet tearing process, either fluid dynamic or brought about by some aspect of the aircraft geometry.

2. From the core and reattachment line surface tracks, additional vortex systems seem to be caused or influenced by the access straps on the wing leading edge. Thus, likely sources of the multiple vortices observed in flight are the disturbances associated with these straps.

3. Increasing the Reynolds number, through either an altitude decrease or a Mach number increase, generally delays or suppresses large-scale separation and promotes the formation of multiple vortices. Conversely, decreasing the Reynolds number (altitude increase) leads to large-scale, organized flow separation beginning on the wing at the lower test angles of attack. This separation reduces the number of vortex systems present by reducing the influence of the leading-edge distortions (i.e., the access straps) and causes the outermost vortex system to be more inboard. These features are present in both the vapor-screen images and the resulting surface track summaries.

4. Reattachment point estimates from vapor-screen images and from out-of-phase pressure results agree fairly consistently in the wing regions where both techniques provided an indication of reattachment. Moreover, the vapor-screen image technique is a more versatile technique because it yielded reattachment point locations at angles of attack not indicated by the out-of-phase method. This may be partly due to the out-of-phase technique not being calibrated for multiple primary vortices.

5. Except at one test condition, the pressure data, based on a sparse port spacing, do not indicate the influence of more than one primary vortex, even though more than one is observed and reported herein. A comparison, based on the vortex-core tracks and surface pressures, shows good agreement between the number and location of vortices and the suction-pressure peaks for this test condition as well as for two other conditions dominated by a single vortex.

6. The primary effect of the loaded (transonic) maneuver on the pressure distribution for a nominal angle of attack of 14.8° is associated with the Mach number increase. This causes the vortex system to flatten, as evidenced by the peak suction values occurring over a wider section of the middle of the wing, and to appear on the forward portion of the wing at a lower angle of attack.

7. The pressure distributions for the loaded maneuvers at $2.6g$ and $3.7g$ have an angle-of-attack dependence that closely approximates that at $1g$.

8. The surface oil flow on this cambered, round-edged wing is complex at angles of attack of 13° to 19° because of the existence of vortex systems both inboard and outboard of the wing slot. Identifiable portions of the flow field have been attributed to the influence of the access straps around the wing leading edge. Reattachment point locations are naturally better defined from surface oil-flow patterns than from the vapor-screen images. Nevertheless, for angles of attack of 17° and above, the overall agreement in both number of vortices detected and their placement is good.

9. As a result of this agreement, the use of the vertical projection technique to determine the top-camera reattachment points is reasonable.

10. A comparison between wind-tunnel and flight tests (at 35 000 ft) shows the vortex-system characteristics agree fairly well over the forward part of the wing for angles of attack of 14.8° and above, where only a single vortex was present. In particular, vortex-system locations determined in the wind tunnel give a reasonably good estimate of the flight values for angles of attack from 16° to 20° even on a cambered wing having a small leading-edge radius. Valid comparisons over the aft part of the wing are not possible because of insufficient vapor-screen coverage in flight.

11. The angle-of-attack values reported from the previous flight test have been found to be in error. In fact, there are two ranges of error, about 2.5° too high for angles of attack below about 15° and about 4° too high for angles above about 15°. Based on the comparison that led to establishing the error ranges, the good agreement that exists in the number of vortices present at comparable angles-of-attack supports the corrections.

12. Flow visualization software written to display computational fluid dynamics (CFD) results on high-performance workstations can be readily used to display experimental flight vapor-screen images, vortex-system characteristics, and surface oil-flow patterns relative to the aircraft geometry. When CFD computations are available, they can be directly compared with experimental results. The flow visualization software used in this experiment was the Flow Analysis Software Toolkit (FAST).

NASA Langley Research Center
Hampton, VA 23681-0001
August 23, 1993

Appendix A

Flight Research Systems and Operational Procedures

This appendix consists of two main topics: (1) a description of the various flight research systems used to obtain and record both visual (flow visualization) data and nonvisual data, and (2) the flight operational procedures used to gather both types of data.

Aircraft Instrumentation System

The Aircraft Instrumentation System (AIS) was the principal data acquisition system for this flight experiment. The basic components of the AIS were as follows:

1. A 14-track magnetic-tape recorder
2. A time-code generator (Greenwich mean time)
3. A video-character generator for angle of attack α and light sheet angle Φ[7]
4. Two electronically scanning pressure (ESP) transducers
5. Flight-control position transducers
6. A total-air temperature probe
7. An accelerometer package located at the aircraft center of gravity
8. A rate-gyro package
9. A research nose boom for total- and static-pressure measurements and angle-of-attack and angle-of-sideslip vanes
10. Associated signal conditioning and recording electronics

In addition to recording the aircraft state, this system also recorded parameters from the research equipment. These parameters included two seeding temperatures, mercury-arc light "on" indicator, and propylene glycol pump voltage for the vapor-screen systems. The pressure data were recorded at 20 sps; all other data were recorded at 50 sps. The signal conditioning and recording equipment was located on a pallet in the missile bay.

[7] Thanks to W. Elliott Schoonover, Jr., of NASA Langley Research Center for determining that all flight-recorded values of Φ, including those for the vapor-screen images and for the white lines on the aircraft, needed to be increased by 3° to account for a shift in the measured zero position. This increase has been applied to all Φ values reported herein.

The AIS tape recording time available was nominally 50 minutes after ground calibrations were recorded. The AIS integral telemetry system was used to transmit all the flight data, except pressures, to the Langley Research Aircraft Ground Station (RAGS) and the flight-test control rooms at both the Langley Research Center and the NASA Wallops Flight Facility. These data were recorded at RAGS and selected parameters were presented via on-line recorders for real-time monitoring by the test teams. In addition to the onboard Vortac-ILS navigation systems, the aircraft was equipped with an inertial navigation system (INS).

Vapor-Screen Systems

This section documents the changes made to the vapor-screen component systems previously flown and reported (ref. 3).

Seeding System

The seeding system was composed of the plumbing to produce propylene glycol vapor—a clear vapor that turns white when suddenly cooled. This vapor was generated inside the missile bay of the aircraft, as in the 1985 flight test (ref. 4), and then ducted through a heated hose that exited the aircraft underneath the left wing near the leading edge. The hose used in the current test had a much higher heat input to the vapor than the one used before (90 versus 20 W/ft) so that a larger fraction of the vapor generated would remain in gaseous form until it reached the probe tip. The probe was located in the same position as that of "probe-tip location 1" from the 1985 flight test for two reasons: (1) the position was one of two determined to be suitable for flow seeding, and (2) its selection reduced installation time. This location was 52.625 in. along the leading edge from the wing-fuselage juncture and 8.50 in. inboard perpendicular to the leading edge, with the probe center 0.81 in. below the lower surface. The 0.50-in.-outside-diameter pipe had its tip angled 10° toward the leading edge to give the probe a sweep of 50°. The installed probe on the underside of the left wing is shown in figure A1.

Image Recording System

The image recording system consisted of two charged-coupled-device (CCD) video cameras, three VCR's, a backseat monitor, and two video character generators (VCG's). In addition to the top camera, a video camera was mounted on the left inlet which could look in the apex region and along the wing

upper surface. Both of these cameras were more advanced than the single camera flown in 1985. The side camera was also capable of producing color images, and the top one had a higher resolution than that previously used. An attempt to measure the camera positions and their orientation angles was made at the conclusion of the test program so that the images could be resolved in 3-D space through the image display process described in appendix B. It turned out that these numbers were not accurate enough, and the values that gave the best fit were obtained through space resection (see appendix C) and a process of trial and error. The final positions and orientations, as well as camera focal length, are FS 287.92, BL 1.58, WL 42.03, $\omega = 64.92°$, $\phi = 55.26°$, $\kappa = 20.72°$, and 16.69 mm for the top camera, and FS 303.49, BL 46.74, WL 11.08, $\omega = 29.79°$, $\phi = 57.30°$, $\kappa = -29.13°$, and 6.00 mm for the side camera for the early flights. (See figs. 1 and C4.) During flight 91-16 there was a one-time movement of the side camera on its ball support, so that from F/S 91-16/07 to the end of the test program the angles changed to $\omega = 35.76°$, $\phi = 61.07°$, and $\kappa = -33.10°$.

The top camera could only image the flow-field height from 45.9 to 25.9 in. above the leading edge (determined from the geometry model of the camera pyramid top and wing leading edge) as the light sheet rotated from 70° to 125°. (See fig. A2 for the top-camera effective region of the camera pyramid superimposed on the aircraft surface geometry.) Of course, the top camera could not image all the way to the leading edge because of wing camber. This visualization restriction was also a part of the 1985 flight test, and for that reason the image height reported in reference 4 was only the distance above the upper surface at the leading edge, a value of 34 in. The side camera had similar flow-field-height imaging restrictions based on its camera pyramid and the wing leading-edge geometry. These values ranged from 32.0 to 35.1 in. above the leading edge as the light sheet rotated from 40° to 70°. The side camera could obtain images along the leading edge at $\Phi > 70°$, but they generally became more difficult to capture because of the reduction in reflected light. Figure A2 also shows the side-camera effective region of the camera pyramid.

The three VCR's—two VHS and one Super VHS—allowed for each camera output to be recorded separately and provided a third recorder for the video signal sent to the 5-in. monitor in the rear cockpit. (For coordination and documentation purposes the AIS time code was added to each video signal.) The monitor-input signal could be selected from either camera and was annotated (via VCG) with angle-of-attack and light-sheet-position information. The latter character information was added to the video system in order to assist in performing real-time and postflight analyses. However, the signals that produced these characters were always first recorded by the AIS, before being sent to the VCG for processing, in order to ensure that the information was not corrupted. This signal routing turned out to be advantageous because the VCG output degraded during the latter parts of many flights. This led to a reliance on the displayed time code for data correlations.

Illuminating System

The illuminating (light-sheet) system had the most significant change from the 1985 system, as can be seen by comparing figures 1 and 4. In addition to being relocated to the top of the fuselage, where it was put into a streamwise fairing, the light-sheet source and optical barrel, or "periscope," were mounted on a turntable so they could rotate and thereby illuminate the flow over most of the upper surface of the wing. Figure A3 shows the internal arrangement of the mercury-arc light-sheet system, that is, the light box, the slit, the optical barrel, the lenses, and the front-sided mirror. A slit width of 0.048 in. was selected for use because of early flight experiments that determined a smaller width produced insufficient illumination over the aft part of the wing. The light-sheet longitudinal location was at FS 438.68, instead of the specified value of FS 412.00, because of a mounting error. This error was not harmful to either the aircraft flying characteristics or the data sought. The lateral placement of the optical periscope was biased 0.40 in. off the centerline toward the left wing in order to reduce the amount of interference between the light sheet and either the top of the fairing or the aircraft fuselage. The vertical position of the light source, in terms of the location of the center of the front-sided mirror, was at WL 51.54.

There was an initial concern that the seemingly large, top-mounted streamwise fairing could have two detrimental effects on the lateral-control characteristics of the aircraft, in particular, the stick-handling forces and the lateral-directional characteristics. The first effect stemmed from the use of ram air for reducing the stick forces needed in order to control the aircraft under high dynamic-pressure conditions. (The ram air was introduced to the aircraft through pipes located about ⅔ up the vertical-tail leading edge.) This problem was addressed by having water-tunnel tests on an aircraft model at 0° and nonzero

degree sideslip conducted by a colleague.[8] The result of these tests was that the flow off the fairing was not a problem as it did not extend that high. The second effect was associated with additional lateral forces and moments from the enlarged side projection of the test aircraft and fairing combination. Low-speed wind-tunnel tests[9] conducted in the Langley 14- by 22-Foot Subsonic Tunnel indicated no adverse aerodynamic effects associated with the fairing.

Cockpit Instrumentation System

The front cockpit was equipped with a precision angle-of-attack system comprised of a boom-mounted α vane, a control and display panel, and a head-up display on the glare shield. The color-coded indexer lights in the head-up display would indicate off angle with a deviation of over $\pm 0.25°$ from a preset angle. Next to the head-up display was a sensitive g-meter with graduations every $0.2g$. Also located in the front cockpit were an AIS data on/off switch and a "kill" switch to turn off all research systems. The aft cockpit contained the primary controls for the AIS, INS, vapor-screen systems, and video recording system. These controls and displays are shown in figures A4 to A7. The AIS had an event marker capable of annotating the AIS tape and, through telemetry, the strip chart at Langley. Also, there was a digital time counter that indicated how long the AIS tape had been recording. The video system also had a selector switch that determined which camera signal was displayed on the monitor.

Pressure Instrumentation System

The right wing contained 30 active static ports within 4 pressure belt sets. Each belt set was composed of 6 smaller belts (5 tubes per belt, a total of 30 ports available) plus upstream and downstream fairing ramps. The center 10 tubes or so of each station were used for pressure measurements, with the orifice closest to the wing leading edge located in the most downstream tube. The installed total width and height of each station were 8.4 in. and about 0.2 in., respectively, including the foam-padded double-back tape. (See fig. A8.) The tubing connecting the pressure stations with the ESP transducers was faired over the wing and routed through holes into the wheel well and tip areas. The two ESP transducers were referenced to a common manifold in the missile bay with equidistant tubes and had a range of 5 psid with ± 0.8 percent full-scale accuracy.

Operational Procedures

The flight operational procedures for obtaining visual data with both the vapor-screen technique and the surface oil-flow technique are detailed here.

Vapor-Screen Technique

The flight operations were conducted in restricted airspace over the Chesapeake Bay at night when the Moon was down. Pretaxi checks for the research equipment included cycling the illuminating (mercury-arc lamp) and seeding systems. The AIS and video recorders were turned on for takeoff, and although the video recorders remained on for the duration of each flight, the AIS recorder was turned off at an altitude of 2 000 ft and the seeding system was activated. Calibration maneuvers were usually performed at 250 KIAS and an altitude of 15 000 ft while the aircraft proceeded to the test area. These maneuvers consisted of stick and rudder pulses and $2g$ turns left and right.

Two types of maneuvers were flown: fixed α at constant altitude and fixed α and M during a spiral descent. The constant-altitude maneuvers were flown at target values of 15 000, 25 000, and 35 000 ft—altitudes that could be maintained without significant loss except at some of the combinations of higher α and altitude. Because of the low thrust-to-weight ratio of this 1950-vintage aircraft, spiral descents—loaded maneuvers from $2g$ to $5g$—were entered near 40 000 ft with recoveries initiated at 20 000 ft or higher. It was possible, however, to use the engine in its afterburner mode, but this would cause rapid fuel consumption and exacerbate the problem of video-camera sensitivity to light-intensity change (i.e., blooming and temporary loss of image). Note that during the 1985 flight test the loaded spiral descents were conducted with the afterburner used, and the video camera utilized was less sensitive than those presently employed.

The test procedures used in flight were as follows:

1. Upon entering the test area and nearing the first on-point, or initiation of flight/serial, condition, the illuminating system was turned on, the seeding system flow rate was set, and the aircraft external lights were turned off.
2. The aircraft was positioned by the test pilot as carefully as possible to prevent the two cameras from recording ground lights.

[8] Thanks to John H. Del Frate of NASA Dryden Flight Research Facility for supporting this project by performing the necessary water-tunnel tests.

[9] Thanks to Jarrett K. Huffman of NASA Langley Research Center for supporting this project by performing the necessary wind-tunnel tests.

3. The AIS recorder was turned on just prior to the light sheet being swept.
4. "On point" was called by the test pilot, who maintained a constant α with a variation of no more than $\pm 0.5°$ during the data taking.
5. The light sheet was swept forward by the flight-test engineer in the manual mode from $\Phi \approx 129°$ to 43°, with the video input to the monitor (recorder) set to the top camera.
6. The input was then switched to the side camera and the light sheet was swept manually aft to $\Phi \approx 129°$.
7. The AIS recorder was turned off between serials to ensure sufficient tape throughout the flight.
8. The light sheet was then rotated to a set of preselected angles ($\Phi = 43°$, 61°, 76°, 91°, 106°, 113°, 121°, and 128°) and a few seconds of video data were recorded for each.[10]
9. The vapor-screen systems were shut down at the conclusion of testing.

Following each flight, the aircraft and the external research equipment were inspected. In addition, the data on the AIS tape and the videotape were reviewed in preparation for the next flight.

Surface Oil-Flow Technique

The flight operations were conducted during the day while the Sun angle was high to minimize shadows over the wing and to provide maximum contrast. The oil-flow visualization segment of the flight was the first maneuver after takeoff. The remainder of the flight typically was used for performance flight testing. Thirty minutes before each oil-flow visualization flight, the left wing was painted along the leading edge and aft approximately 4 ft with a mixture of mineral oil, titanium dioxide, and oleic acid. The oil mixture was applied with a paint brush in distinctive swirl patterns so that patterns due to the airflow over the wing could easily be distinguished from the initial application. This mixture gave a very bright white color, which provided contrast with the black wing.

For each of the oil-flow flights, the procedure was to establish the desired angle of attack with the airplane immediately after takeoff to allow the oil-flow pattern to begin to form. This procedure resulted in nonstandard takeoff and climb speeds. Immediately after takeoff, the F-106B was joined by a chase airplane to photograph the oil patterns on the wing surface. The chase airplane directed the F-106B to fly appropriate headings to minimize shadows over the area of interest on the wing. Photographs were obtained from several positions. The flight generally was progressing toward the flight-test area during this time. The flow visualization portion of the flight was conducted at altitudes generally below 10 000 ft and was typically completed 10 minutes after takeoff. (From the lower altitudes up to 15 000 ft, an altitude by which most of the oil had been scrubbed off the wing, the oil-flow patterns did not change. Hence, the patterns are reported as being at 15 000 ft.) Following the flow visualization portion of the flight, the F-106B accelerated and climbed to the flight-test area either over the Chesapeake Bay or over the Atlantic Ocean.

Immediately following each flight, the oil mixture residue was cleaned from the F-106B wing. Data obtained were photographs of the oil-flow patterns on the surface of the wing. Each frame had a time code on the negative to correlate later with actual flight conditions. Markings on the wing, which indicated light-sheet intersections with the wing and wing leading-edge segments, helped identify the location of observed oil-flow features on the wing.

[10]These angles generally differ from the Φ values given for the reference white lines on the aircraft because the video cameras would have become saturated if those values had been used.

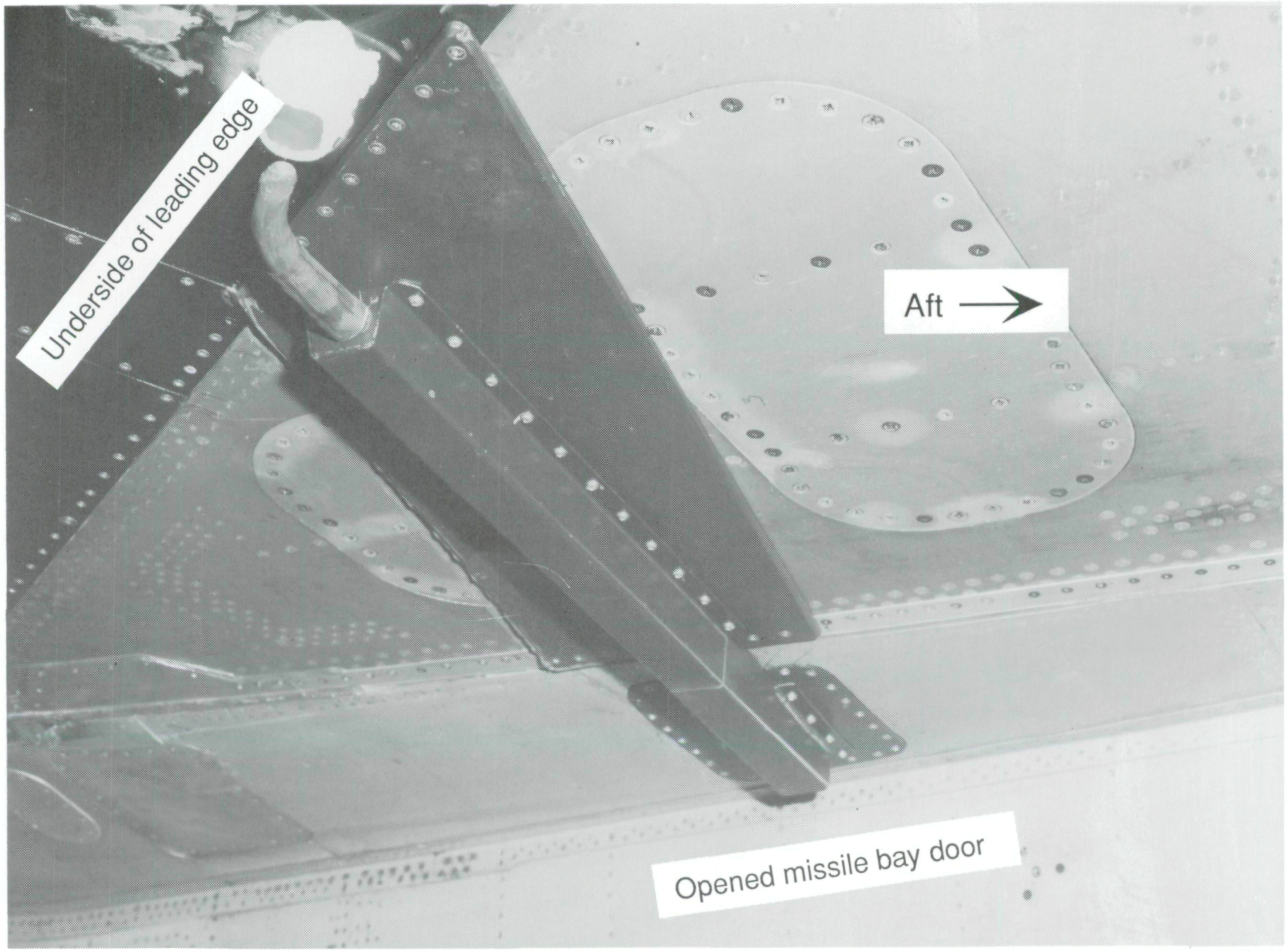

L-91-3941

Figure A1. Probe tip mounted underneath left wing.

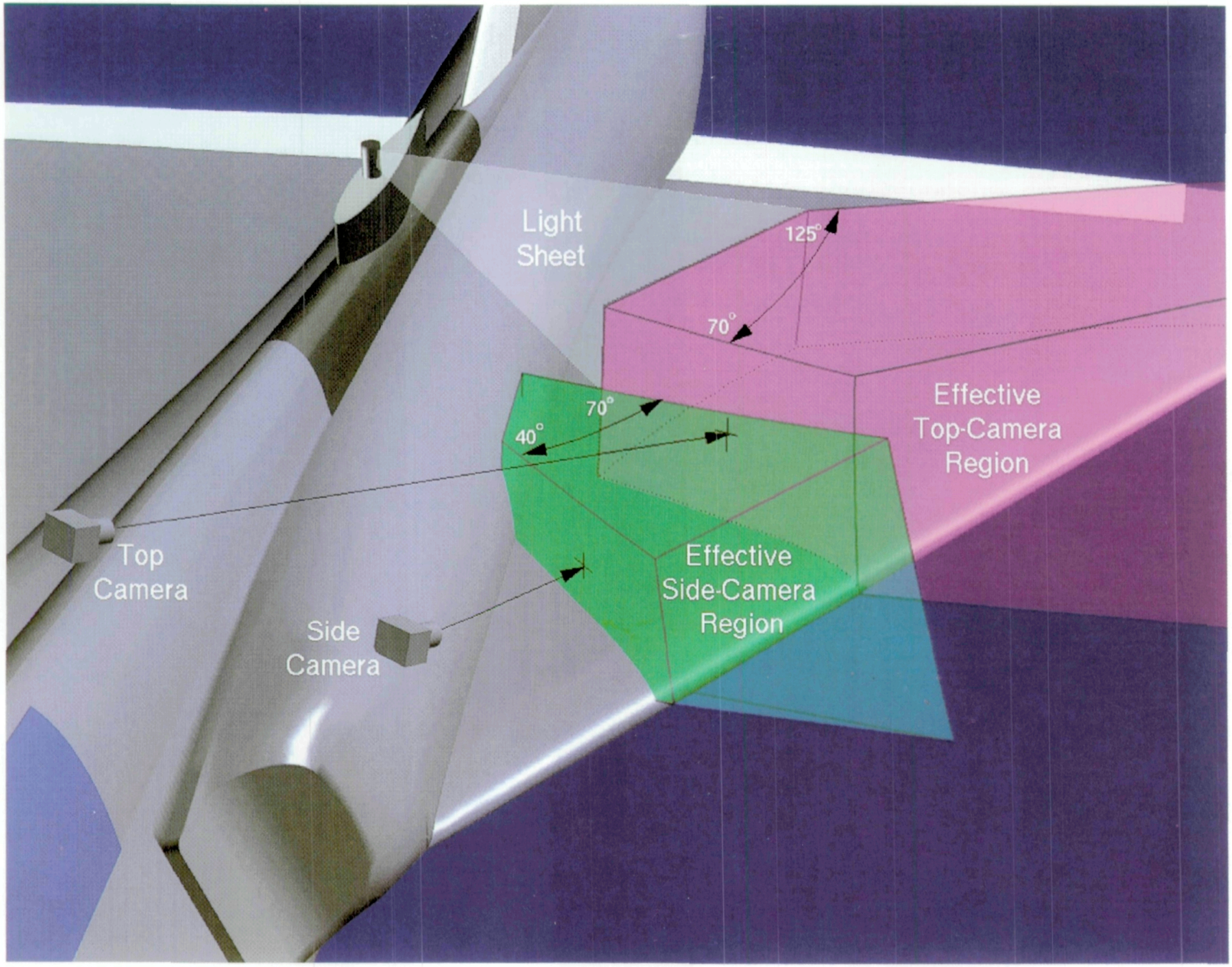

Figure A2. Effective top- and side-camera regions superimposed on aircraft surface geometry.

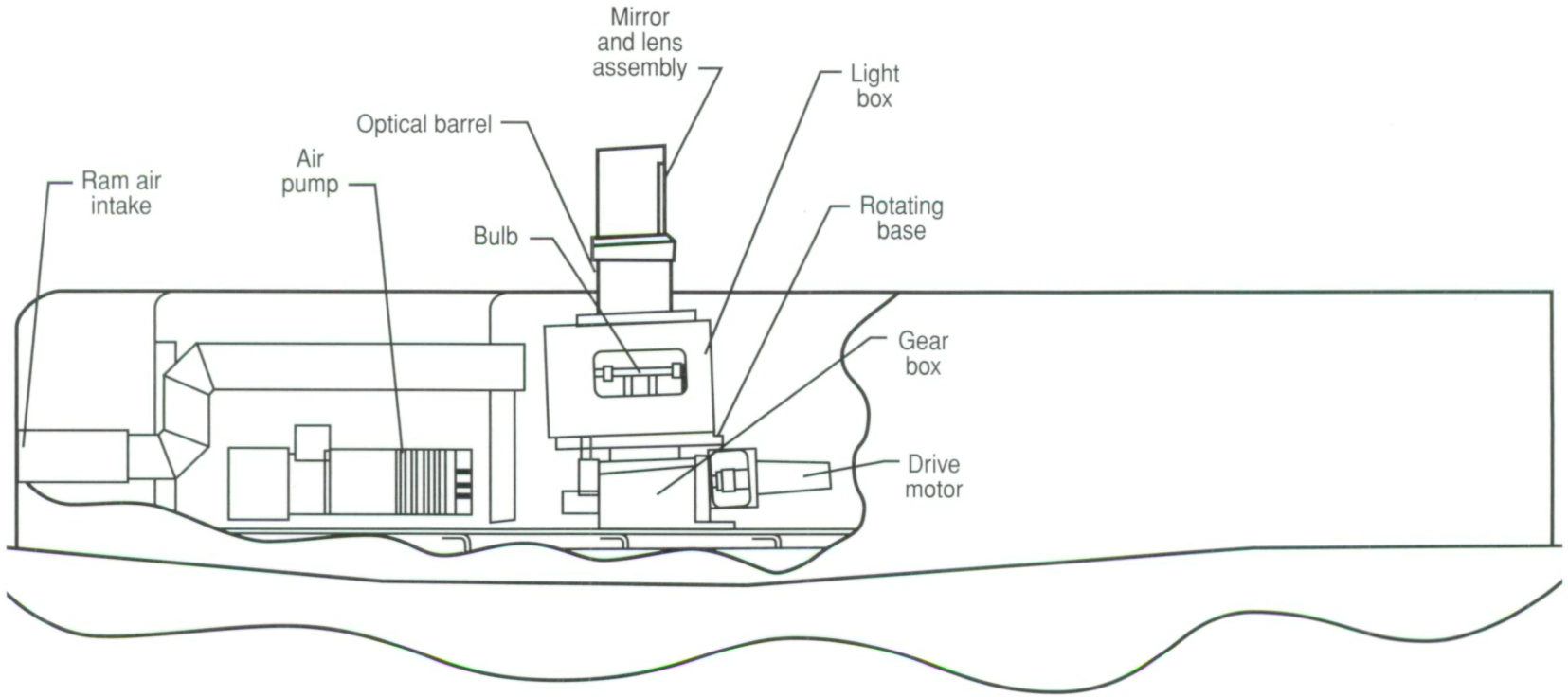

Figure A3. Illuminating system components.

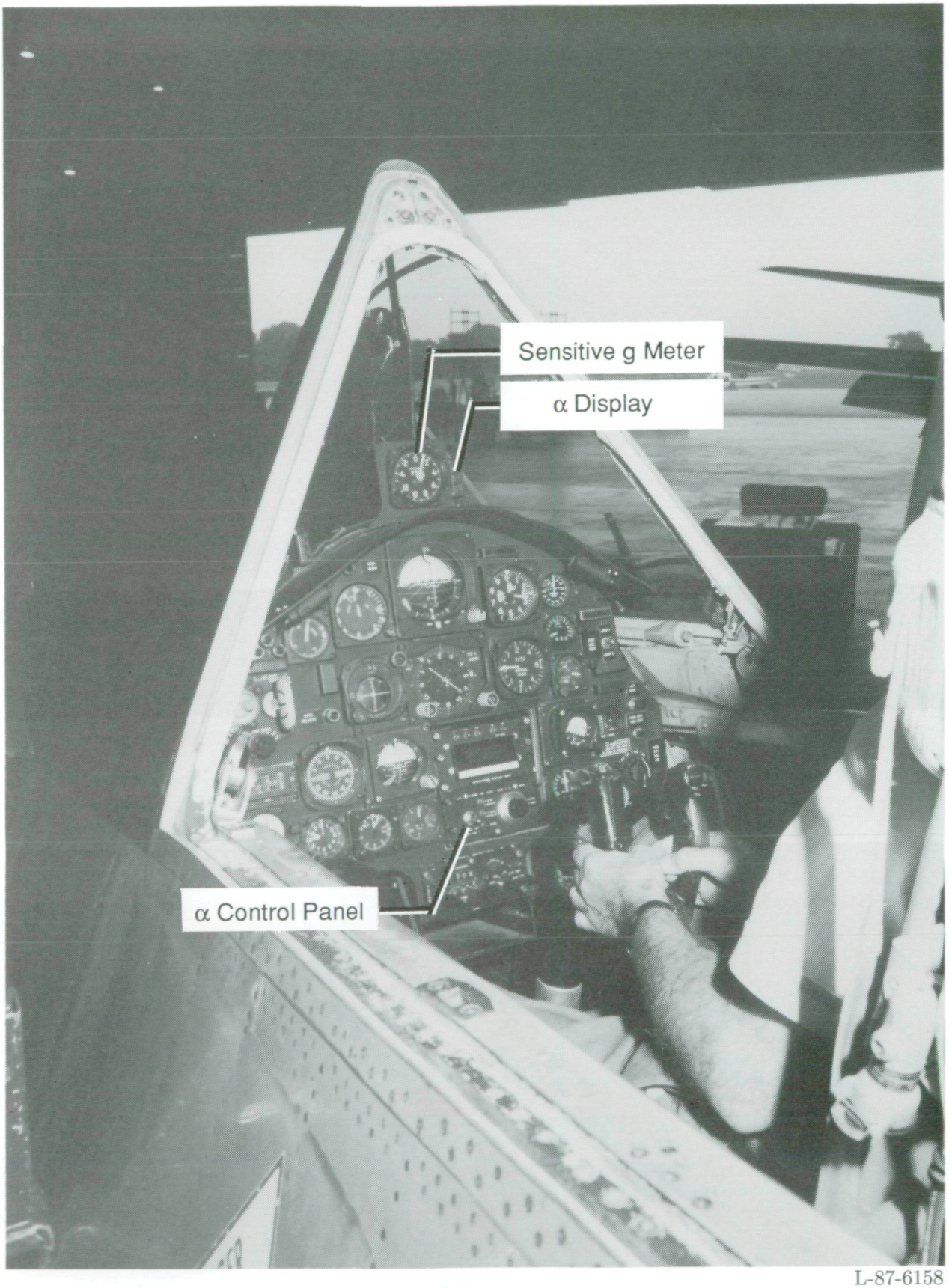

L-87-6158

Figure A4. View of front cockpit showing two research-instrument displays.

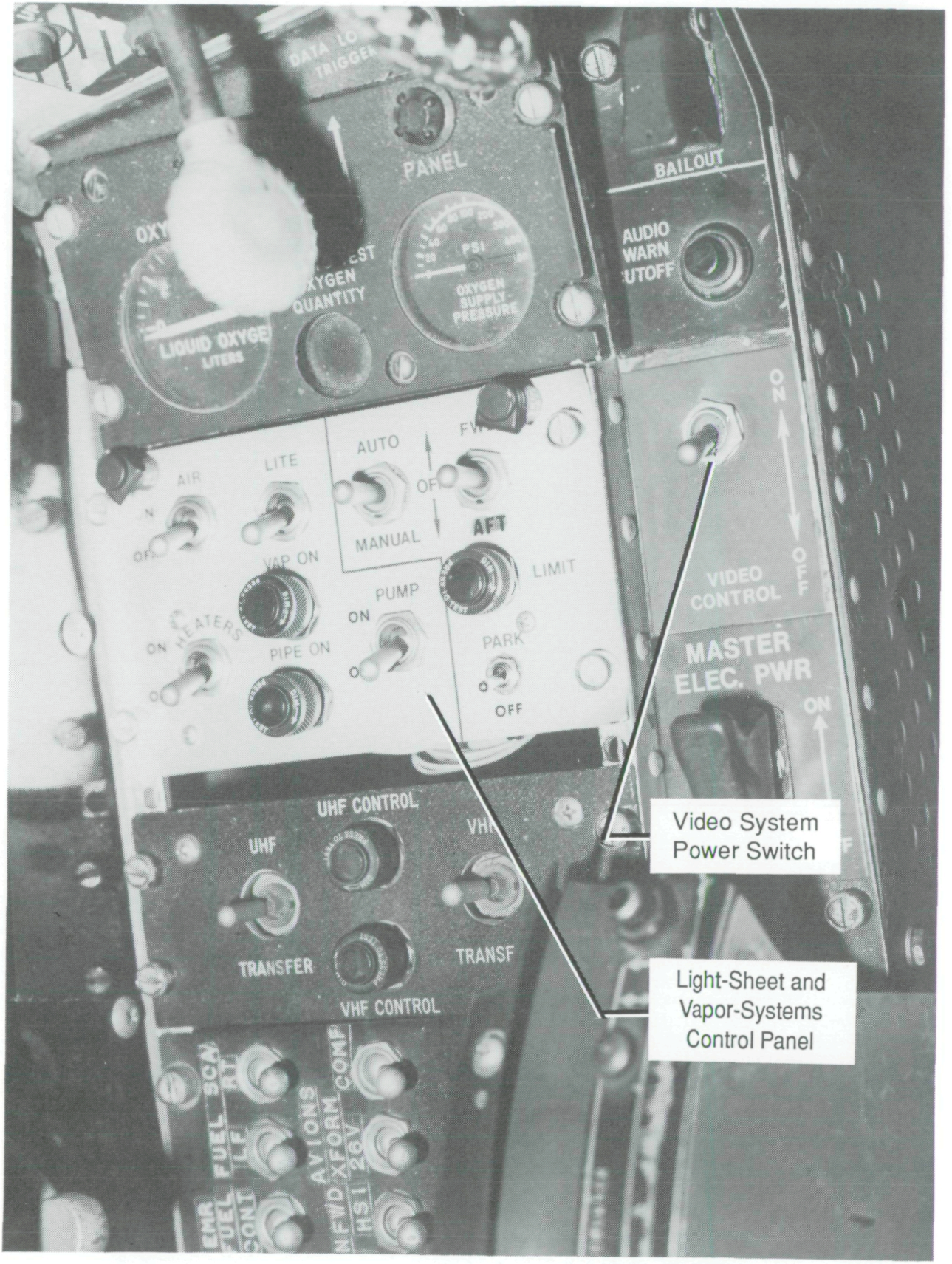

L-90-742

Figure A5. View of aft cockpit showing left console panel.

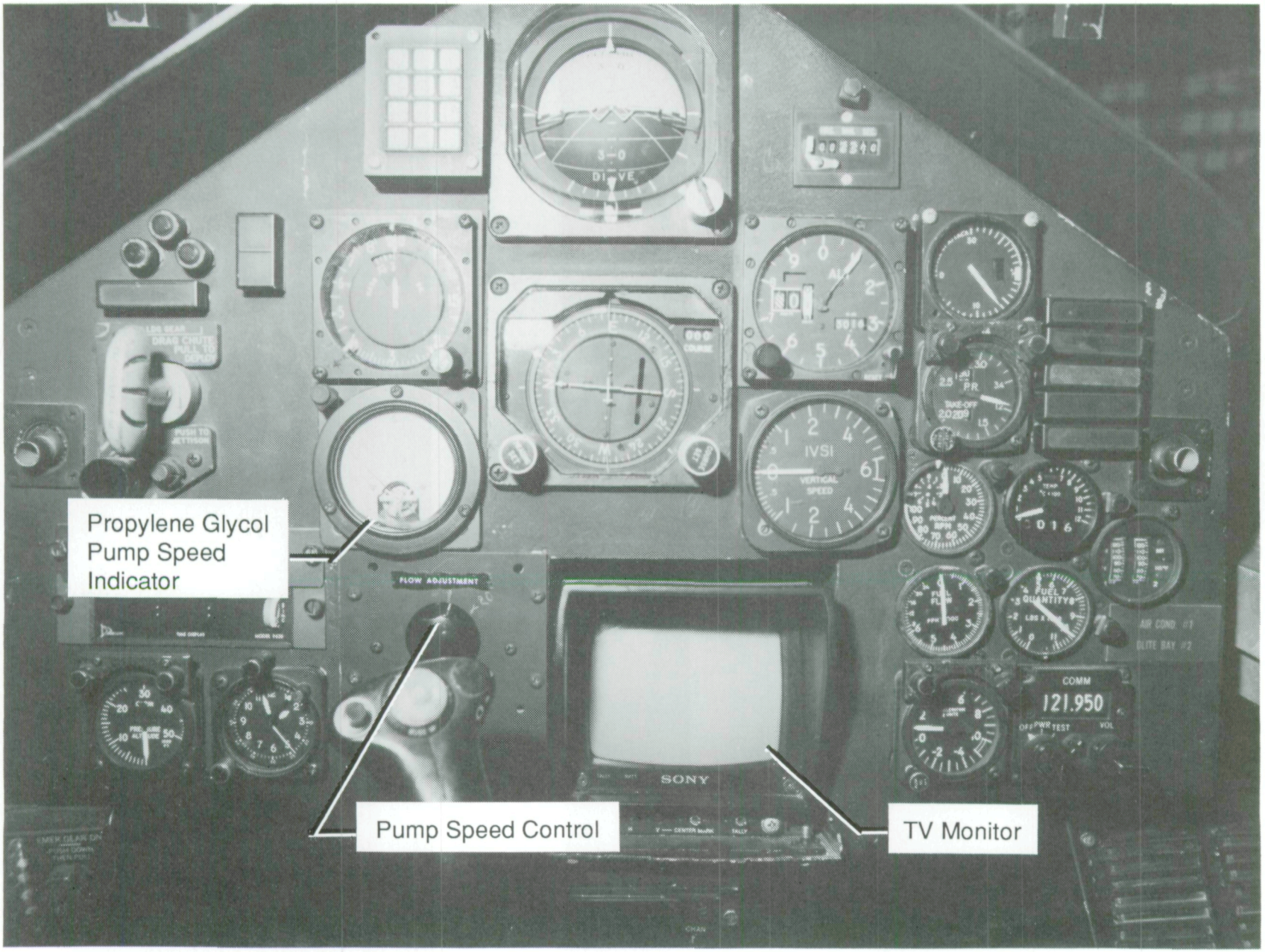

L-90-5581

Figure A6. View of aft cockpit showing instrument panel.

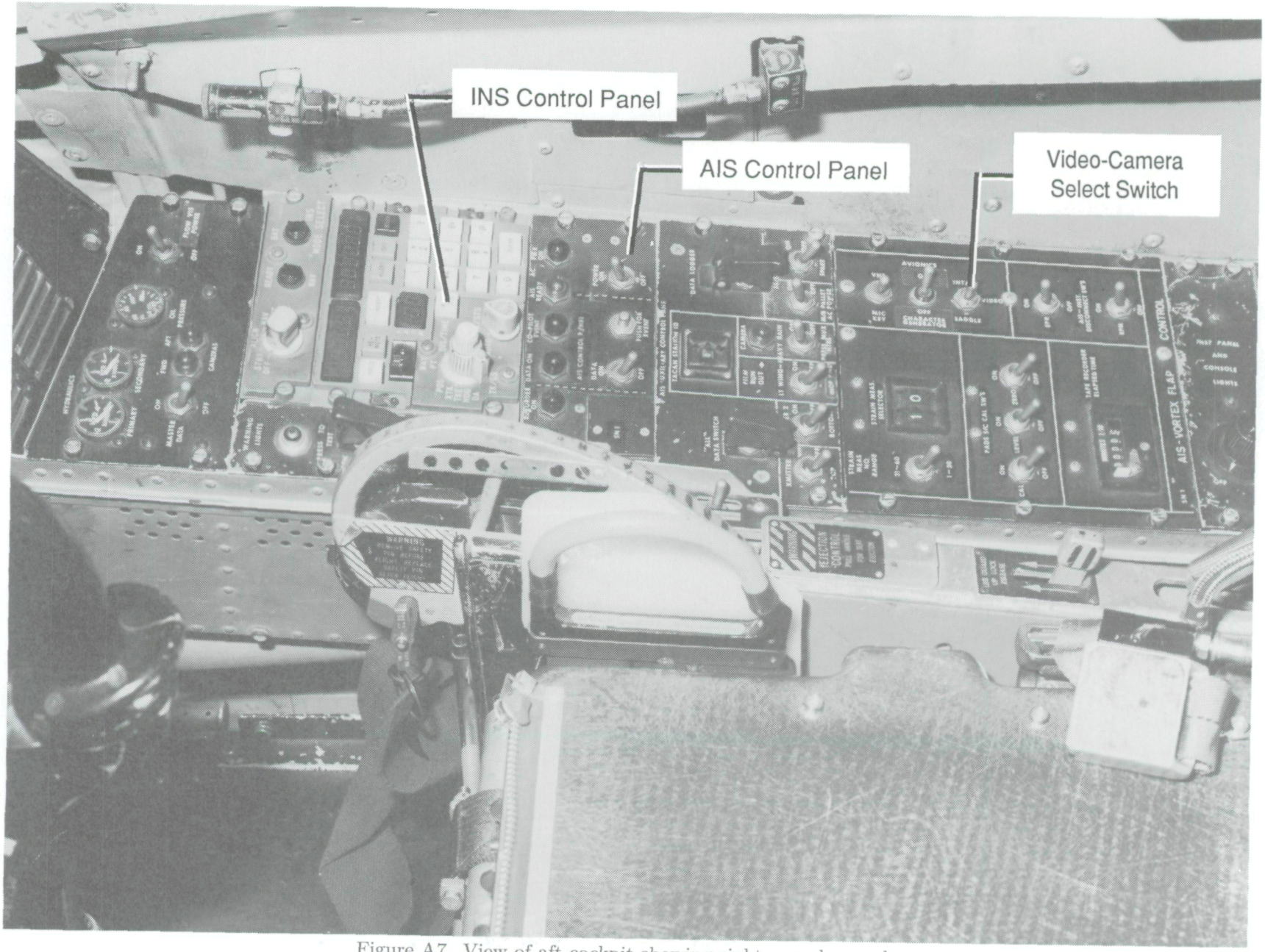

Figure A7. View of aft cockpit showing right console panel.

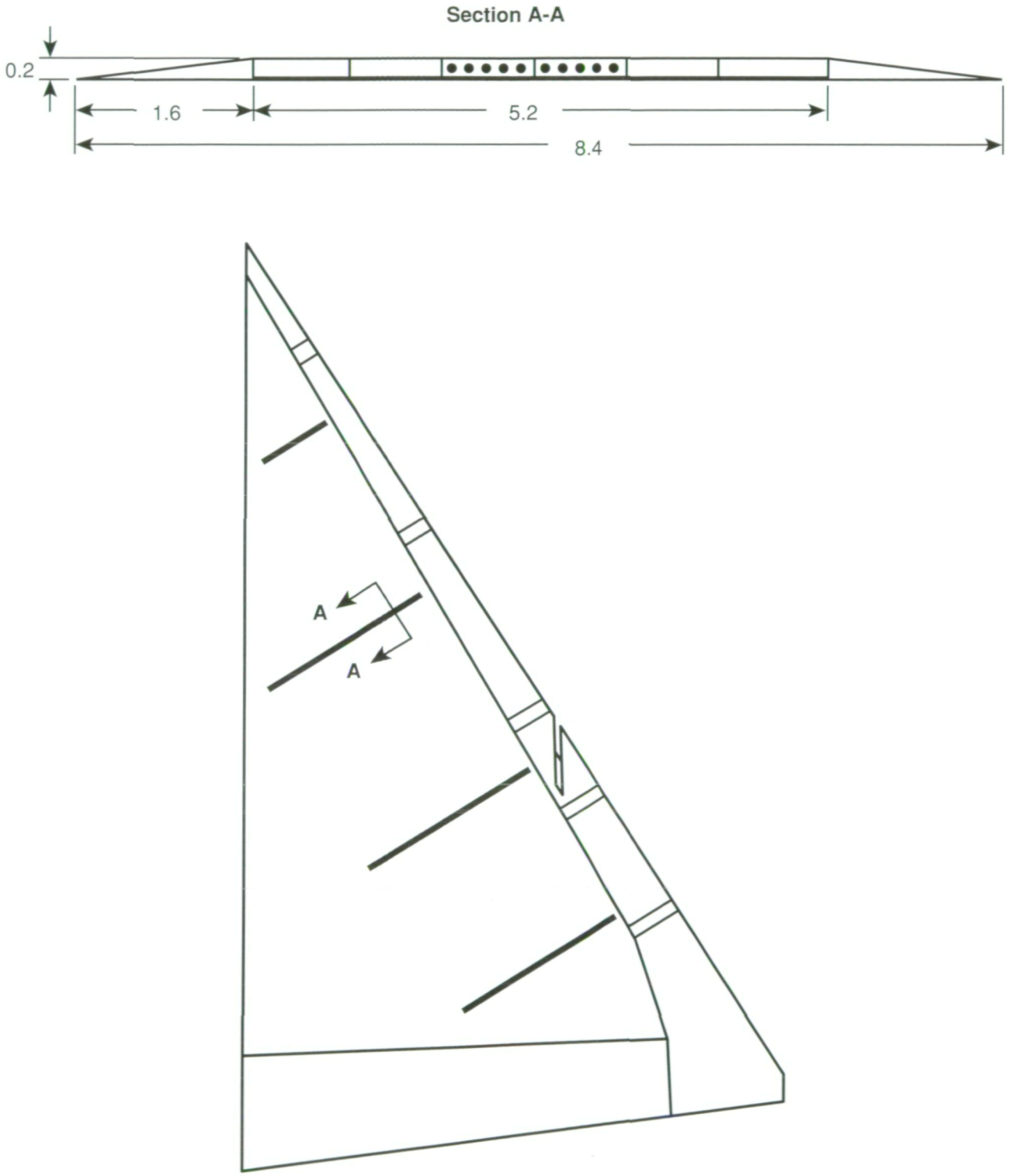

Figure A8. Cross section of pressure belt set as mounted on F-106B aircraft. Dimensions are in inches.

Appendix B

Description and Features of Computer Process for Image Analysis

A computer process was developed to aid in the quantitative and qualitative analysis of images produced by the off-surface rotating vapor-screen technique. The process is a combination of digital-image processing, computer graphics, and photogrammetric reconstruction techniques for projecting 2-D images into 3-D images. This appendix describes each step of the computer process, beginning with the digitization of the flight-test videotapes and ending with an interactive computer graphics environment for displaying 3-D vapor-screen images, core paths, and reattachment points above the surface of the F-106B wing. Figure B1 illustrates the data flow of the computer process and serves as a guide for this appendix.

Digitization Procedure

The selected frames from the videotapes for each flight/serial and from the 1987 wind-tunnel test were digitized on the Video Image Processing System (VIPS) at the Langley Data Visualization and Animation Laboratory (DVAL). The VIPS is a combination of hardware and software designed to provide an interactive capability for processing videotape images of wind-tunnel or flight experiments. The system is controlled from a Sun Microsystems Sun-3 host computer and consists of an Imaging Technologies Series 150/151 Modular Image Processing Subsystem, various video equipment, and a Storage Concepts Real-Time Digital Disk (RTDD). The software interface is the Noesis Vision VISILOG Image Processing Software. The VISILOG software includes a software script mode that allows recording and playback of a sequence of instructions for achieving a specific goal. This feature was used to facilitate digitizing the flight/serial video images. A script was written that included commands for digitizing sequences of video frames and storing the digitized images on the RTDD. Once a sequence of frames was stored on the RTDD, a program for computing the corresponding real-time disk frame location from a specified time code was employed to recall and save only the frames of interest. The time codes for these video frames were obtained from the event time column of the tables detailing specific video frames of interest for each flight/serial. The visual time code located in the lower left corner of each image was compared to the time code in the event time column for verification. A similar procedure was used to digitize the wind-tunnel videos. Although there was no visual time code on the wind-tunnel videos, a table of event times indicating relative locations for the frames of interest was used in conjunction with audio cues indicating angle of attack, Mach number, and light-sheet station to ensure accuracy.

The 2-D digital images are composed of 512 by 480 pixels. Each pixel location has an integer gray-level value from 0 (black) to 255 (white) assigned to it, determined by the brightness of the image at that location. The digital image can be thought of as a 2-D array of values, $G(m, n)$ for $m = 0, 1, \ldots, 511$ and $n = 0, 1, \ldots, 479$, where $0 \leq G(m, n) \leq 255$. The array indices m and n are used to determine the column and row locations, respectively, of a pixel in the image.

Image File Naming Convention

The results for each digitized flight image were saved according to a naming convention based on the flight number, the camera location (top or side), the serial number, and the light-sheet angle Φ. (Note that for this appendix and associated figures, the year (91) is omitted from the flight number to save keying effort.) A typical path name for a digitized and saved image with its ".vis" suffix would have been Flight15/Top/05/112.8.vis. A schematic of the directory structure is as follows:

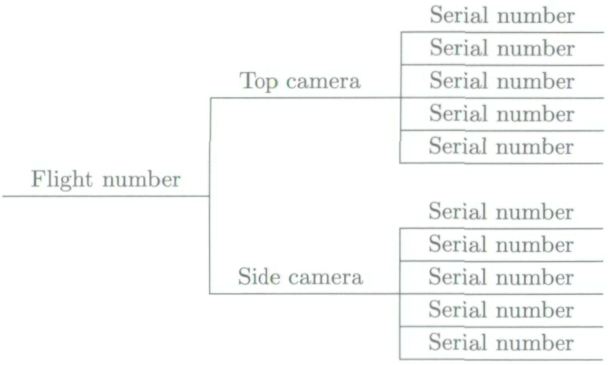

A similar naming convention was used for the wind-tunnel images. The serial number in that case was the angle of attack of the model, and the light-sheet station was used in place of the light-sheet angle.

Image Enhancement and Feature Extraction Procedures

Two separate procedures for processing the 2-D vapor-screen images were developed at the DVAL using the Precision Visuals Workstation Analysis

and Visualization Environment (PV~WAVE) software system on a Sun workstation. The procedures take advantage of the many built-in capabilities of the PV~WAVE software system for analyzing and displaying image data. One procedure, **Enhancer**, provides an interactive capability for enhancing the flight vapor-screen images. The second procedure, **Extractor**, provides an interactive capability for extracting core and reattachment points inside a region of interest. Each procedure is discussed separately below.

Enhancer *Procedure*

The **Enhancer** procedure (see video sequence 7 in supplement) consists of capabilities for enhancing flight and wind-tunnel vapor-screen images using standard image processing techniques (ref. 19). The procedure has two main stages. The first stage, `Image Selection`, provides file management capabilities for creating a list of image files with common attributes. The second stage, `Image Enhancement`, provides enhancement capabilities for the list of images created during the `Image Selection` stage.

`Image Selection` *stage.* This stage creates a partial list of image files for processing based on a specified range of light-sheet angles. A file containing the complete list of image files spanning all the flight directories can be used as input to this stage, or files containing subsets of the complete list can be used to reduce the number of images considered for processing during a given session. The user is prompted as follows (typical responses are shown in boldface type):

`Enter starting light sheet angle to process` > **100**

`Enter ending light sheet angle to process` > **102**

`Enter filename containing group of files to consider` > **group1**

A previewing window appears in the center of the Sun workstation display, and each image satisfying the light-sheet range criteria is displayed one at a time along with its full path name. As each new image appears, a menu of options is displayed:

`File Review Options`

`Use file`

`Do not use file`

`Stop`

The process continues until the user selects the `Stop` option or until all the images corresponding to the specified range of light-sheet angles have been displayed. Once the `Image Selection` stage is complete, only those images for which the `Use file` option was selected will be considered for processing in the `Image Enhancement` stage.

`Image Enhancement` *stage.* This stage allows a sequence of processing steps to be applied to the images in the list and the processed images to be saved to the workstation hard disk. A window entitled "Original Image" appears in the upper left corner of the display. The first image selected during the `Image Selection` stage is displayed in this window along with its full path name. Pseudocolor, an arbitrary assignment of color to gray-level value, is applied to the image in an attempt to make contrast variations more evident. A menu of options is displayed:

`Choose:`

`Enhance this image`

`Continue to next image`

`View a movie of the list`

`Exit the program`

Only the first option in the menu is discussed in detail below; the other options are self-explanatory.

In the `Enhance this image` option a window entitled "Enhanced Image" appears in the lower right corner of the workstation display. The results of each step of the enhancement process appear in this window so the user can compare the differences between the original image in the top left "Original Image" window and the enhanced image in the bottom right "Enhanced Image" window. The output of each step in the processing sequence becomes the input to the subsequent step. At any time the user can opt to return to the original image and start over. The following submenu of options appears:

`Choose:`

`Smooth image`

`Contrast stretch`

`Contour`

Each option in the submenu is discussed below. For more detail on these three processing options, see reference 19.

The `Smooth image` option performs a 3- by 3-pixel "running average" of the input image G to produce an output image G'. Note that regardless of the process, or the iteration of a particular process, the input image is always called G and the output

image is always called G'. Each pixel in G' is the average of the corresponding pixel and its eight nearest neighbors in G, as shown in the following equation:

$$G'(m,n) = \frac{1}{9} \sum_{i=-1}^{1} \sum_{j=-1}^{1} G(m-i, n-j)$$

This option is typically exercised three times before proceeding to the next step.

The `Contrast stretch` option performs a linear contrast stretch on the input image. The technique improves the contrast of an image by linearly mapping each gray-level value within a user-specified range onto the entire gray-level range of 0 to 255. The technique automatically finds the minimum and maximum gray-level values in the input image and displays these values in a separate menu, followed by options to either use this range of values or specify a different range. If the user specifies values greater than the minimum value and less than the maximum value, then values in the image below the specified range are cropped to black and values above the specified range are cropped to white.

The `Contour` option highlights selected gray-level values in the input image by turning them black. A cursor positioned inside a color bar is used to interactively select the contours. Using the computer mouse, the user positions the cursor over a desired color to be made black and presses the mouse button. The capability to undo contours also exists.

A sample session of the **Enhancer** procedure is shown in figure B2(a). The top left image window displays the original vapor-screen image, along with the full path name indicating the image was obtained from the top camera during flight 17, serial 07, with a light-sheet angle of 84.6°. The application of pseudocolor to the image is evident. The image displayed in the bottom right window is the result of an enhancement sequence with smoothing, contrast stretching, and contouring steps. A menu is displayed in the "Enhanced Image" window with the following options:

```
Choose:

Continue enhancements to this image

Start over, enhance original image

Save enhanced flight image

Save enhanced wind tunnel image

Exit enhance menu, do not save image
```

The user indicates the processing of this image is complete by choosing the `Save enhanced flight image` option. The enhanced image is then stored on the disk in Sun raster file format. An additional step is performed prior to saving enhanced wind-tunnel images. A monochrome image of the wind-tunnel model is combined with each color-enhanced vapor-screen image. A special lookup table that has a gray-scale ramp in the lower half and a pseudocolor scale in the upper half is used for this purpose. The combined image G' is defined in terms of the enhanced vapor-screen image G and the model image M as follows:

$$G'(m,n) = \begin{cases} (1/2)\,G(m,n) + 128 & \text{for all } m \text{ and } n \text{ such that } G(m,n) > \texttt{clip} \\ (1/2)\,M(m,n) & \text{elsewhere} \end{cases}$$

where the value of the parameter `clip` can be increased or decreased to allow less or more, respectively, of the vapor-screen image to appear.

Extractor *Procedure*

General. The **Extractor** procedure (see video sequence 4 in supplement) computes the weighted centroid of pixels having gray levels within a specified range and located within a user-defined region of interest in a 2-D image. The procedure is capable of locating up to four centroids per image, after which the column and row centroidal results for each core are output to a file. The procedure creates a list of all the image files in the current directory for processing. Therefore, the user must change to the desired directory (e.g., Flight16/Top/07) before starting the procedure. The default name for the output file containing the centroid locations is `core_locations`. The `core_locations` file contains nine columns of output. The light-sheet angle, obtained from the image file names, is output to the first column. The other eight columns, initialized to -1, contain column and row locations for up to four centroids.

At the start of the procedure, a window, entitled "Original Image," appears in the upper left corner of the display. The first image on the list is displayed in this window with pseudocolor applied. The following menu of options is displayed:

```
Select one:

Enhance this image

Define region of interest for this image

Continue to next image

Show movie of this directory
```

Each option in the menu is discussed in detail below.

The `Enhance this image` option allows a sequence of processing steps to be applied to the images

on the list and the processed images to be used for computing the centroids. The same three processing techniques discussed for the **Enhancer** procedure—smoothing, contrast stretching, and contouring—are available here.

The `Define region of interest for this image` option provides the user with an interactive capability for defining an irregular region of interest in the image by using the mouse. Only pixels inside this region of the image will be considered when computing the centroid. Once the user has finished defining the region of interest, the procedure begins the centroid computation. A detailed discussion of the centroid computation is given in the next section.

The `Continue to next image` option allows the user to skip over an image on the list.

The `Show movie of this directory` option provides a capability for looking forward and backward through the image sequence. Mouse buttons are used to control the direction of the movie. Only images on the list will be displayed.

Weighted centroid computation. The centroid computation is initiated each time a region of interest is defined for an image. The actual computation is restricted to region-of-interest pixels having gray-level values within a specified interval. The following steps are performed:

1. Find the local maximum gray level inside the region of interest and call this gray-scale value `max`.
2. For a given value of k, define a gray-level range from $l_1 = \texttt{max} - k + 1$ to $l_k = \texttt{max}$.
3. Find the subset S of region-of-interest pixels with gray levels in the above range.
4. Solve the following equations for finding the respective column and row locations of the weighted centroid:

$$m_{\text{centroid}} = \left[\sum_{w=1}^{k}\sum_{i=1}^{c(l_w)} m_i\,(l_w)\,w\right] \Bigg/ \left[\sum_{w=1}^{k} c\,(l_w)\,w\right]$$

and

$$n_{\text{centroid}} = \left[\sum_{w=1}^{k}\sum_{i=1}^{c(l_w)} n_i\,(l_w)\,w\right] \Bigg/ \left[\sum_{w=1}^{k} c\,(l_w)\,w\right]$$

where w serves as a weighting factor, $c(l_w)$ is the number of pixels in S with gray level l_w, and $m_i(l_w)$ and $n_i(l_w)$ are the column and row locations, respectively, of the ith pixel with gray level l_w.

For example, if $\texttt{max} = 230$ and $k = 5$, then region-of-interest pixels with gray-level values from 226 to 230 are included in the weighted centroid computation. Increasing the value for k increases the number of pixels contributing to the centroid location. The computation weights pixel locations with gray-level values near the upper end of the interval more than locations with values near the lower end of the interval.

After the computation of the weighted centroid is complete, the user is prompted to specify a core number, 1 to 4. This number is used to match up vortex cores with the various light-sheet angles. After a core number has been specified, the computed location for the core is indicated in the "Original Image" window as the intersection of a white cross. Pixels contributing to the location of the core are made black for easy identification. The user has the capability to zoom in on any region of the "Original Image" window by positioning the mouse cursor over the desired center of the zoom and pressing a mouse button. The expanded region is displayed in a new window. A sample session of the process is shown in figure B2(b). The white cross indicating the location of the core and the black pixels representing the subset of the region of interest used in the computation are evident. The region centered about the white cross can be inspected more closely by examining the "Zoomed Image" window. After zooming is completed, a new menu of options is displayed:

`Save these values and continue to next image`

`Locate an additional core for this image`

`Increase intensity range for finding centroid`

`Redefine region of interest`

`Display all core locations for this image`

`Exit`

Each option is discussed below.

The `Save these values and continue to next image` option allows the user to save all the centroid locations found for the current image and continue to the next image on the list.

The `Locate an additional core for this image` option allows the user to specify multiple cores (up to four) for the current image.

The `Increase intensity range for finding centroid` option allows the user to increase the value

for k used in the weighted centroid computation. Initially, k is set to 5. Each time this option is selected for an image, k is increased by 5. The effect of increasing k is to allow more pixels to contribute to the centroid location.

The `Redefine region of interest` option allows the user to redefine the region of interest. A new centroid location is found based on the new region.

With the `Display all core locations for this image` option, locations for all cores previously defined for the current image are displayed in the "Original Image" window as the intersections of white crosses.

Photogrammetric Reconstruction Procedures

The result of applying the digitization and extraction procedures to all flight/serial combinations of interest is a data base, on a Sun workstation, consisting of core locations and reattachment points for each light-sheet angle. Although this data base is inherently 2-D, quantitative 3-D information can be extracted by implementing the photogrammetric reconstruction techniques described in appendix C. The calculations and interactive displays are performed on a Silicon Graphics IRIS 340/VGX Graphics Workstation. This implementation consists of two procedures: (1) the **Reconstructor**, which was developed at the DVAL to access the selected flight/serial and performs the 3-D projection, and (2) the Flow Analysis Software Toolkit (FAST), which renders the results for viewing.

The reconstruction technique requires parameters that describe the placement of the cameras and the rotating light-sheet system onboard the F-106B. Once these parameters are known, the intersection of the camera viewing pyramid with a light-sheet plane can be quantitatively determined. With the camera calibration and subsequent refinement procedures described in appendix C, three sets of parameters were obtained to describe the position, orientation, and imaging properties of the top, side, and dislocated (during F/S 91-16/07) side cameras. In addition, the position of the light-sheet mirror was obtained from measurements on the aircraft. These parameters were placed in ASCII files on the IRIS workstation in a format accessible to the **Reconstructor** procedure.

The **Reconstructor** procedure is a set of UNIX scripts and C-language programs that allow a user to select a flight/camera/serial combination for subsequent 3-D projection and display. The following command, for example, is issued at the UNIX prompt to request a specified host IRIS to reconstruct the data obtained from the top camera during flight 16, serial 07:

```
unix% show top 16 07 irishost
```

Images from the side camera may be displayed separately or simultaneously. The script accesses core locations, reattachment points, vapor-screen images, and light-sheet angles from the specified directory on the Sun computer (Flight16/Top/07 in this example). This information is combined with the camera and light-sheet parameters on the IRIS workstation to produce a complete set of inputs for the photogrammetric calculations.

The task of the **Reconstructor** procedure is to assign four floating-point values (floats) to each pixel in a vapor-screen image: an intensity value and its three Cartesian coordinates. The intensity value is obtained from the original digitized image, and the coordinates are determined using the photogrammetric equations in appendix C. However, because of memory, disk space, and speed limitations on the IRIS workstation, it is necessary to reduce the resolution of the reconstructed images. Each 512- by 480-pixel image requires 7.5 megabytes of storage space when reconstructed, and a typical serial containing 20 images would therefore require 150 megabytes:

$$(20 \text{ images}) \left[\frac{(512)\,(480) \text{ pixels}}{\text{image}} \right] \left(\frac{4 \text{ floats}}{\text{pixel}} \right)$$

$$\times \left(\frac{8 \text{ bytes}}{\text{float}} \right) \left(\frac{1 \text{ megabyte}}{2^{20} \text{ bytes}} \right) = 150 \text{ megabytes}$$

This result exceeds the 64-megabyte physical memory capacity of the IRIS workstation and introduces significant delays when an interactive display is attempted. However, by reducing the number of rows and columns used to 25 percent, only 9 megabytes of storage space are required to describe a typical set of reconstructed vapor-screen images. This size is well within the physical memory capacity of the IRIS workstation and provides a highly interactive environment when rendered by FAST.

The resolution is reduced through a subsampling of each image such that each pixel in the smaller image represents the average of a 4- by 4-pixel region in the original image. The loss in spatial resolution due to subsampling is alleviated somewhat by the smooth rendering capabilities of the FAST package and becomes apparent only when reconstructed side-camera images are viewed closely. The size of the subsampling region (M_s by N_s) is actually made adjustable in case higher resolution is required. The

subsampled image is obtained with the following equation:

$$G'(m', n') = \frac{1}{M_s N_s} \sum_{i=0}^{M_s-1} \sum_{j=0}^{N_s-1} G\left(m' M_s + i, n' N_s + j\right)$$

for $m' = 0,\ 1, \ldots,\ M/M_s$ and $n' = 0,\ 1, \ldots,\ N/N_s$, where $M = 512$ and $N = 480$.

Vortex cores and reattachment points obtained from the **Extractor** procedure are projected into 3-D in much the same manner as individual pixels within an image. Each centroid represents one pixel location that is mapped onto the light-sheet plane. Successive vortex cores from one flight/serial are reconstructed to comprise a core path, and several reattachment points make up a reattachment line. The **Reconstructor** procedure also computes the distance of each core and reattachment point from the leading edge along the light-sheet footprint for later analysis.

The **Reconstructor** procedure produces three output files. The first file is a binary PLOT3D (ref. 20) geometry file that contains 3-D coordinates of vapor-screen images, vortex-core paths, reattachment lines, and leading-edge intersection points. The second file is a PLOT3D function file that associates a scalar value for each coordinate in the geometry file. The scalar values include image intensities, light-sheet angles, and distances of cores and reattachment points from the leading edge. An additional file containing all but the vapor-screen data is created in the Transferable Output ASCII Data (TOAD) format (ref. 21). This file is saved within the data base on the Sun SPARCstation and facilitates the production of 2-D plots such as those shown in figures 17 to 23 and figures 30 to 33.

The binary geometry and function files produced by the **Reconstructor** procedure are automatically accessed by a script that initiates the FAST package. This script also reads in a geometric description of the F-106B and pertinent wing features including access straps, paint lines, and leading-edge slot. The FAST package allows the simultaneous display of 3-D core paths, reattachment lines, vapor-screen images, and leading-edge intersection points in relation to the wing features. Using the FAST controls, the user may view this data set from any angle, extract the 3-D coordinates of any point, and display image intensities within any given range. Additional features include transparency, contouring, isosurfaces, and animation. The animation capability within FAST was used to generate several sequences in the video supplement.

Technique Developed for 1985 Flight Images

The images from the 1985 flight experiment have been analyzed and reported in reference 4. Two-dimensional analysis techniques sufficed for these images because the light sheet was stationary. In order to map the digital images saved from the 1985 flight experiment into 3-D space for viewing in FAST, a new technique was required. The photogrammetric reconstruction technique developed for the 1991 flight images could not be applied to the 1985 images because the required camera parameters were not obtained at the time of the 1985 flight experiment. The new technique developed was aided by the existence of a digital image from 1985 of a grid composed of 6-in. squares, laid out on a 4- by 8-ft plywood sheet. (See fig. B3.) The grid was positioned along the light-sheet footprint and imaged with the camera in its flight position (only a 4- by 7-ft area was visible to the camera). The three basic steps to the technique were as follows:

1. Correct the vapor-screen images, viewed at an angle, for perspective distortion.
2. Create a 6- by 6-in. grid in 3-D space to represent the physical grid.
3. Distribute the pixels from the corrected image evenly over the grid that was created.

Step 1 was achieved by performing a polynomial warping of the vapor-screen images. Single pixels representing the intersections of the horizontal and vertical grid lines in the digital image were used as control points, or tie points, in the procedure. The original location of each of these points was known with respect to an arbitrary origin. Also, the pixel coordinates (m, n) of each control point in the acquired image were known. Based on this knowledge, it was possible to obtain the polynomial coefficients to transform the acquired image into an undistorted image. The PV∼WAVE Users' Library procedure POLYWARP was used to obtain the polynomial coefficients to perform a third-order polynomial warping. The PV∼WAVE function POLY 2D was used to actually perform the geometrical transformation based on the coefficients computed by POLYWARP. The undistorted images were saved for use in the third step.

Step 2, which involved estimating the 3-D coordinates of the physical grid, was achieved with the knowledge of the constraints used to place the grid above the wing:

1. The grid was constrained to the light-sheet plane.

2. The most outboard point along the bottom edge of the grid was directly above the leading edge.
3. The bottom of the grid was flush with most of the upper surface of the wing.
4. Each square was 6 in. on a side.

The light sheet was emitted from a lamp at FS 480.0 and BL 37.0, was oriented at an angle of 78.8° to the aircraft centerline, and remained perpendicular to the left-wing surface. The 3-D coordinate at which this plane intersected the leading edge was determined by inspecting the wing geometry in the FAST environment. This coordinate represented the approximate location of the most outboard point along the bottom of the grid. The remaining points were computed by using 6-in. spacing horizontally and vertically within the light-sheet plane. A rotation transformation within the light-sheet plane was then applied to the entire 3-D grid until its bottom edge was flush with most of the upper surface of the wing.

The transformations required to generate this 3-D representation of the gridded plywood sheet were applied to step 3 of the technique, which evenly distributed pixels from an undistorted image over the grid. Knowing that the pixels of the undistorted image corresponded to a region of 4 by 7 ft in object space, the user could determine the appropriate horizontal and vertical spacing between pixels. When this spacing was used in place of the 6-in. spacing above, the 3-D coordinates of a reconstructed image covering the desired area were obtained.

The **Reconstructor** procedure was modified such that images from the 1985 flight could be displayed within the FAST environment along with data from the rotating vapor screen in 1991. As a result, core paths and reattachment points obtained from the rotating vapor screen could be correlated with the vortex structures present in the stationary vapor screen.

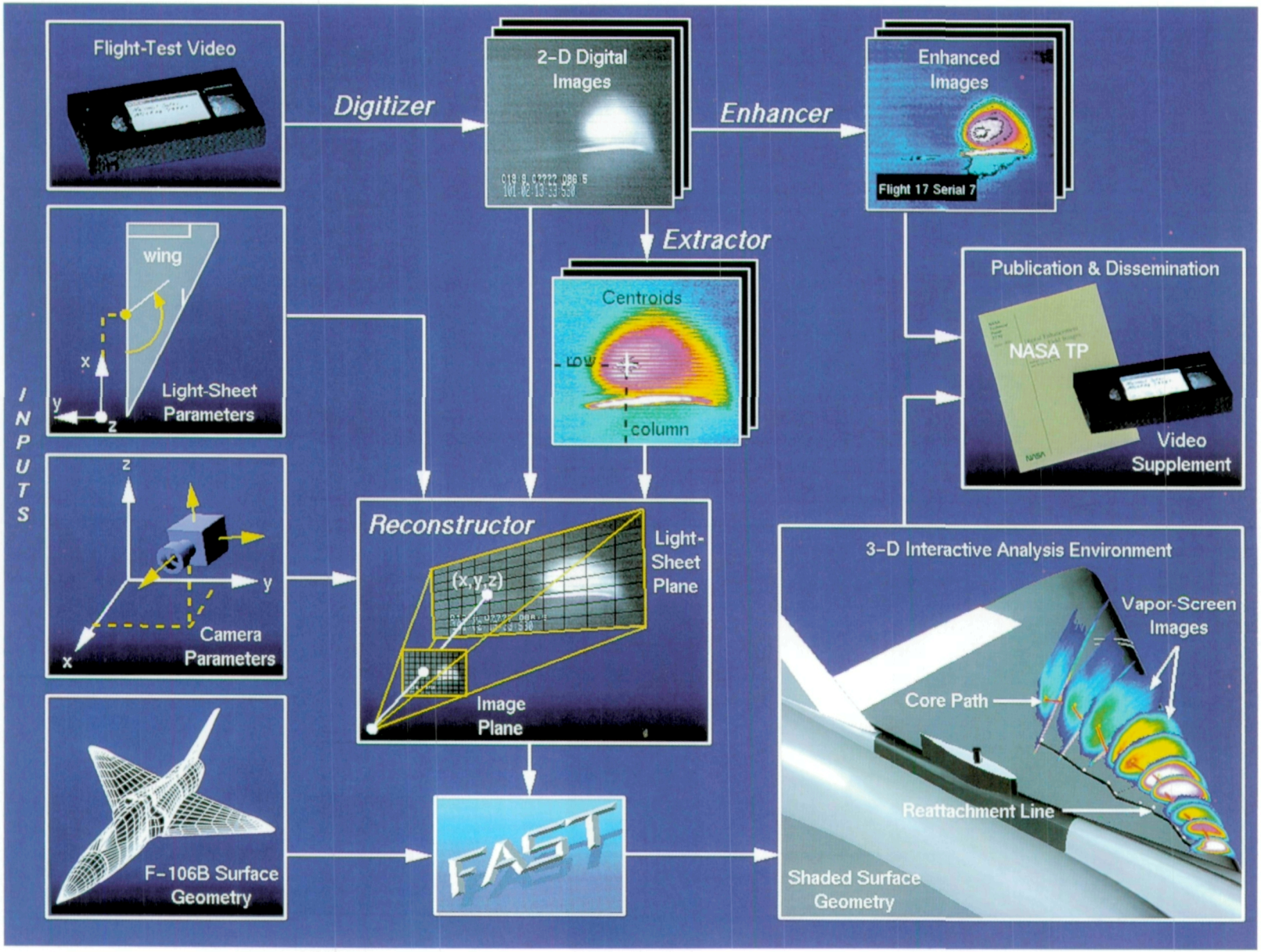

Figure B1. Data flow diagram of computer process for analyzing images.

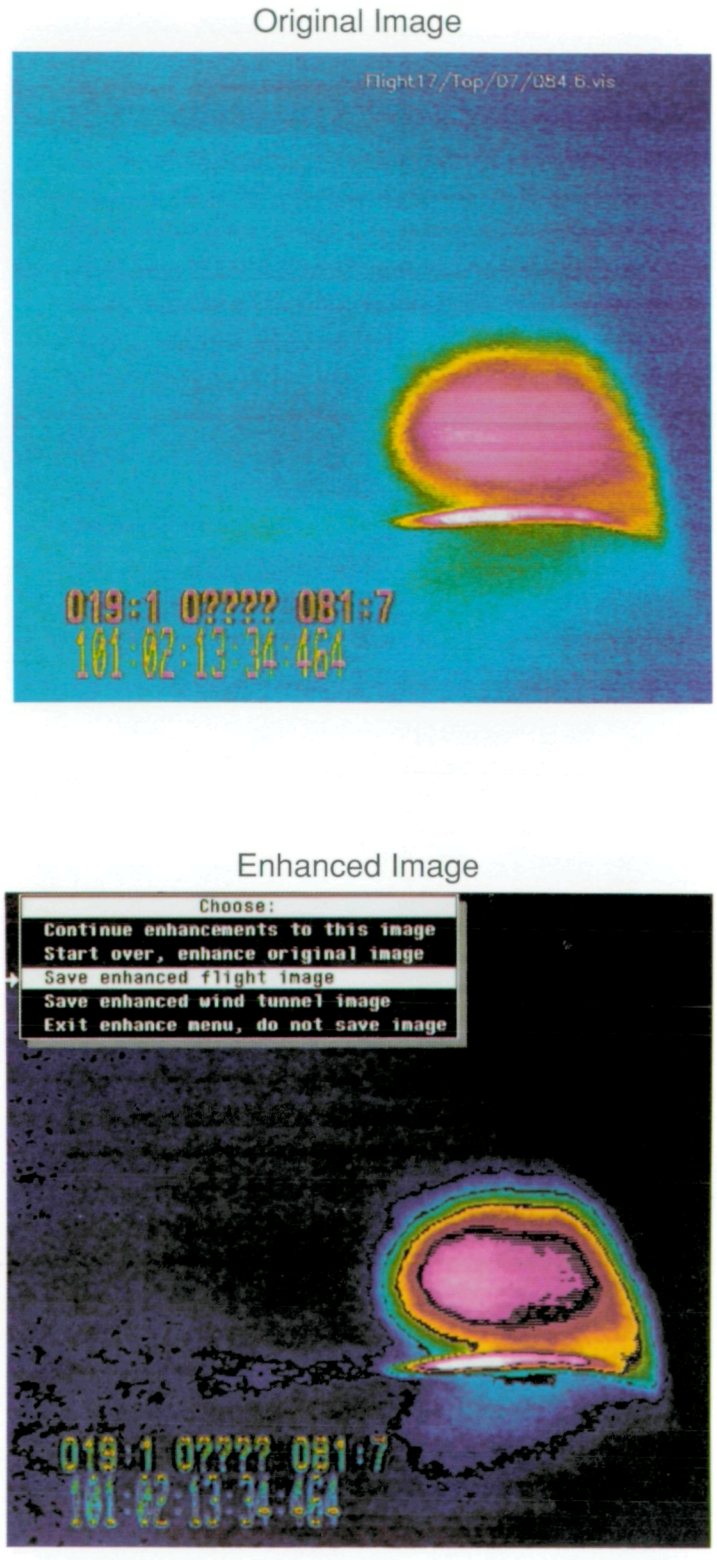

(a) **Enhancer** procedure.

Figure B2. Screens from interactive computer sessions for image-processing procedures.

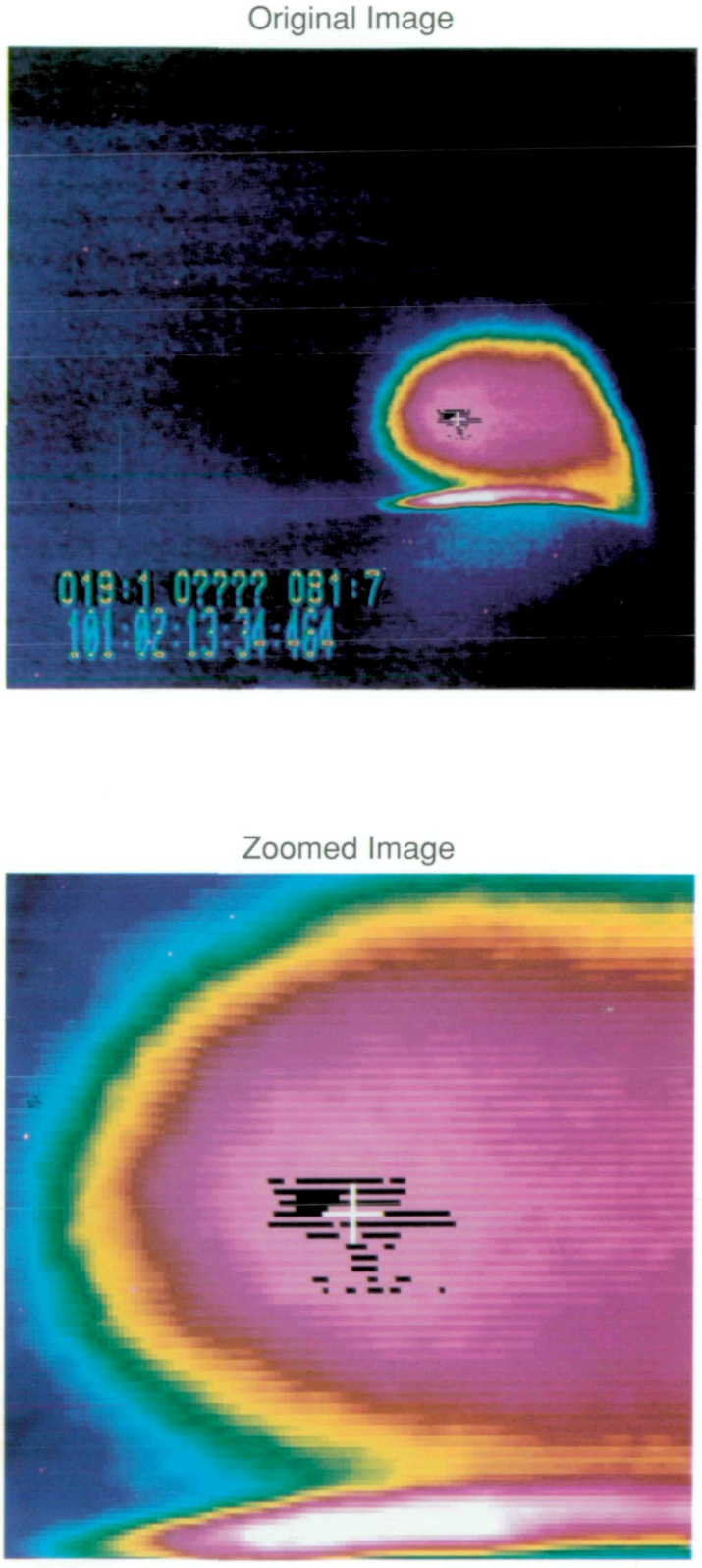

(b) **Extractor** procedure. (White cross indicates core locations and black pixels indicate those pixels used to compute core.)

Figure B2. Concluded.

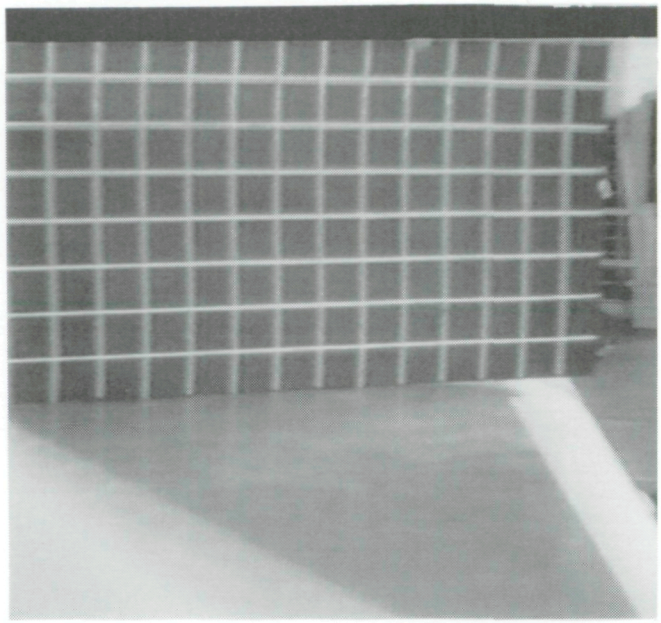

L-93-33

(a) Grid image.

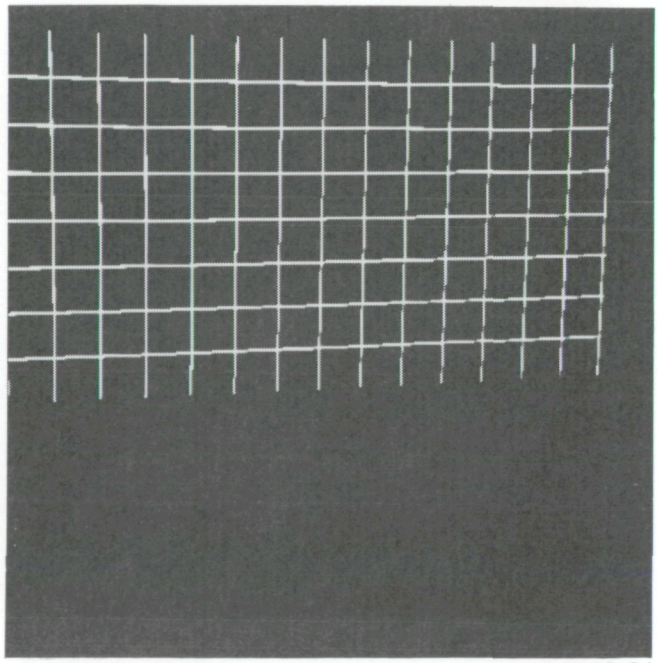

L-93-34

(b) Warping board representation of grid.

Figure B3. Grid image from top camera in hangar during 1985 flight test of F-106B aircraft.

Appendix C

Photogrammetric Reconstruction of Light-Sheet Images

This appendix addresses the technique used to derive 3-D data from the F-106B vapor-screen flow visualization system described in this report. A more detailed description of the general technique is given in reference 22. The technique is a modified form of close-range stereo photogrammetry. *Photogrammetry* has been described as "the science or art of obtaining reliable measurements by means of photography." (See ref. 23.) It is based on modeling the imaging properties of a camera as an ideal pinhole camera. (See ref. 24.) For a pinhole camera, a ray of light travels in a straight line from the object to be measured, through the pinhole, and intersects the image plane. For simple lenses, the pinhole can be approximated with the center of the lens aperture. If the locations of the image and the aperture are known, an equation for a line passing through the object can be written. The position of the object is still unknown because it can lie anywhere on the line and the light ray from it will always strike the same image location. If another camera view of the object is available, a second equation for a line passing through the object is obtained and its location is given by the intersection of the two lines. This triangulation technique with two cameras is known as *stereo photogrammetry*. The simple case where the camera axes are parallel is illustrated in figure C1.

When only one view is available, the object location can still be determined if additional information is available restricting the object's position along the line. In this experiment, the extra information is the equation of the plane in which the data must lie because only a single light-sheet plane is viewed in each image. The object location is determined by finding the intersection of the line with the plane, analogous to standard stereo photogrammetry. In figure C2, one of the cameras is replaced with a light sheet. The equations used for reconstructing the light-sheet data are developed below.

The position vectors of the aperture, image, and object are, respectively,

$$\mathbf{a} = \begin{bmatrix} x_a \\ y_a \\ z_a \end{bmatrix} \quad \mathbf{i} = \begin{bmatrix} x_i \\ y_i \\ z_i \end{bmatrix} \quad \text{and} \quad \mathbf{o} = \begin{bmatrix} x \\ y \\ z \end{bmatrix}$$

The parametric equations for the line connecting these points can be found by observing that the desired object point is on the line if and only if $\mathbf{o} - \mathbf{a}$ and $\mathbf{a} - \mathbf{i}$ are parallel, or equivalently,

$$\mathbf{o} - \mathbf{a} = t\,(\mathbf{a} - \mathbf{i}) \tag{1}$$

for some scalar t. This is illustrated in figure C3. The image corresponds to $t = -1$, and the aperture corresponds to $t = 0$. Values for $t > 0$ produce the range of possible object points.

An illustration of the position vectors with respect to aircraft and light sheet, in the coordinate system used, is shown in figure C4. (The relationship between distances along the coordinate axes and distances on the aircraft is given subsequently.) Let

$$k_1 x + k_2 y + k_3 z + k_4 = 0 \tag{2}$$

represent the plane of the light sheet. The location of the object point can be found by substituting the x and y parametric equations for the line into the equation for the plane and solving for t. The result is

$$t = -\frac{k_1 x_a + k_2 y_a + k_3 z_a + k_4}{k_1 (x_a - x_i) + k_2 (y_a - y_i) + k_3 (z_a - z_i)} \tag{3}$$

Substituting this value for t into equation (1) yields the following 3-D coordinates for the object points:

$$\left.\begin{aligned} x &= t\,(x_a - x_i) + x_a \\ y &= t\,(y_a - y_i) + y_a \\ z &= t\,(z_a - z_i) + z_a \end{aligned}\right\} \tag{4}$$

With the aid of figure C4 the coefficients representing the *rotating* light sheet for this experiment have been determined to be $k_1 = 1$, $k_2 = \frac{-1}{\tan \Phi}$, $k_3 = 0$, and $k_4 = \frac{0.40}{\tan \Phi} + 438.68$.

A powerful extension of this technique can be used to map real imagery onto an arbitrary surface comprised of polygons. The typical computer model of an aircraft surface is a polygonal surface such as the one used to represent the F-106B in this experiment. An equation like equation (2), appropriately bounded, represents one facet of such a polygonal surface. This technique was used to map surface oil-flow images onto the F-106B wing-surface geometry model, as shown in figure 50. This technique is discussed in greater detail in reference 22.

The raw data consist of video images of vapor-scattered light which were recorded in flight. Of the active horizontal video lines, 480 were divided into 512 8-bit samples to create a 245 760-byte digital image. A typical image from each camera is shown in the top two images of figure 6. Each sample, called a pixel, is assigned to an image location **i** through a careful calibration procedure discussed below. The aperture location is also determined as part of the calibration procedure. Using equation (4), every pixel's scattered light intensity value is assigned to its appropriate location with respect to the aircraft.

Although the above analysis is straightforward, the technique is complicated by the need to account for the nonideal behavior of the real imaging system and to determine the location and orientation of the camera and the light-sheet plane in the aircraft reference frame.

The calibration procedure involves three steps. The first step, performed in the laboratory, is to calibrate the camera-VCR-digitization system to ensure that the system functions very nearly like a pinhole camera. This procedure, called *analytic self calibration*, corrects for lens distortion and decentering and scale changes in the digitization process and determines the focal length of the lens. (See ref. 25.) The camera calibration process determines a total of 10 parameters known as elements of *interior orientation.*

The second calibration step, called *space resection*, is performed with the camera located on the aircraft in the proper flight position. By imaging targets with known locations in the aircraft reference frame, the location of the camera aperture **a** and a rotation matrix describing the camera orientation are determined. (See ref. 26.) An image from each camera showing the set of resection targets used is shown in the bottom two images of figure 6. The space resection process determines six parameters for each camera. These parameters are called elements of *exterior orientation.* The exterior orientation parameters used are reported in appendix A, with FS $= -x$, BL $= y$, and WL $= z$. In order to correctly interpret these orientation parameters, the camera aperture should be located at the origin, with the camera pointing along the negative z-axis and the y-axis exiting the top of the camera. The camera aperture is translated into position **a**, and then the camera is rotated first about the x-axis, then the y-axis, and finally the z-axis. The rotations are defined to be positive in the counterclockwise direction as viewed from the positive end of an axis looking toward the origin.

In the third step, the coefficients of the equation representing the rotating plane of the light sheet are determined. No procedure equivalent to the analytic techniques for the first two calibration steps was performed for locating the light sheet. The light was installed on the aircraft at the location described in appendix A. The sheet was normal to the planform of the wing and rotated about a line passing through $x = -438.68$ and $y = 0.40$. With the measured angle Φ and equation (2), the equation for the light-sheet plane for every image could be determined.

The application of this new technique came very late in the flight schedule and was given a low priority. The result of this nonrigorous approach was weak experimental control from a photogrammetric point of view. In a normal photogrammetric application, it is important that all the orientation parameters be determined as accurately as possible, that the imagery is optimized (often *not* resulting in an image that appeals to the eye), and that an accurate set of resection targets is available. For this experiment, these conditions were minimally met. When the data were reconstructed, the footprint of the light sheet was observed to be slightly offset from the upper surface of the wing-surface geometry model. This error was likely due to a combination of four sources: (1) the waterline values for the resection targets were inaccurately measured, (2) the quality of the resection targets (because of wing placement and lighting) was poor, (3) the accuracy of the light-sheet angle was unknown, and (4) the accuracy of the wing-surface model used (developed from original manufacturer's drawings) to represent the wing flown was unknown.

Because the major error source was estimated to be the waterline values for the resection targets, improved values were obtained by replacing them with values interpolated from the surface geometry model. Adequate footprint matches were subsequently obtained.

It is not possible to determine the accuracy of the reconstruction without an independent measurement. However, based on the consistency of the results obtained and the favorable comparison of light-sheet footprint profiles with the wing geometry model, the worst case error for this experiment is estimated to be under 3 in.

Images obtained from the side camera beginning with F/S 91-16/07 indicate that the camera orientation had been adjusted. Because of the designed adjustability of the mounting bracket, it was reasonable to assume that camera translation was negligible

and only rotation was responsible for the orientation change. The rotation angles were varied until favorable light-sheet footprint matches were obtained. The worst case error for this series of flights is speculative at best. An error estimate of under 3 in. may still be considered reasonable because the light sheet as viewed from the side camera is closer than the top camera and less susceptible to errors in the rotation angles.

For future flight applications it is recommended that a careful photogrammetric survey of the aircraft be performed in advance of flight testing in order to provide the necessary control points for the space resection process. These points can also be used as a check on the surface profile model developed. Also, because the light-sheet rotation-axis location and angle are critical, improved methods for their accurate determination should be incorporated.

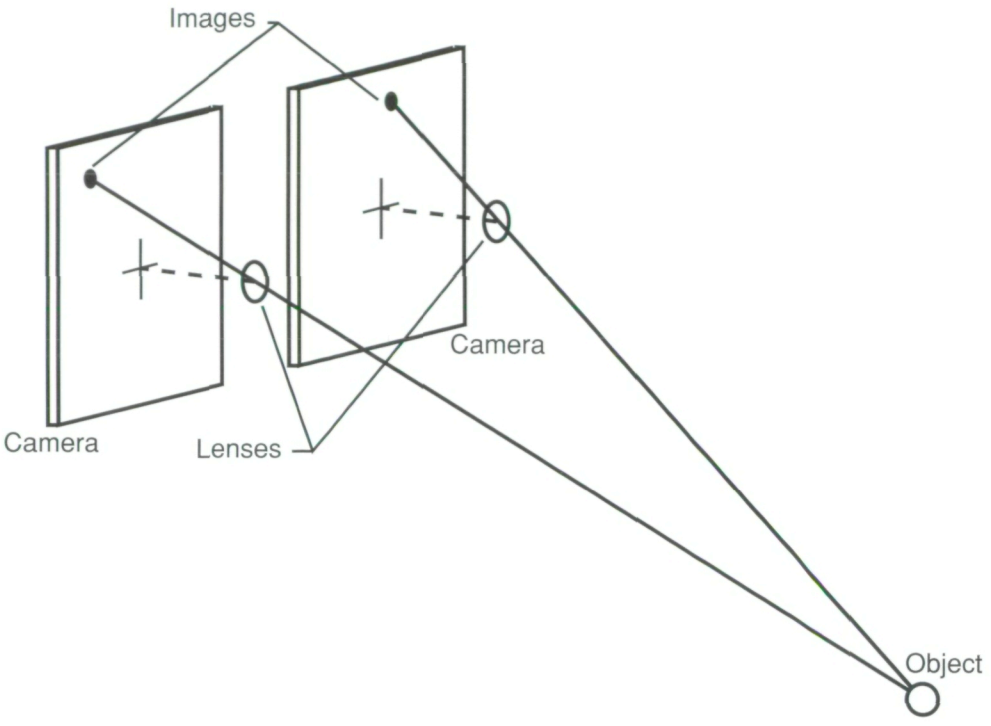

Figure C1. Stereo photogrammetry with parallel two-camera geometry.

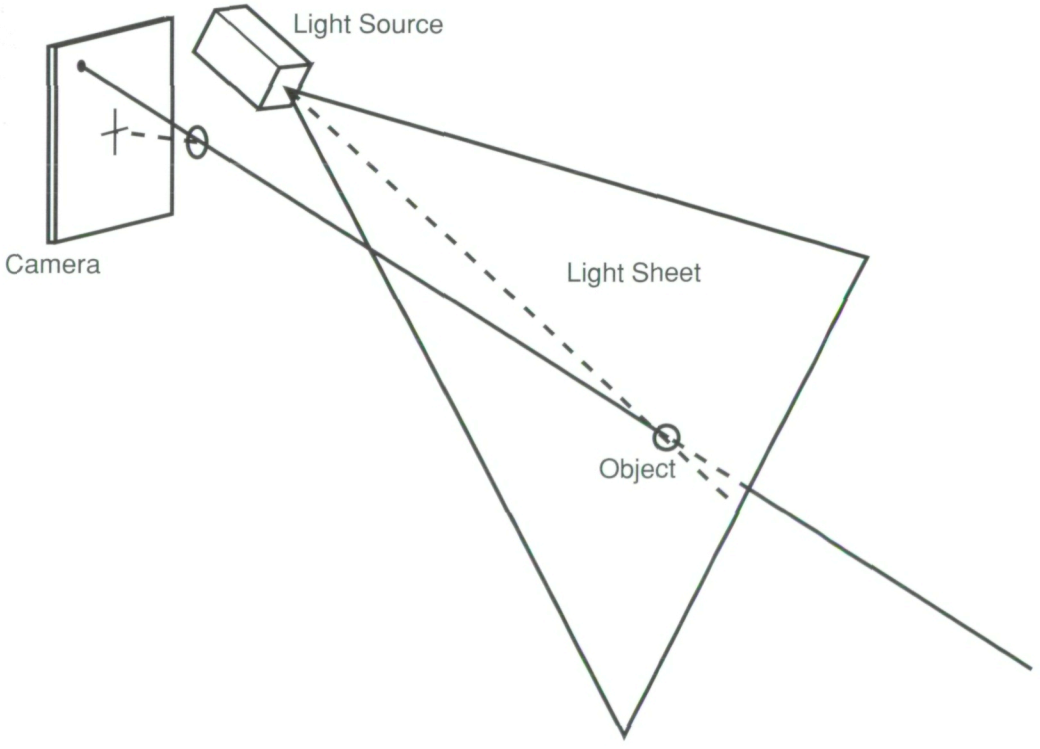

Figure C2. Modified stereo photogrammetry using directed light sheet.

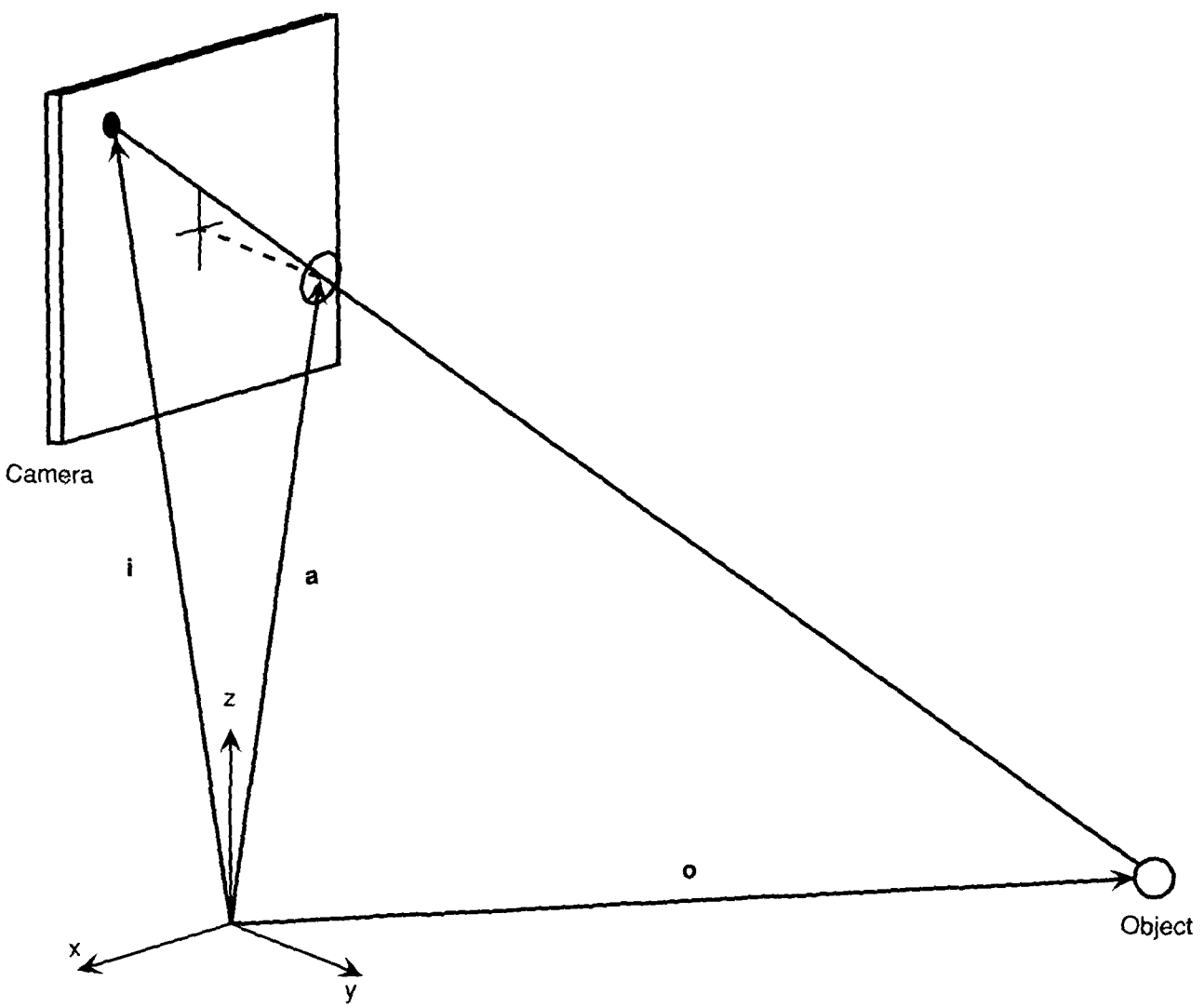

Figure C3. Geometry for deriving parametric equation for line connecting object, image, and aperture.

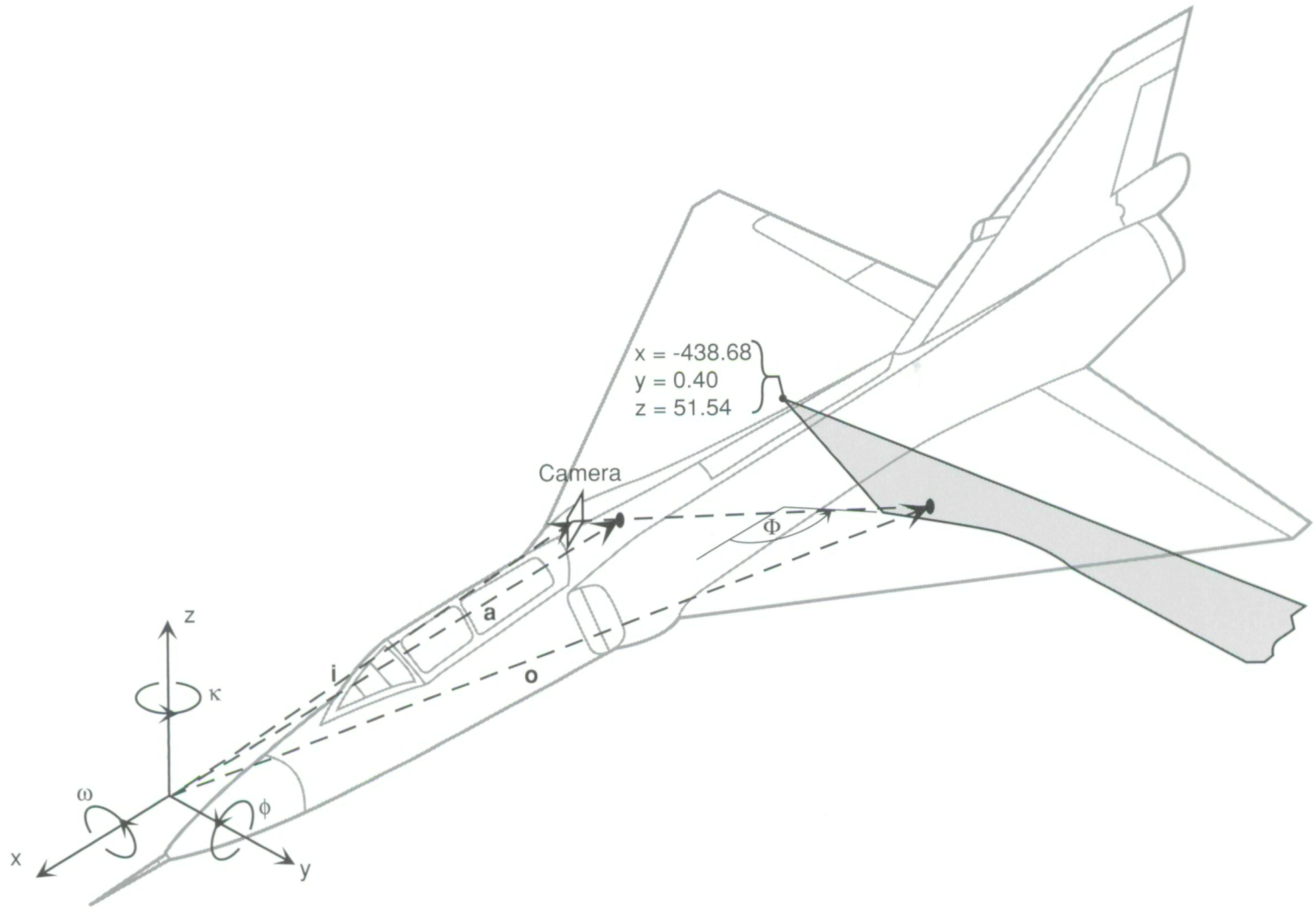

Figure C4. Geometry for light-sheet reconstruction.

Appendix D

Description of Wind-Tunnel Test and Vapor-Screen Systems

A vapor-screen wind-tunnel test on a 5-percent-scale F-106 model was conducted in the Ames 6- by 6-Foot Transonic/Supersonic Wind Tunnel during March 1987. The test included Mach numbers of 0.6, 0.9, and 1.2, with corresponding Reynolds numbers of 1.78×10^6, 1.78×10^6, and 1.48×10^6. A sketch of the test setup is shown in figure D1, and a photograph of the model is given in figure D2. The white markings on the side of the fuselage corresponded to vapor-screen stations of interest and occurred at longitudinal locations of $x/c_r = 0.22$, 0.3, 0.5, 0.6, 0.7, 0.9, and 1.1.

The specific makeup of the vapor-screen systems employed for this test was water vapor for seeding, laser light sheet for illumination, and both a video and a still camera for image recording. Seeding was accomplished by spraying water through several nozzles in the test section ahead of the model. Laser-light-sheet illumination of the left side of the model was done through a glass window in the side of the wind tunnel. The light sheet rotated in pitch with the model as angle of attack changed; thus, the light sheet remained essentially perpendicular to the wing upper surface and could be translated fore-and-aft in order to cover the model flow field from forward to aft of the wing on that side. A typical test run at a fixed Mach number included illuminating the flow above the wing at the previously given values of x/c_r over the α range, then translating the laser at a fixed α, and finally varying α at fixed longitudinal positions. The video image was recorded with the camera pointing forward inside a slender box mounted onto the left side of the sting body. The video lens was near tunnel station 1043.[11] Still-camera photographs were taken through the wind-tunnel glass window from a three-quarter left-front view.

[11]Thanks to W. Morel Whitcomb of NASA Ames Research Center for his assistance in obtaining video-camera information for this work.

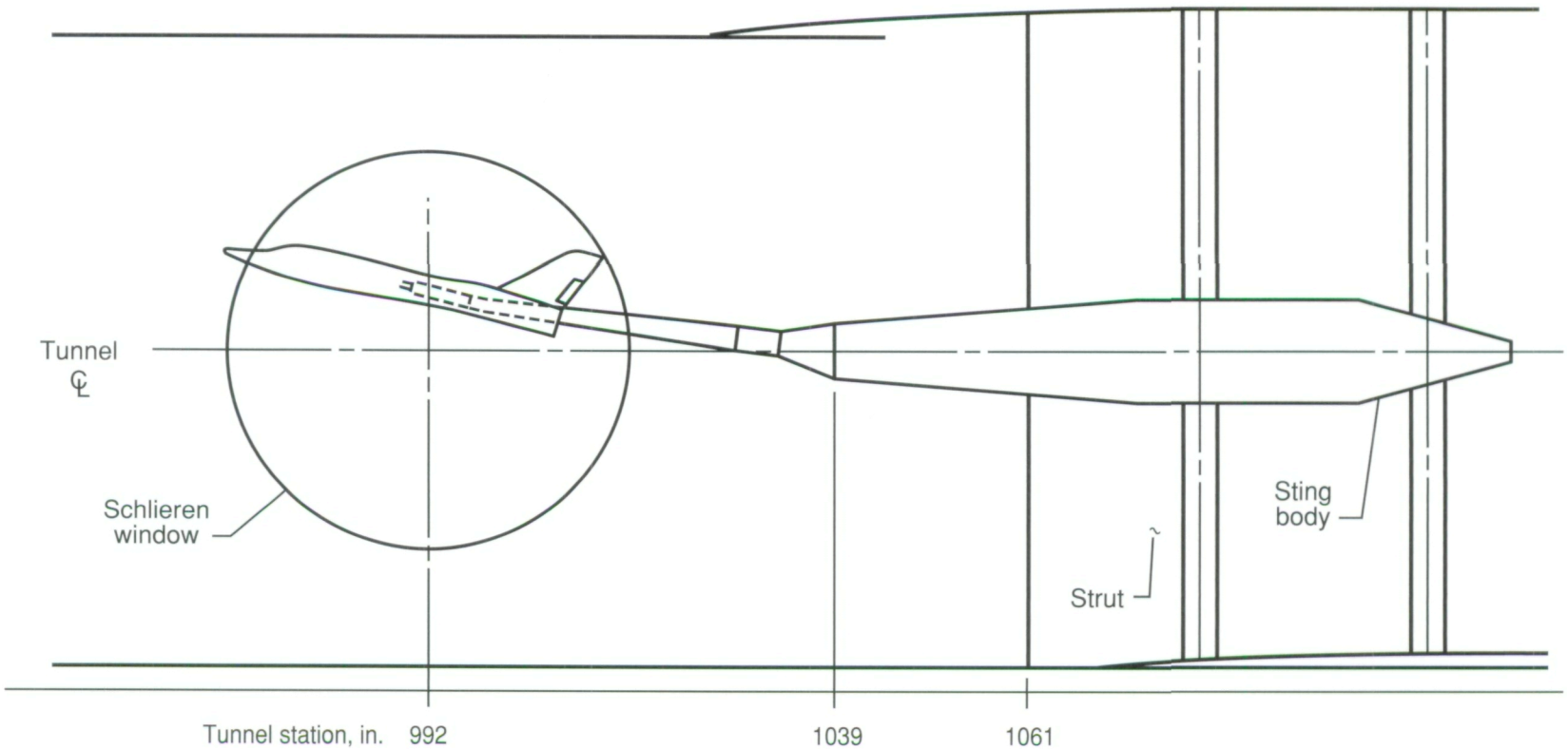

Figure D1. Model of F-106 installed in Ames 6- by 6-Foot Transonic/Supersonic Wind Tunnel.

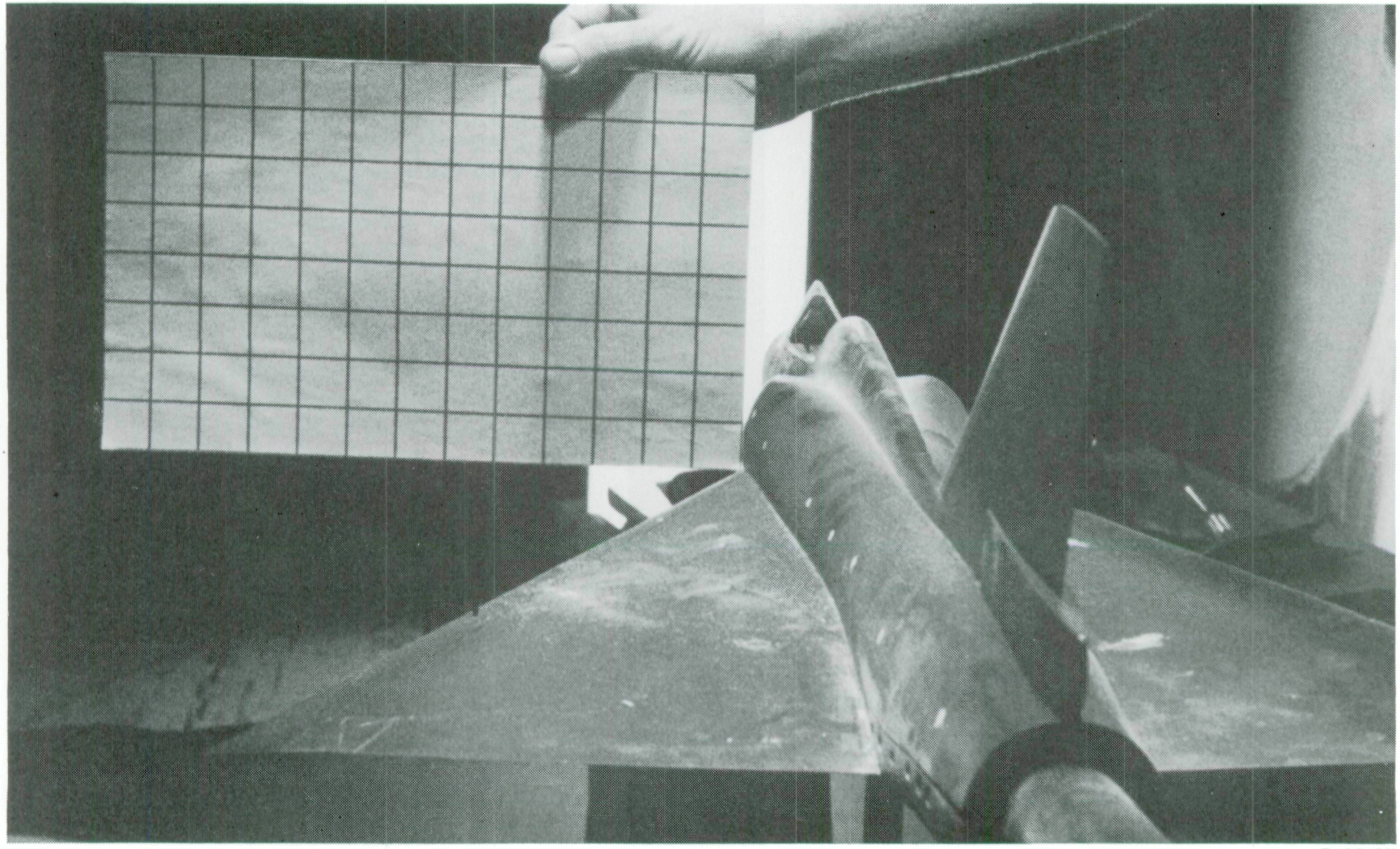

L-93-35

Figure D2. Model of F-106 and grid in 6- by 6-ft test section.

References

1. Burdin, I. Yu.; Zhirnov, A. V.; Kulesh, V. P.; Orlov, A. A.; Pesetskiy, V. A.; and Fonov, S. D. (Foreign Technology Div., Wright-Patterson Air Force Base, transl.): *Use of Laser Methods for the Study of Detached Flows in a Wind Tunnel and in Flight.* FTD-ID(RS)T-1053-82, U.S. Air Force, Oct. 20, 1982, pp. 2–19. (Available from DTIC as AD B069 459.)

2. Lamar, J. E.; Bruce, R. A.; Pride, J. D., Jr.; Smith, R. H.; and Brown, P. W.: In-Flight Flow Visualization of F-106B Leading-Edge Vortex Using the Vapor-Screen Technique. *J. Aircr.*, vol. 25, no. 2, Feb. 1988, pp. 113–120.

3. Lamar, John E.; Brown, Philip W.; Bruce, Robert A.; Pride, Joseph D., Jr.; Smith, Ronald H.; and Johnson, Thomas D., Jr.: *Operational Performance of Vapor-Screen Systems for In-Flight Visualization of Leading-Edge Vortices on the F-106B Aircraft.* NASA TM-4004, 1987.

4. Lamar, John E.; and Johnson, Thomas D.: *Sensitivity of F-106B Leading-Edge-Vortex Images to Flight and Vapor-Screen Parameters.* NASA TP-2818, 1988.

5. Maltby, R. L., compiler: *Flow Visualization in Wind Tunnels Using Indicators.* AGARDograph 70, Apr. 1962.

6. Campbell, James F.; and Chambers, Joseph R.: *Patterns in the Sky—Natural Visualization of Aircraft Flow Fields.* NASA SP-514, 1993.

7. Lamar, J. E.; Hallissy, J. B.; Frink, N. T.; Smith, R. H.; and Johnson, T. D., Jr.: Review of Vortex Flow Flight Projects on the F-106B. *A Collection of Technical Papers—AIAA 5th Applied Aerodynamics Conference*, Aug. 1987, pp. 145–153. (Available as AIAA-87-2346.)

8. *U.S. Standard Atmosphere, 1962.* NASA, U.S. Air Force, and U.S. Weather Bureau, Dec. 1962.

9. Werlé, H.: *Outline on the Experimental Possibilities of the O.N.E.R.A. Hydrodynamic Tunnel for Visualization.* ONERA-NT-48, Nov. 1958.

10. Gregoriou, Gregor: Modern Missile Design for High Angle-of-Attack. *High Angle-of-Attack Aerodynamics*, AGARD-LS-121, Dec. 1982, pp. 5-1–5-23.

11. Walatka, Pamela P.; Clucas, Jean; McCabe, R. Kevin; Plessel, Todd; and Potter, Rick: *FAST 1.0 User Guide.* RND-92-015, NASA Ames Research Center, Nov. 1992.

12. Lamar, John E.: In-Flight and Wind Tunnel Leading-Edge Vortex Study on the F-106B Airplane. *Vortex Flow Aerodynamics, Volume I*, James F. Campbell, Russell F. Osborn, and Jerome T. Foughner, Jr., eds., NASA CP-2416, 1986, pp. 187–201.

13. Wood, Richard M.; and Watson, Carolyn B.: *Study of Lee-Side Flows Over Conically Cambered Delta Wings at Supersonic Speeds.* NASA TP-2660, 1987.

14. Dimotakis, Paul E.; and Brown, Garry L.: The Mixing Layer at High Reynolds Number: Large-Structure Dynamics and Entrainment. *J. Fluid Mech.*, vol. 78, pt. 3, Dec. 7, 1976, pp. 535–560.

15. Pierrehumbert, R. T.; and Widnall, S. E.: *The Structure of Organized Vortices in a Free Shear Layer. J. Fluid Mech.*, vol. 102, Jan. 1981, pp. 301–313.

16. Hess, Robert W.; Cazier, F. W., Jr.; and Wynne, Eleanor C. (appendix by E. Carson Yates, Jr.): *Steady and Unsteady Transonic Pressure Measurements on a Clipped Delta Wing for Pitching and Control-Surface Oscillations.* NASA TP-2594, 1986.

17. Chu, Julio; and Lamar, John E.: *Pressure Measurements on a Thick Cambered and Twisted 58° Delta Wing at High Subsonic Speeds.* NASA TP-2713, 1987.

18. Jorgensen, Leland Howard: *Prediction of Static Aerodynamic Characteristics for Slender Bodies Alone and With Lifting Surfaces to Very High Angles of Attack.* NASA TR R-474, 1977.

19. Kudlinski, Robert A.; and Park, Stephen K.: *Digital Enhancement of Flow Field Images.* NASA TP-2770, 1988.

20. Walatka, Pamela P.; Buning, Pieter G.; Pierce, Larry; and Elson, Patricia A.: *PLOT3D User's Manual.* NASA TM-101067, 1990.

21. Bingel, Bradford; and Hammond, Dana: *Transferable Output ASCII Data (TOAD) File Format Description.* NASA CR-178361, 1987.

22. Stacy, Kathryn; Severance, Kurt; and Childers, Brooks A.: *Computer-Aided Light Sheet Flow Visualization Using Photogrammetry.* Proposed NASA TP-3416, 1993.

23. Slama, Chester C., ed.: *Manual of Photogrammetry*, Fourth ed. American Soc. of Photogrammetry, c.1980.

24. Hecht, Eugene: *Optics*, Second ed. Addison-Wesley Publ. Co., Inc., c.1987.

25. Brown, Duane C.: *Application of Close-Range Photogrammetry to Measurements of Structures in Orbit, Volume 2, (Appendices).* GSI Tech. Rep. No. 80-012 (Contract No. MOM7DNS-895942), Geodetic Services Inc., Sept. 15, 1980.

26. Wolfe, Paul R.: *Elements of Photogrammetry.* McGraw-Hill, Inc., c.1974.

Table I. Data Summary for Flight Vapor Screen

[Serial-averaged nominal values]

Group	Flight/serial	α, deg	h, ft	g	M_∞	R_n	Figure
I	91-15/12	12.9	14 900	1.0	0.36	39.1×10^6	17, 24, 40
	91-15/13	13.9	14 800	1.0	.34	37.3	17, 24, 40
	91-15/17	15.1	14 900	1.0	.34	37.0	17, 24, 40
	91-16/09	15.8	16 200	1.0	.33	33.0	17, 24, 40
	91-16/10	16.9	15 800	1.0	.31	31.4	17, 24, 40, 49, 50
	91-16/11	17.8	15 800	1.0	.29	30.1	12, 17, 24, 40
	91-17/07	18.6	16 500	1.0	.29	30.0	17, 24, 40, 51
	91-17/09	20.2	16 200	1.0	.27	28.3	17, 24, 40
	91-17/10	21.3	15 500	1.0	.26	27.5	17, 24, 40
II	91-13/11	13.9	24 600	1.0	0.42	35.1×10^6	11, 13, 18, 25, 41, 61
	91-13/05	14.9	24 600	1.0	.41	34.6	14, 18, 25, 36, 38, 41, 43, 61
	91-13/10	16.1	25 500	1.0	.39	32.0	18, 25, 41
	91-13/06	17.0	24 300	1.0	.38	32.0	18, 25, 37, 39, 41, 43, 61
	91-13/07	18.8	24 000	1.0	.35	29.9	15, 18, 25, 41, 43, 61
	91-13/08	20.5	25 500	1.0	.34	27.8	18, 25, 41
	91-13/09	22.5	24 700	1.0	.32	26.6	16, 18, 25, 41
III	91-15/06	13.9	35 400	1.0	0.54	30.8×10^6	19, 26, 34, 42
	91-14/07	14.8	36 900	.9	.53	29.2	9, 19, 20, 26, 27, 42, 44
	91-15/08	15.8	36 600	.9	.50	27.6	19, 26, 42
	91-14/08	16.8	37 100	.9	.49	26.8	9, 19, 26, 42
	91-14/09	17.7	37 200	1.0	.47	25.8	19, 26, 42
	91-14/10	18.7	37 300	1.0	.45	24.6	19, 26, 42
	91-14/11	19.7	37 200	1.0	.44	23.8	19, 26, 42
	91-14/12	20.5	36 300	1.0	.42	23.7	19, 26, 42
	91-15/10	21.9	36 200	1.0	.40	22.6	19, 23, 26, 42
IV	91-17/05	14.7	37 400	1.6	0.68	35.5×10^6	20, 27, 44
	91-15/11	14.8	33 000	2.5	.73	45.7	20, 21, 27, 28, 44, 45
	91-16/07	14.8	27 200	3.9	.80	57.3	20, 22, 27, 29, 44, 46
	91-16/05	16.8	34 400	2.9	.78	44.6	21, 28, 45
	91-16/08	17.3	33 100	3.8	.81	48.4	22, 29, 46
	91-17/06	18.6	36 900	2.3	.67	35.6	21, 28, 45
	91-16/06	19.4	29 400	3.4	.69	46.6	22, 29, 46
V	91-13/04	8.5	15 200	1.1	0.50	55.9×10^6	36, 37
	91-15/09	21.7	35 900	1.0	.41	23.1	23

Table II. Vortex Flow Type Expected on F-106B Wing Over Angle-of-Attack Range

$$\left[\begin{array}{l} \alpha_N = \tan^{-1}(\tan\alpha/\cos\Lambda);\ M_N = M_\infty \cos\Lambda(1+\sin^2\alpha\tan^2\Lambda)^{1/2}; \\ \delta_{f,N}\ (\text{LE deflection angle, normal}) = 22^\circ;\ \delta_{f,s}\ (\text{LE deflection} \\ \text{angle, streamwise}) = \tan^{-1}\ (\cos\Lambda_{\text{HL}}\tan\delta_{f,N}) = 11.42^\circ;\ \Lambda_{\text{HL}} \\ (\text{Hinge line sweep}) = \Lambda\ (\text{Wing leading-edge sweep}) = 60^\circ; \\ M_\infty = 0.4 \end{array}\right]$$

α, deg	α_N, deg	M_N	$\alpha_N - \delta_{f,s}$, deg	Vortex-flow type expected
8	15.70	0.206	4.28	LE separation bubble
9	17.58	.207	6.16	LE separation bubble
10	19.43	.209	8.01	Classical
11	21.24	.211	9.82	↓
12	23.03	.213	11.61	
13	24.78	.215	13.36	
14	26.50	.217	15.08	
15	28.18	.219	16.76	
16	29.83	.222	18.41	
17	31.44	.224	20.02	
18	33.02	.227	21.60	
19	34.55	.230	23.13	
20	36.05	.232	24.63	
21	37.51	.235	26.09	

Table III. Reattachment Point Determination With Different Projection Techniques

[F/S 91-15/10]

Φ, deg	Reattachment point, r, in.		Difference, in.
	Original (a)	Redetermined	
66.0	35.57	[a]35.67	0.10
72.7	40.53	[a]40.73	.20
80.6	47.02	[a]46.76	−.26
88.4	54.77	[a]54.62	−.15
93.6	60.11	[b]58.54	−1.57
101.2	74.36	[b]67.95	−6.41
110.7	92.49	[b]84.41	−8.08
116.3	113.34	[b]108.11	−5.23

[a]Vertical projection.
[b]Perpendicular-to-surface projection.

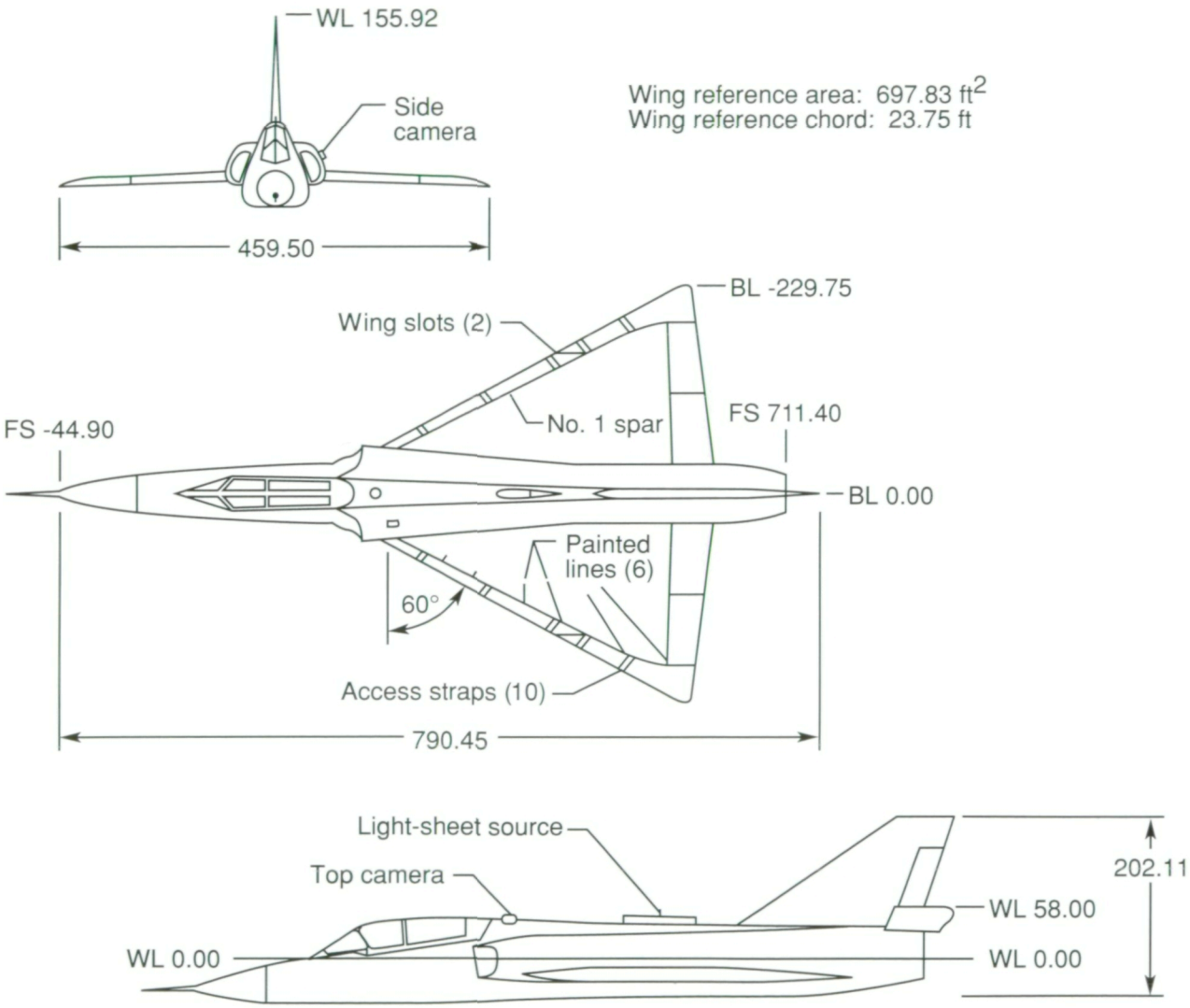

Figure 1. Three-view sketch of F-106B aircraft. Dimensions are in inches unless otherwise noted.

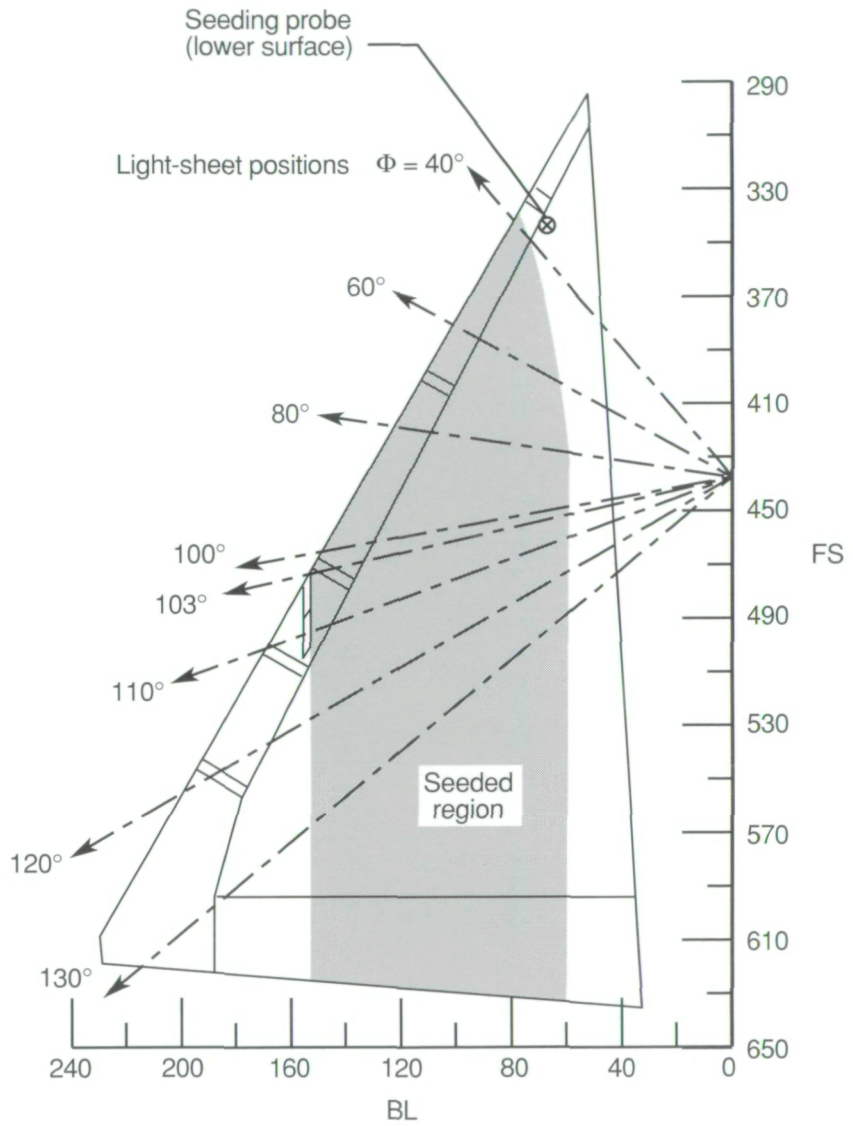

Figure 2. Regions of wing covered by seeding and light-sheet systems.

Belt set	Port	FS	BL
2	C2S01	361.222	-73.806
	C2S03	363.157	-70.454
	C2S04	364.387	-68.324
	C2S05	365.887	-65.726
	C2S06	367.827	-62.366
	C2S07	370.557	-57.637
	C2S08	375.222	-49.557
3	C3S01	425.131	-106.912
	C3S02	427.261	-103.223
	C3S03	429.721	-98.962
	C3S04	432.626	-93.930
	C3SF05	436.931	-86.474
	C3SF06	441.631	-78.333
	C3SF08	447.631	-67.941
	C3SF10	453.131	-58.415
	C3S11	458.291	-49.478
4	C4S01	492.091	-141.734
	C4S02	495.511	-135.811
	C4S03	499.456	-128.978
	C4S04	504.126	-120.889
	C4S05	509.841	-110.990
	C4S06	517.211	-98.225
	C4S07	527.596	-80.238
5	C5S02	549.829	-166.930
	C5S03	552.134	-162.937
	C5S06	560.184	-148.994
	C5S08	566.889	-137.381
	C5S09	570.819	-130.574
	C5S10	575.279	-122.849
	C5S11	580.424	-113.938

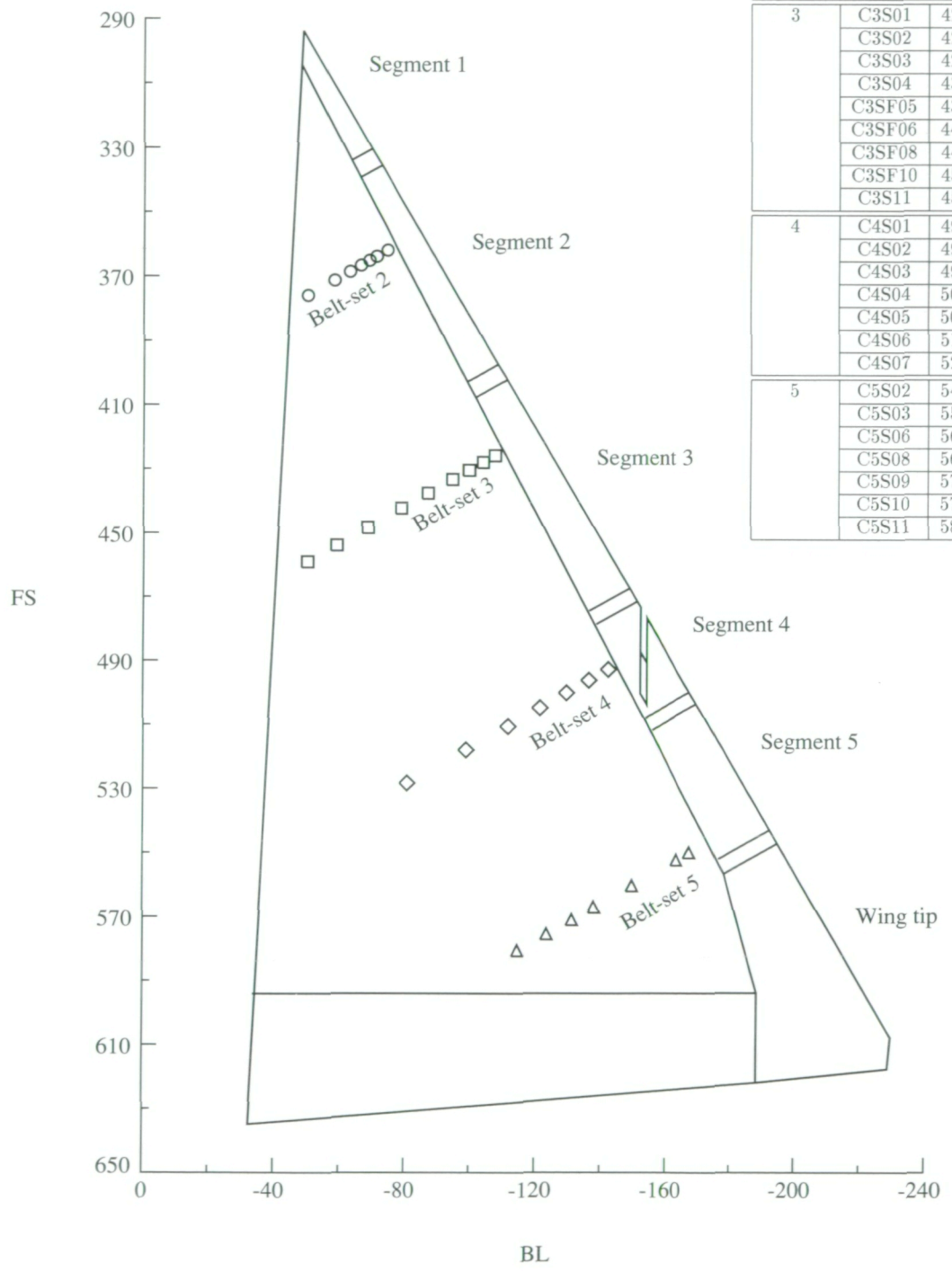

(a) Port coordinates.

Figure 3. Upper-surface pressure locations for F-106B wing.

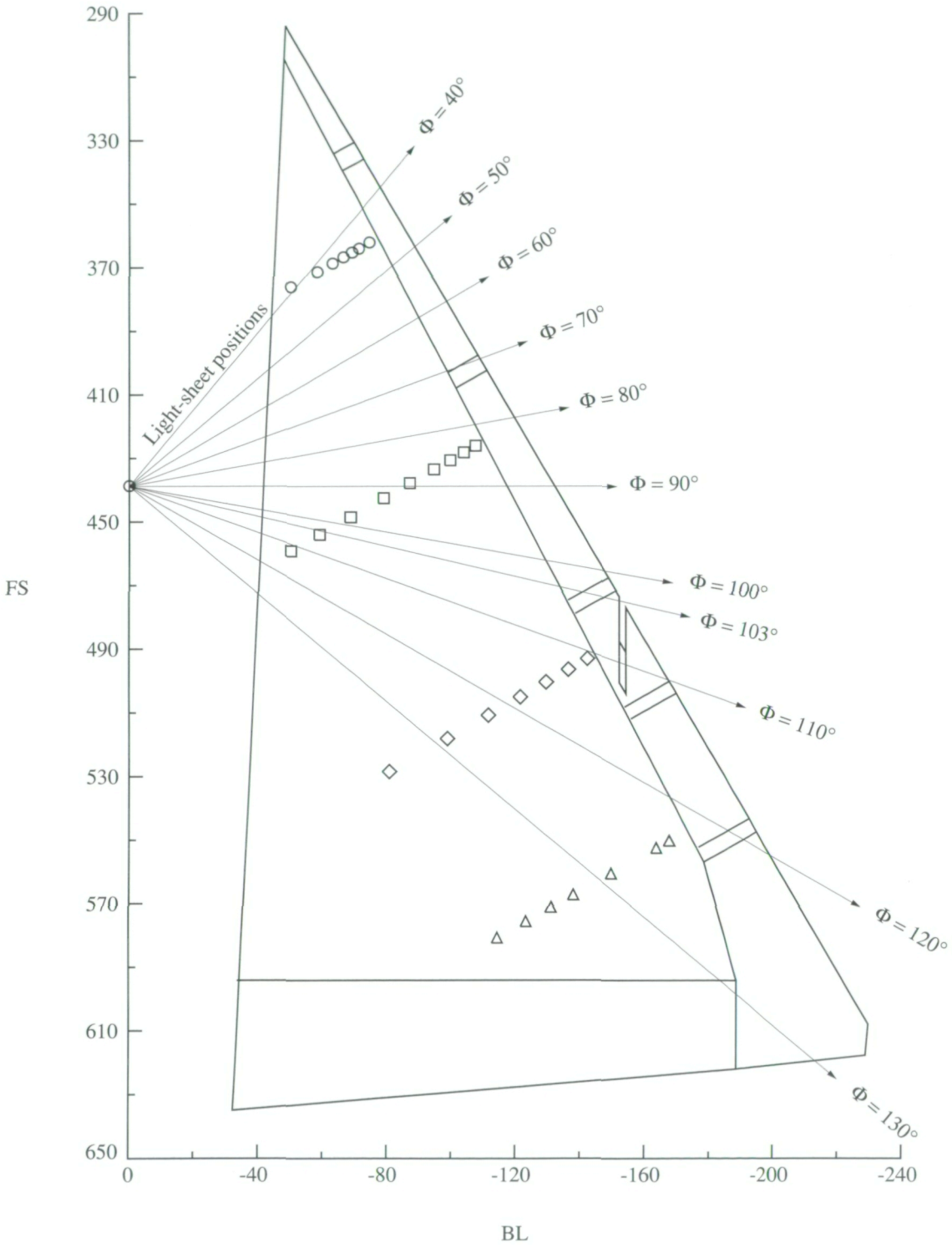

(b) Port locations relative to left-wing light-sheet angles reflected about centerline.

Figure 3. Concluded.

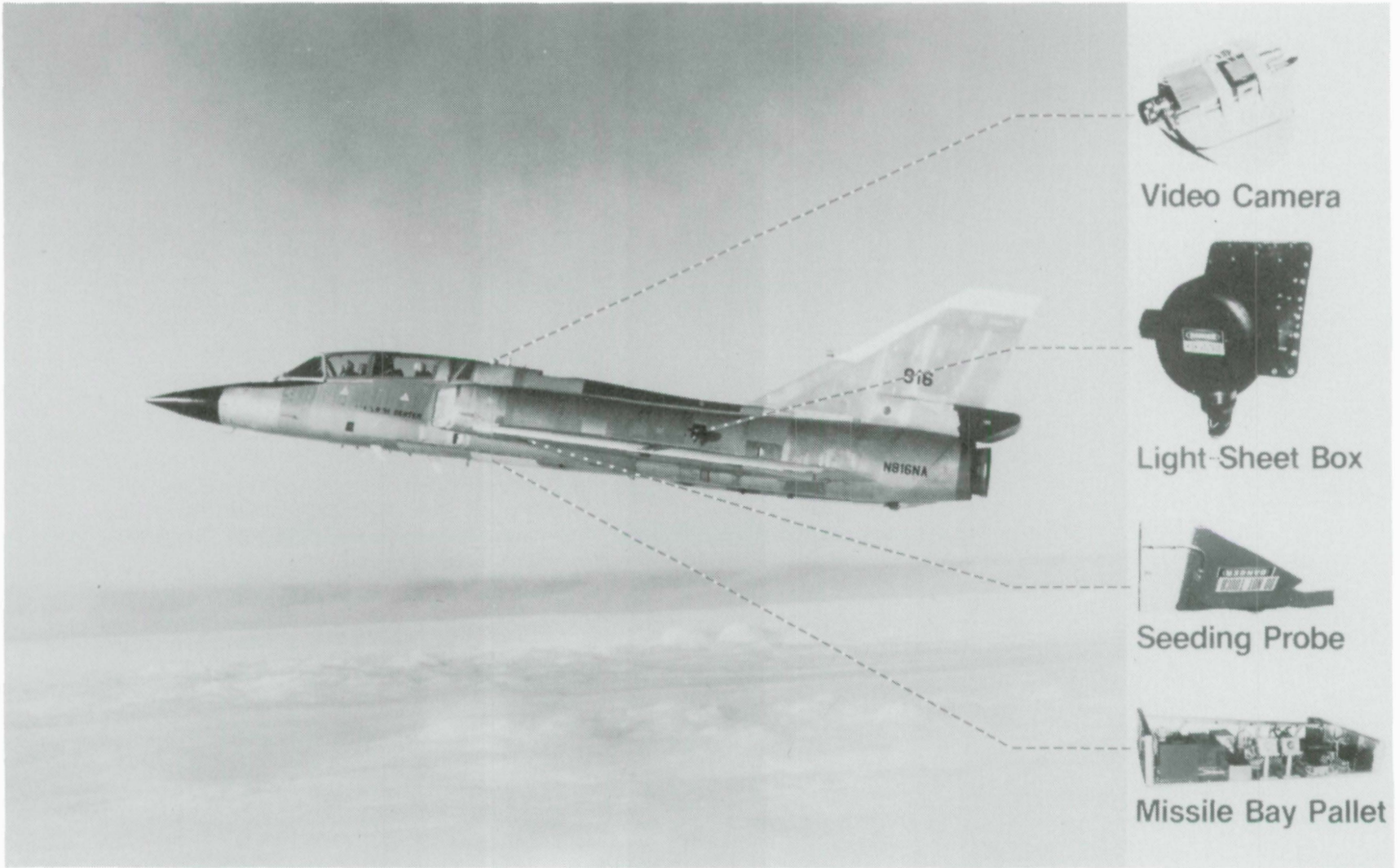

L-85-6276

Figure 4. Vapor-screen systems on baseline F-106B aircraft for 1985 flight test.

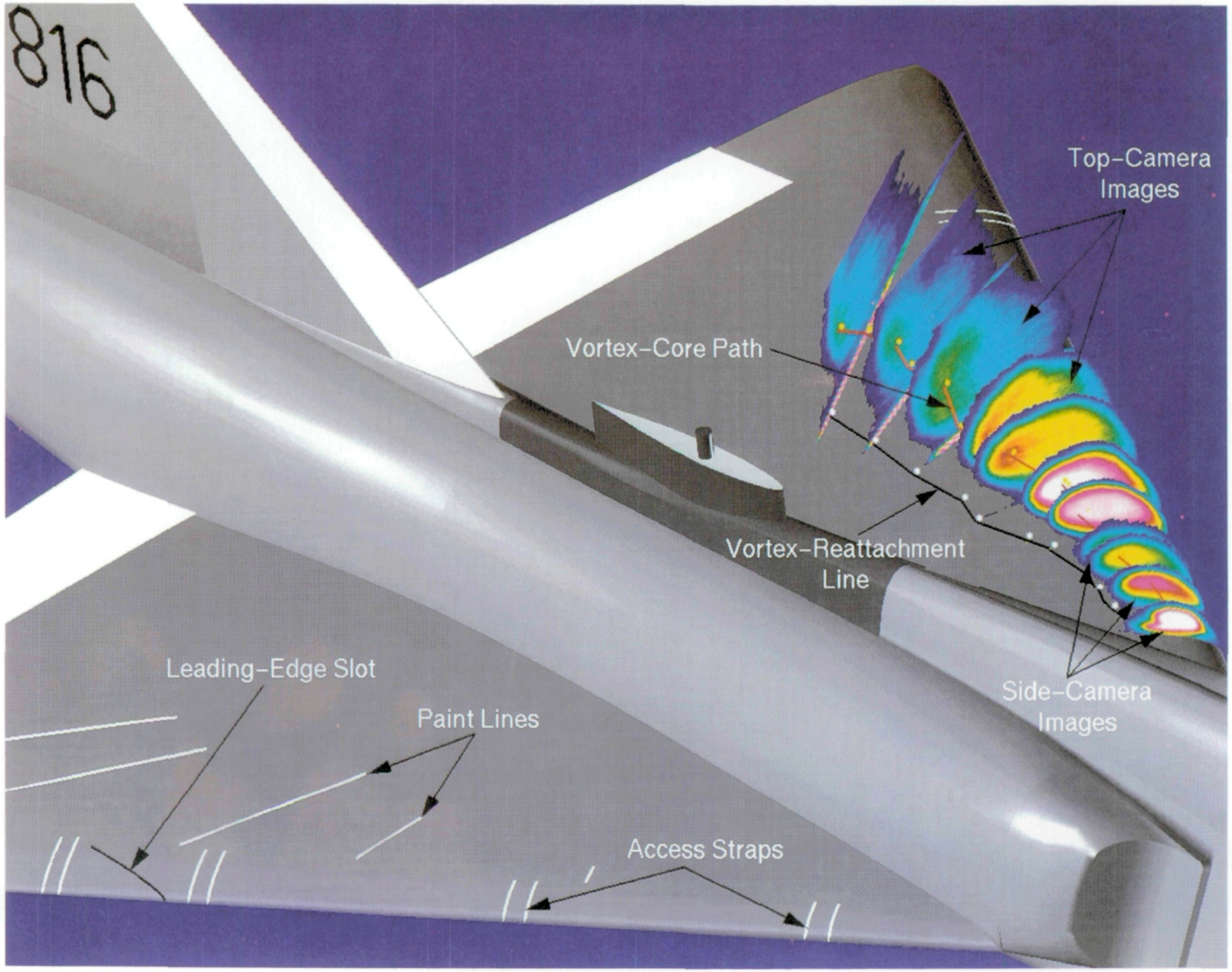

Figure 5. Three-dimensional representation of vortex-system images and characteristics on F-106B numerical surface geometry. (Note that paint lines occur on left wing but are displayed on right wing here, reflected about centerline, to show complete set of pertinent features represented in surface geometry.)

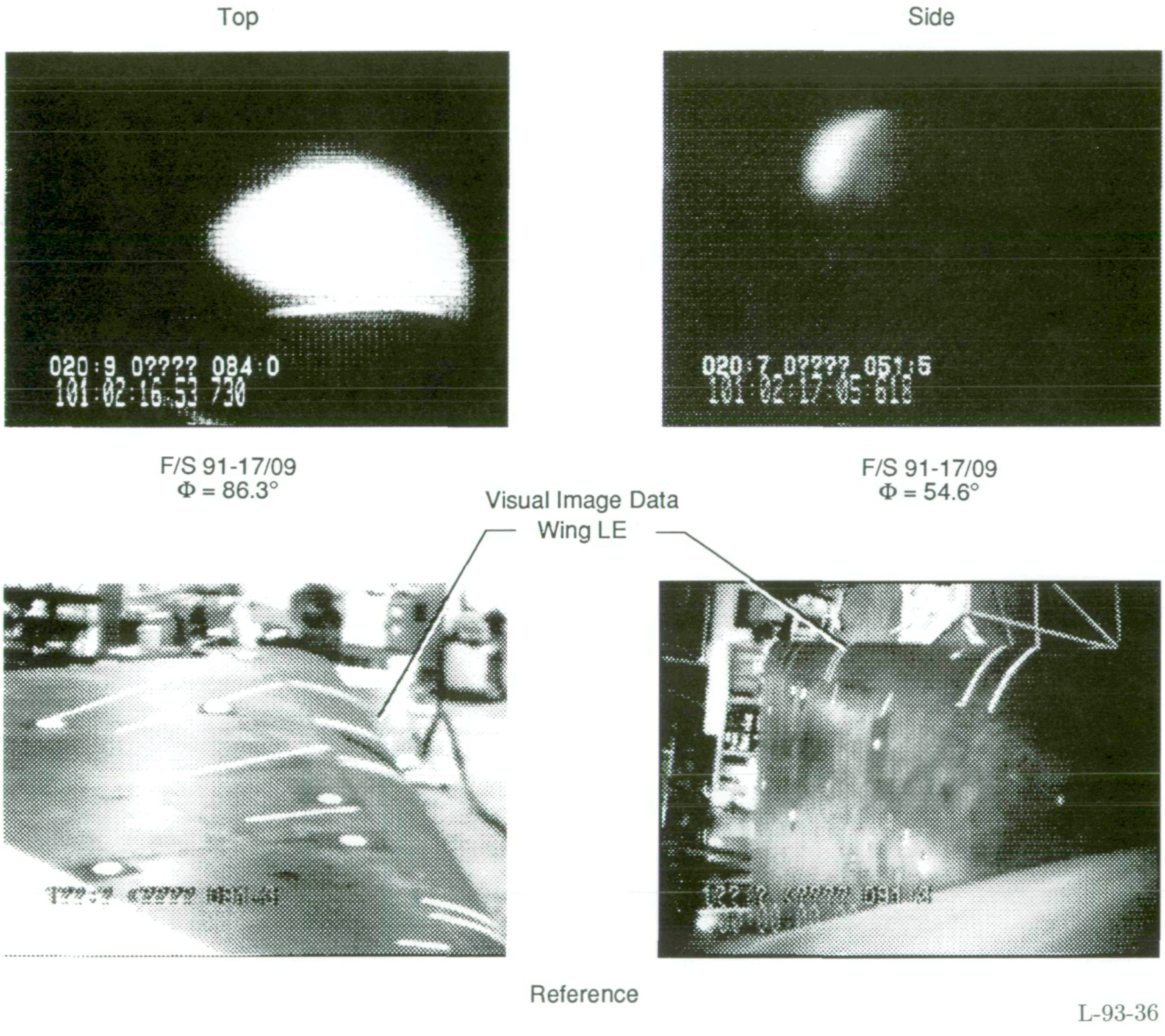

Figure 6. Sample of basic visual image data and reference wing upper surface from top and side cameras.

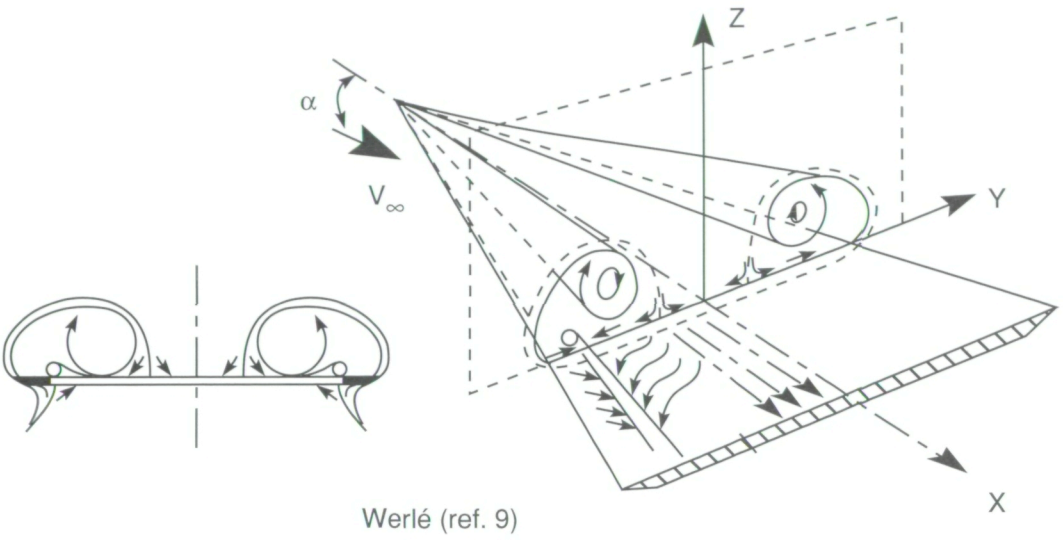

Werlé (ref. 9)

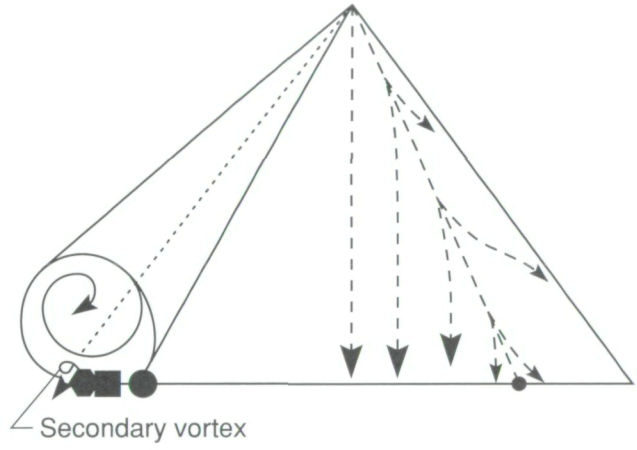

Gregoriou (ref. 10)

Figure 7. Representative sketches of off-surface vortex systems and associated surface flow.

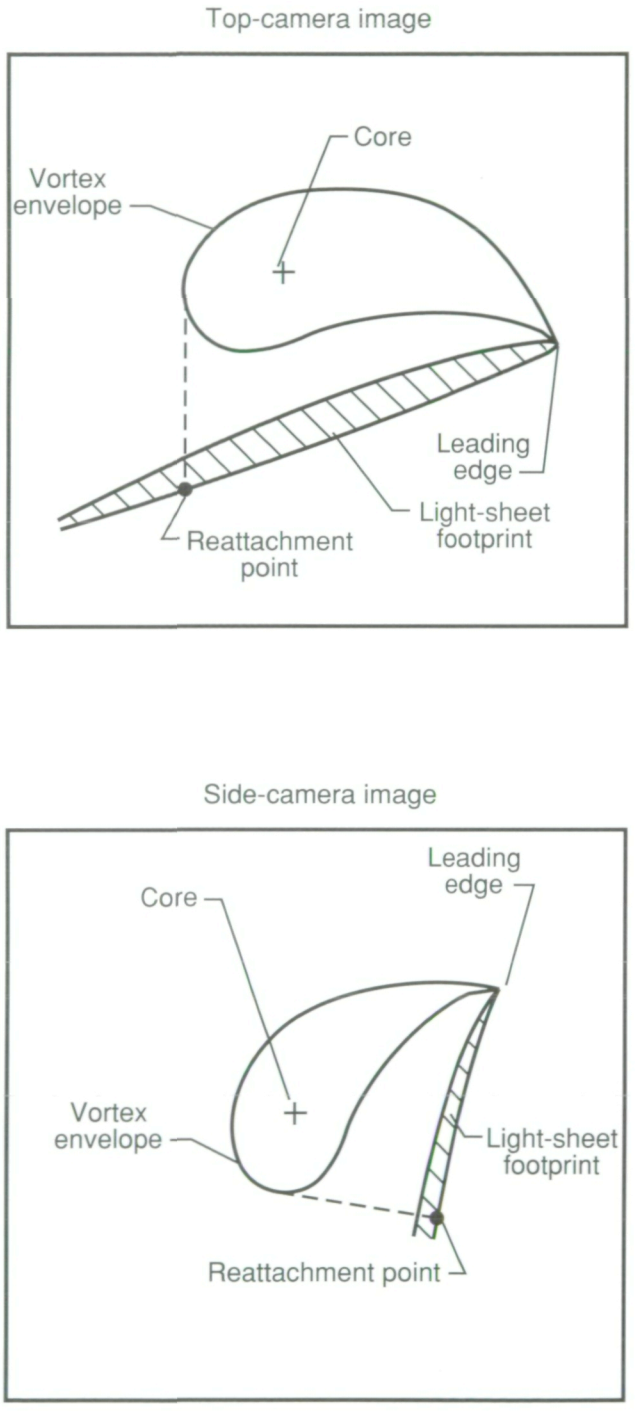

Figure 8. Reattachment-point location determined with **Extractor** procedure.

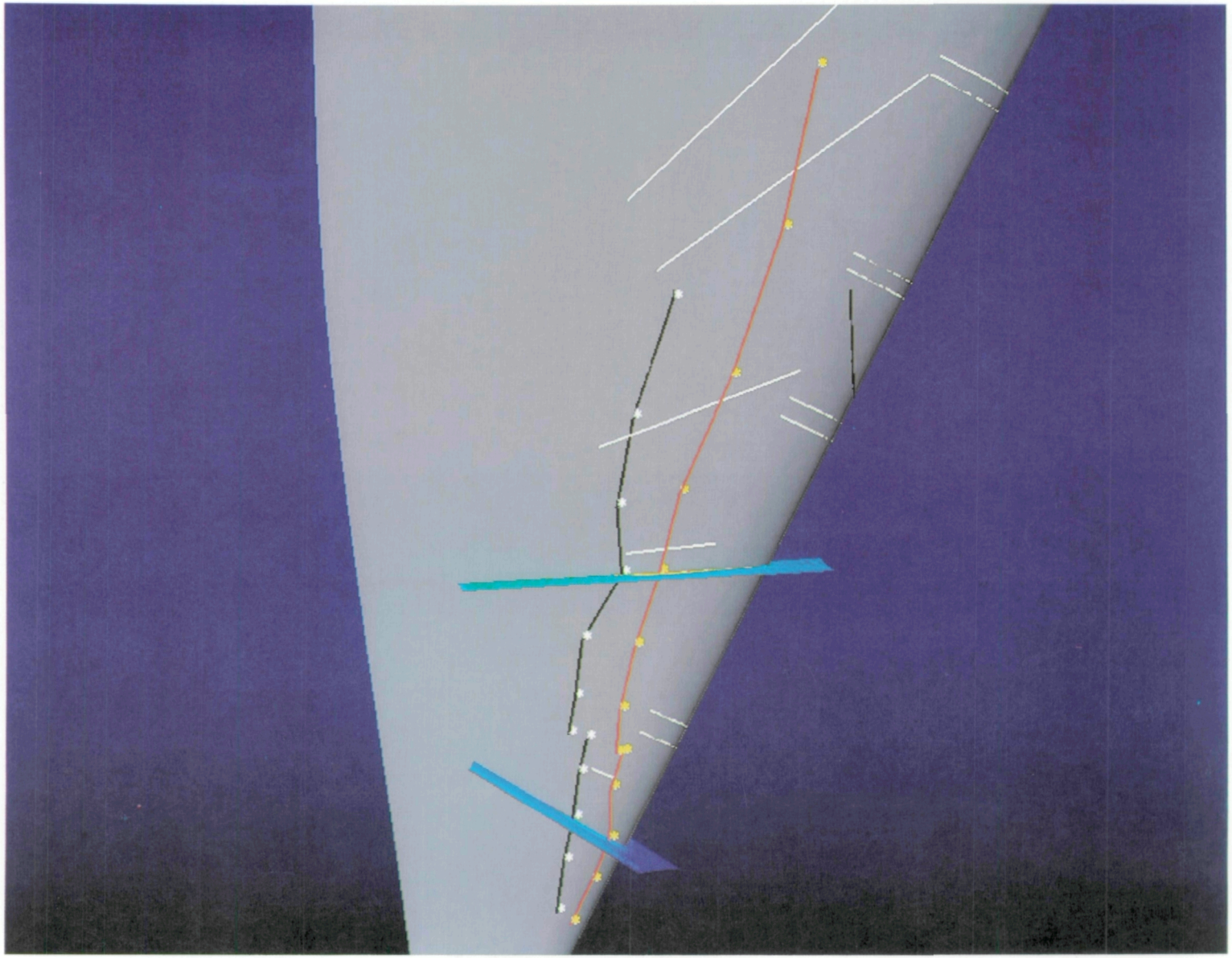

(a) $\alpha = 14.8°$ (F/S 91-14/07).

Figure 9. Two examples of vortex features highlighting the top- and side-camera overlap region. (Vapor-screen-determined cores in red with yellow asterisks and reattachment lines in black with white asterisks.)

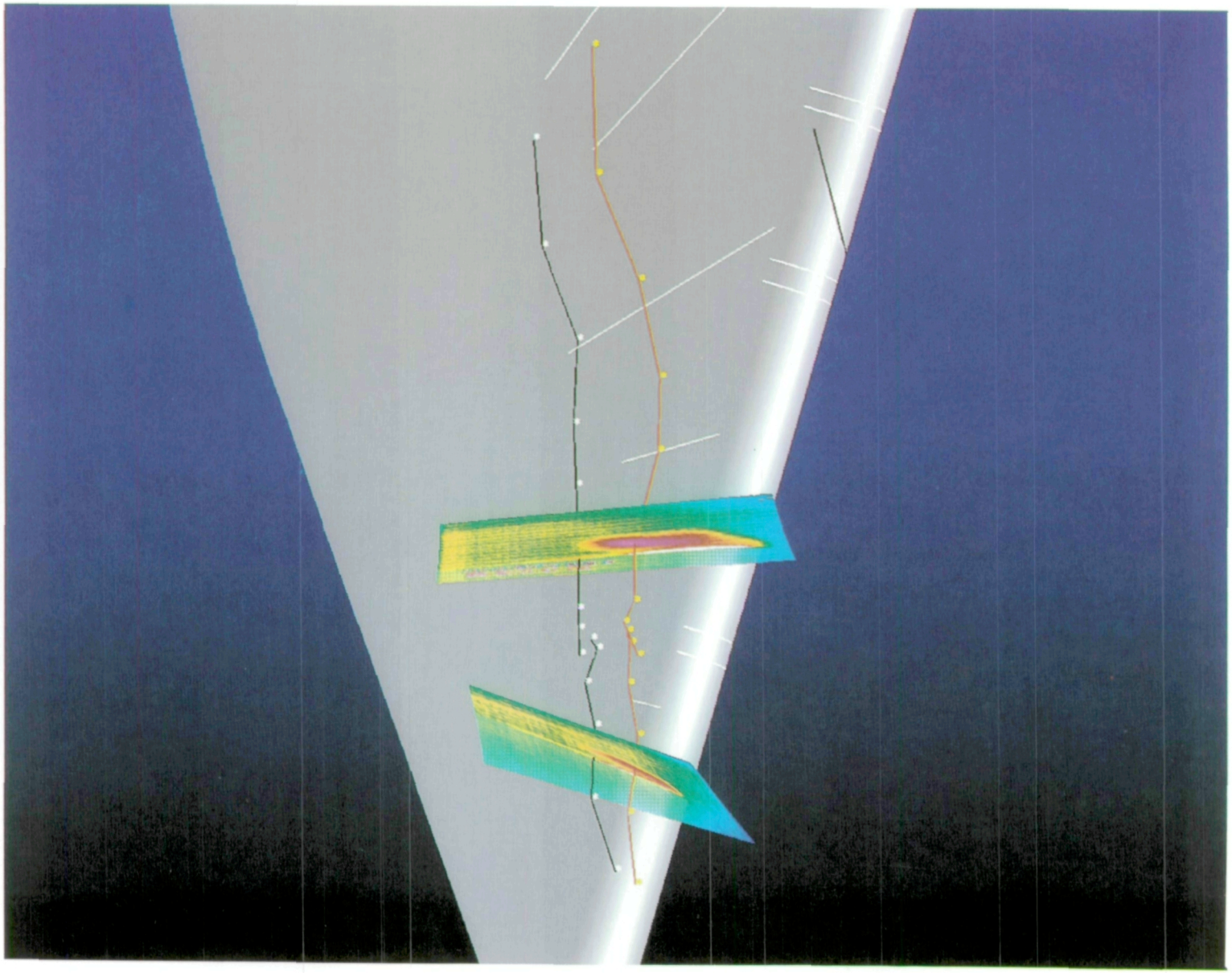

(b) $\alpha = 16.8°$ (F/S 91-14/08).

Figure 9. Concluded.

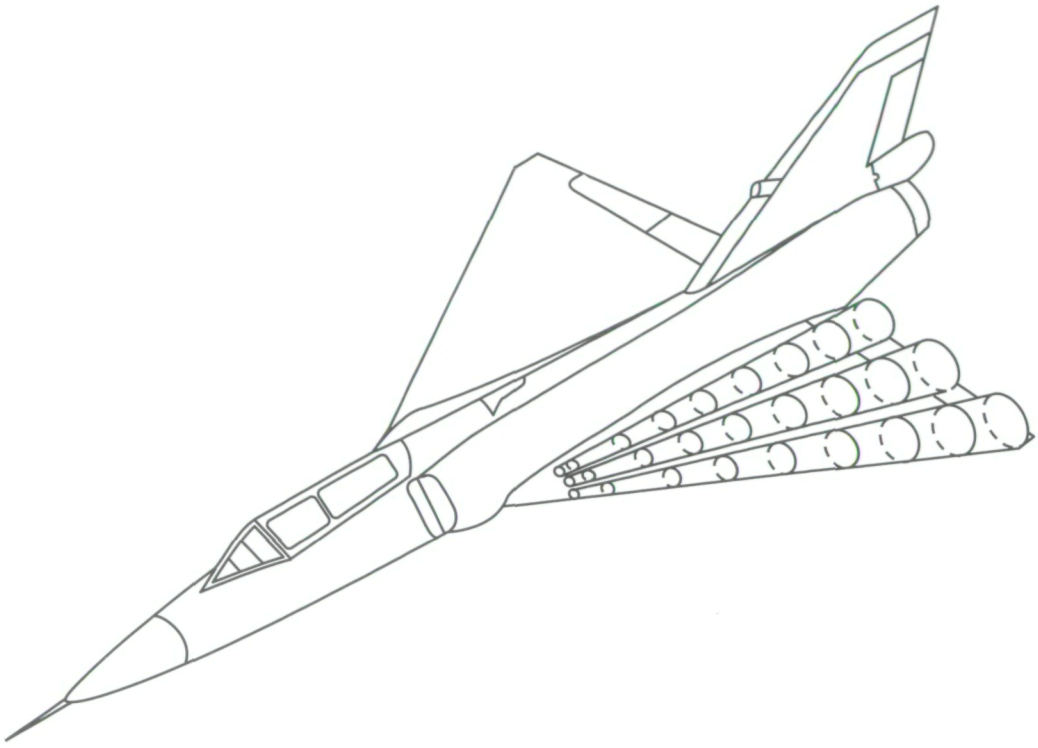

(a) 1985 flight (from ref. 12).

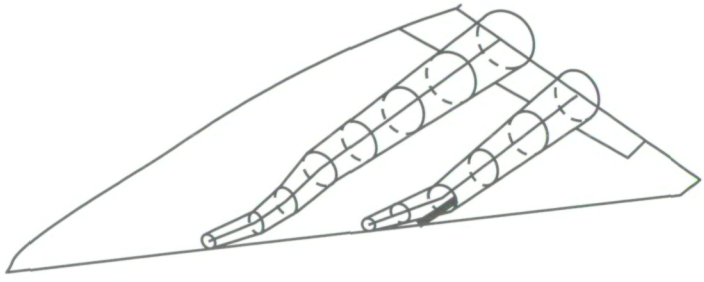

(b) Based on 1991 flight vapor-screen images.

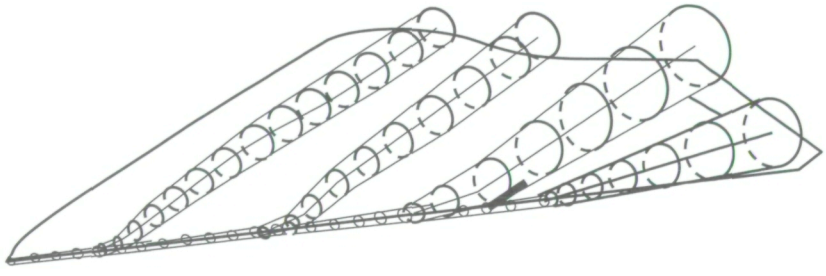

(c) Based on 1991 flight oil-flow patterns.

Figure 10. Three models for origination of multiple vortex systems on F-106B wing.

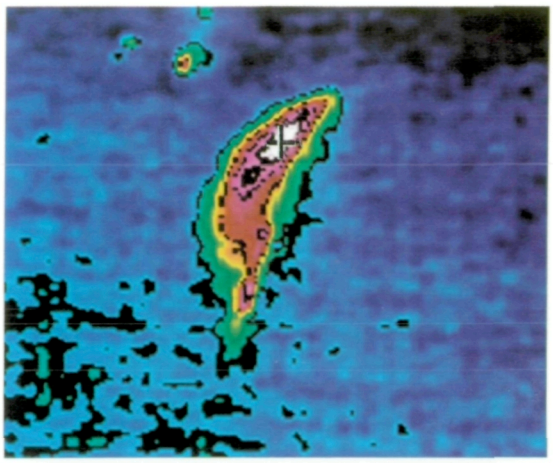

Φ = 63.7°

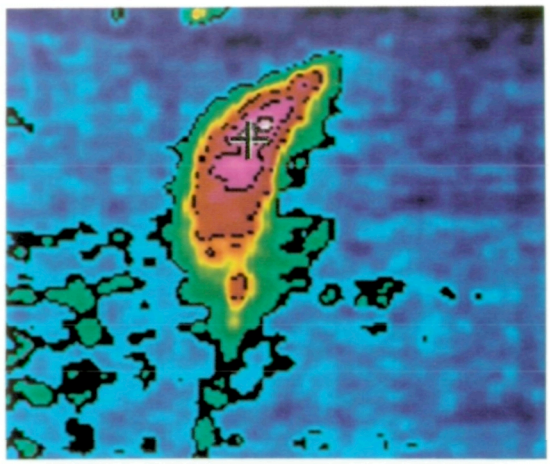

Φ = 66.3°

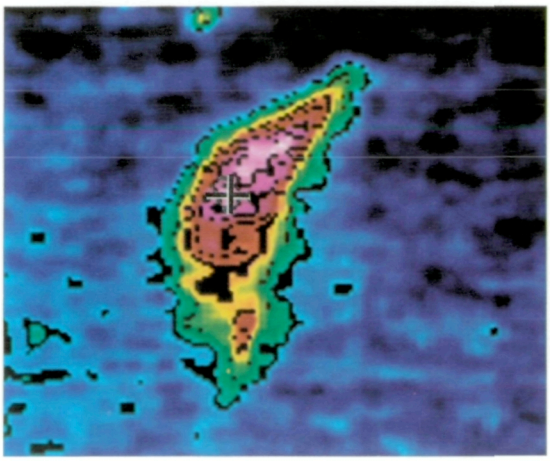

Φ = 66.8°

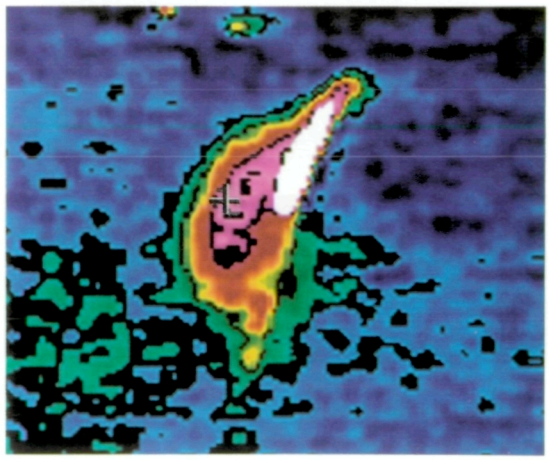

Φ = 68.2°

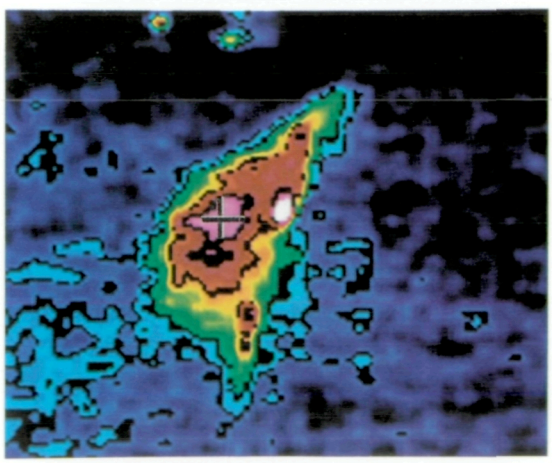

Φ = 69.5°

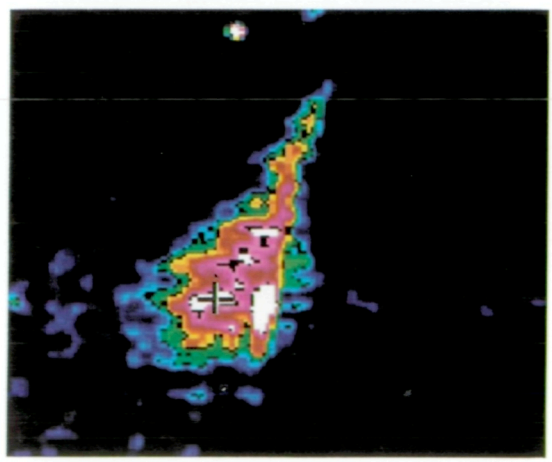

Φ = 80.0°

Figure 11. Growth of enhanced vortex system for $\alpha = 13.9°$ as seen from side camera on F/S 91-13/11. (Vortex core indicated by plus sign.)

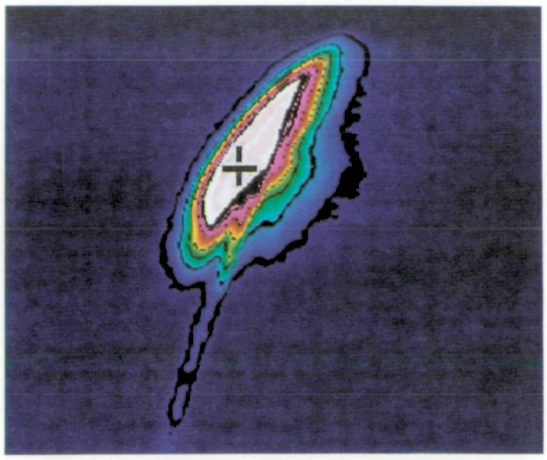

Φ = 44.0°

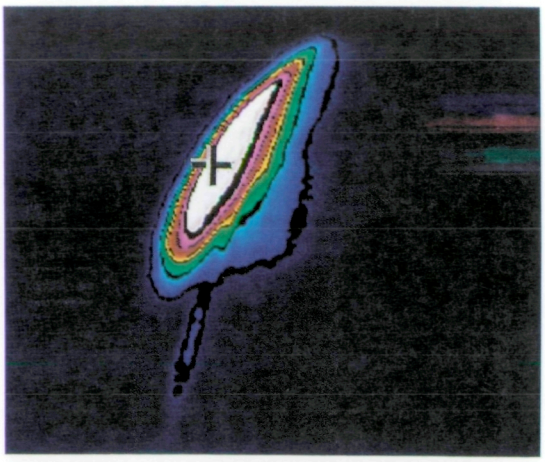

Φ = 46.3°

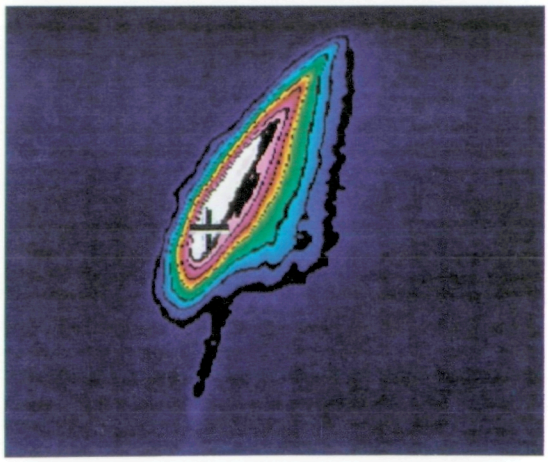

Φ = 48.2°

Φ = 63.0°

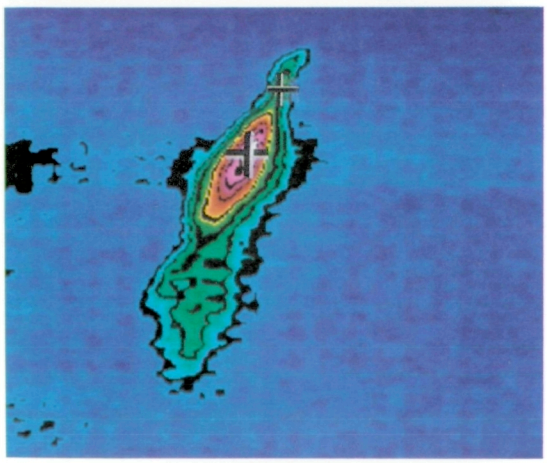

Φ = 64.1°

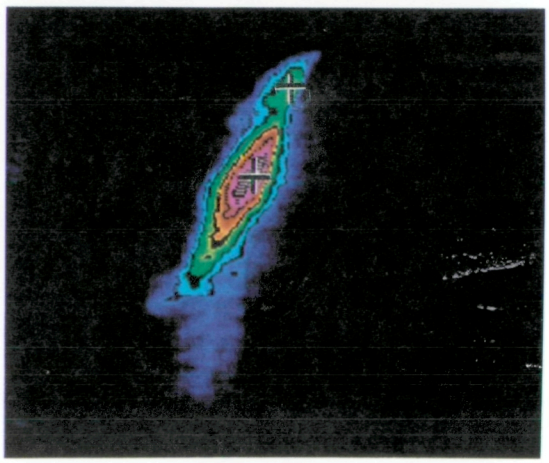

Φ = 65.2°

Figure 12. Growth of enhanced vortex system for $\alpha = 17.8°$ as seen from side camera on F/S 91-16/11. (Vortex core indicated by plus sign.)

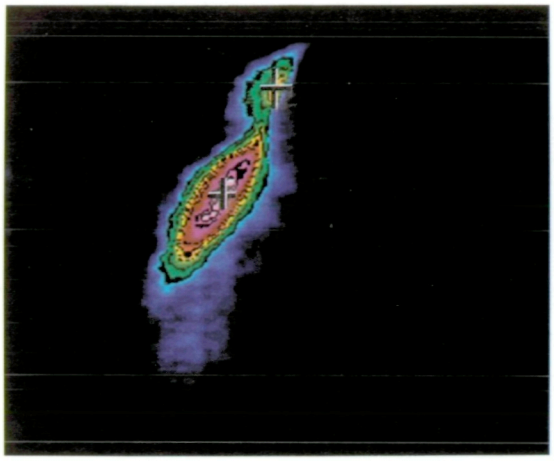

Φ = 66.5°

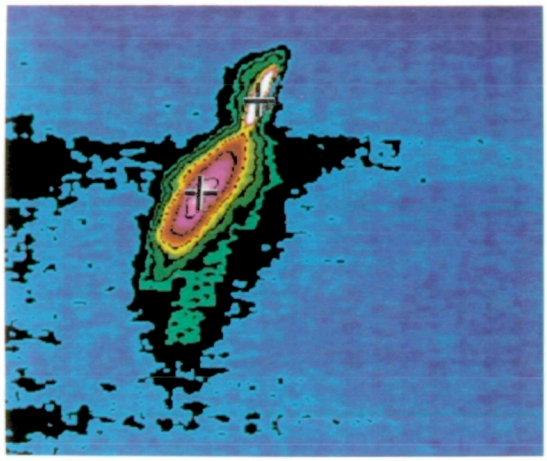

Φ = 68.6°

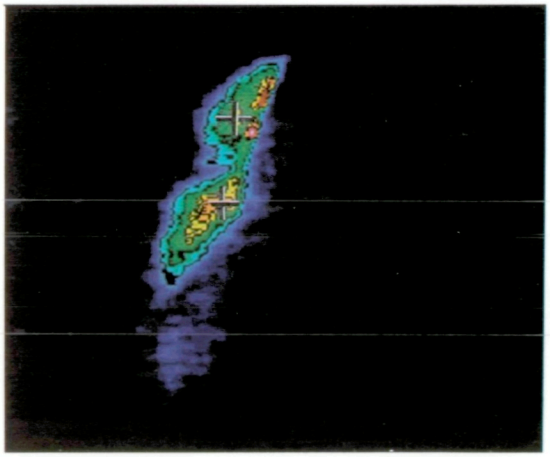

Φ = 72.7°

Figure 12. Concluded.

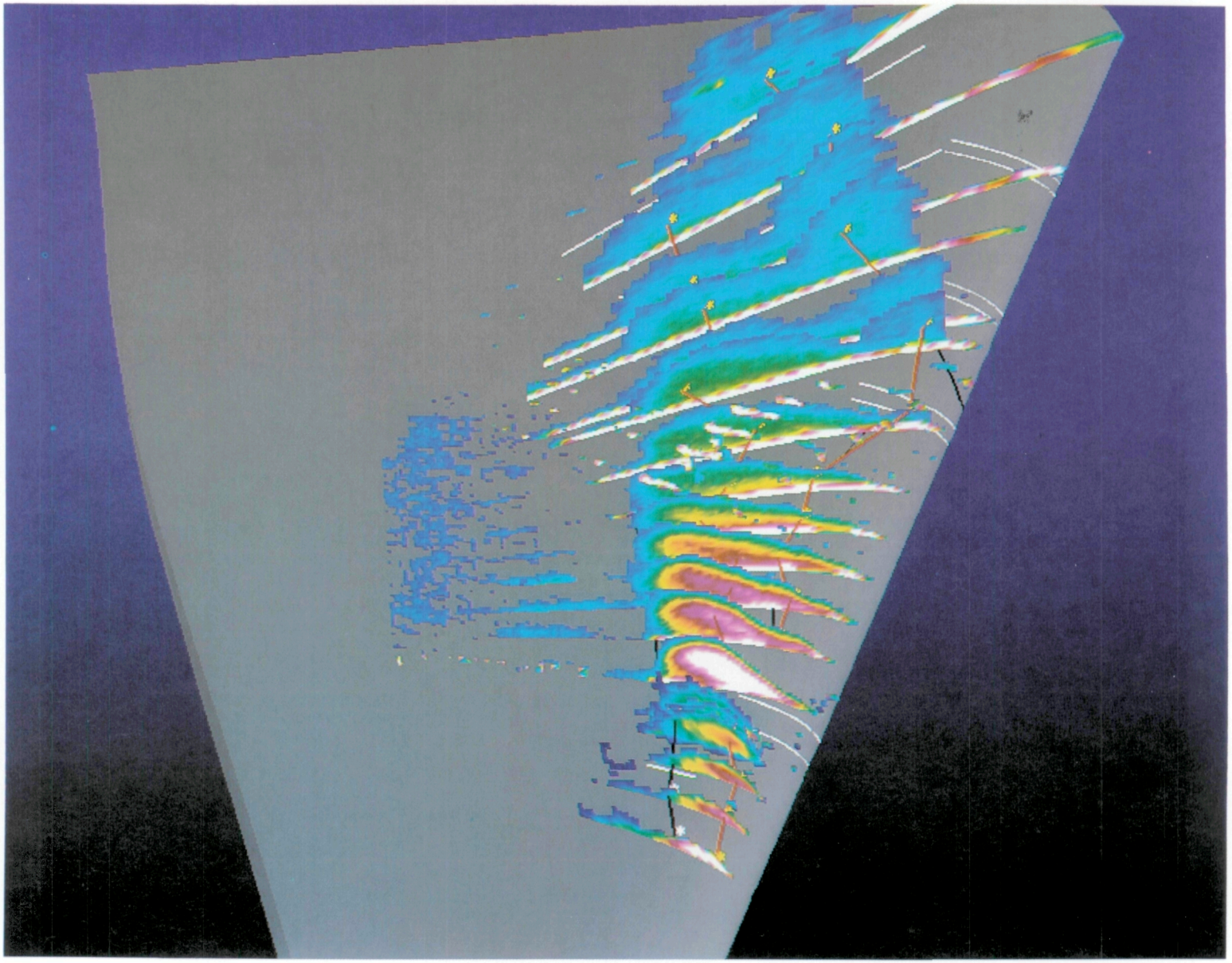

Figure 13. Vortex systems over surface geometry for $\alpha = 13.9°$ (F/S 91-13/11).

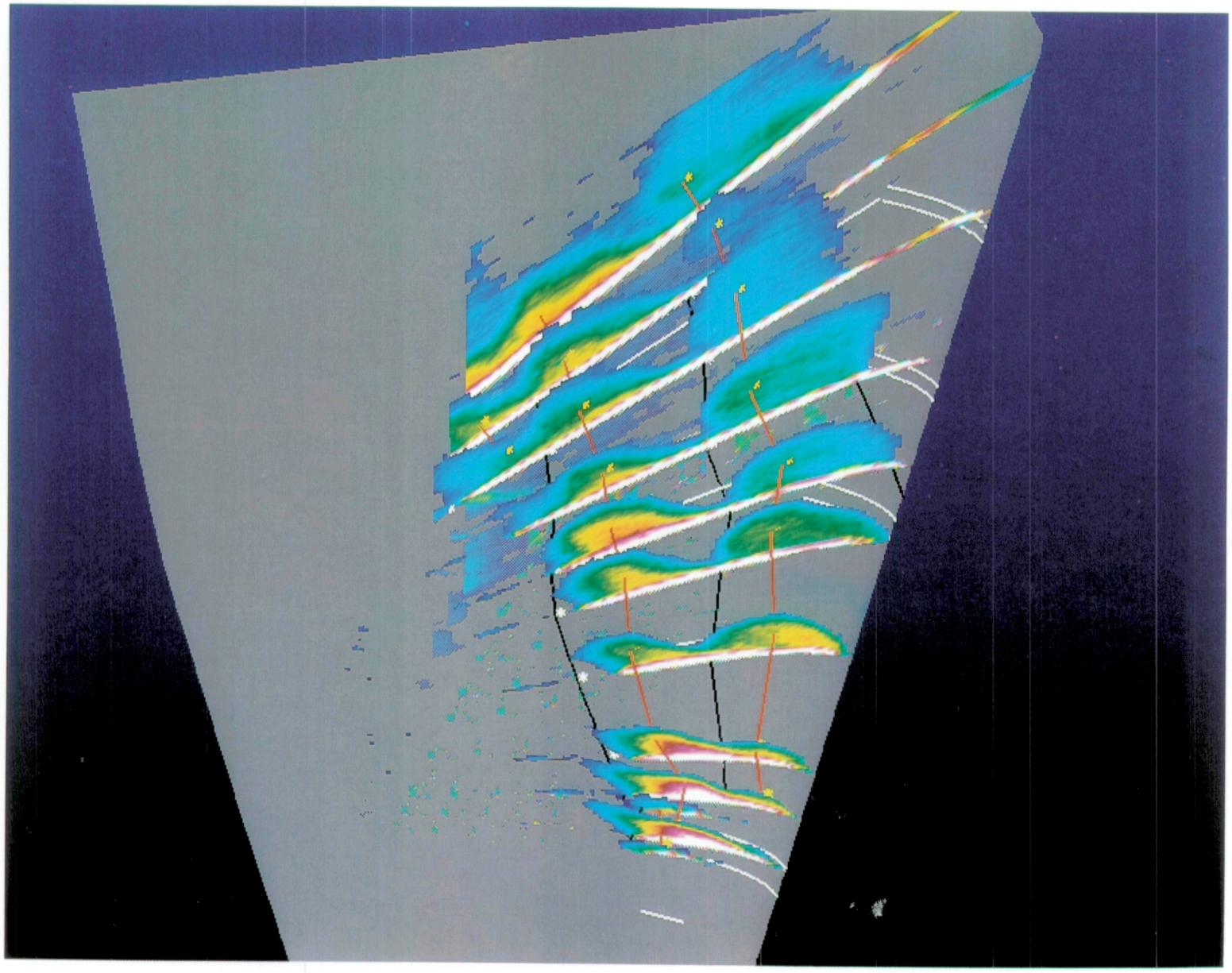

Figure 14. Vortex systems over surface geometry for $\alpha = 14.9°$ (F/S 91-13/05).

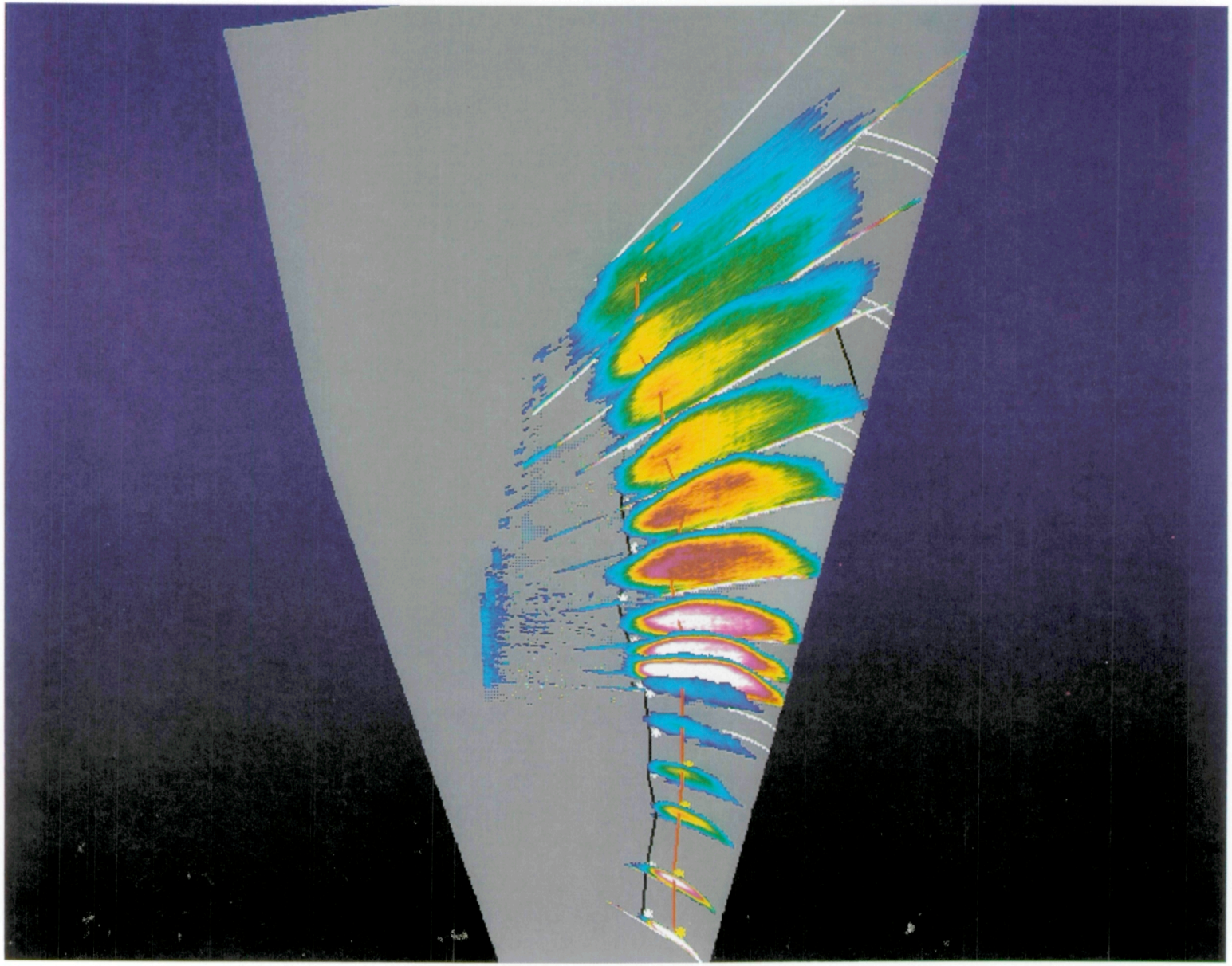

Figure 15. Vortex systems over surface geometry for $\alpha = 18.8°$ (F/S 91-13/07).

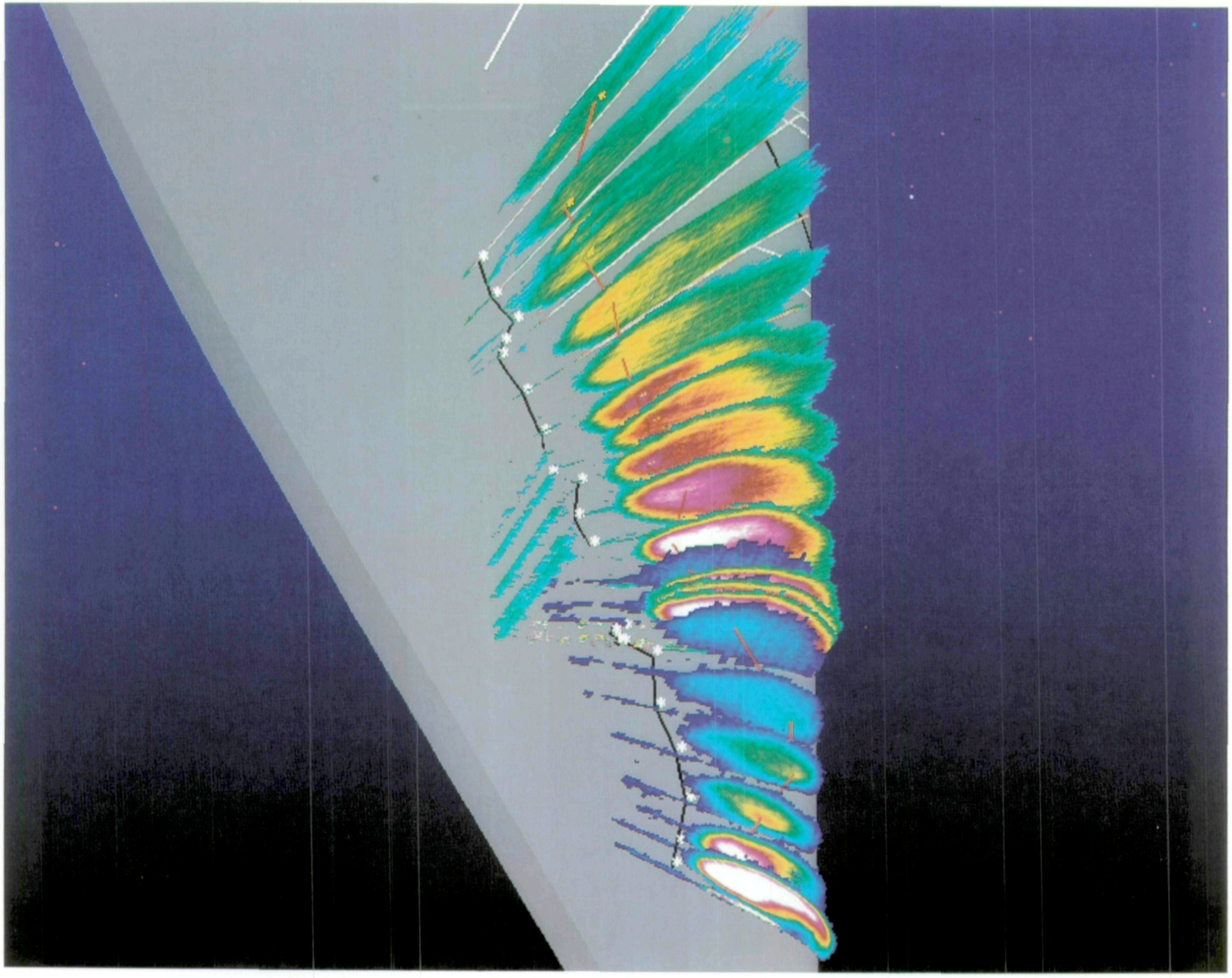

Figure 16. Vortex systems over surface geometry for $\alpha = 22.5°$ (F/S 91-13/09).

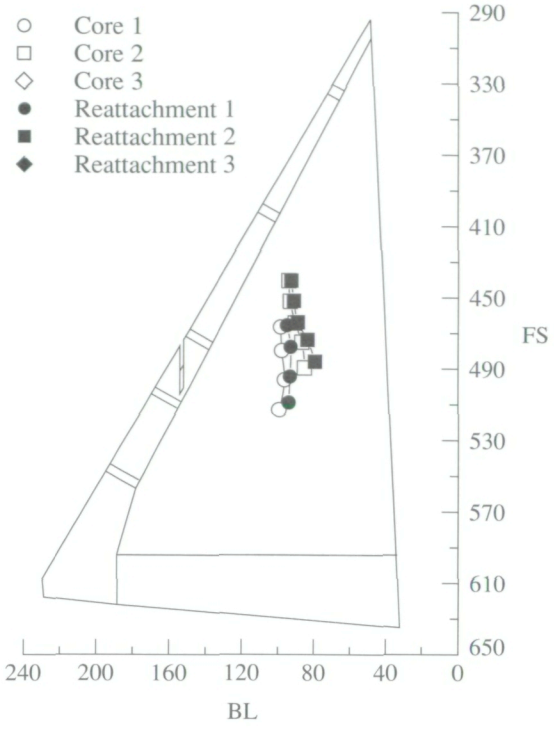

(a) $\alpha = 12.9°$; $M_\infty = 0.36$; $R_n = 39.1 \times 10^6$ (F/S 91-15/12).

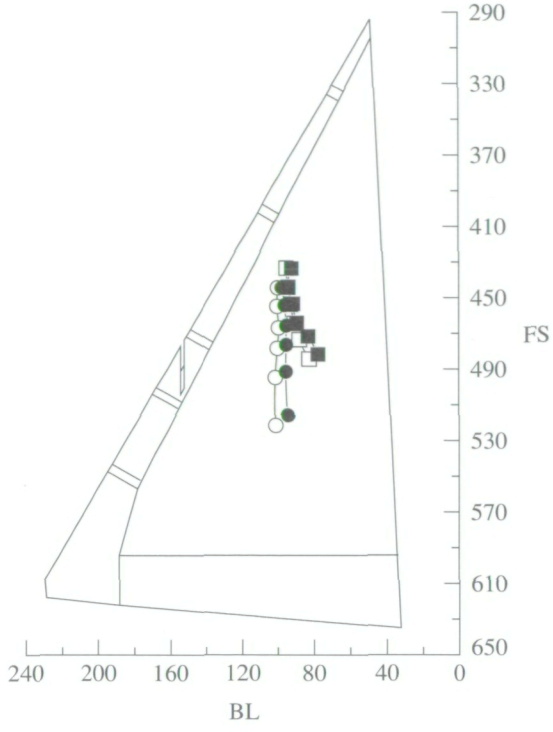

(b) $\alpha = 13.9°$; $M_\infty = 0.34$; $R_n = 37.3 \times 10^6$ (F/S 91-15/13).

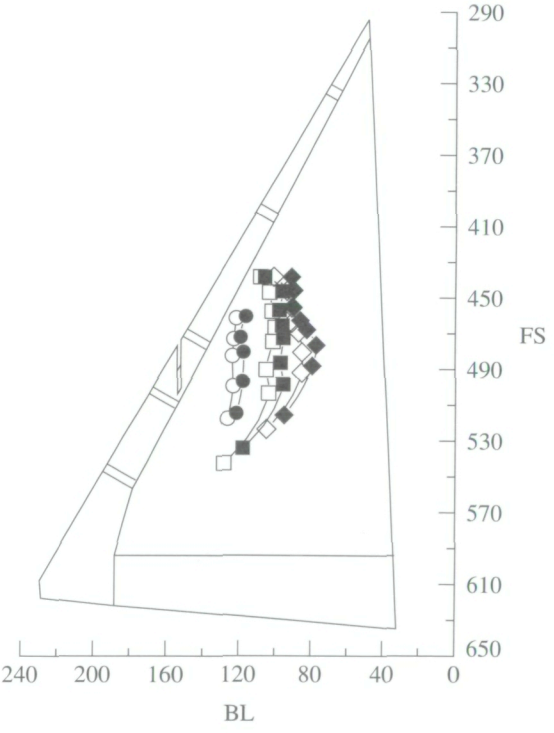

(c) $\alpha = 15.1°$; $M_\infty = 0.34$; $R_n = 37.0 \times 10^6$ (F/S 91-15/17).

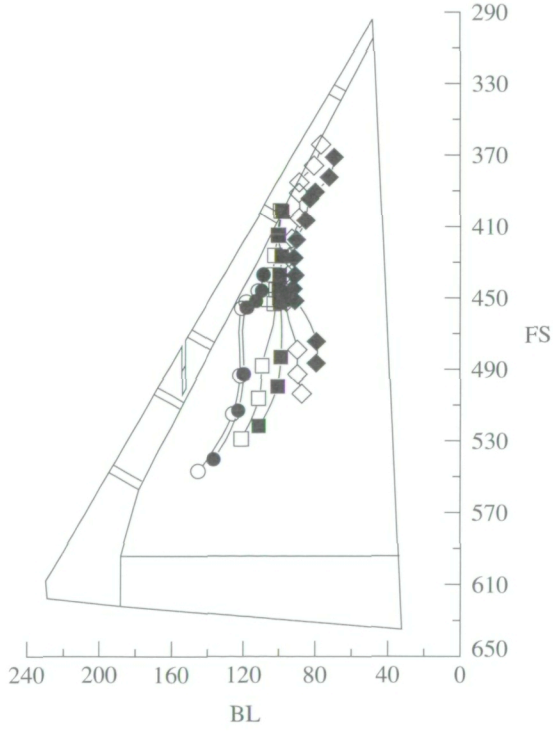

(d) $\alpha = 15.8°$; $M_\infty = 0.33$; $R_n = 33.0 \times 10^6$ (F/S 91-16/09).

Figure 17. Effect of α on vapor-screen vortex core and reattachment tracks at nominal altitude of 15 000 ft and $1g$.

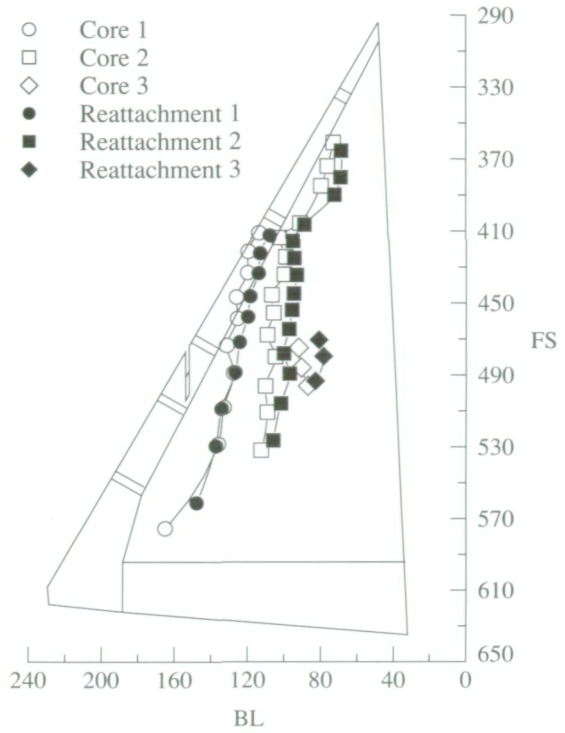

(e) $\alpha = 16.9°$; $M_\infty = 0.31$; $R_n = 31.4 \times 10^6$ (F/S 91-16/10).

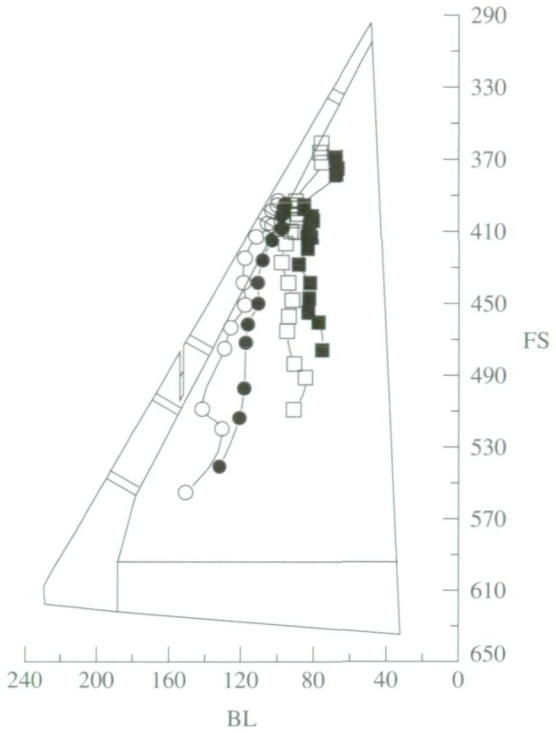

(f) $\alpha = 17.8°$; $M_\infty = 0.29$; $R_n = 30.1 \times 10^6$ (F/S 91-16/11).

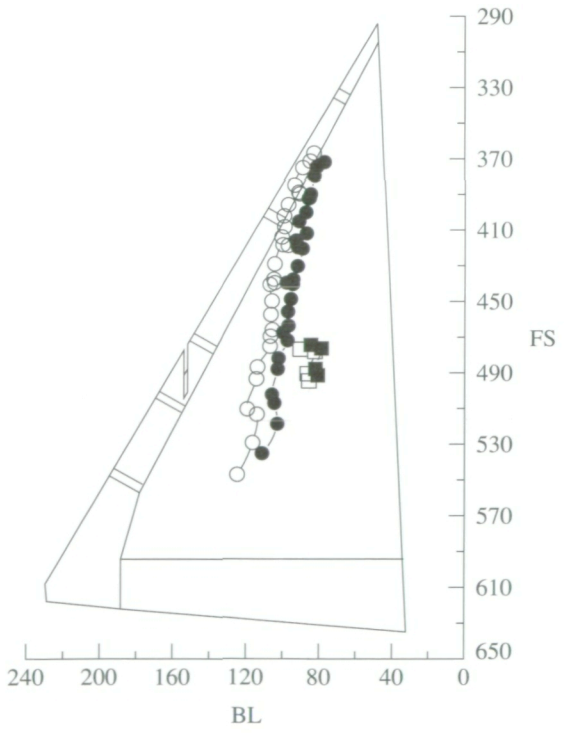

(g) $\alpha = 18.6°$; $M_\infty = 0.29$; $R_n = 30.0 \times 10^6$ (F/S 91-17/07).

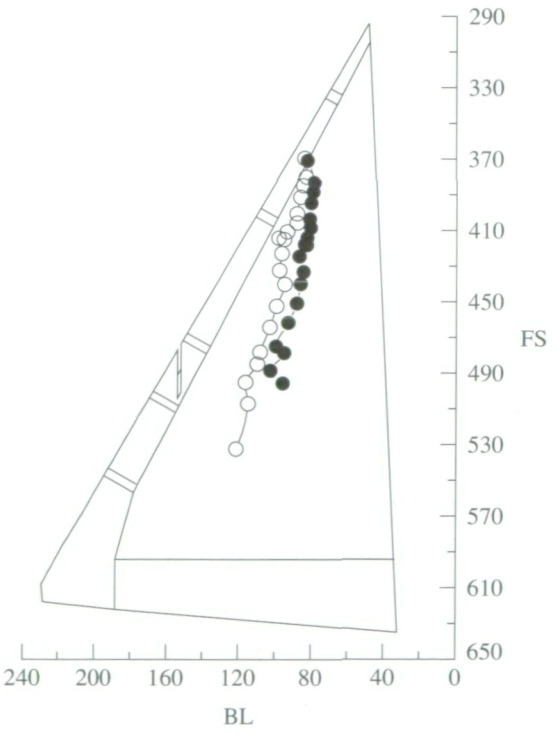

(h) $\alpha = 20.2°$; $M_\infty = 0.27$; $R_n = 28.3 \times 10^6$ (F/S 91-17/09).

Figure 17. Continued.

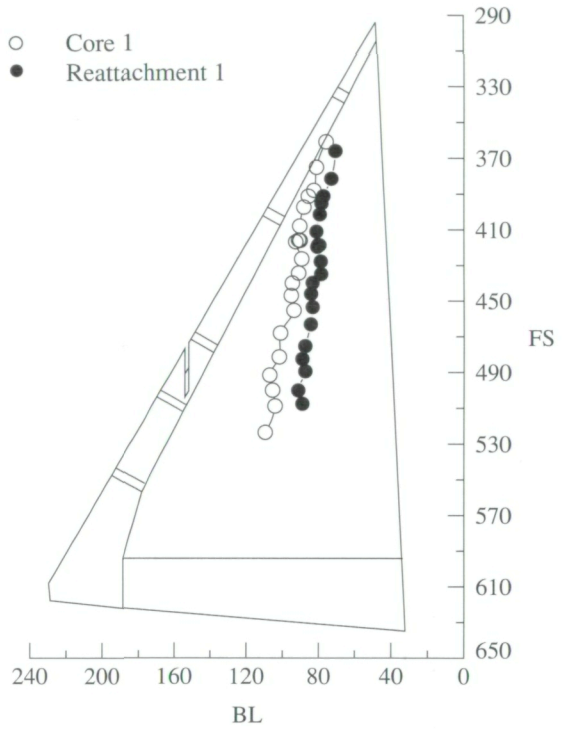

(i) $\alpha = 21.3°$; $M_\infty = 0.26$; $R_n = 27.5 \times 10^6$ (F/S 91-17/10).

Figure 17. Concluded.

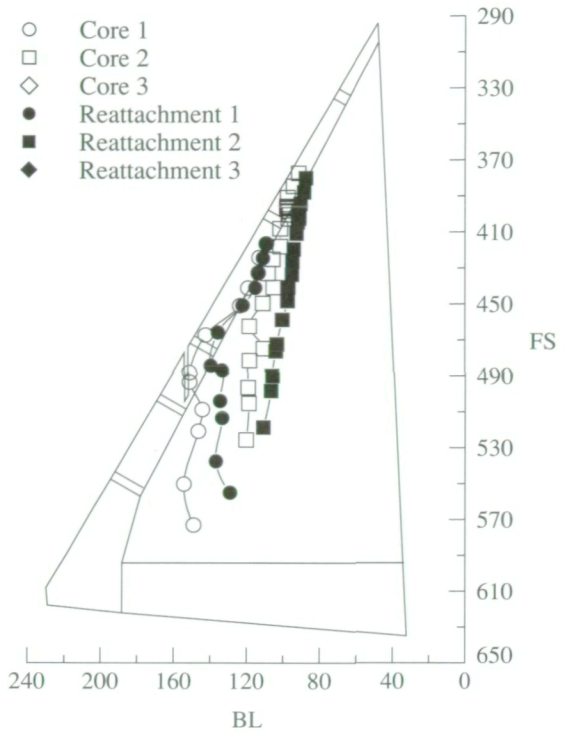

(a) $\alpha = 13.9°$; $M_\infty = 0.42$; $R_n = 35.1 \times 10^6$ (F/S 91-13/11).

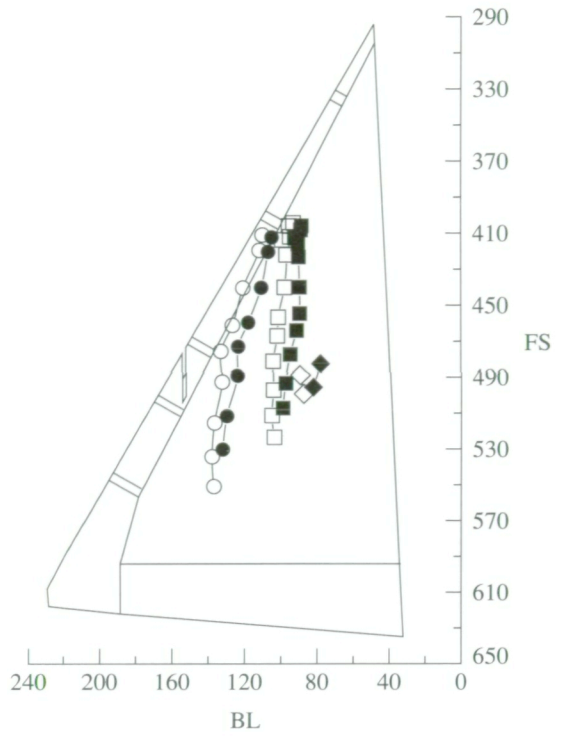

(b) $\alpha = 14.9°$; $M_\infty = 0.41$; $R_n = 34.6 \times 10^6$ (F/S 91-13/05).

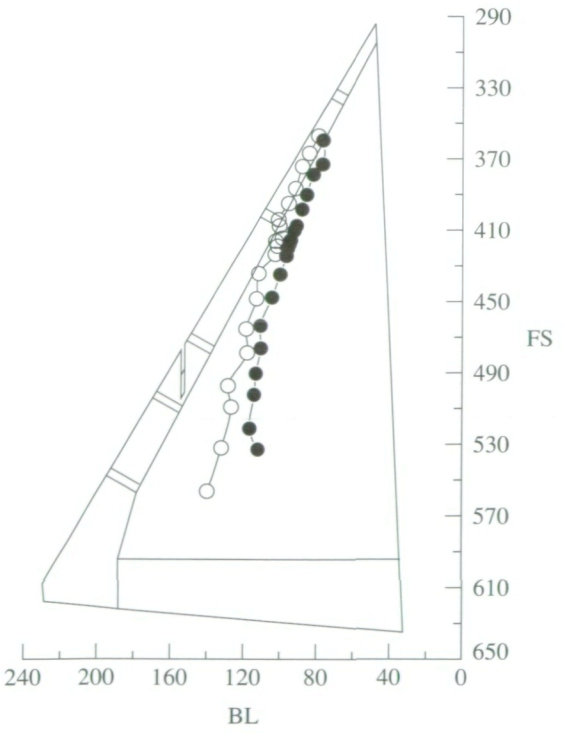

(c) $\alpha = 16.1°$; $M_\infty = 0.39$; $R_n = 32.0 \times 10^6$ (F/S 91-13/10).

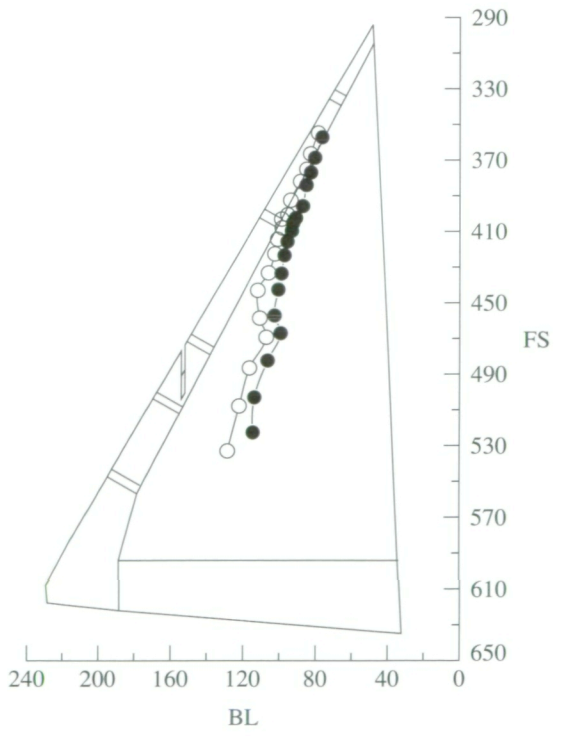

(d) $\alpha = 17.0°$; $M_\infty = 0.38$; $R_n = 32.0 \times 10^6$ (F/S 91-13/06).

Figure 18. Effect of α on vapor-screen vortex core and reattachment tracks at nominal altitude of 25 000 ft and $1g$.

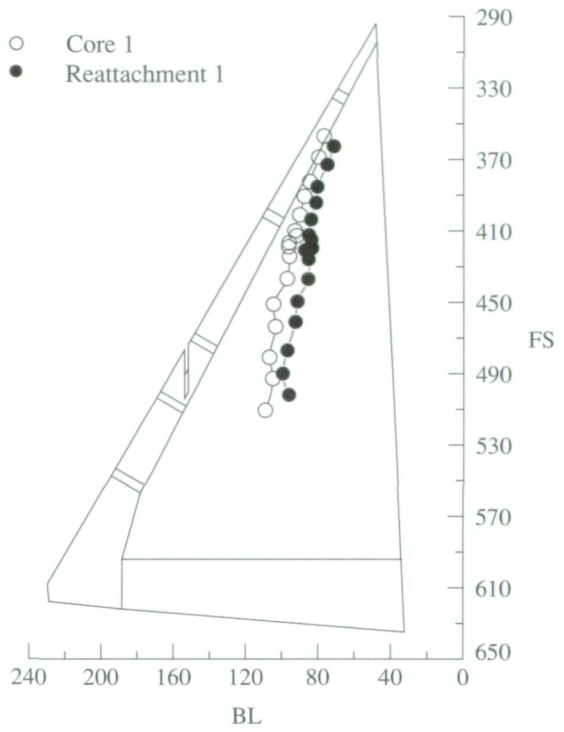

(e) $\alpha = 18.8°$; $M_\infty = 0.35$; $R_n = 29.9 \times 10^6$ (F/S 91-13/07).

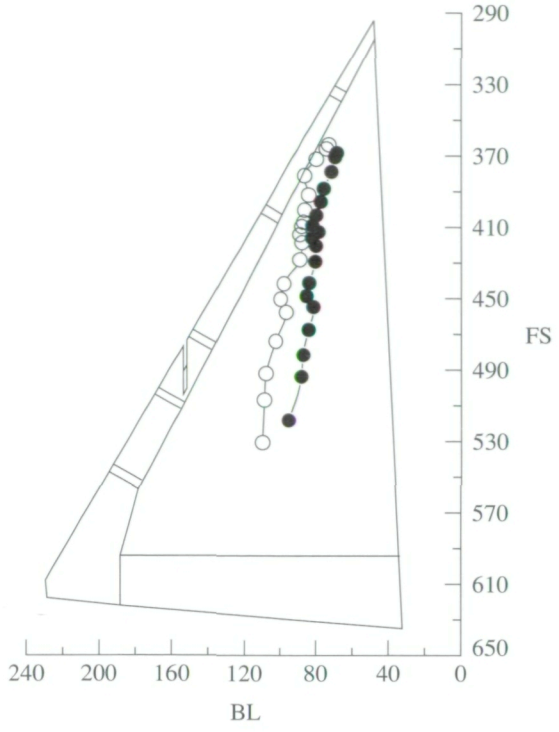

(f) $\alpha = 20.5°$; $M_\infty = 0.34$; $R_n = 27.8 \times 10^6$ (F/S 91-13/08).

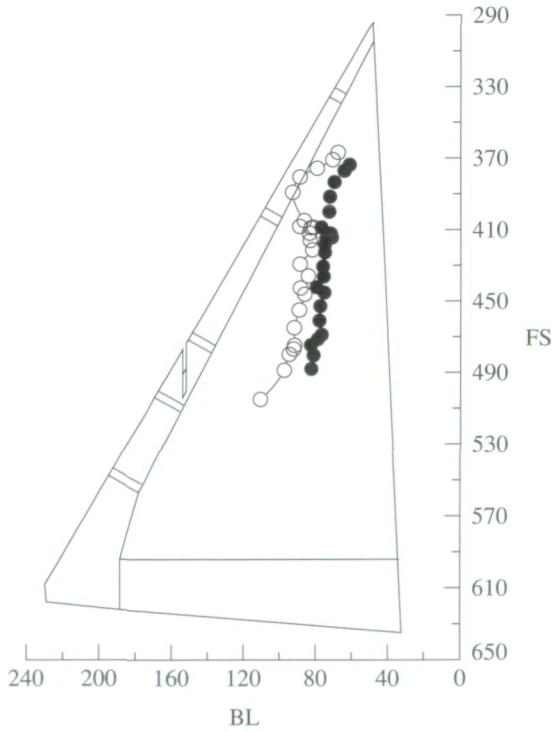

(g) $\alpha = 22.5°$; $M_\infty = 0.32$; $R_n = 26.6 \times 10^6$ (F/S 91-13/09).

Figure 18. Concluded.

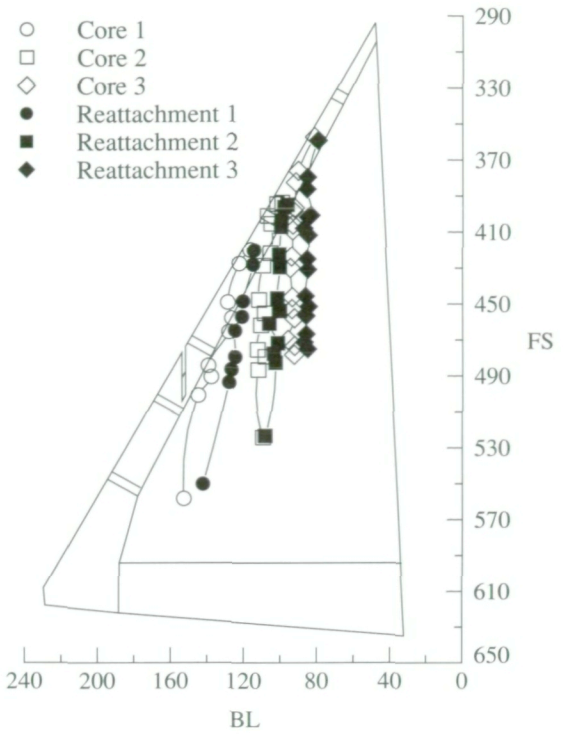

(a) $\alpha = 13.9°$; $M_\infty = 0.54$; $R_n = 30.8 \times 10^6$ (F/S 91-15/06).

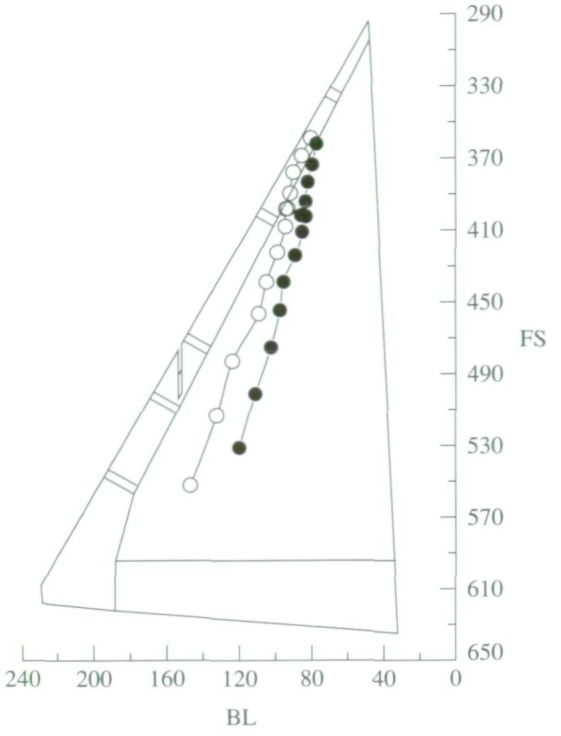

(b) $\alpha = 14.8°$; $M_\infty = 0.53$; $R_n = 29.2 \times 10^6$ (F/S 91-14/07).

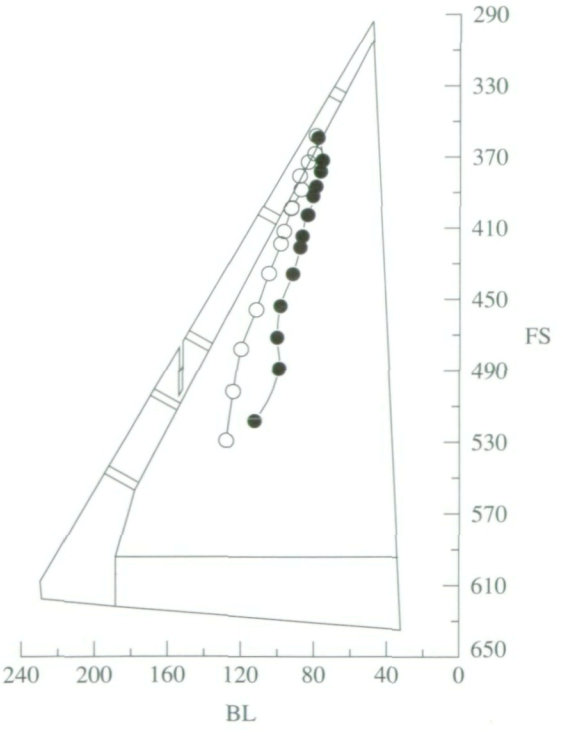

(c) $\alpha = 15.8°$; $M_\infty = 0.50$; $R_n = 27.6 \times 10^6$ (F/S 91-15/08).

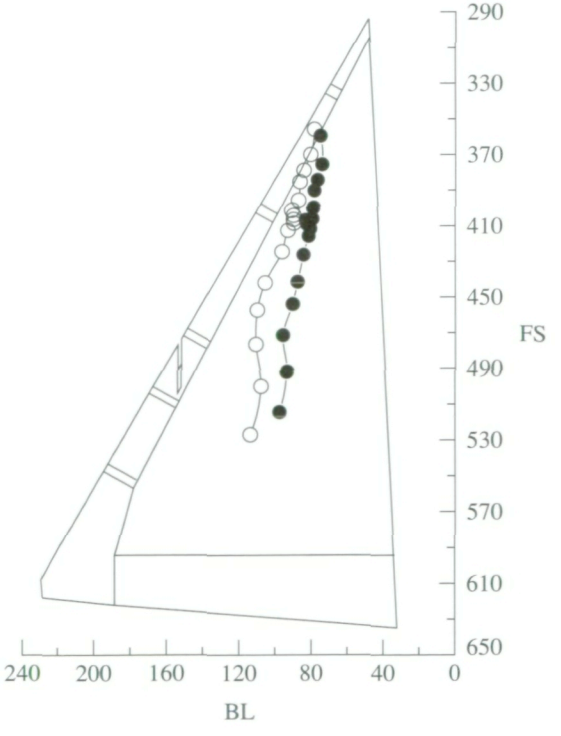

(d) $\alpha = 16.8°$; $M_\infty = 0.49$; $R_n = 26.8 \times 10^6$ (F/S 91-14/08).

Figure 19. Effect of α on vapor-screen vortex core and reattachment tracks at nominal altitude of 35 000 ft and $1g$.

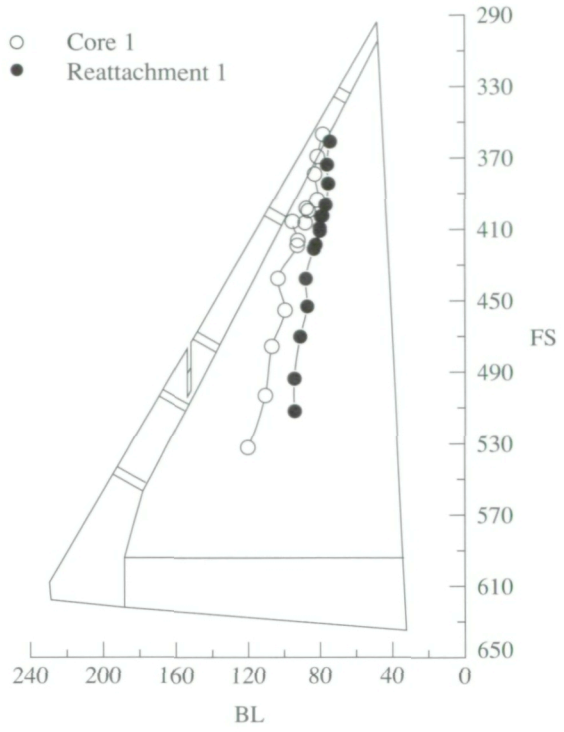

(e) $\alpha = 17.7°$; $M_\infty = 0.47$; $R_n = 25.8 \times 10^6$ (F/S 91-14/09).

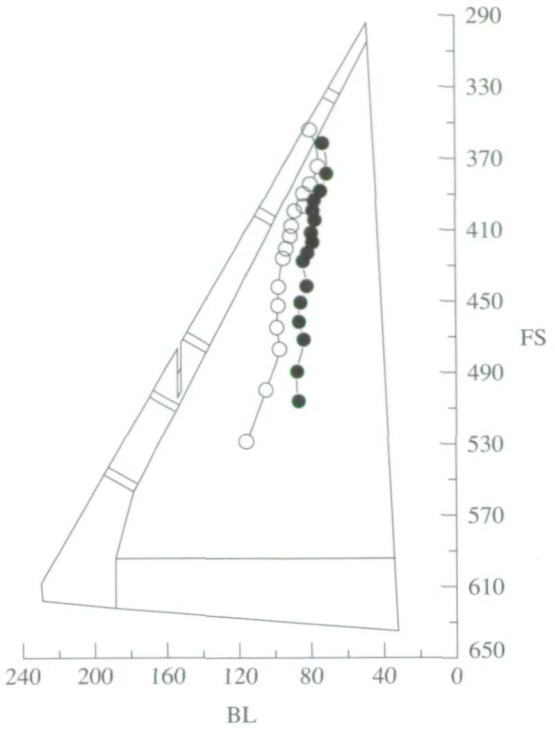

(f) $\alpha = 18.7°$; $M_\infty = 0.45$; $R_n = 24.6 \times 10^6$ (F/S 91-14/10).

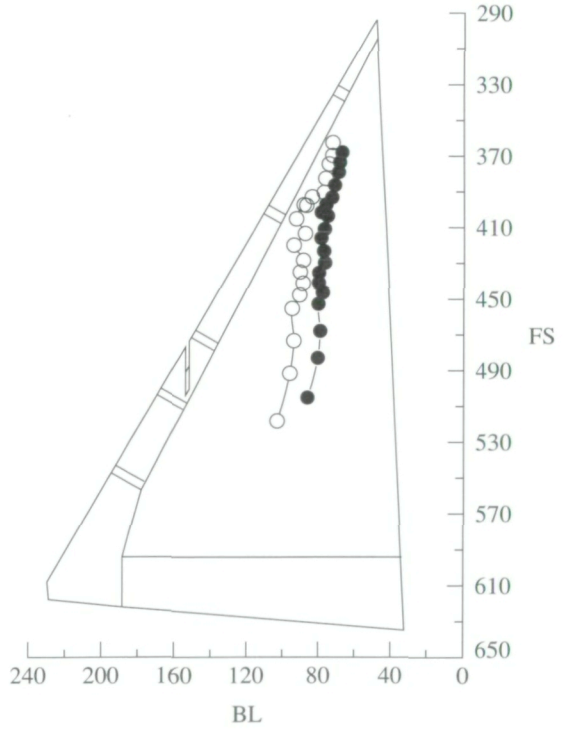

(g) $\alpha = 19.7°$; $M_\infty = 0.44$; $R_n = 23.8 \times 10^6$ (F/S 91-14/11).

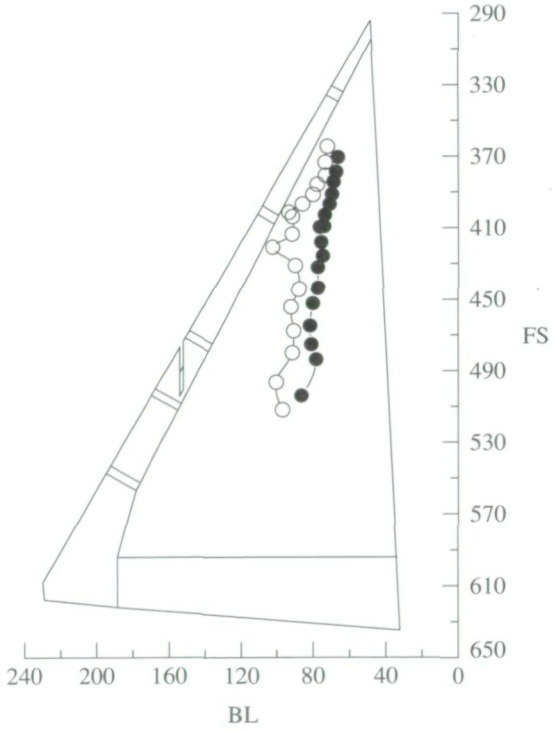

(h) $\alpha = 20.5°$; $M_\infty = 0.42$; $R_n = 23.7 \times 10^6$ (F/S 91-14/12).

Figure 19. Continued.

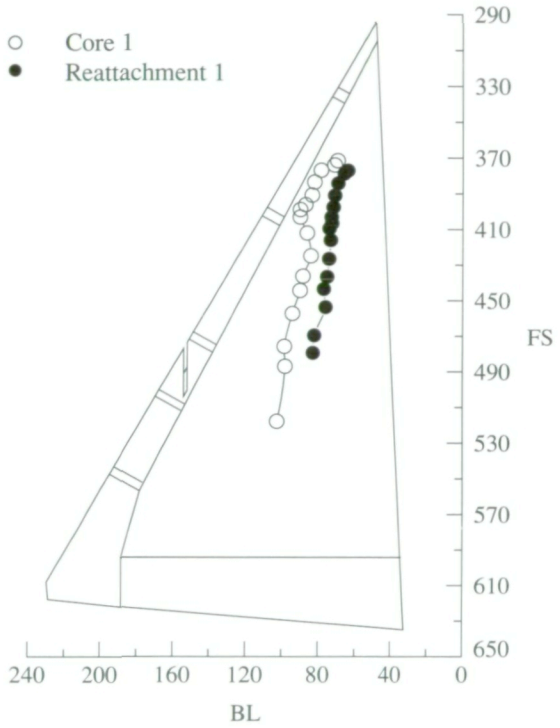

(i) $\alpha = 21.9°$; $M_\infty = 0.40$; $R_n = 22.6 \times 10^6$ (F/S 91-15/10).

Figure 19. Concluded.

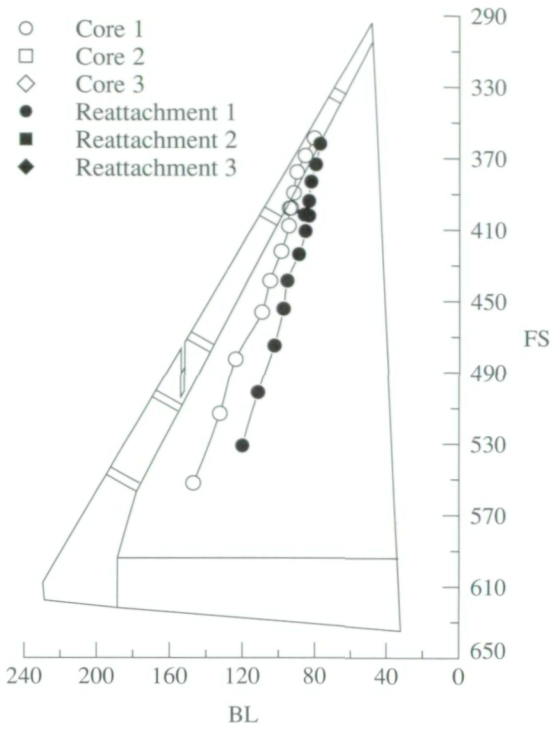

(a) $0.9g$; $M_\infty = 0.53$; $R_n = 29.2 \times 10^6$ (F/S 91-14/07).

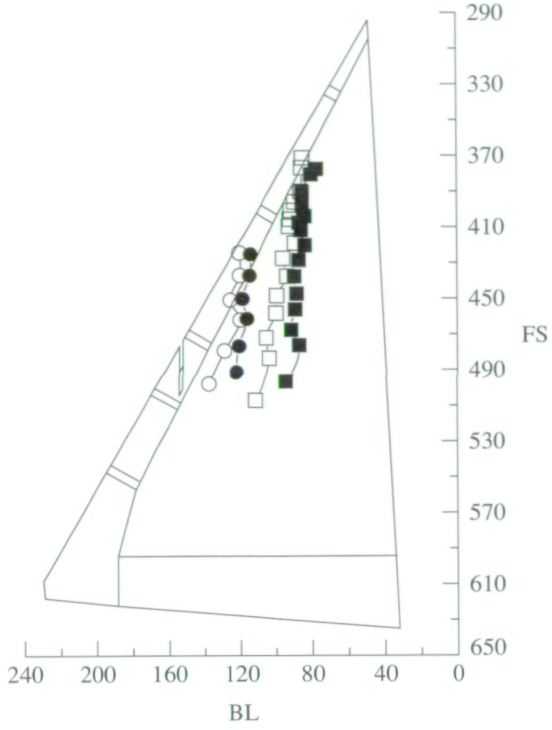

(b) $1.6g$; $M_\infty = 0.68$; $R_n = 35.5 \times 10^6$ (F/S 91-17/05).

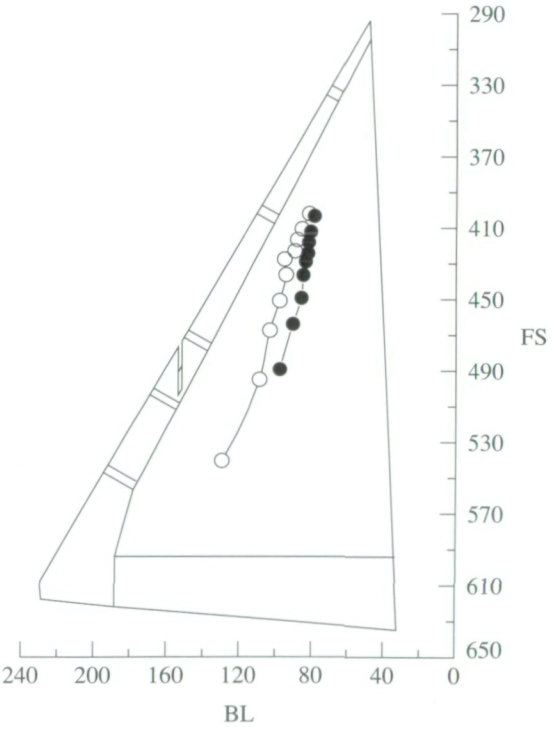

(c) $2.5g$; $M_\infty = 0.73$; $R_n = 45.7 \times 10^6$ (F/S 91-15/11).

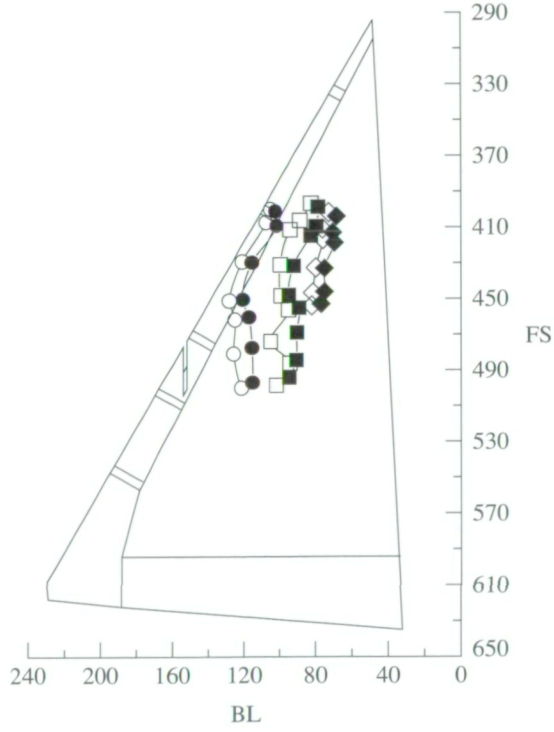

(d) $3.9g$; $M_\infty = 0.80$; $R_n = 57.3 \times 10^6$ (F/S 91-16/07).

Figure 20. Effects of R_n and load factor on vapor-screen vortex core and reattachment tracks at nominal altitude of 35 000 ft and $\alpha = 14.8°$ for spiral descents.

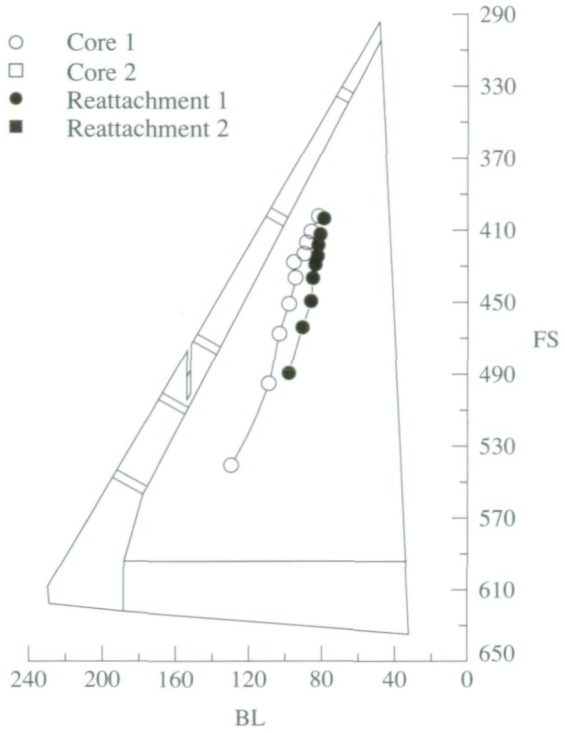

(a) $\alpha = 14.8°$; $M_\infty = 0.73$; $R_n = 45.7 \times 10^6$ (F/S 91-15/11).

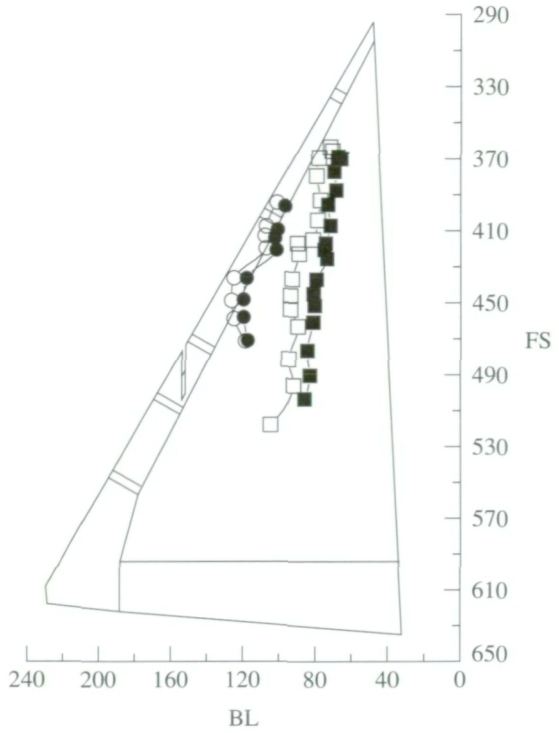

(b) $\alpha = 16.8°$; $M_\infty = 0.78$; $R_n = 44.6 \times 10^6$ (F/S 91-16/05).

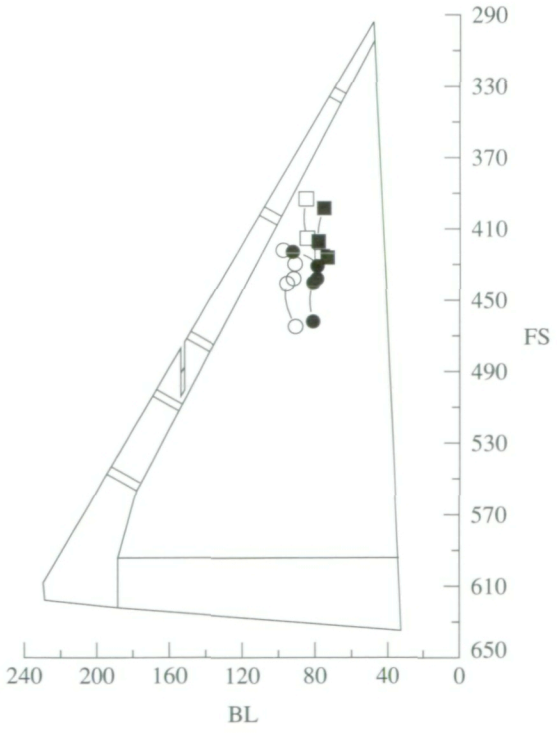

(c) $\alpha = 18.6°$; $M_\infty = 0.67$; $R_n = 35.6 \times 10^6$ (F/S 91-17/06).

Figure 21. Effect of α on vapor-screen vortex core and reattachment tracks at nominal altitude of 35 000 ft and $2.6g$.

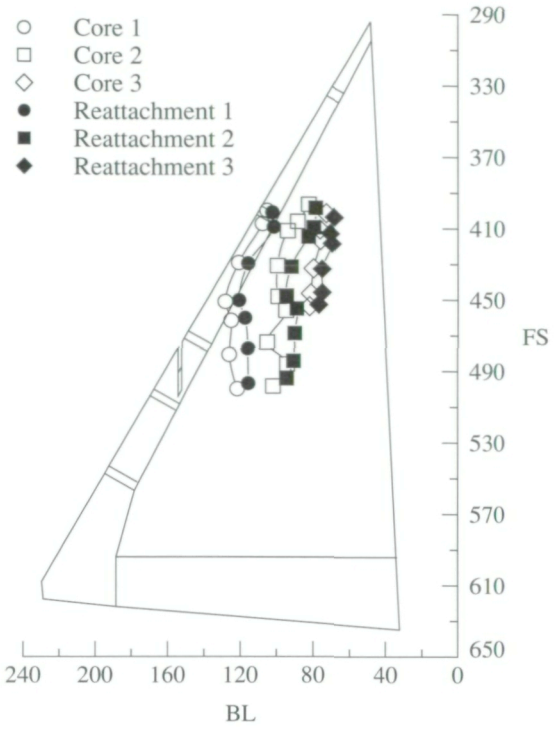

(a) $\alpha = 14.8°$; $M_\infty = 0.80$; $R_n = 57.3 \times 10^6$ (F/S 91-16/07).

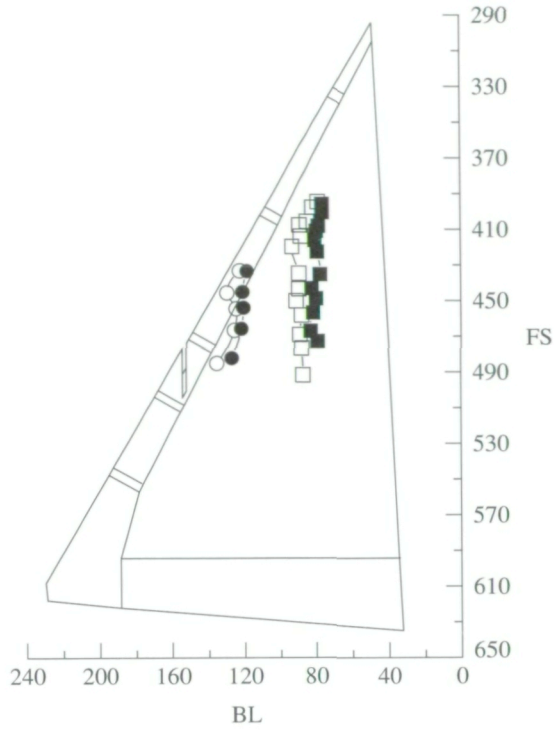

(b) $\alpha = 17.3°$; $M_\infty = 0.81$; $R_n = 48.4 \times 10^6$ (F/S 91-16/08).

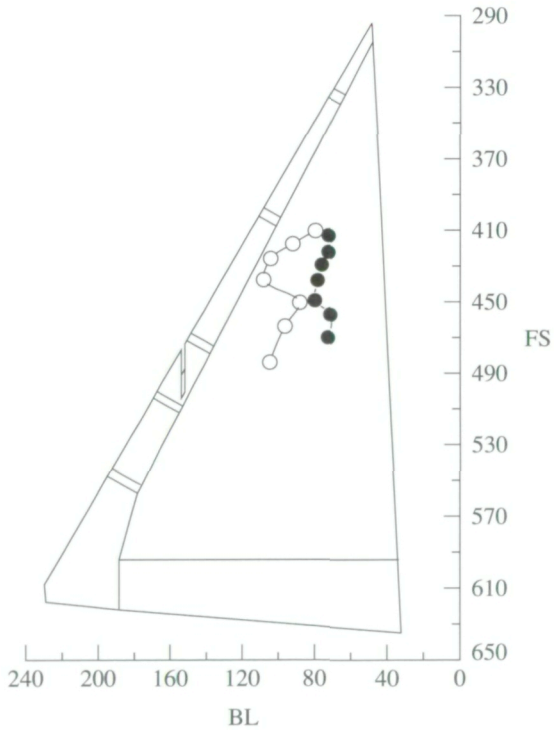

(c) $\alpha = 19.4°$; $M_\infty = 0.69$; $R_n = 46.6 \times 10^6$ (F/S 91-16/06).

Figure 22. Effect of α on vapor-screen vortex core and reattachment tracks at nominal altitude of 30 000 ft and $3.7g$.

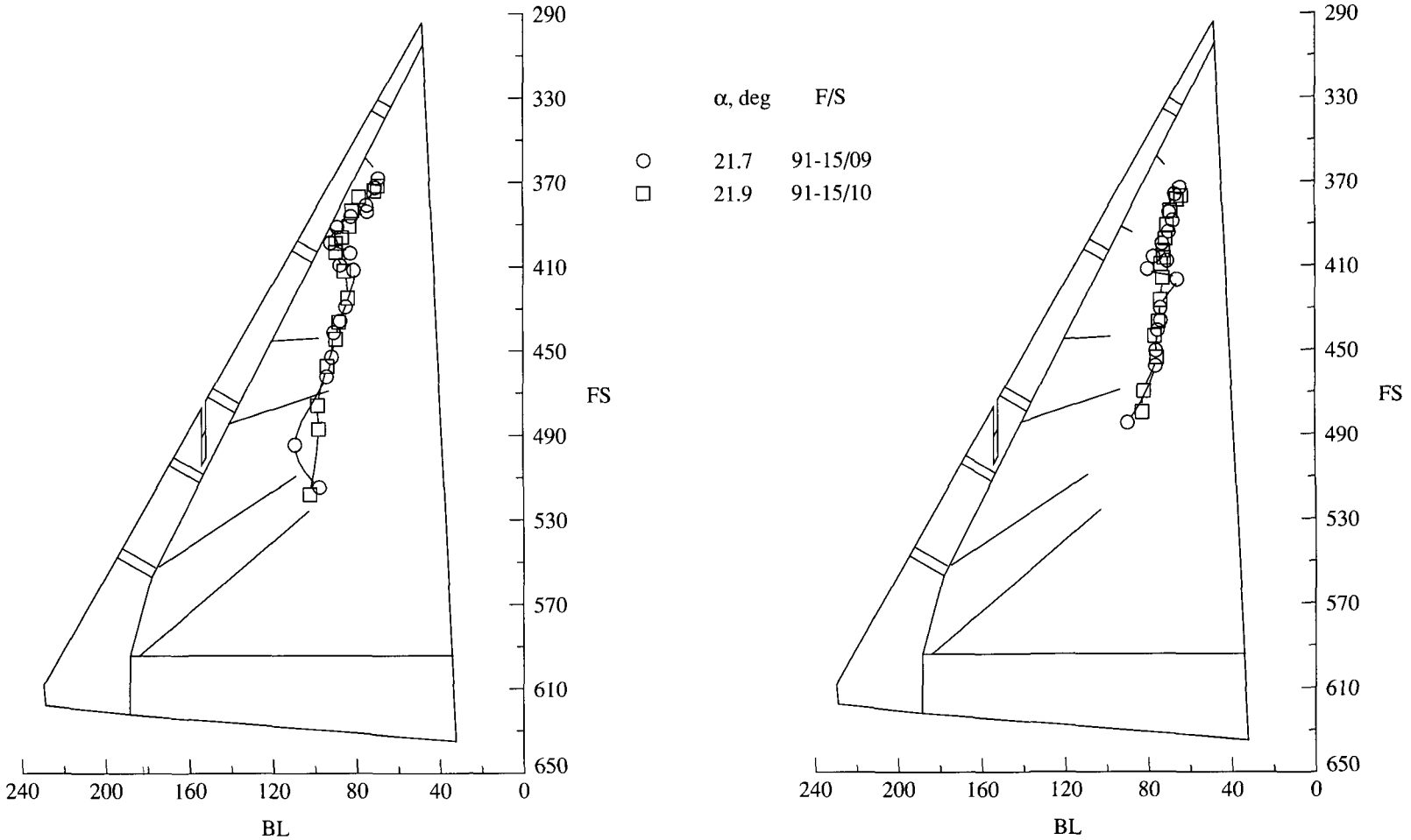

(a) Core tracks.

(b) Reattachment tracks.

Figure 23. Repeatability of vapor-screen vortex core location and reattachment point at nominal altitude of 35 000 ft, $\alpha = 21.8°$, and $1g$.

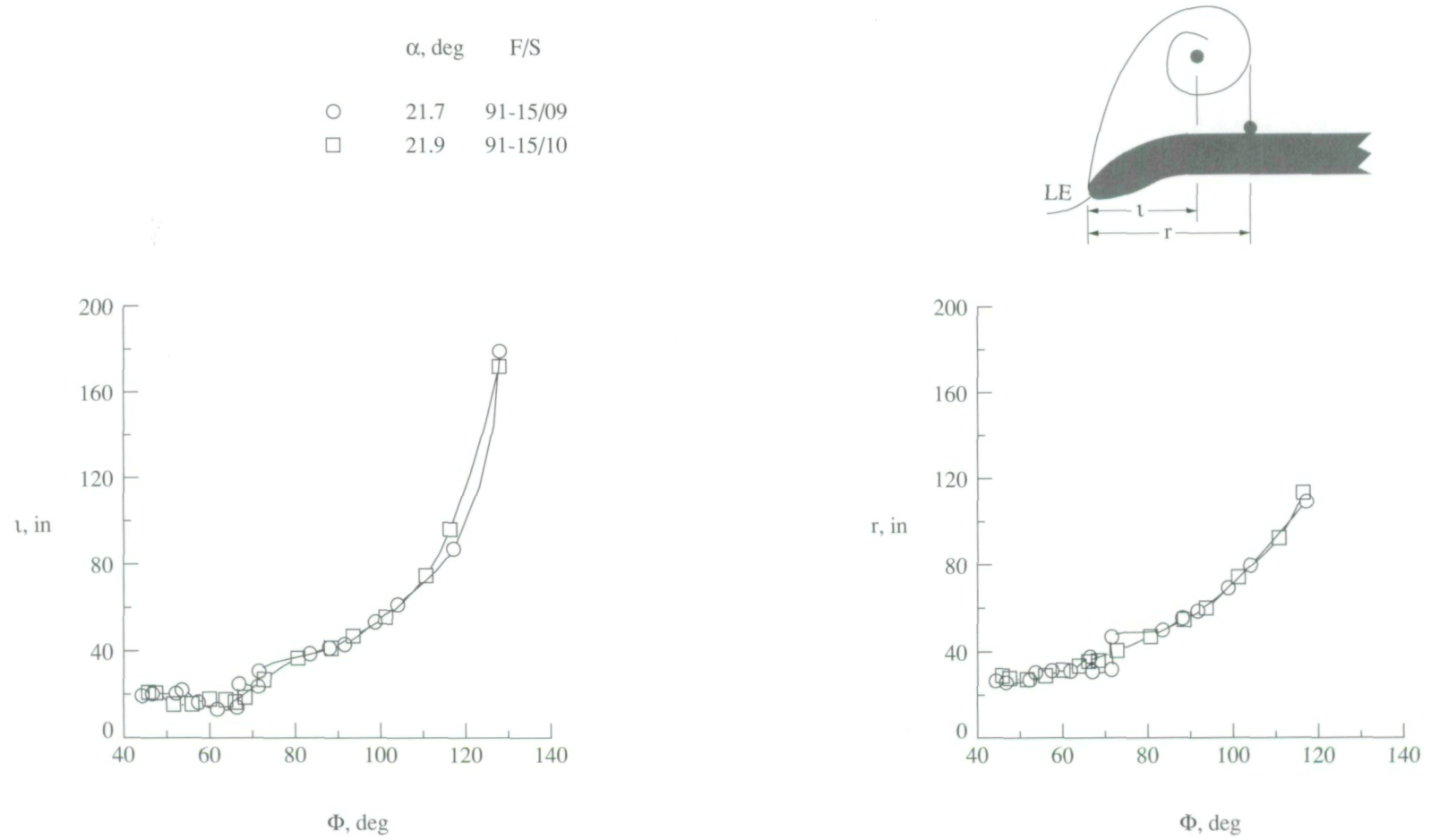

(c) Variation of l and r with Φ.

Figure 23. Concluded.

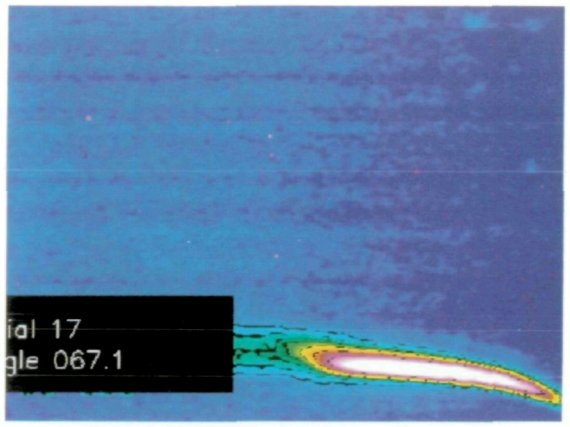

$\alpha = 15.1°$

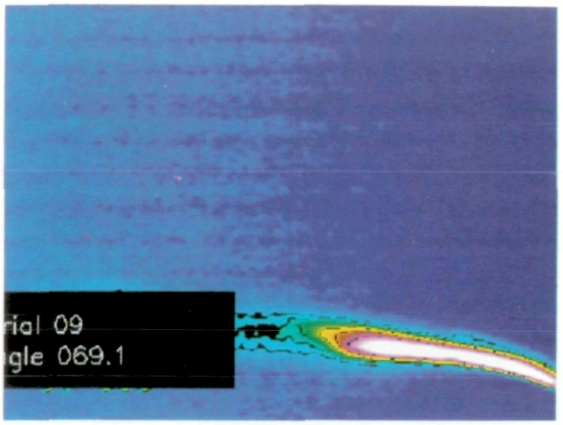

$\alpha = 15.8°$

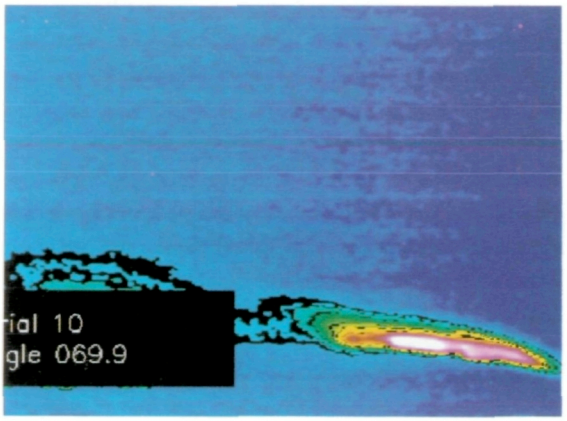

$\alpha = 16.9°$

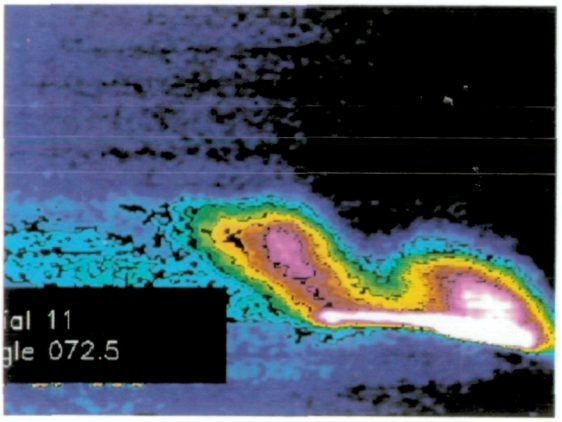

$\alpha = 17.8°$

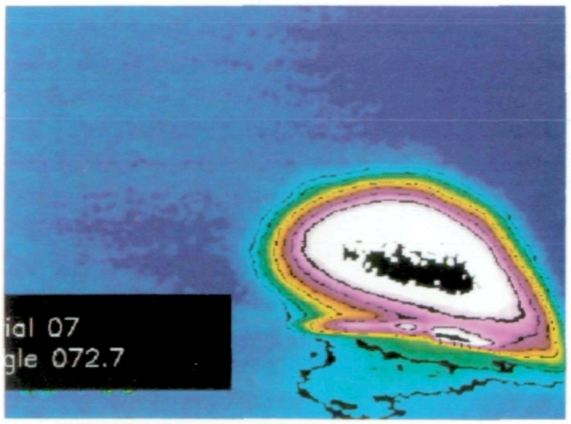

$\alpha = 18.6°$

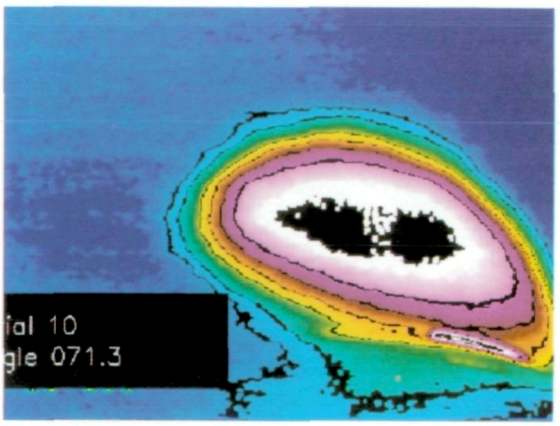

$\alpha = 21.3°$

(a) $\Phi = 70° \pm 3°$.

Figure 24. Effect of α on enhanced 2-D images at nominal altitude of 15 000 ft and $1g$.

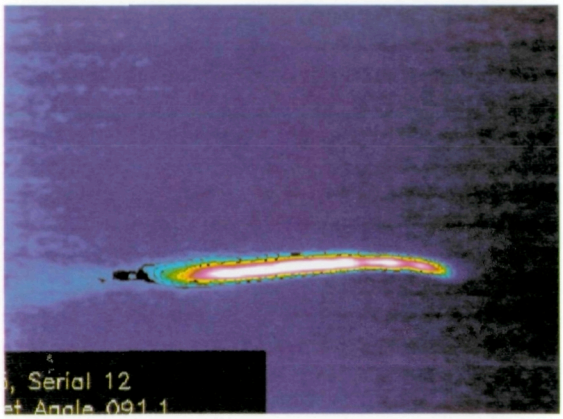

$\alpha = 12.9°$

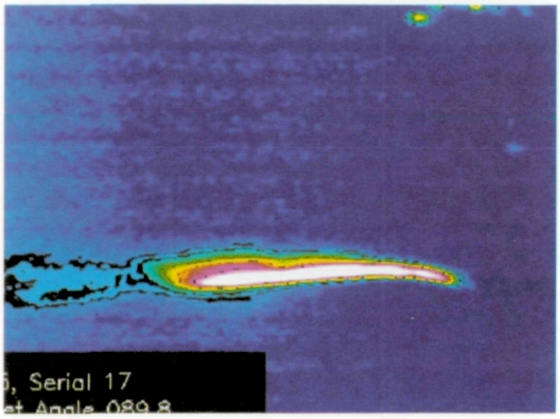

$\alpha = 15.1°$

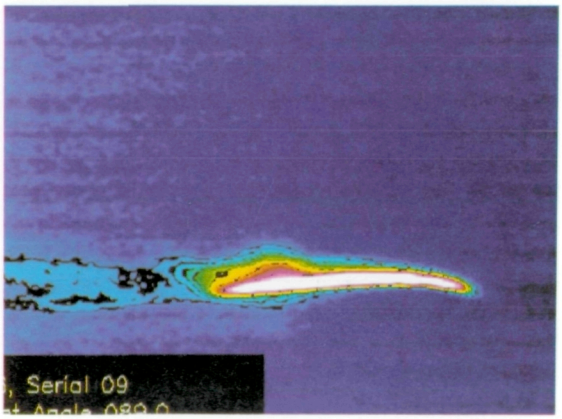

$\alpha = 15.8°$

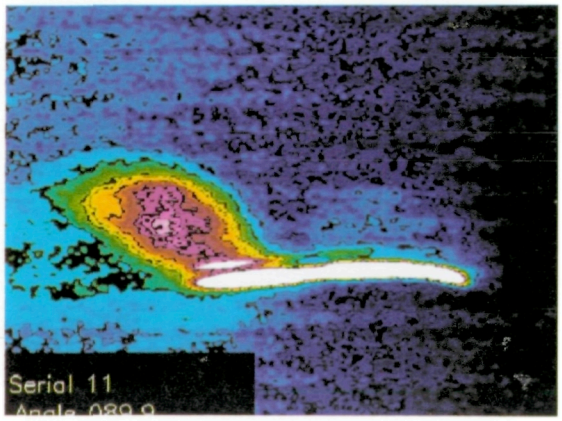

$\alpha = 17.8°$

(b) $\Phi = 90° \pm 3°$.

Figure 24. Continued.

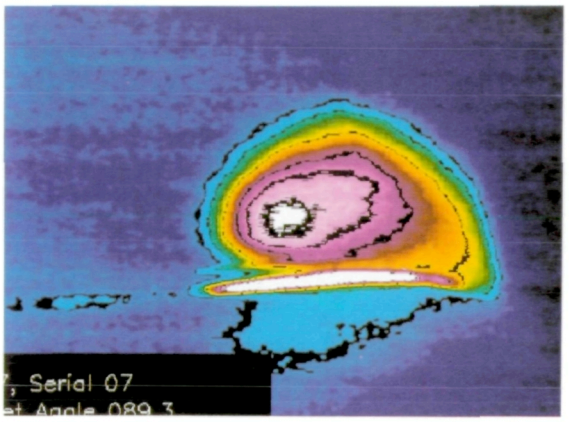

$\alpha = 18.6°$

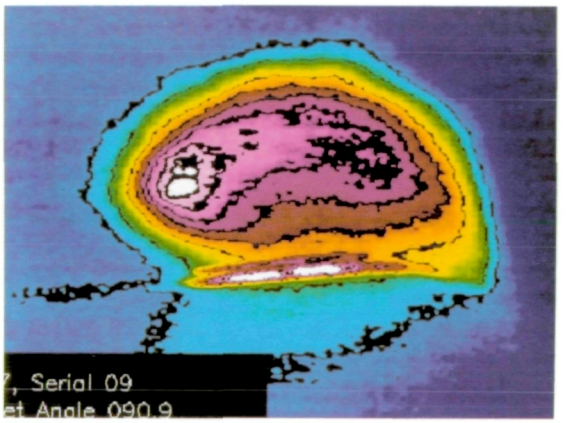

$\alpha = 20.2°$

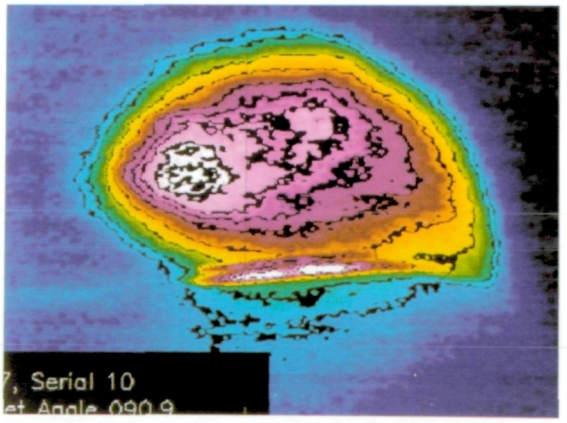

$\alpha = 21.3°$

(b) Concluded.

Figure 24. Continued.

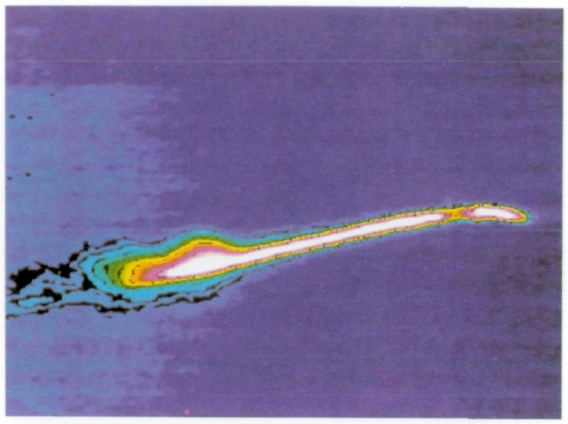

α = 13.9°

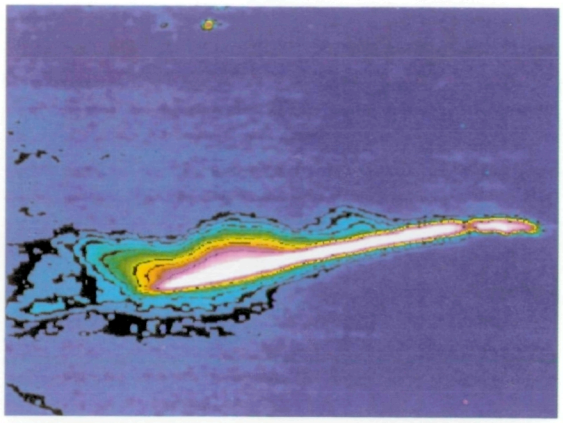

α = 15.1°

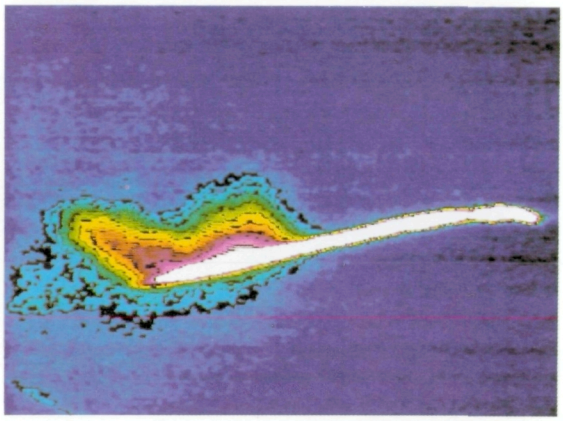

α = 16.9°

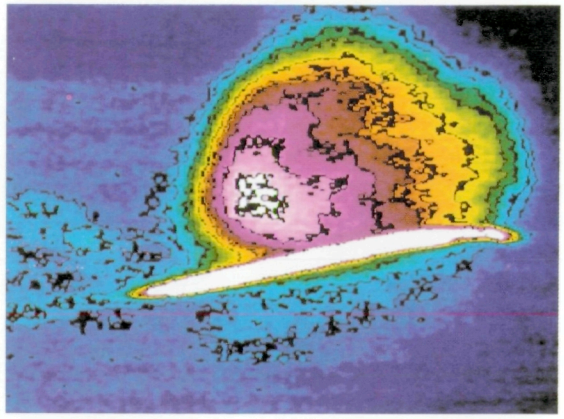

α = 18.6°

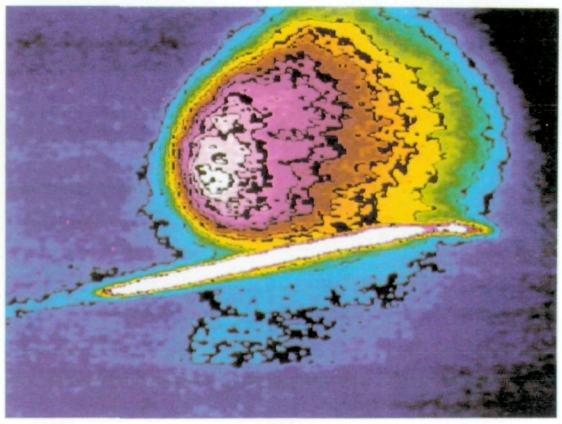

α = 20.2°

(c) $\Phi = 110° \pm 3°$.

Figure 24. Concluded.

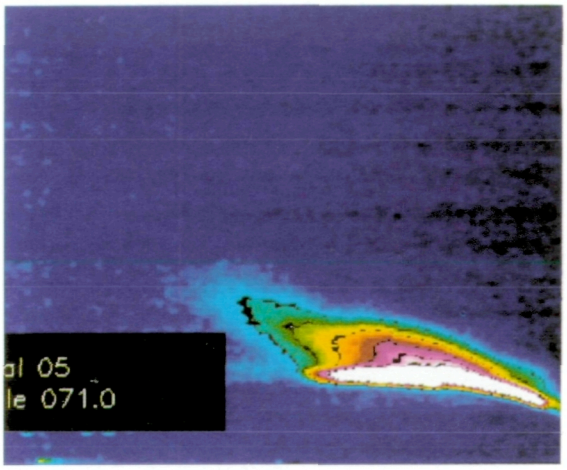

$\alpha = 14.9°$

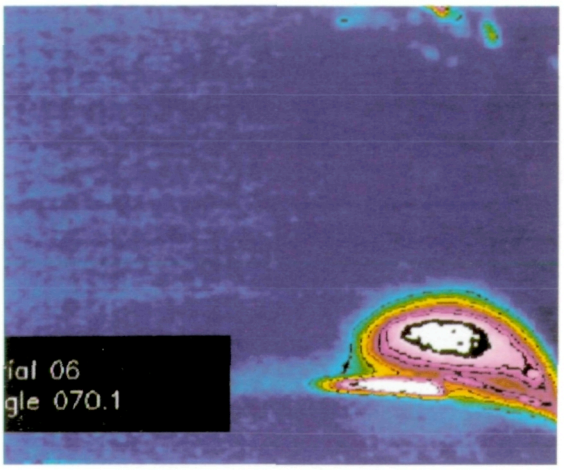

$\alpha = 17.0°$

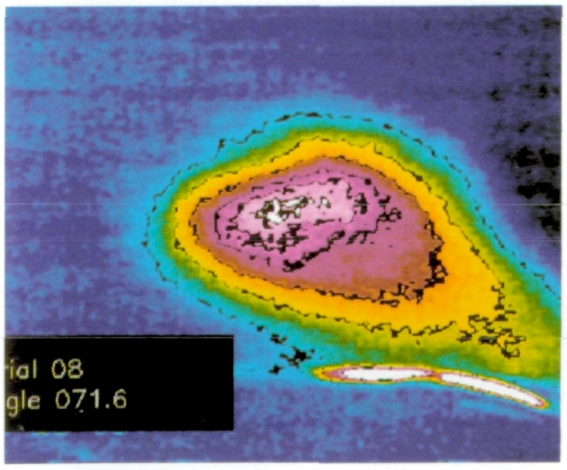

$\alpha = 20.5°$

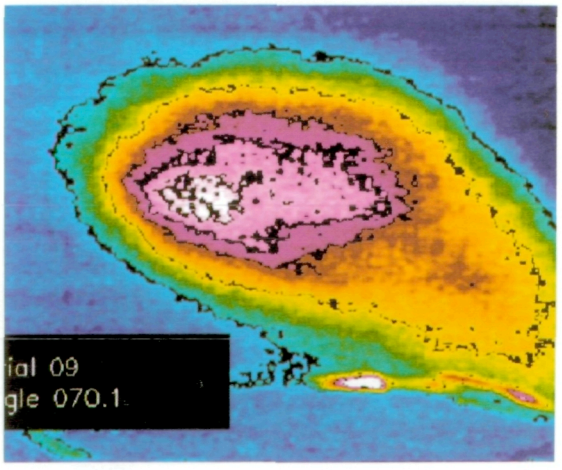

$\alpha = 22.5°$

(a) $\Phi = 70° \pm 3°$.

Figure 25. Effect of α on enhanced 2-D images at nominal altitude of 25 000 ft and $1g$.

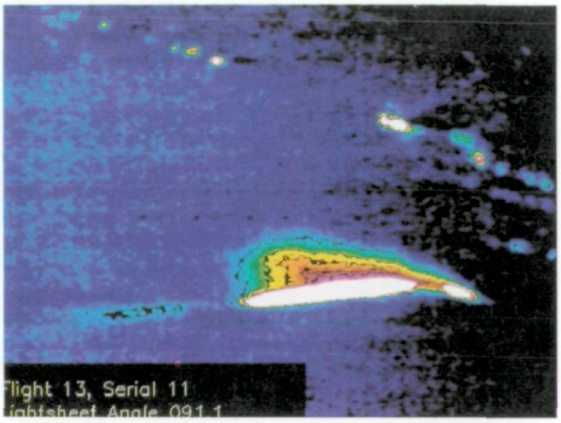

$\alpha = 13.9°$

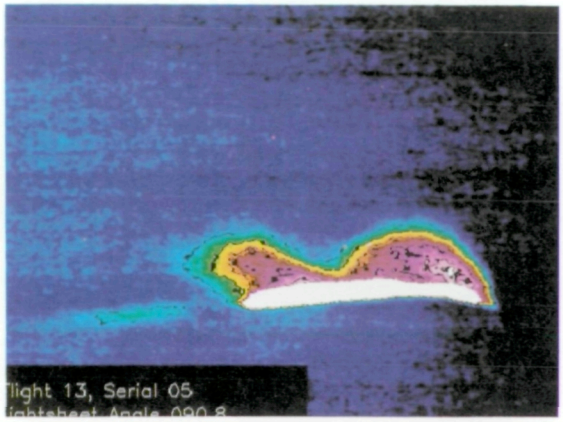

$\alpha = 14.9°$

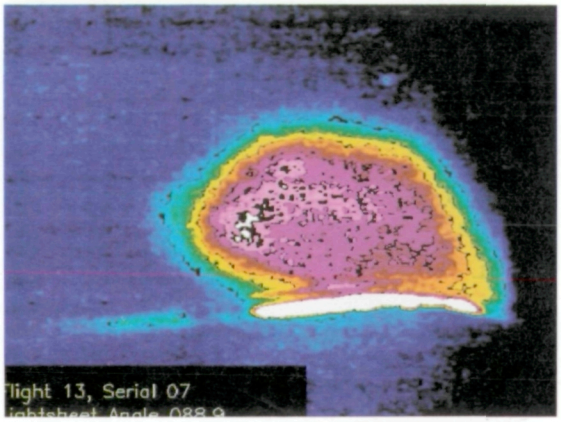

$\alpha = 18.8°$

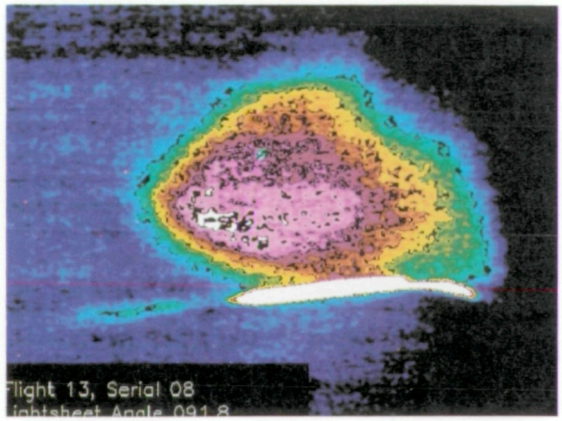

$\alpha = 20.5°$

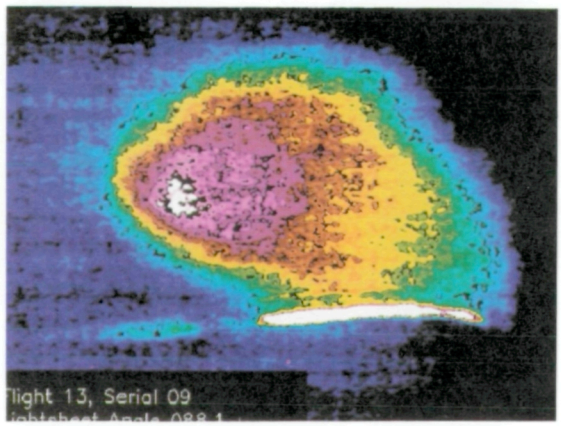

$\alpha = 22.5°$

(b) $\Phi = 90° \pm 3°$.

Figure 25. Continued.

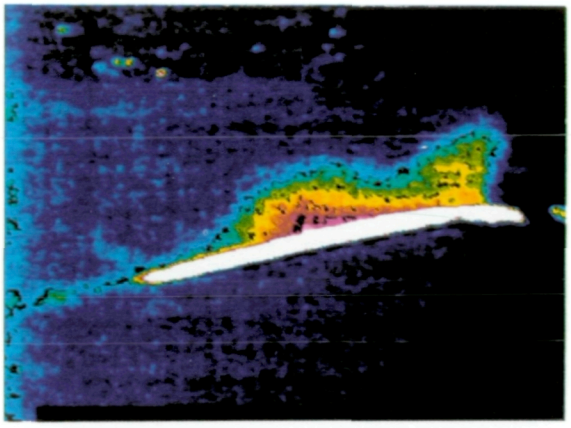

$\alpha = 13.9°$

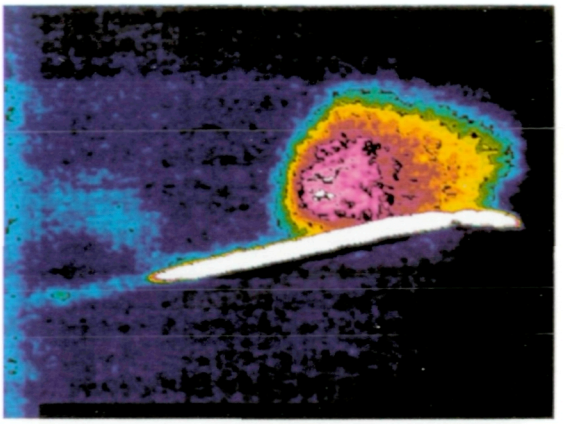

$\alpha = 16.1°$

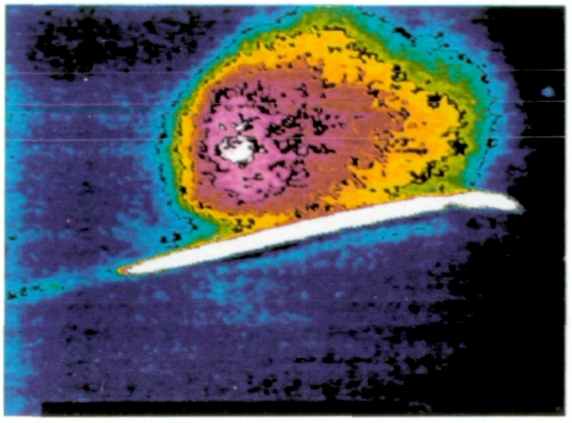

$\alpha = 18.8°$

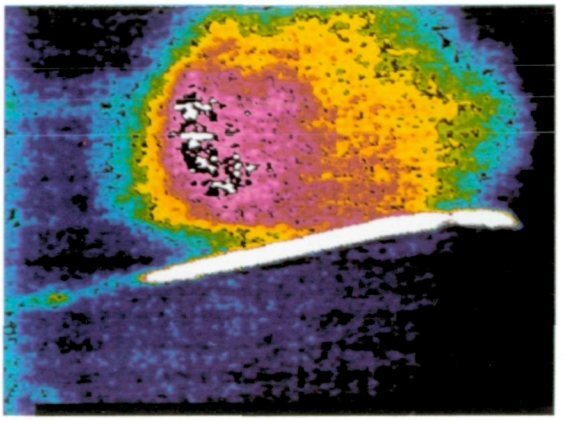

$\alpha = 20.5°$

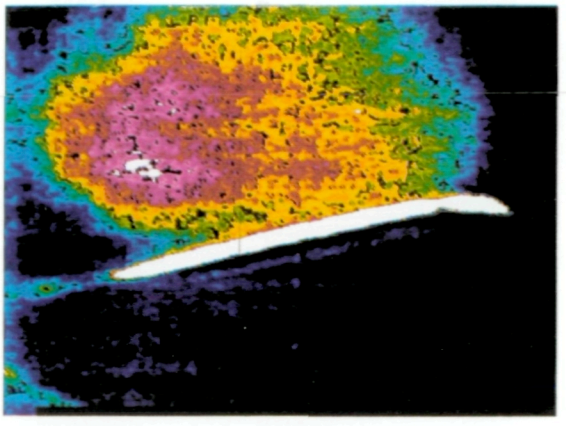

$\alpha = 22.5°$

(c) $\Phi = 110° \pm 3°$.

Figure 25. Concluded.

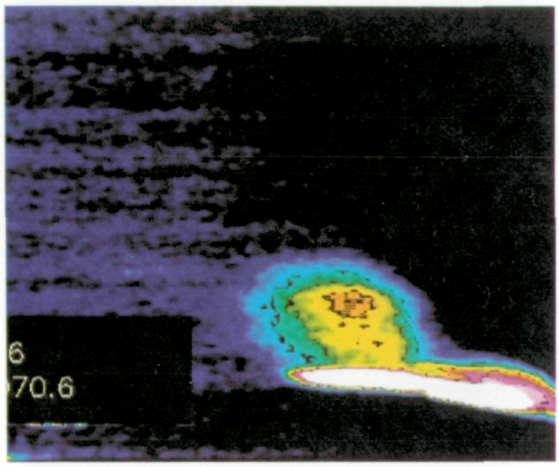

$\alpha = 13.9°$

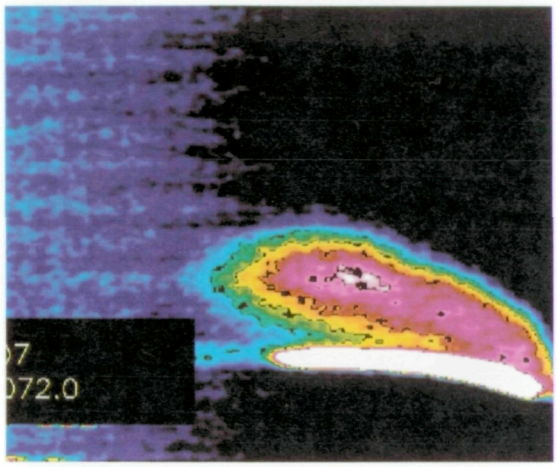

$\alpha = 14.8°$

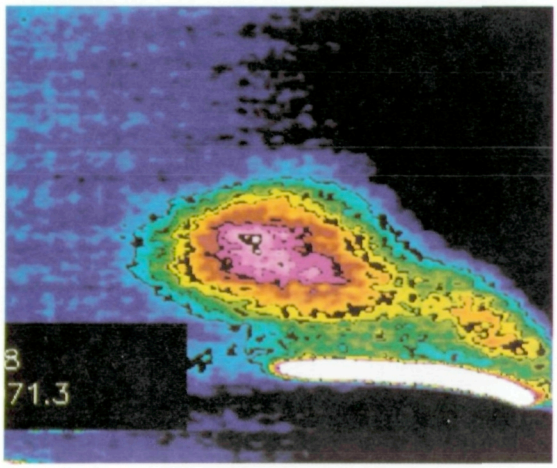

$\alpha = 16.8°$

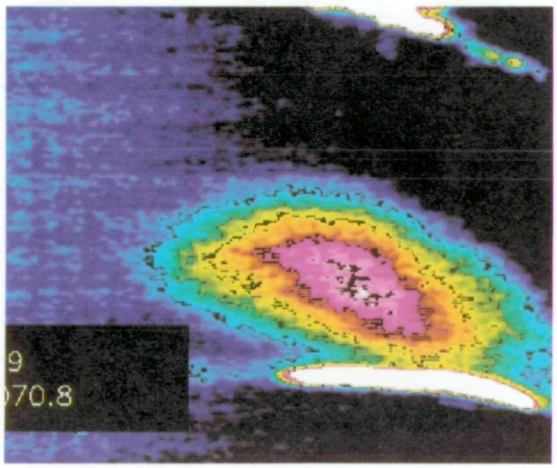

$\alpha = 17.7°$

(a) $\Phi = 70° \pm 3°$.

Figure 26. Effect of α on enhanced 2-D images at nominal altitude of 35 000 ft and $1g$.

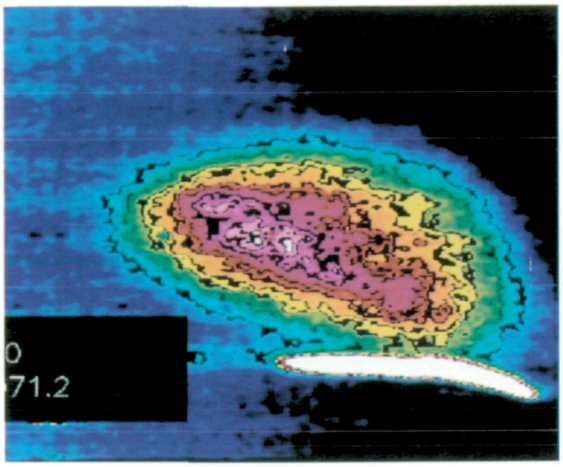

$\alpha = 18.7°$

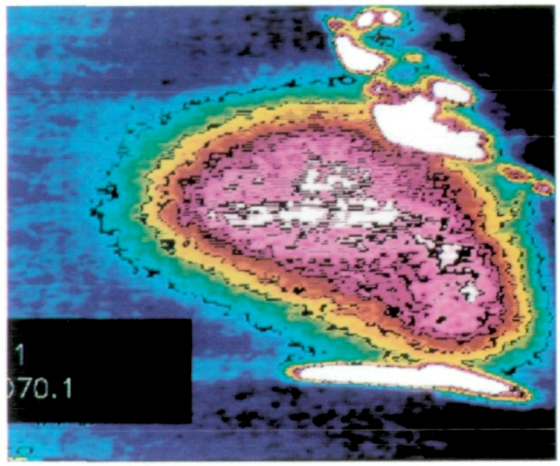

$\alpha = 19.7°$

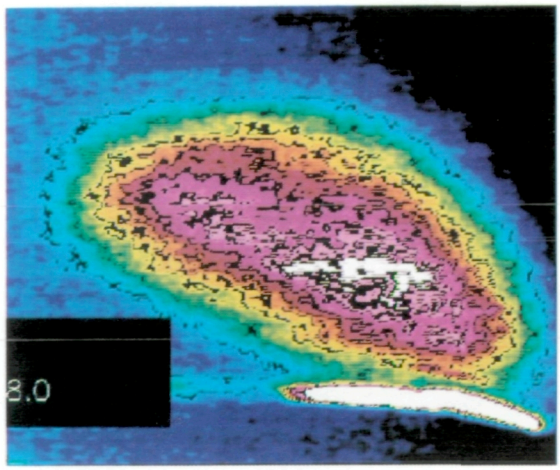

$\alpha = 20.5°$

(a) Concluded.

Figure 26. Continued.

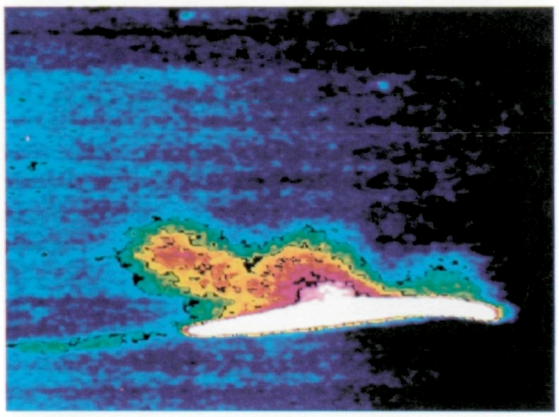

$\alpha = 13.9°$

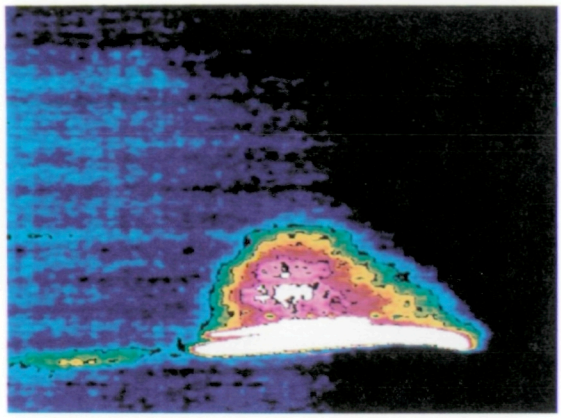

$\alpha = 14.8°$

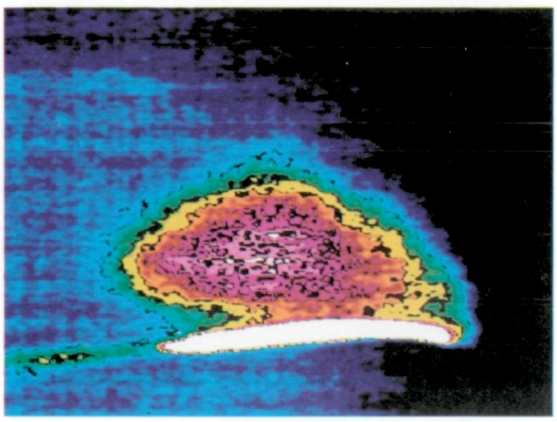

$\alpha = 16.8°$

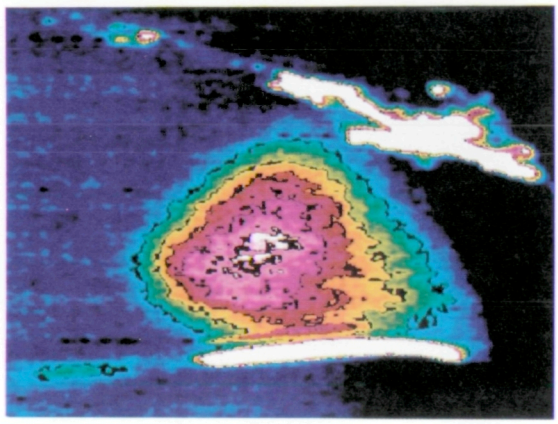

$\alpha = 17.7°$

(b) $\Phi = 90° \pm 3°$.

Figure 26. Continued.

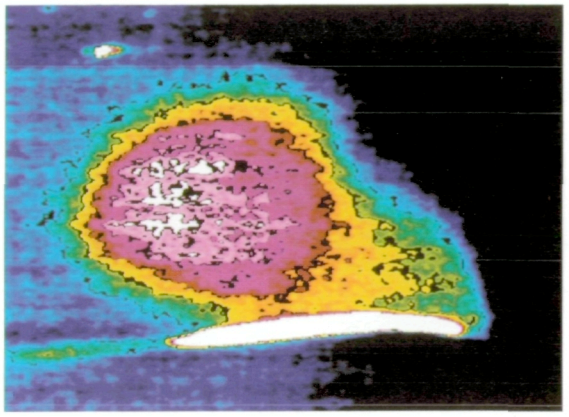

$\alpha = 18.7°$

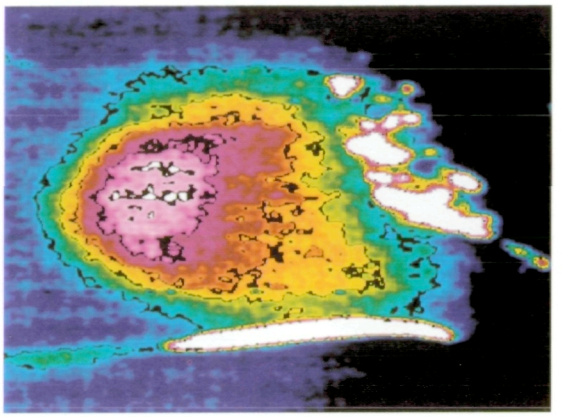

$\alpha = 19.7°$

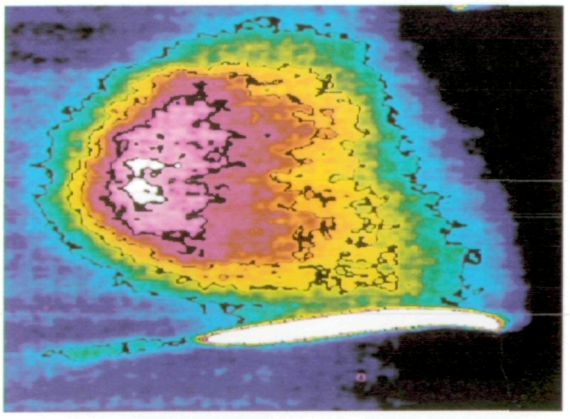

$\alpha = 20.5°$

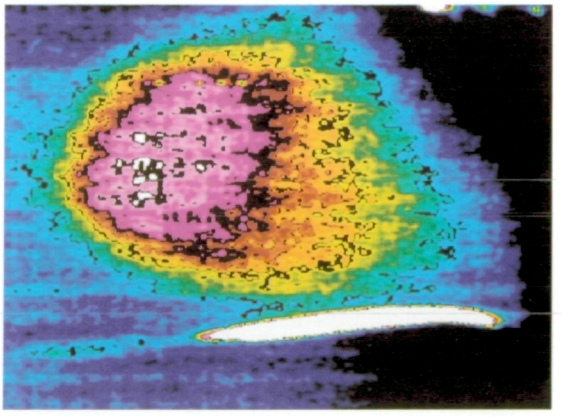

$\alpha = 21.9°$

(b) Concluded.

Figure 26. Continued.

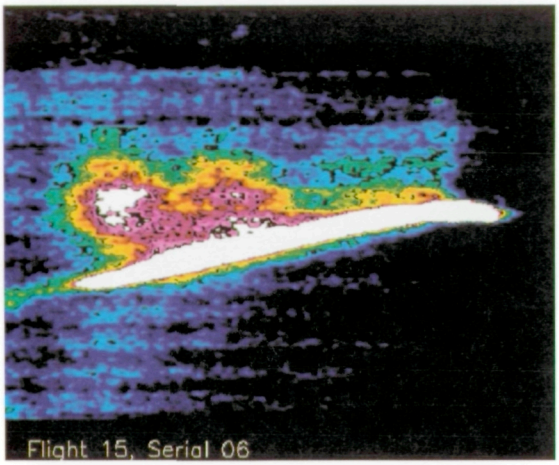

$\alpha = 13.9°$

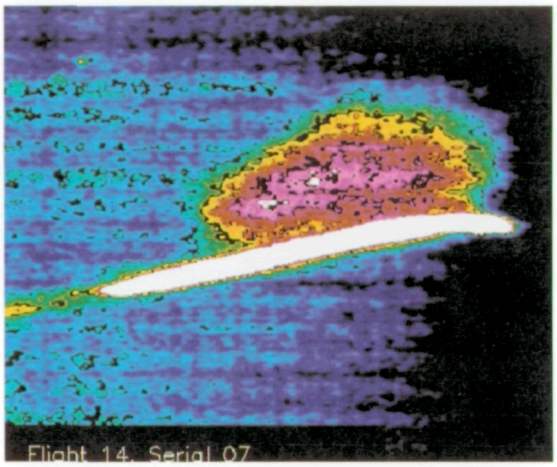

$\alpha = 14.8°$

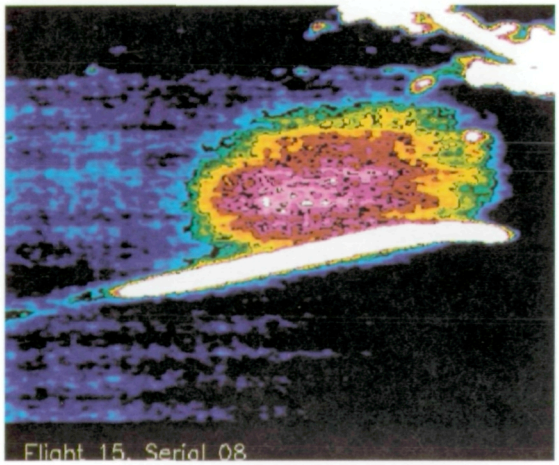

$\alpha = 15.8°$

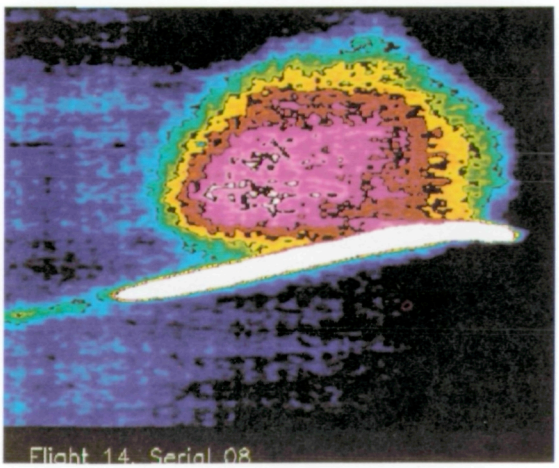

$\alpha = 16.8°$

(c) $\Phi = 110° \pm 3°$.

Figure 26. Continued.

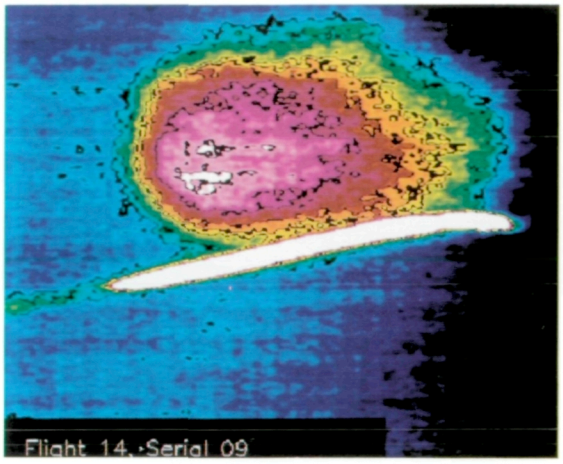

$\alpha = 17.7°$

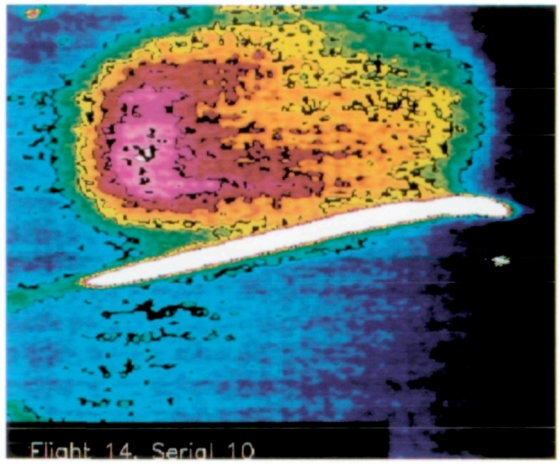

$\alpha = 18.7°$

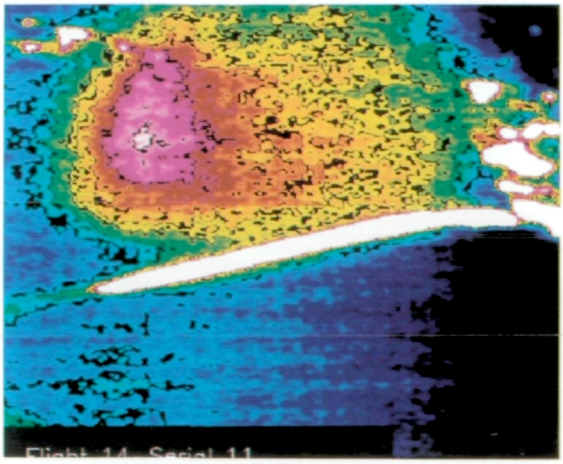

$\alpha = 19.7°$

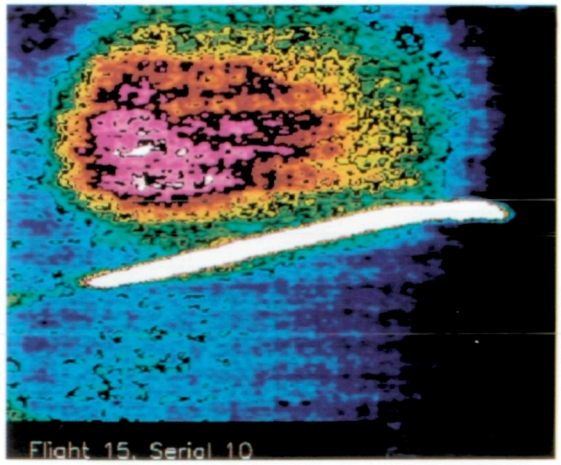

$\alpha = 21.9°$

(c) Concluded.

Figure 26. Concluded.

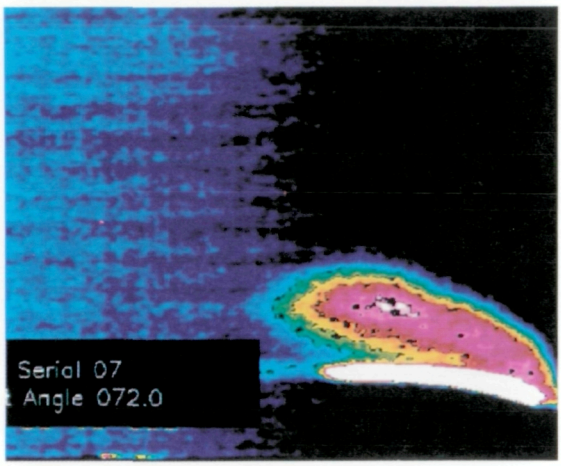

0.9g
$R_n = 29.2 \times 10^6$
$M_\infty = 0.53$

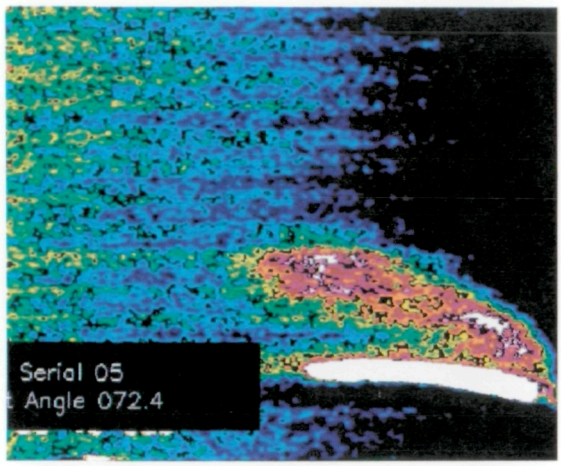

1.6g
$R_n = 35.5 \times 10^6$
$M_\infty = 0.68$

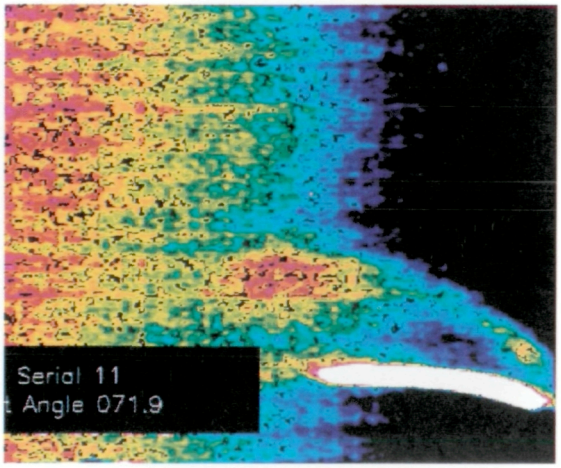

2.5g
$R_n = 45.7 \times 10^6$
$M_\infty = 0.73$

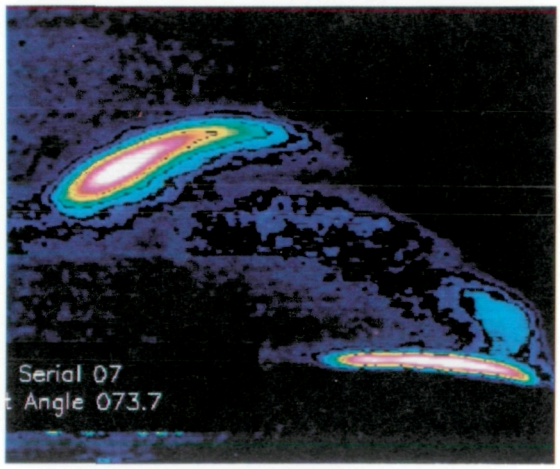

3.9g
$R_n = 57.3 \times 10^6$
$M_\infty = 0.80$

(a) $\Phi = 72^\circ \pm 3^\circ$.

Figure 27. Effects of load factor and R_n on enhanced 2-D images at nominal altitude of 35 000 ft and $\alpha = 14.8^\circ$.

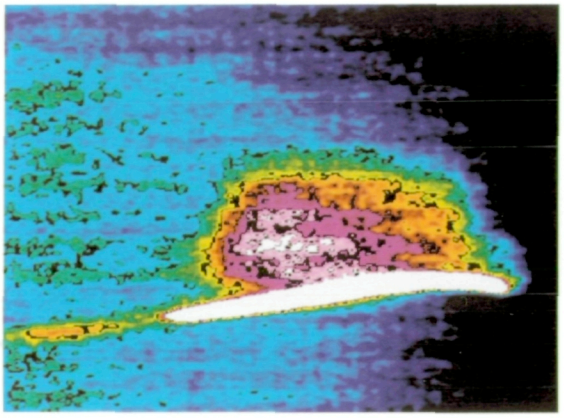

0.9g
$R_n = 29.2 \times 10^6$
$M_\infty = 0.53$

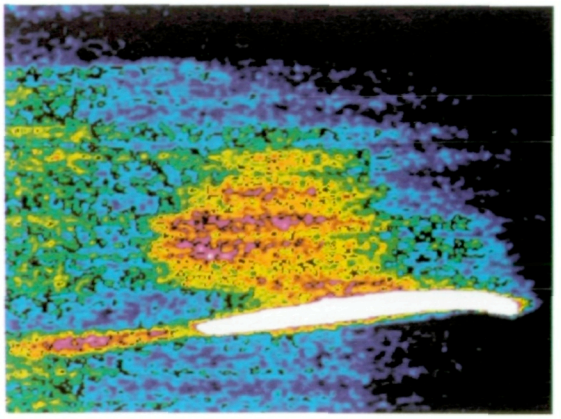

1.6g
$R_n = 35.5 \times 10^6$
$M_\infty = 0.68$

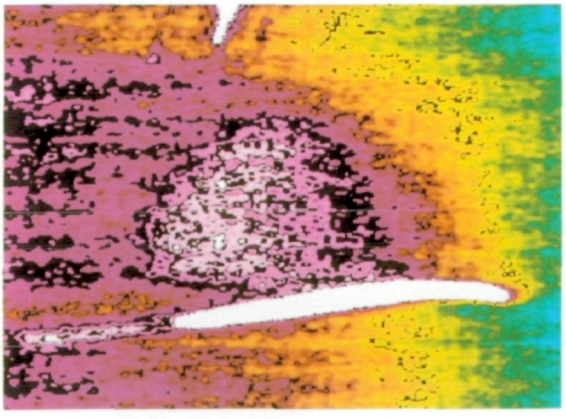

2.5g
$R_n = 45.7 \times 10^6$
$M_\infty = 0.73$

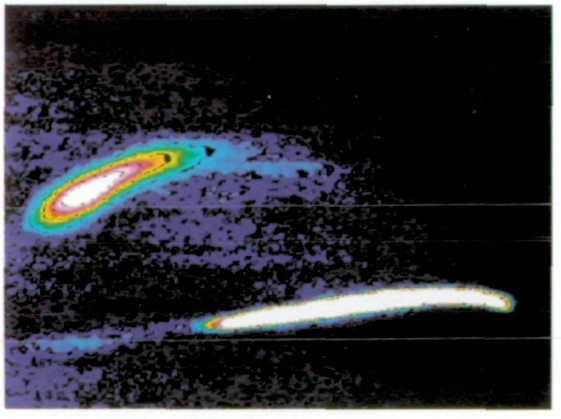

3.9g
$R_n = 57.3 \times 10^6$
$M_\infty = 0.80$

(b) $\Phi = 97.5° \pm 3°$.

Figure 27. Continued.

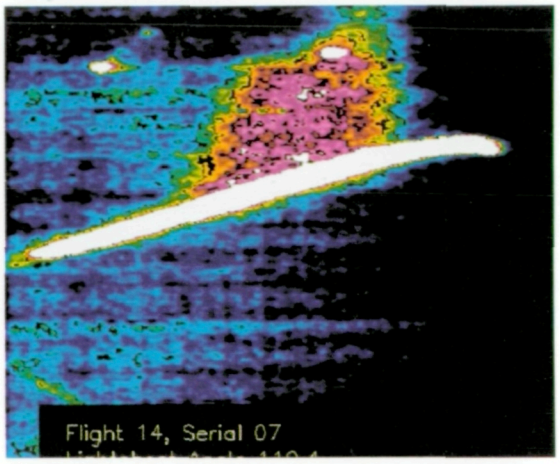

0.9g
$R_n = 29.2 \times 10^6$
$M_\infty = 0.53$

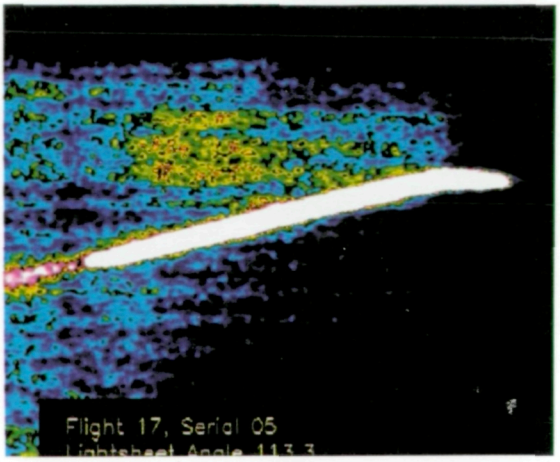

1.6g
$R_n = 35.5 \times 10^6$
$M_\infty = 0.68$

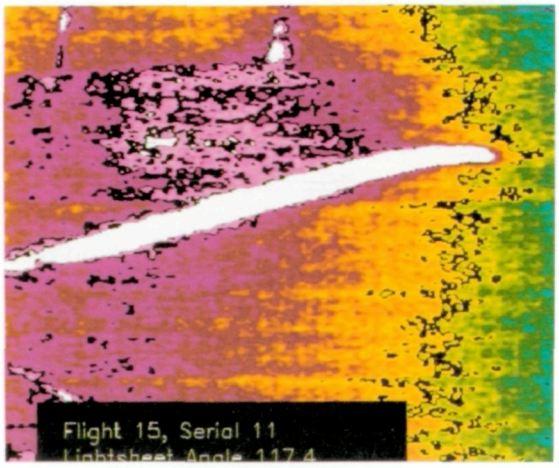

2.5g
$R_n = 45.7 \times 10^6$
$M_\infty = 0.73$

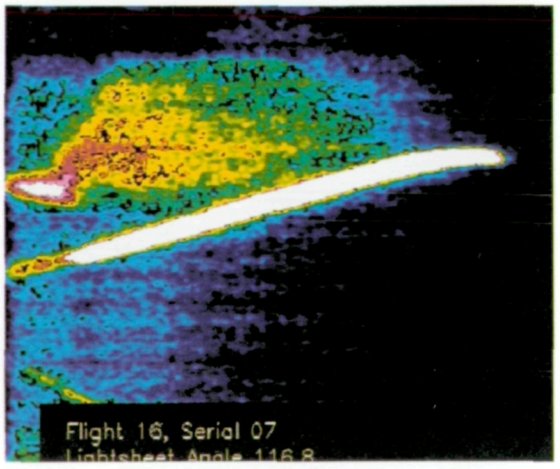

3.9g
$R_n = 57.3 \times 10^6$
$M_\infty = 0.80$

(c) $\Phi = 116.4° \pm 3°$.

Figure 27. Concluded.

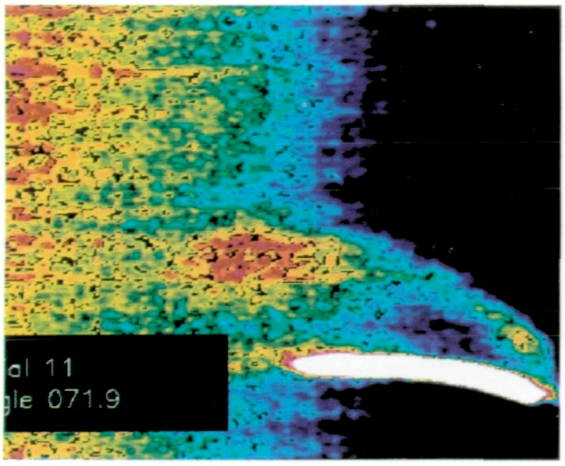

$\alpha = 14.8°$
$R_n = 45.7 \times 10^6$
$M_\infty = 0.73$

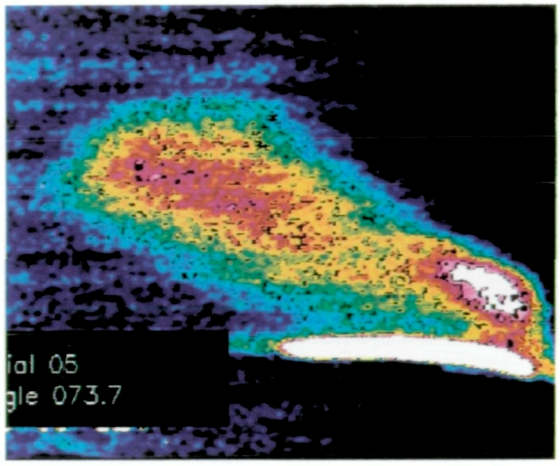

$\alpha = 16.8°$
$R_n = 44.6 \times 10^6$
$M_\infty = 0.78$

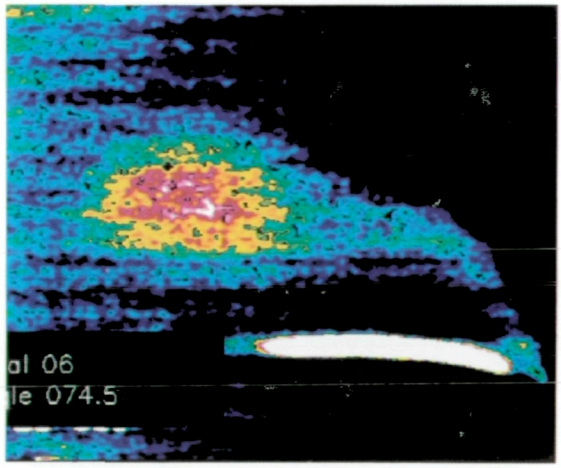

$\alpha = 18.6°$
$R_n = 35.6 \times 10^6$
$M_\infty = 0.67$

(a) $\Phi = 73° \pm 3°$.

Figure 28. Effects of α and R_n on enhanced 2-D images during loaded spiral descents at nominal altitude of 35 000 ft and 2.6g.

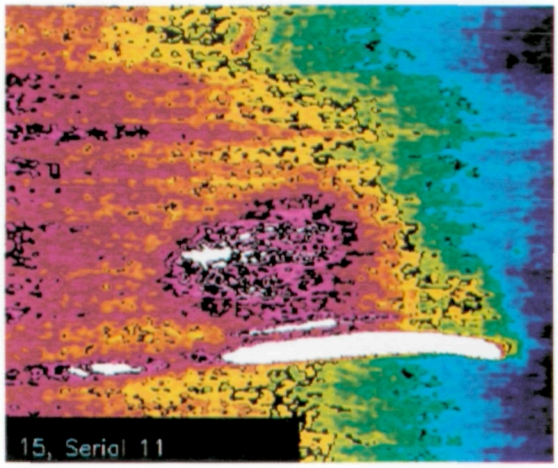

$\alpha = 14.8°$
$R_n = 45.7 \times 10^6$
$M_\infty = 0.73$

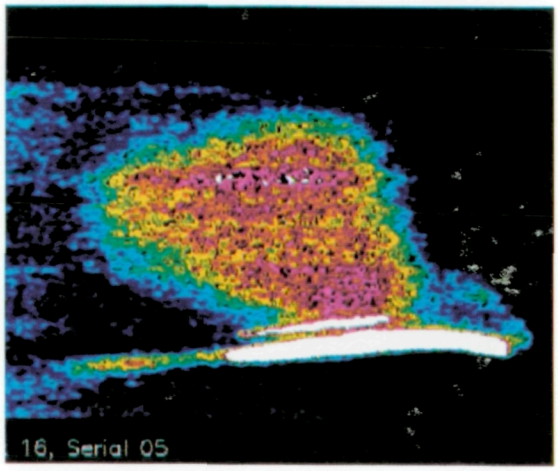

$\alpha = 16.8°$
$R_n = 44.6 \times 10^6$
$M_\infty = 0.78$

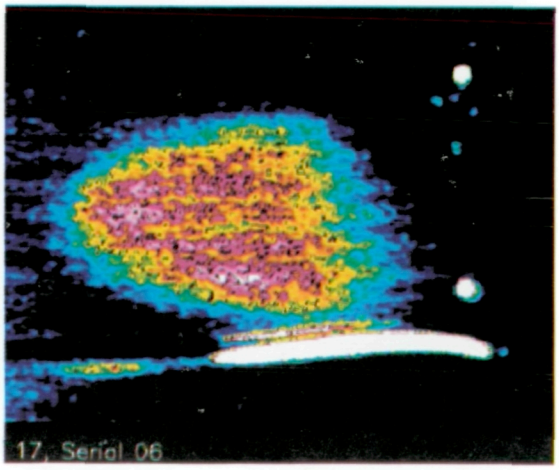

$\alpha = 18.6°$
$R_n = 35.6 \times 10^6$
$M_\infty = 0.67$

(b) $\Phi = 90° \pm 3°$.

Figure 28. Continued.

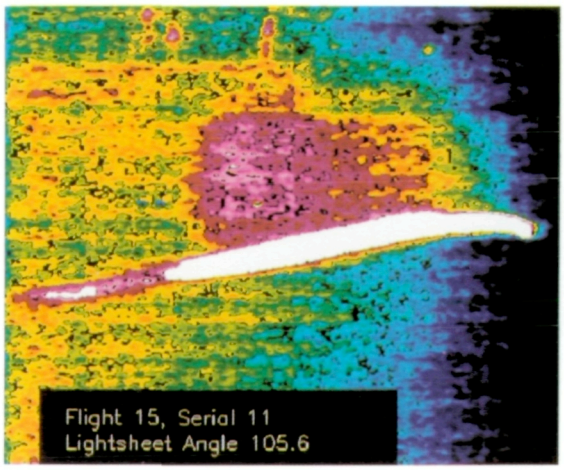

$\alpha = 14.8°$
$R_n = 45.7 \times 10^6$
$M_\infty = 0.73$

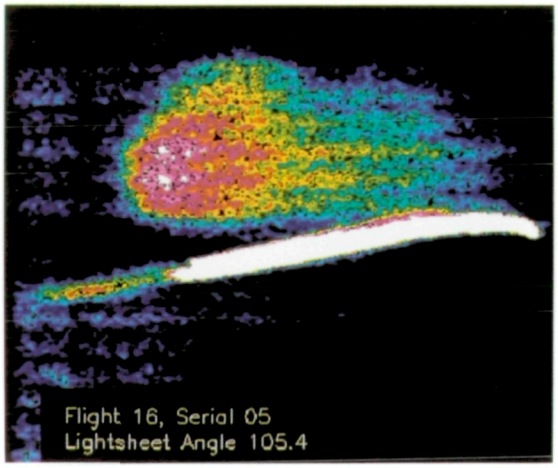

$\alpha = 16.8°$
$R_n = 44.6 \times 10^6$
$M_\infty = 0.78$

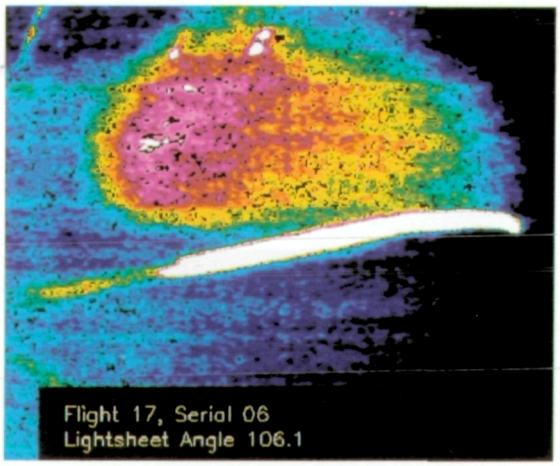

$\alpha = 18.6°$
$R_n = 35.6 \times 10^6$
$M_\infty = 0.67$

(c) $\Phi = 105° \pm 3°$.

Figure 28. Concluded.

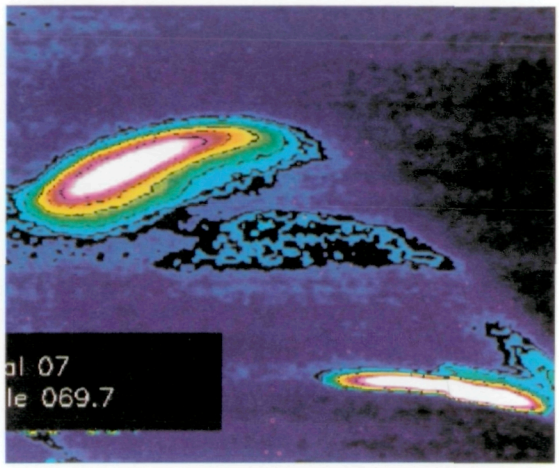

$\alpha = 14.8°$
$R_n = 57.3 \times 10^6$
$M_\infty = 0.80$

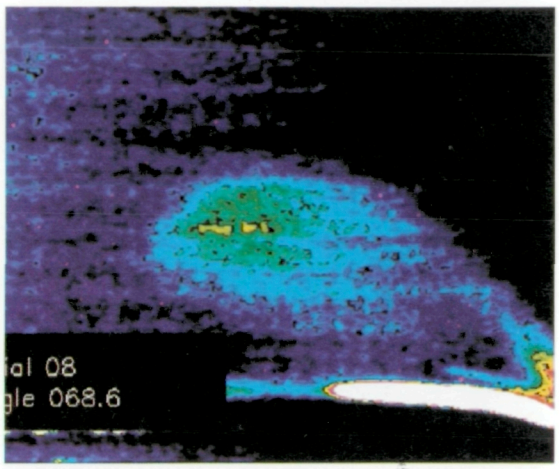

$\alpha = 17.3°$
$R_n = 48.4 \times 10^6$
$M_\infty = 0.81$

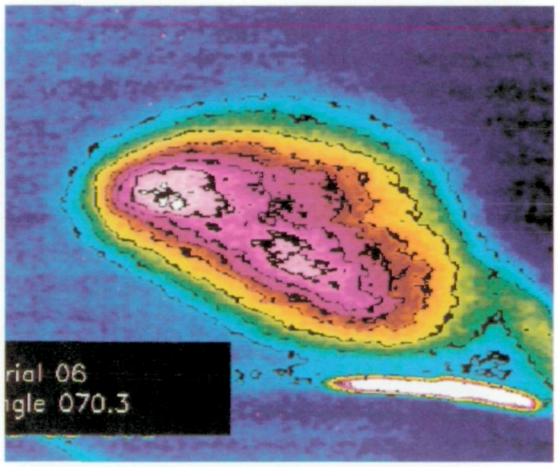

$\alpha = 19.4°$
$R_n = 46.6 \times 10^6$
$M_\infty = 0.69$

(a) $\Phi = 70° \pm 3°$.

Figure 29. Effects of α and R_n on enhanced 2-D images during loaded spiral descents at nominal altitude of 30 000 ft and $3.7g$.

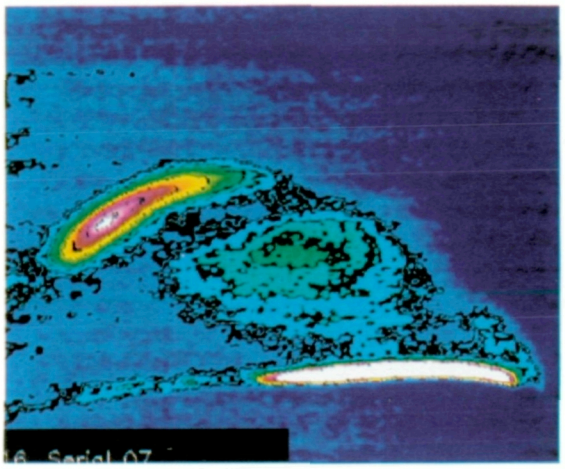

$\alpha = 14.8°$
$R_n = 57.3 \times 10^6$
$M_\infty = 0.80$

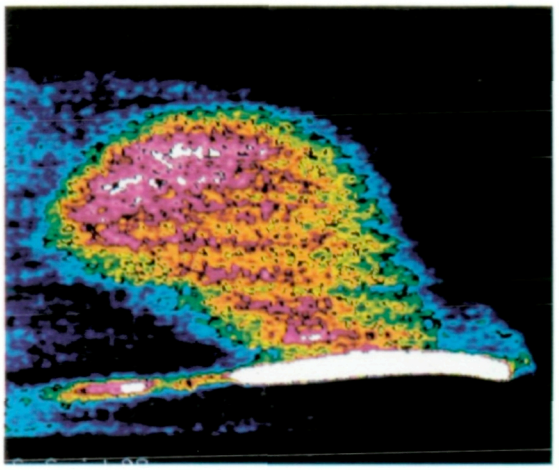

$\alpha = 17.3°$
$R_n = 48.4 \times 10^6$
$M_\infty = 0.81$

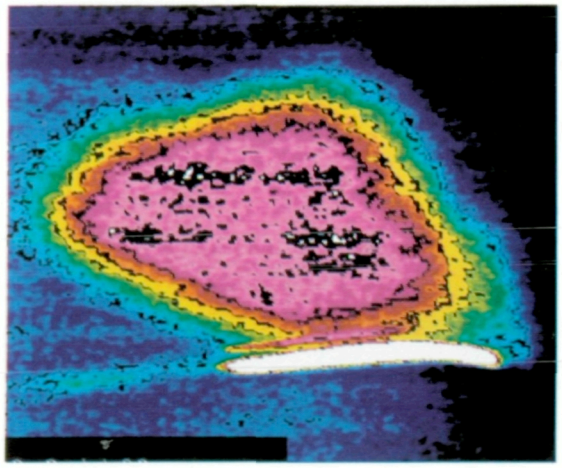

$\alpha = 19.4°$
$R_n = 46.6 \times 10^6$
$M_\infty = 0.69$

(b) $\Phi = 87.5° \pm 3°$.

Figure 29. Continued.

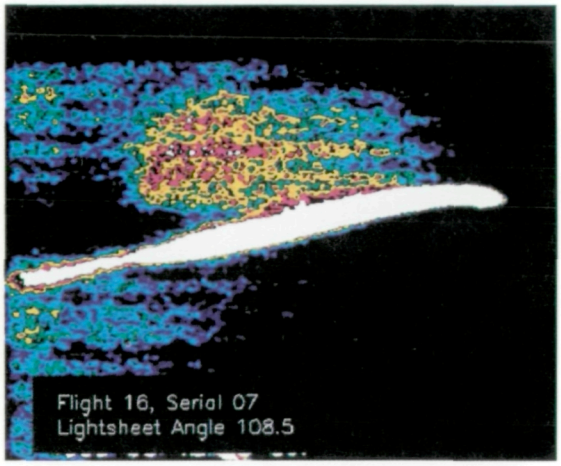

$\alpha = 14.8°$
$R_n = 57.3 \times 10^6$
$M_\infty = 0.80$

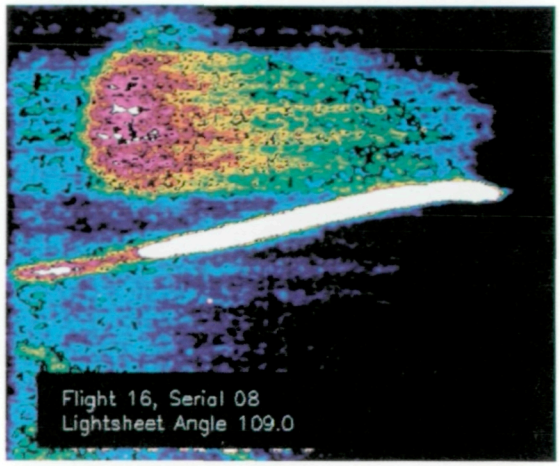

$\alpha = 17.3°$
$R_n = 48.4 \times 10^6$
$M_\infty = 0.81$

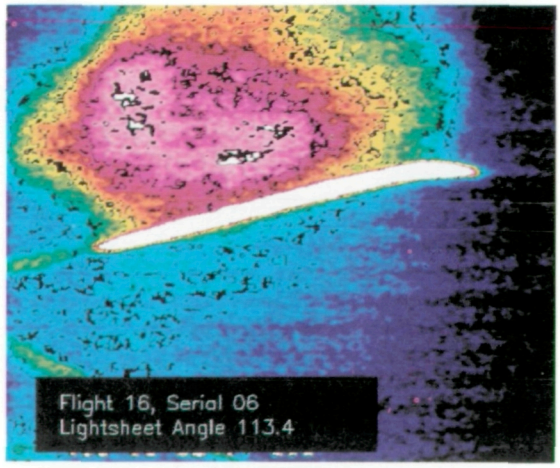

$\alpha = 19.4°$
$R_n = 46.6 \times 10^6$
$M_\infty = 0.69$

(c) $\Phi = 111° \pm 3°$.

Figure 29. Concluded.

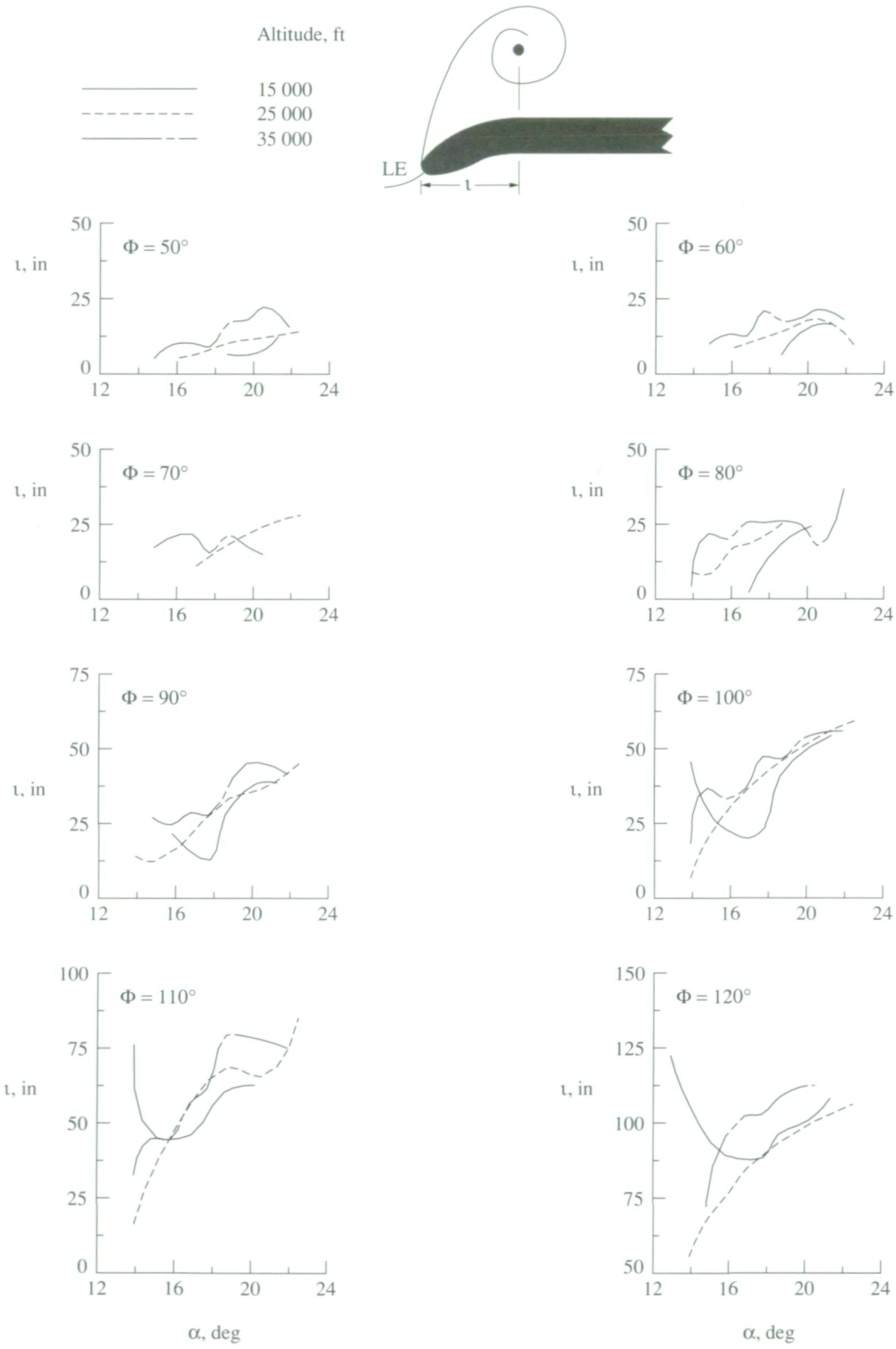

(a) Core distance.

Figure 30. Effect of altitude on distance from outermost vapor-screen vortex-system features to local leading edge along light-sheet ray at $1g$. (See table I for ranges of R_n.)

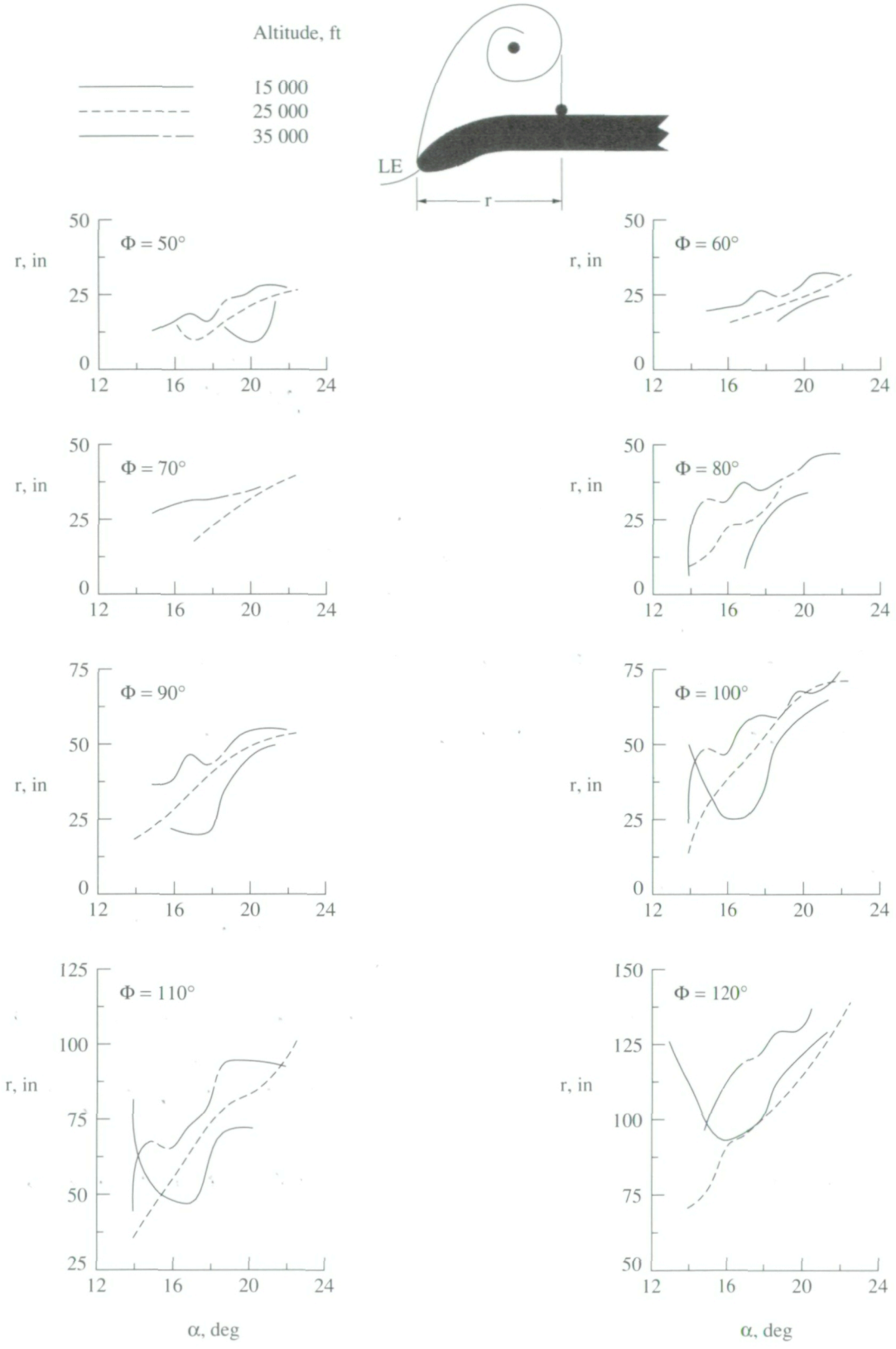

(b) Reattachment-point distance.

Figure 30. Concluded.

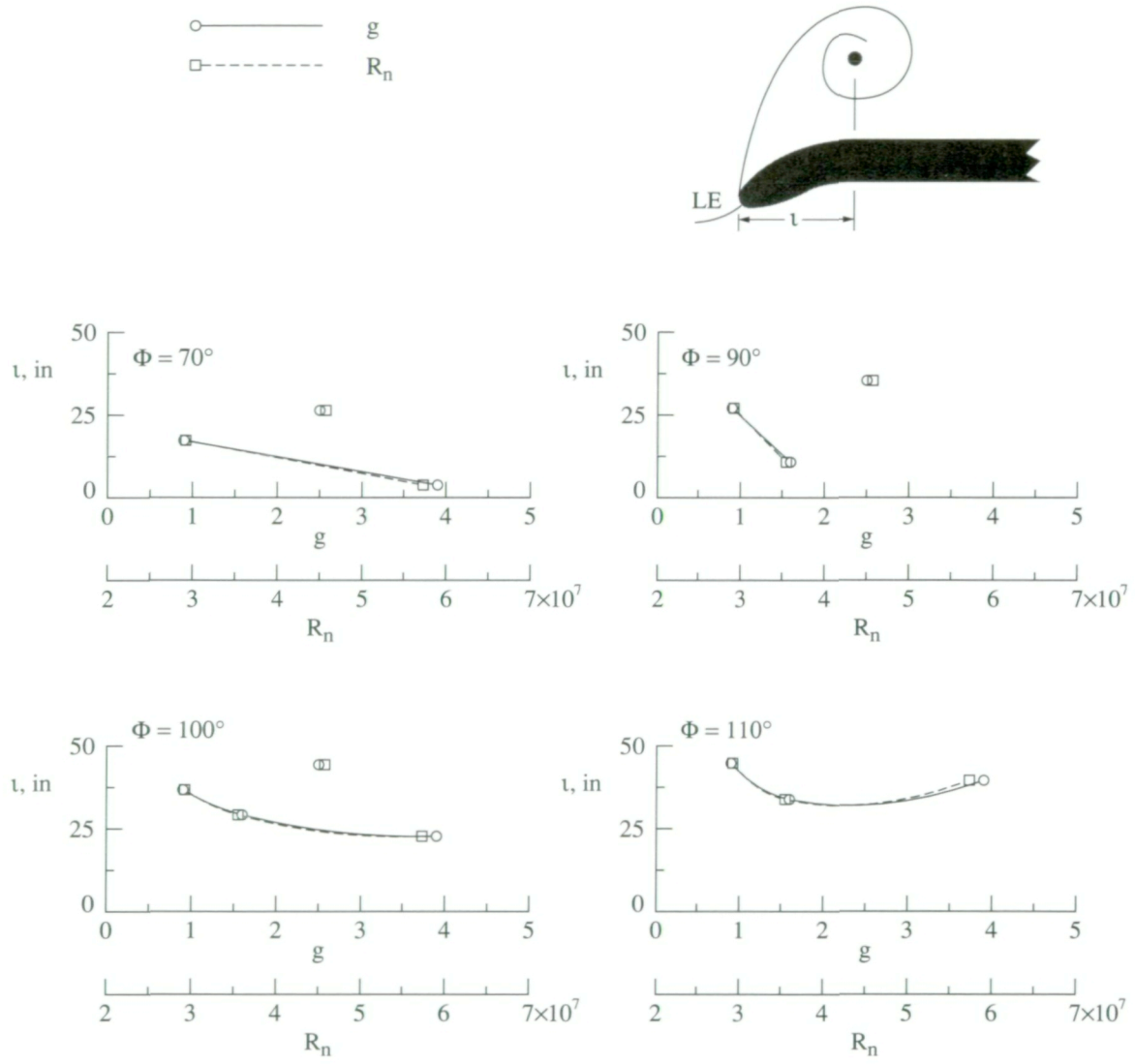

Figure 31. Effects of R_n and load factor on outermost vapor-screen core distance to local leading edge along light-sheet ray at nominal altitude of 35 000 ft and $\alpha = 14.8°$.

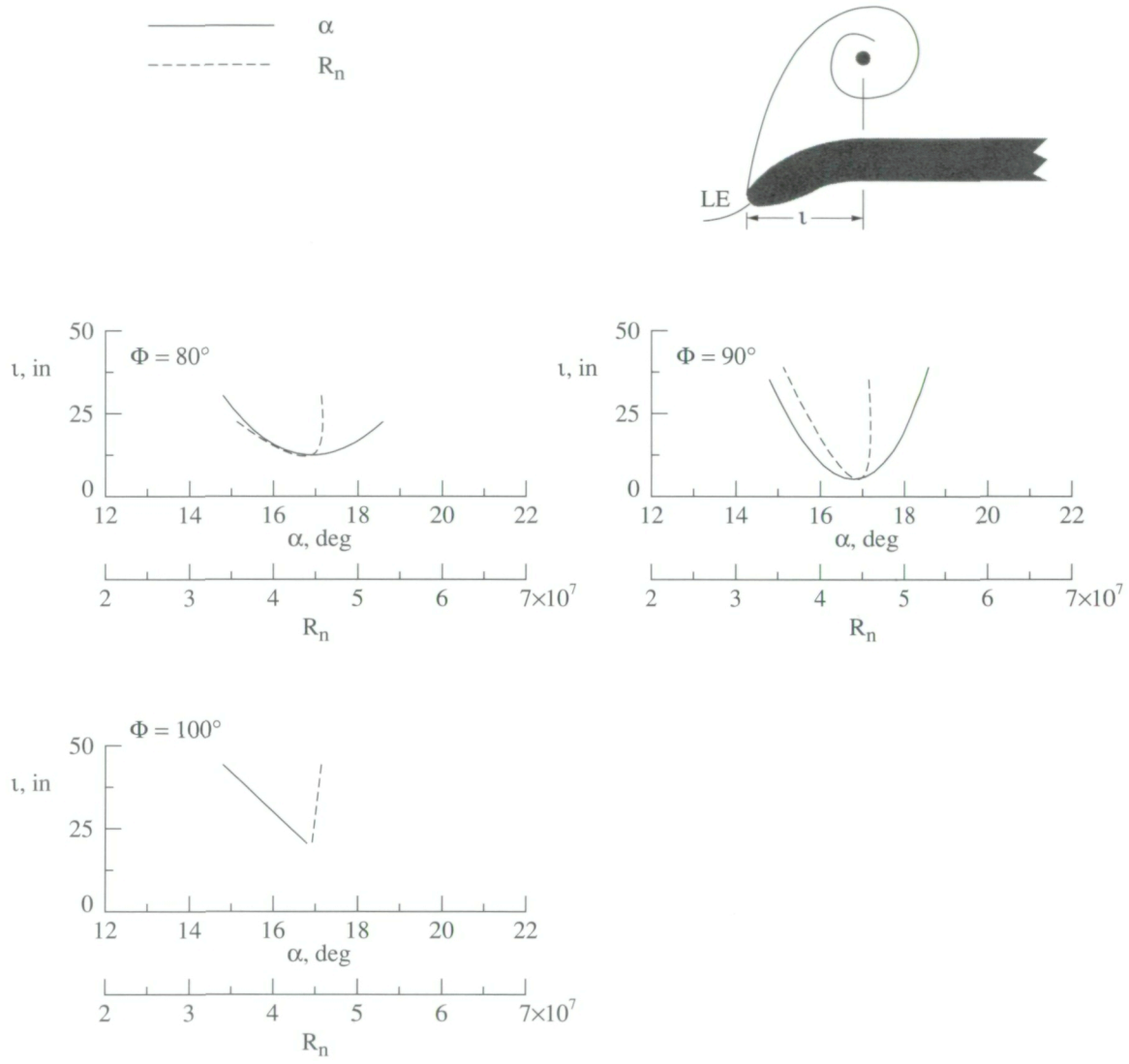

Figure 32. Effects of α and R_n on outermost vapor-screen core distance to local leading edge along light-sheet ray at nominal altitude of 35 000 ft and 2.6g.

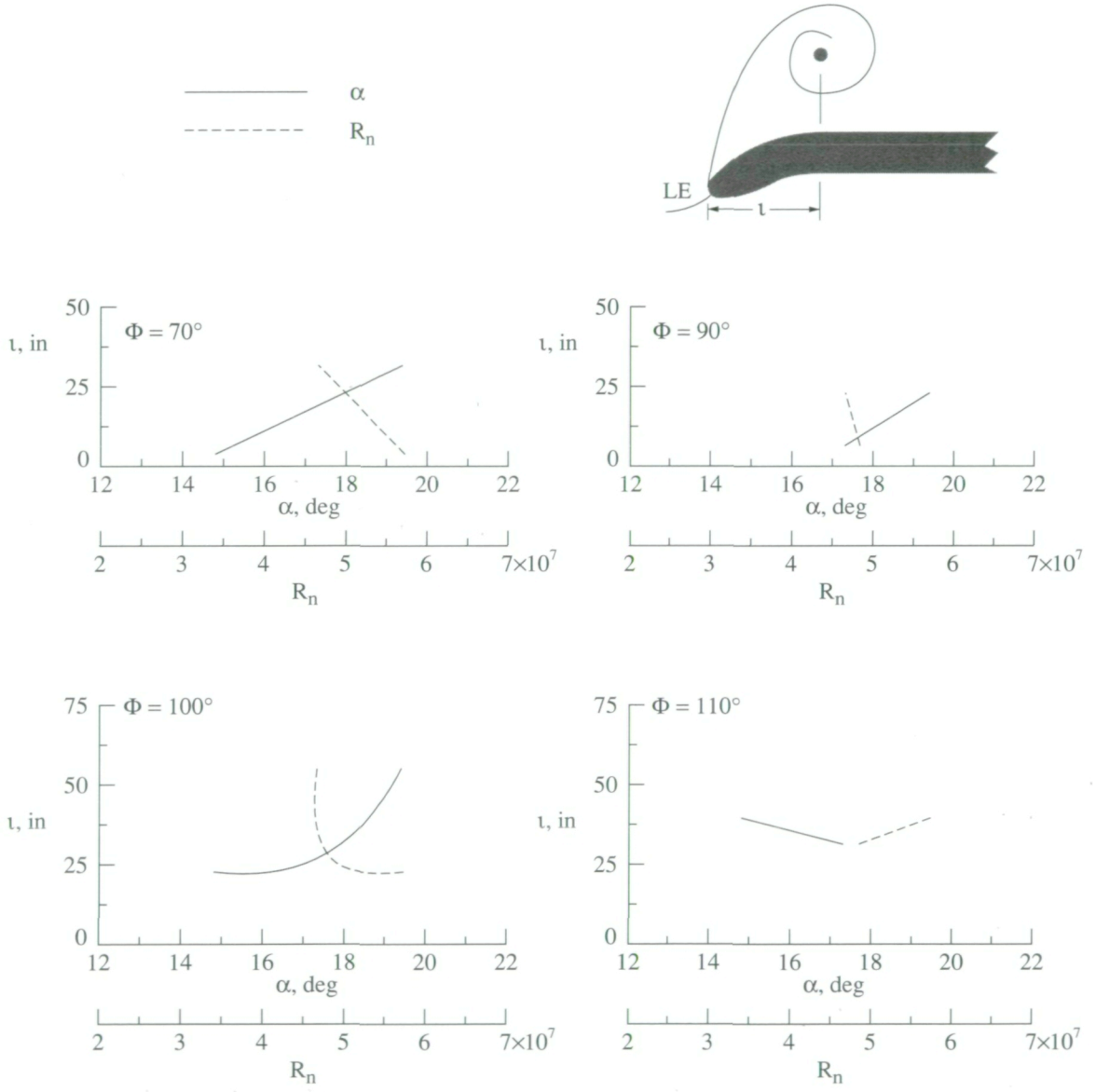

Figure 33. Effects of α and R_n on outermost vapor-screen core distance to local leading edge along light-sheet ray at nominal altitude of 30 000 ft and $3.7g$.

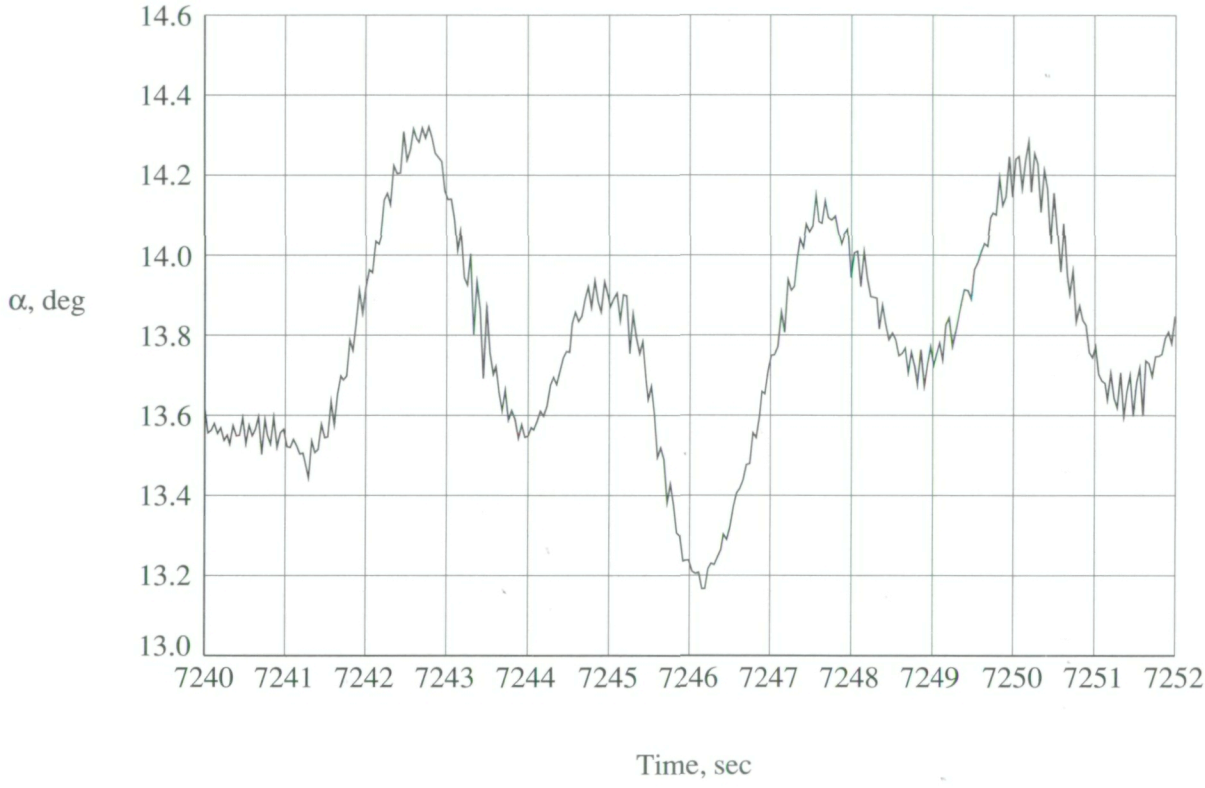

Figure 34. Typical time-history plot of α (F/S 91-15/06).

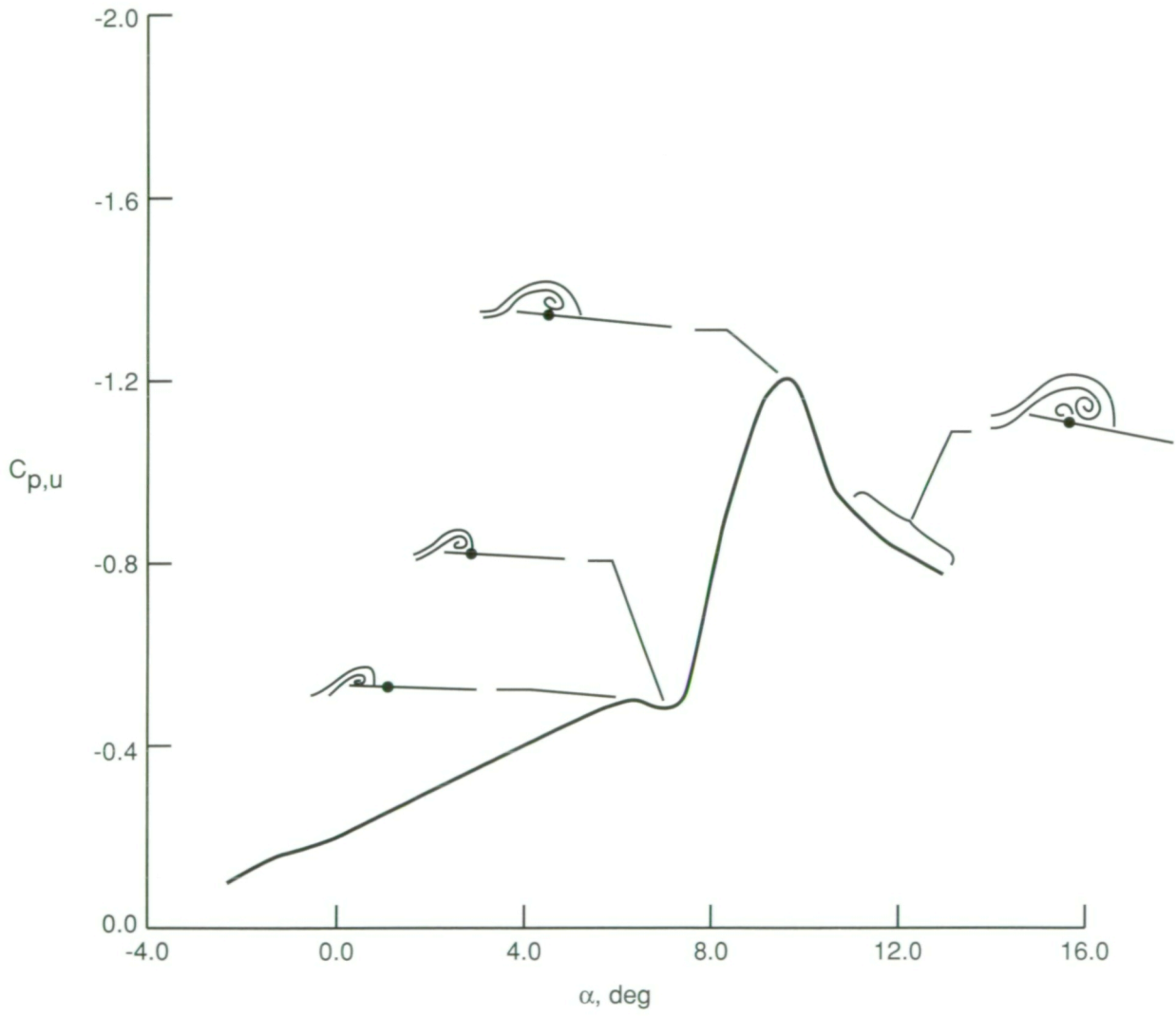

Figure 35. Typical variation of $C_{p,u}$ with α for upper-surface pressure port on 58° thick delta wing. (Fig. 6 from ref. 17.)

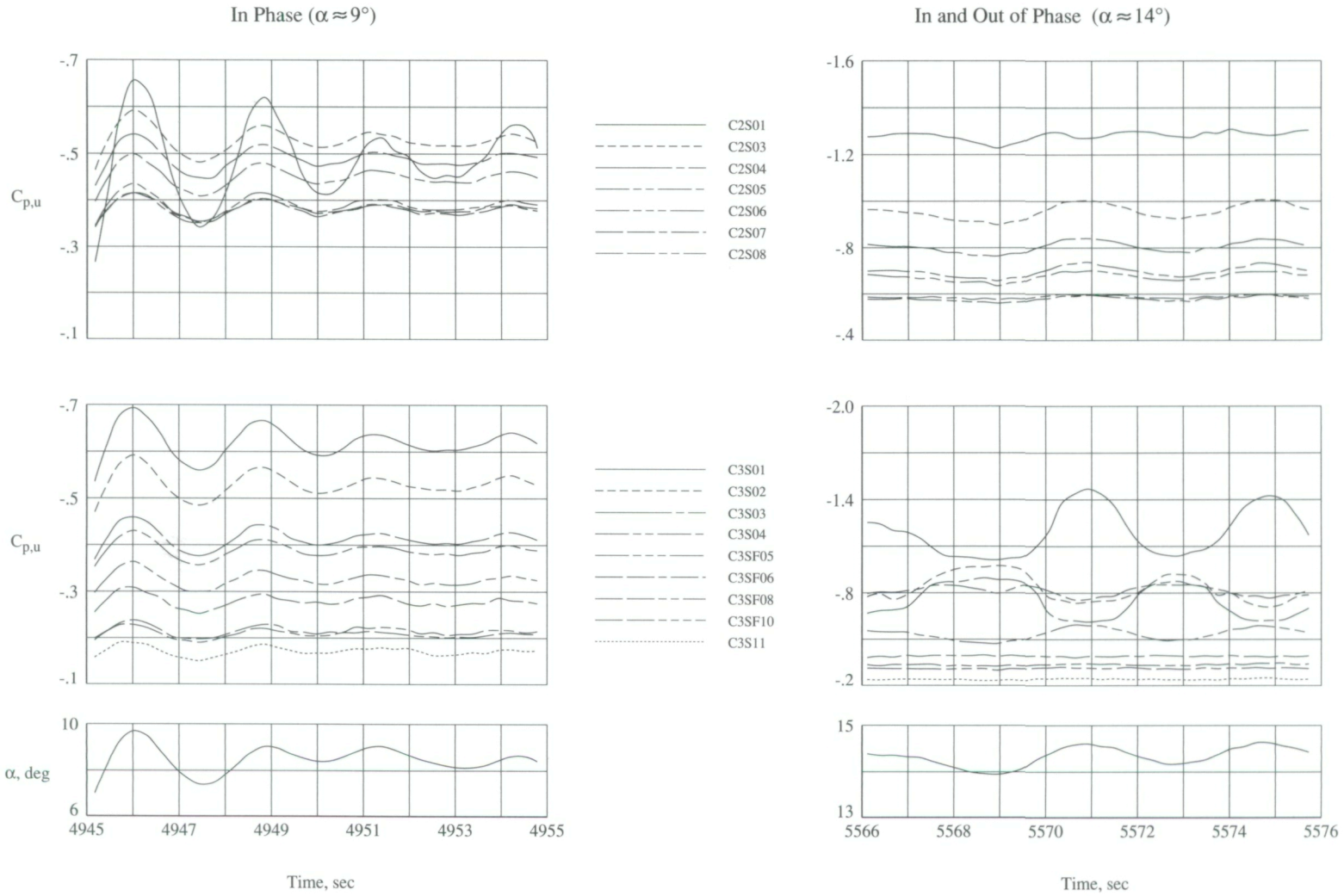

Figure 36. Time-history plots of $C_{p,u}$ for $\alpha \approx 9°$ (F/S 91-13/04) and 14° (F/S 91-13/05).

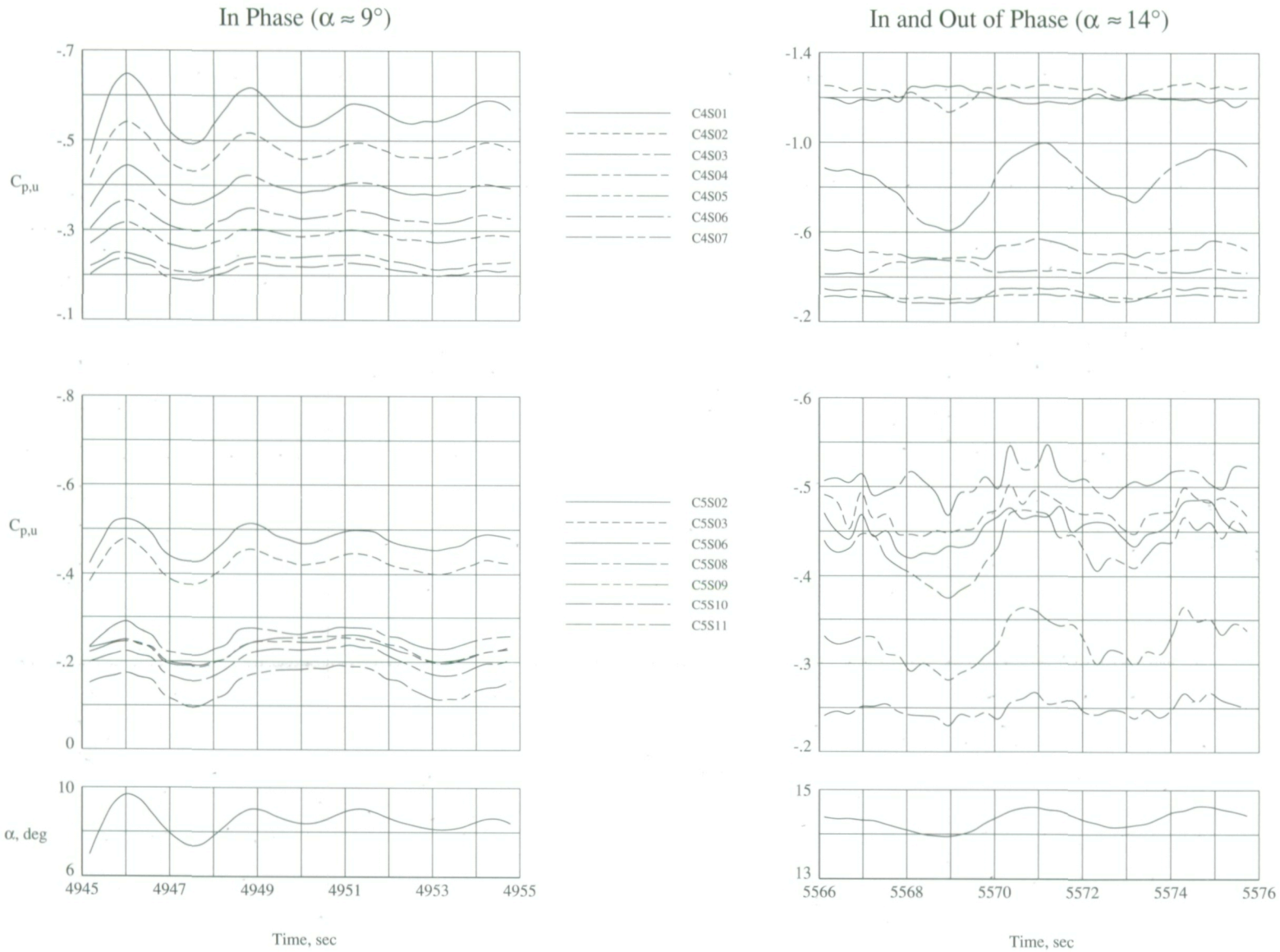

Figure 36. Concluded.

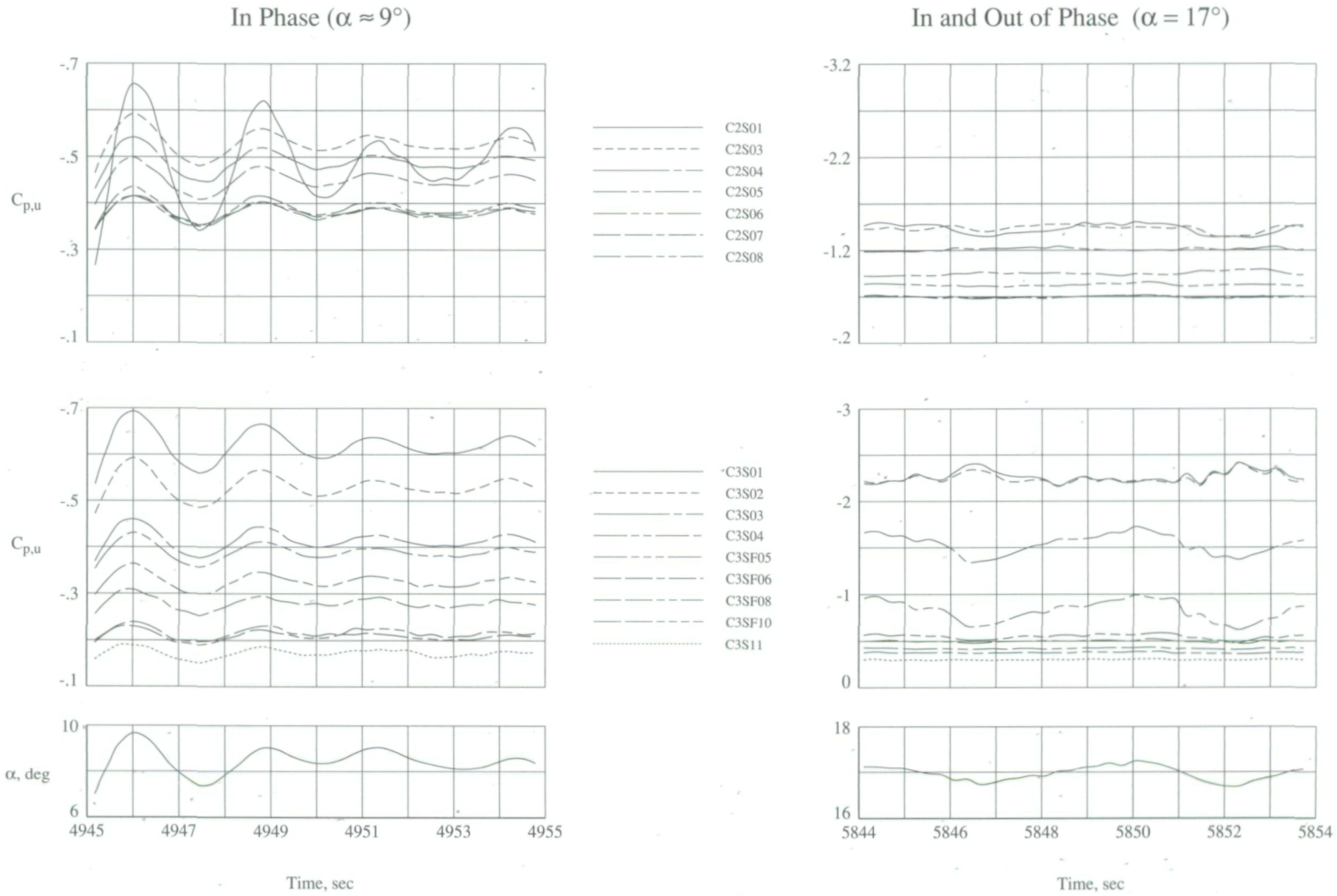

Figure 37. Time-history plots of $C_{p,u}$ for $\alpha \approx 9°$ (F/S 91-13/04) and 17° (F/S 91-13/06).

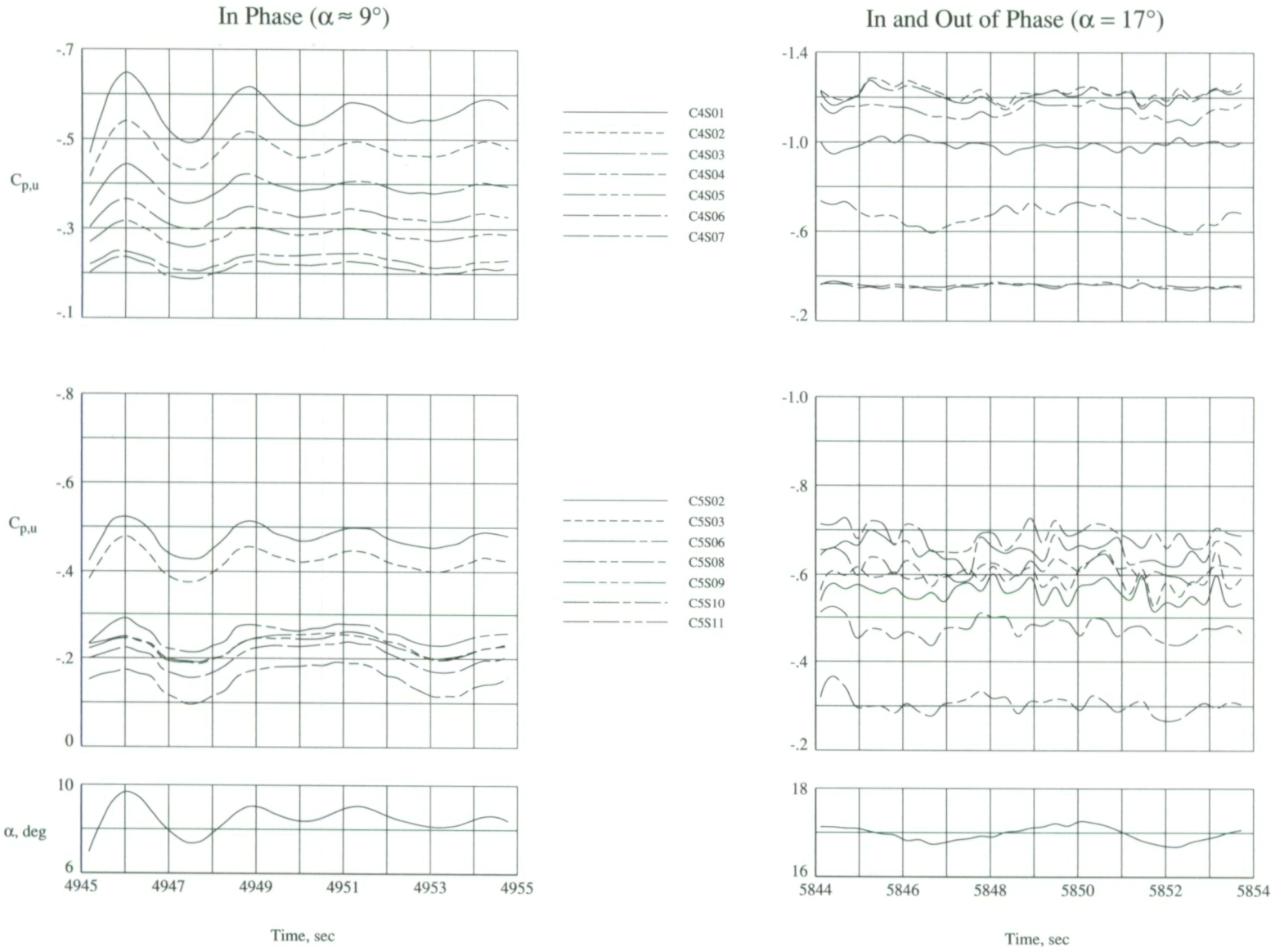

Figure 37. Concluded.

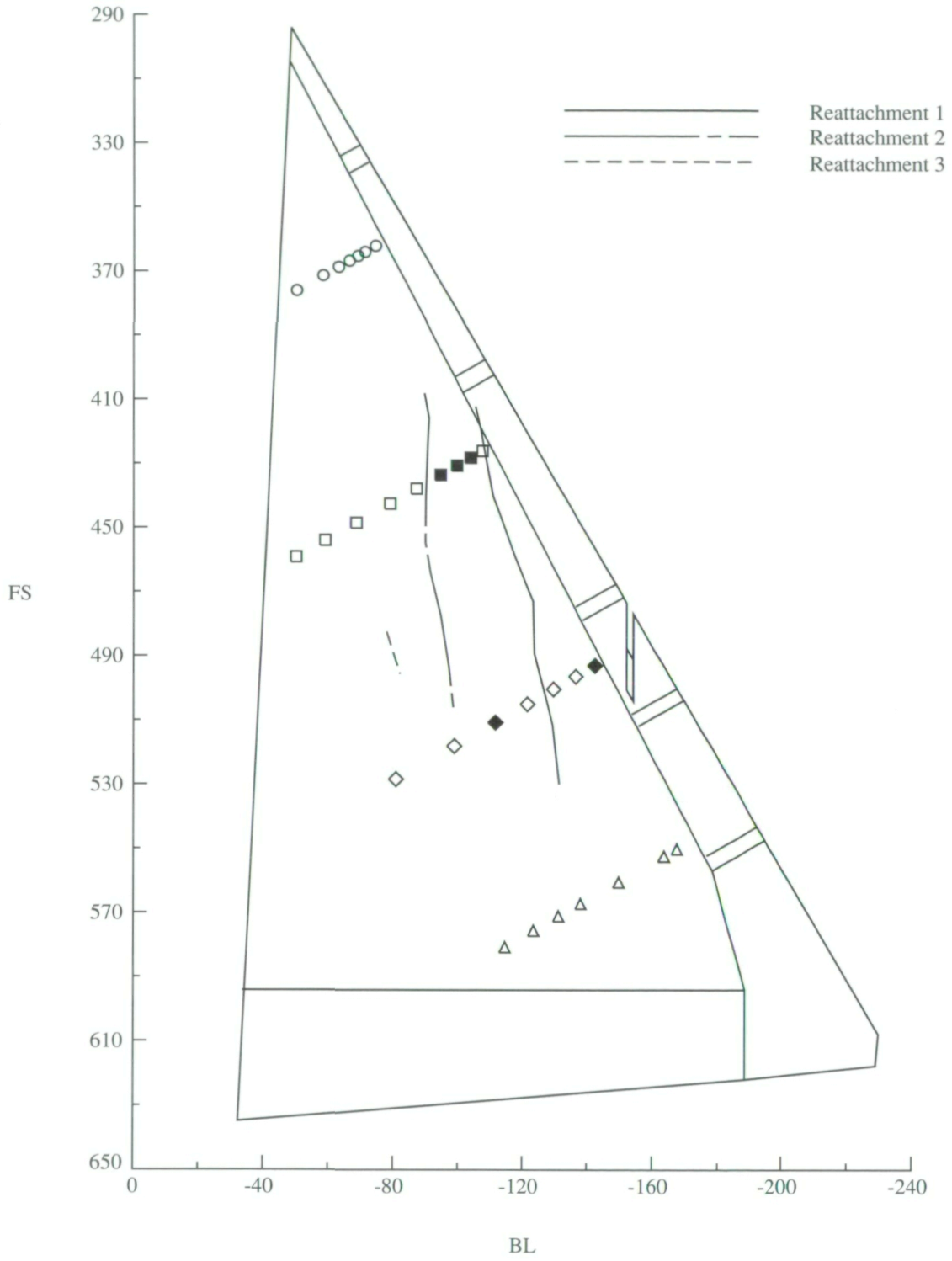

Figure 38. Vortex reattachment points from pressure ports ($\alpha \approx 14°$) and lines from vapor-screen images ($\alpha \approx 15°$; F/S 91-13/05). (Solid symbol indicates port that has out-of-phase pressure variation with α.)

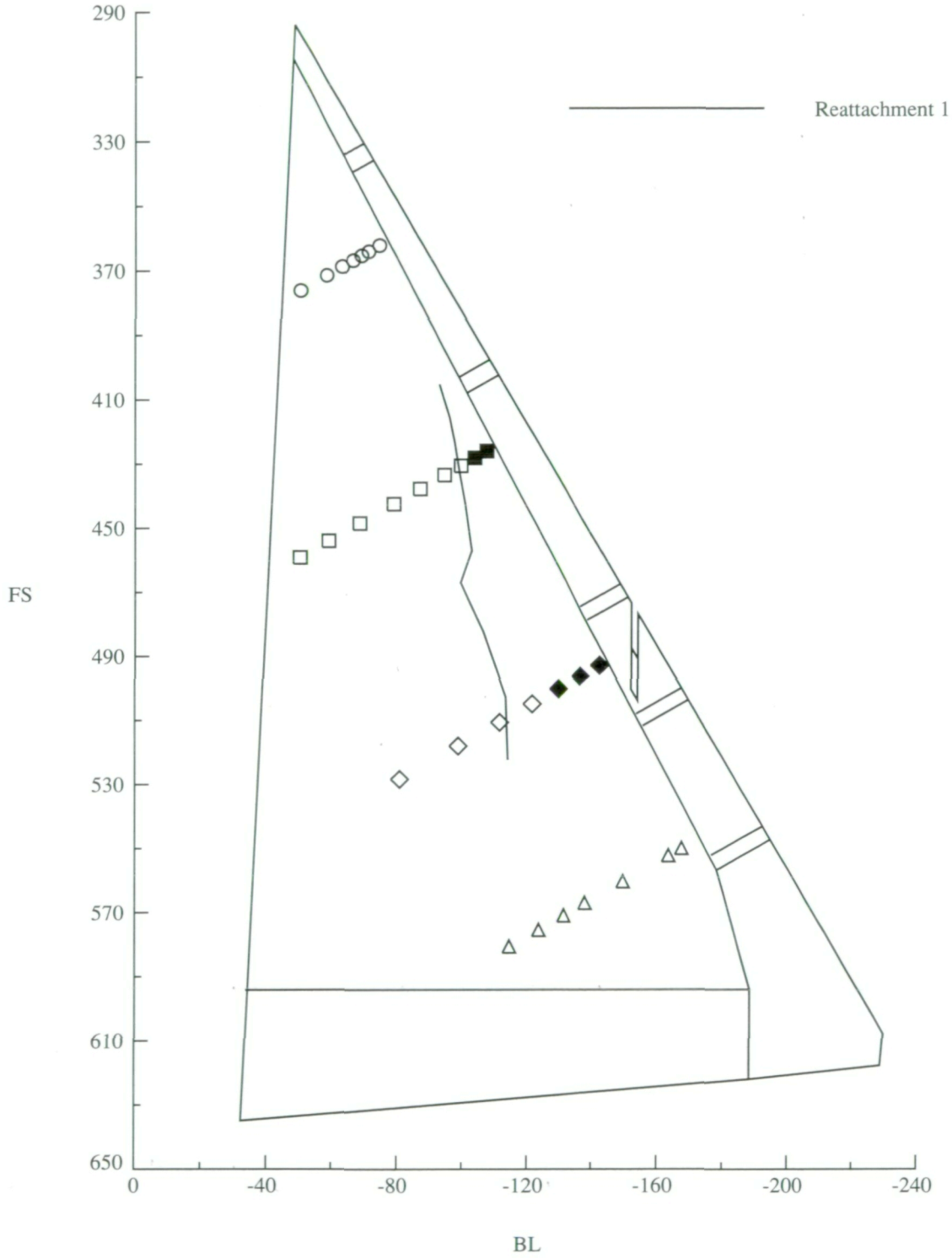

Figure 39. Vortex reattachment points from pressure ports and line from vapor-screen images for $\alpha \approx 17°$ (F/S 91-13/06). (Solid symbol indicates port that has out-of-phase pressure variation with α.)

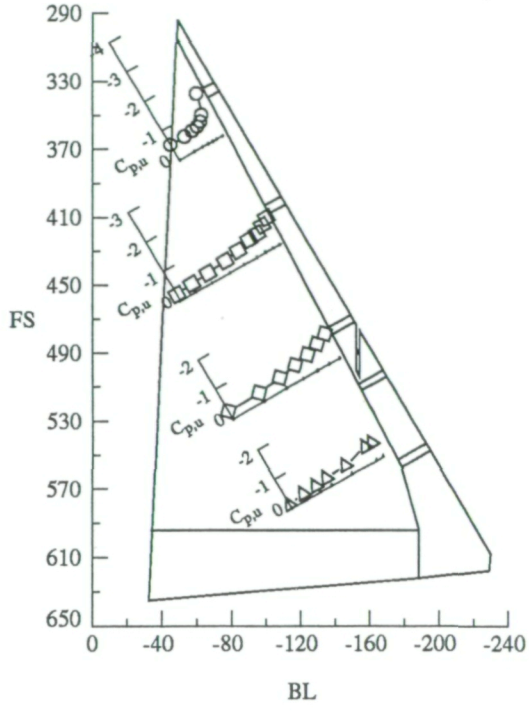

(a) $\alpha = 12.9°$; $M_\infty = 0.36$; $R_n = 39.1 \times 10^6$ (F/S 91-15/12).

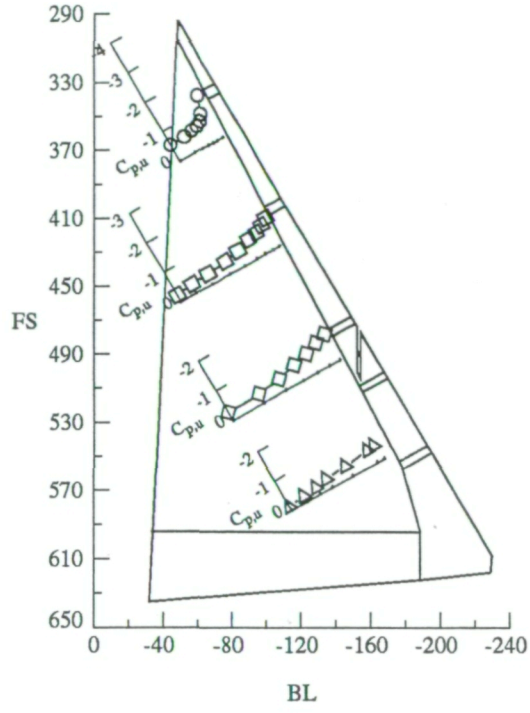

(b) $\alpha = 13.9°$; $M_\infty = 0.34$; $R_n = 37.3 \times 10^6$ (F/S 91-15/13).

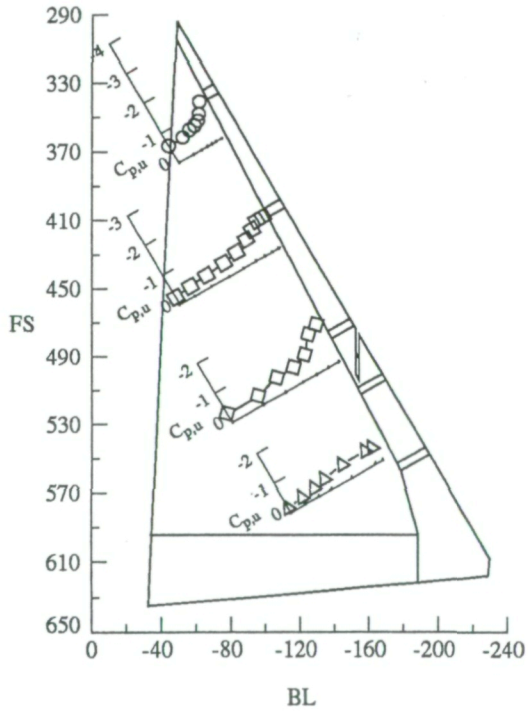

(c) $\alpha = 15.1°$; $M_\infty = 0.34$; $R_n = 37.0 \times 10^6$ (F/S 91-15/17).

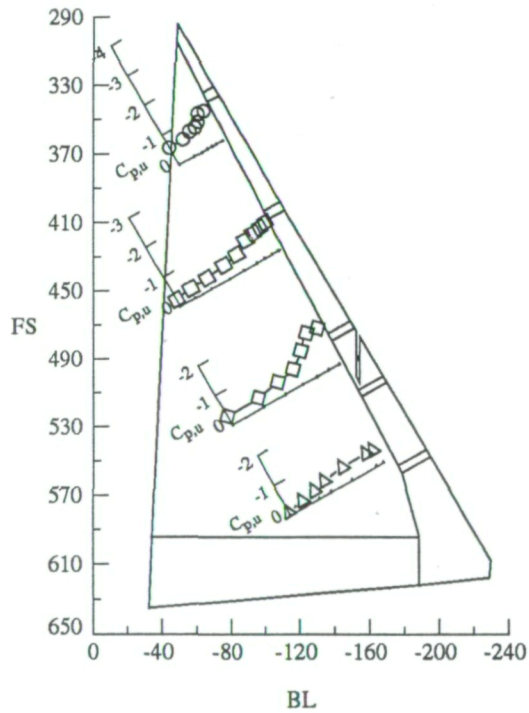

(d) $\alpha = 15.8°$; $M_\infty = 0.33$; $R_n = 33.0 \times 10^6$ (F/S 91-16/09).

Figure 40. Basic upper-surface pressure data for flight/serials at nominal altitude of 15 000 ft and $1g$.

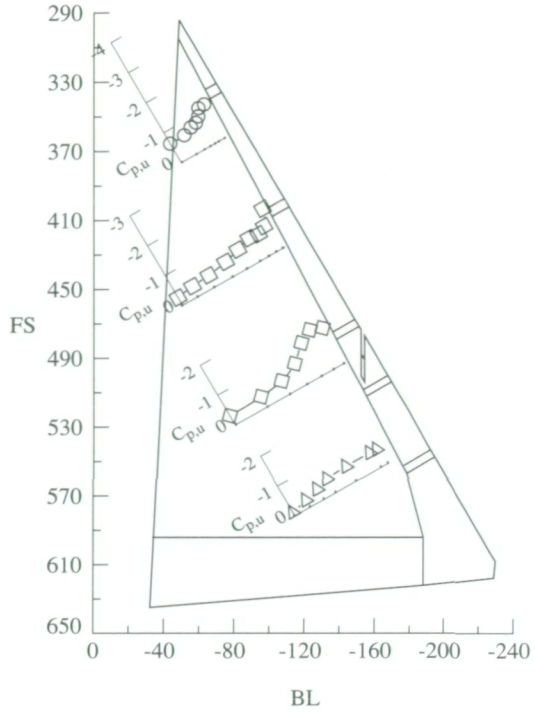

(e) $\alpha = 16.9°$; $M_\infty = 0.31$; $R_n = 31.4 \times 10^6$ (F/S 91-16/10).

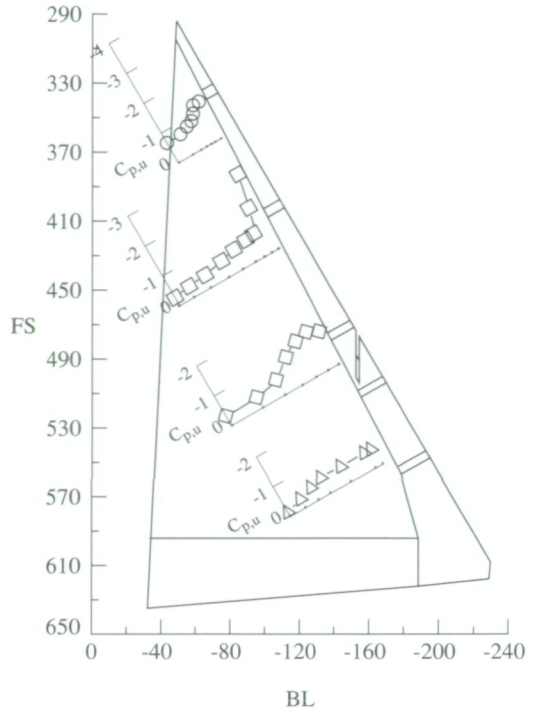

(f) $\alpha = 17.8°$; $M_\infty = 0.29$; $R_n = 30.1 \times 10^6$ (F/S 91-16/11).

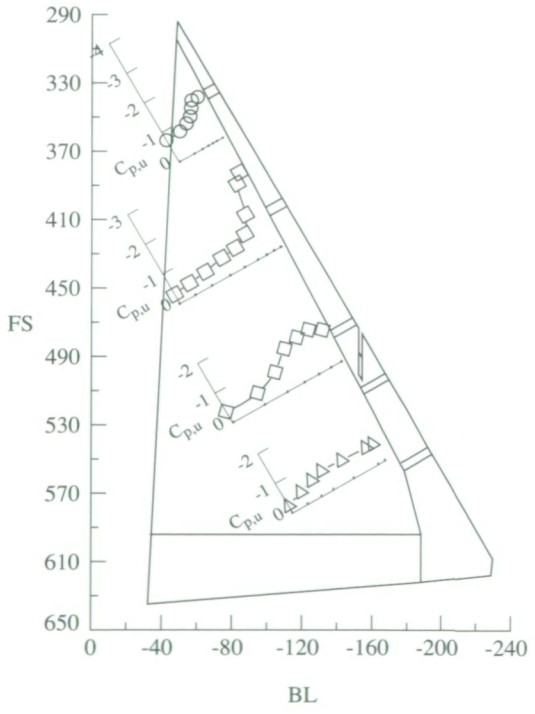

(g) $\alpha = 18.6°$; $M_\infty = 0.29$; $R_n = 30.0 \times 10^6$ (F/S 91-17/07).

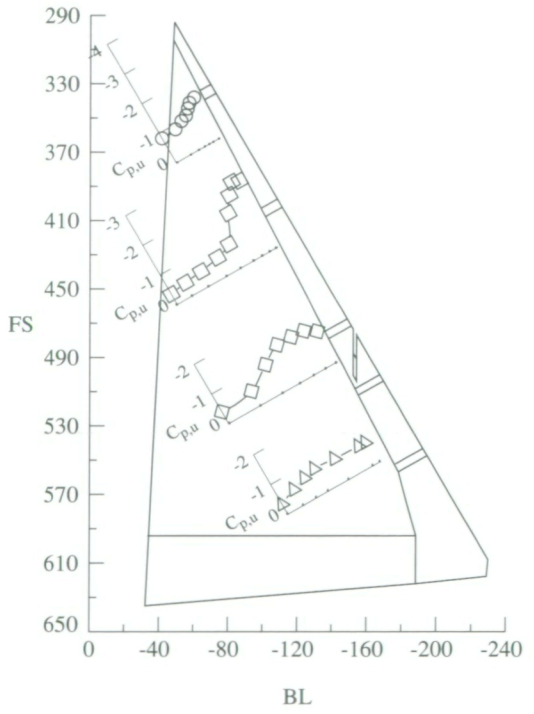

(h) $\alpha = 20.2°$; $M_\infty = 0.27$; $R_n = 28.3 \times 10^6$ (F/S 91-17/09).

Figure 40. Continued.

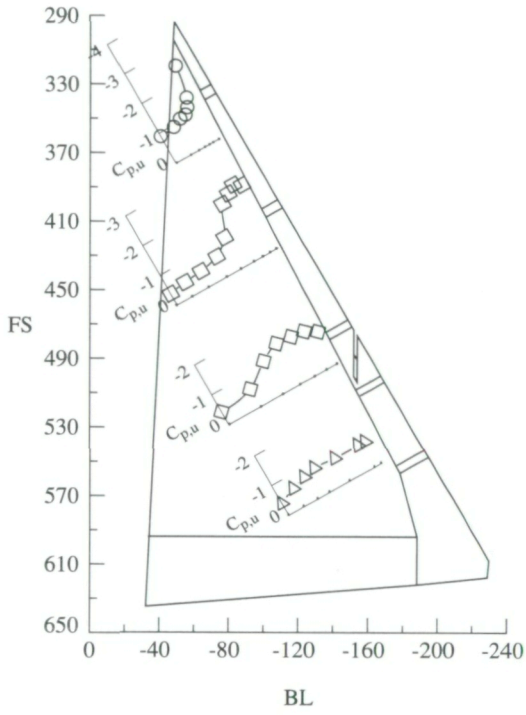

(i) $\alpha = 21.3°$; $M_\infty = 0.26$; $R_n = 27.5 \times 10^6$ (F/S 91-17/10).

Figure 40. Concluded.

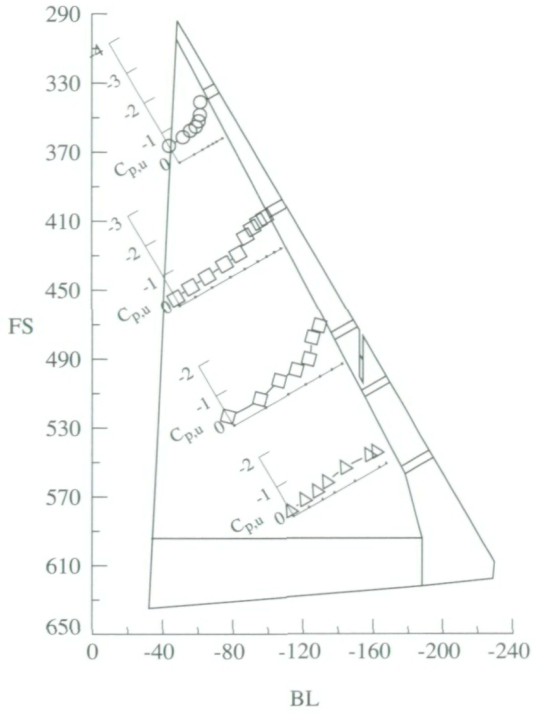

(a) $\alpha = 13.9°$; $M_\infty = 0.42$; $R_n = 35.1 \times 10^6$ (F/S 91-13/11).

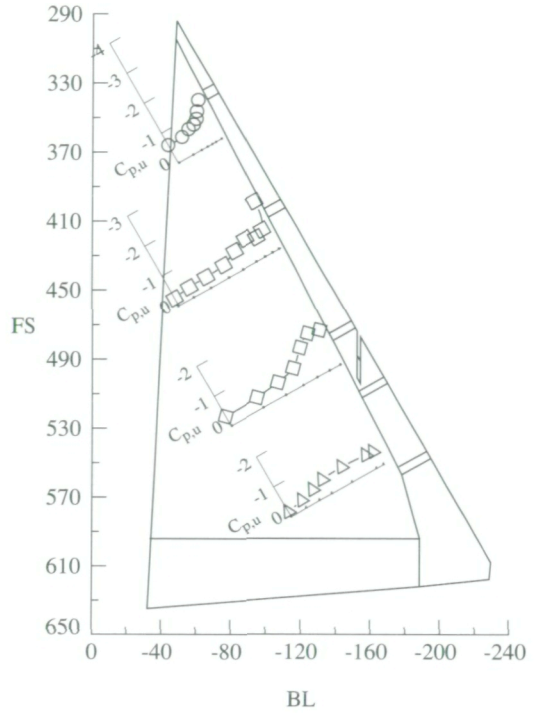

(b) $\alpha = 14.9°$; $M_\infty = 0.41$; $R_n = 34.6 \times 10^6$ (F/S 91-13/05).

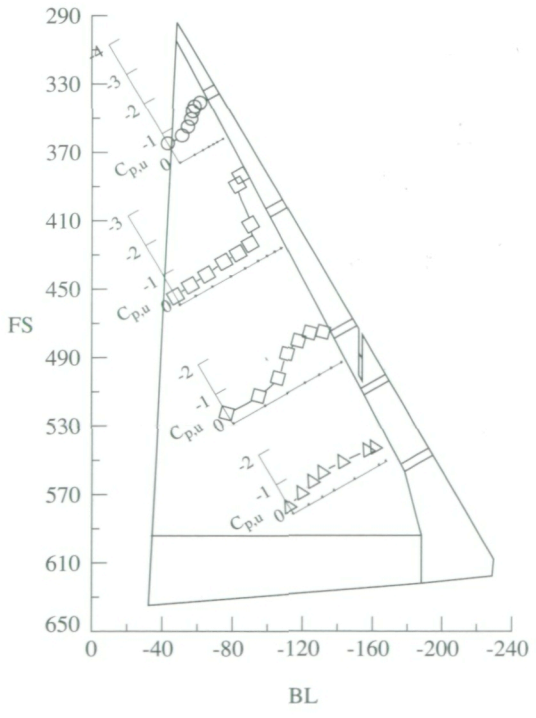

(c) $\alpha = 16.1°$; $M_\infty = 0.39$; $R_n = 32.0 \times 10^6$ (F/S 91-13/10).

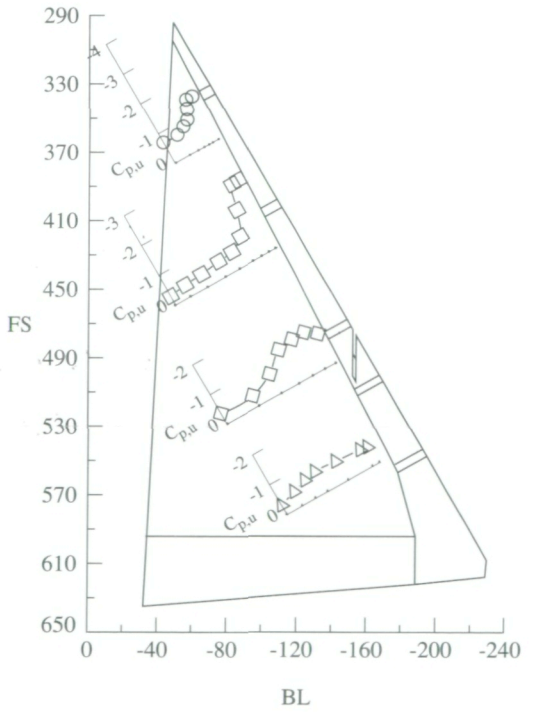

(d) $\alpha = 17.0°$; $M_\infty = 0.38$; $R_n = 32.0 \times 10^6$ (F/S 91-13/06).

Figure 41. Basic upper-surface pressure data for flight/serials at nominal altitude of 25 000 ft and $1g$.

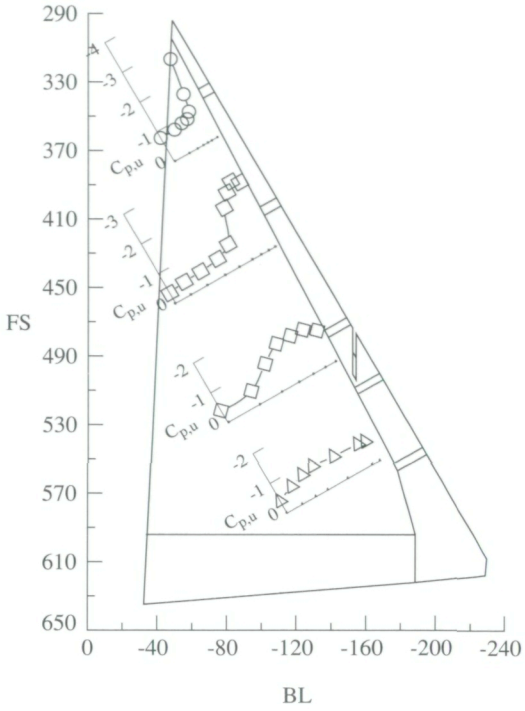

(e) $\alpha = 18.8°$; $M_\infty = 0.35$; $R_n = 29.9 \times 10^6$ (F/S 91-13/07).

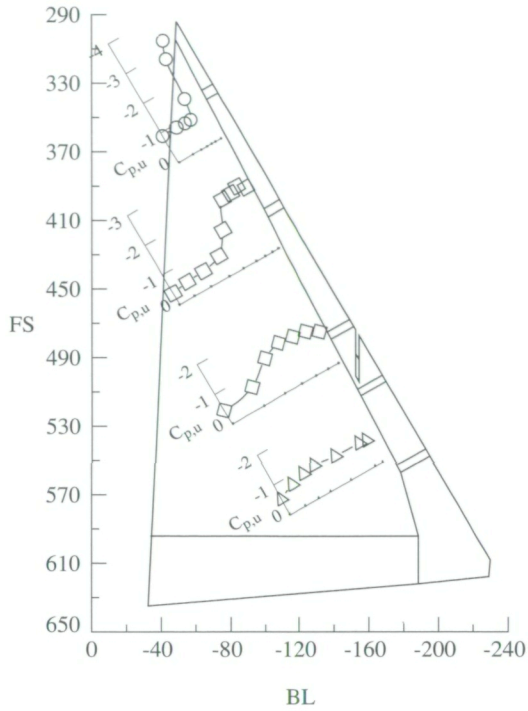

(f) $\alpha = 20.5°$; $M_\infty = 0.34$; $R_n = 27.8 \times 10^6$ (F/S 91-13/08).

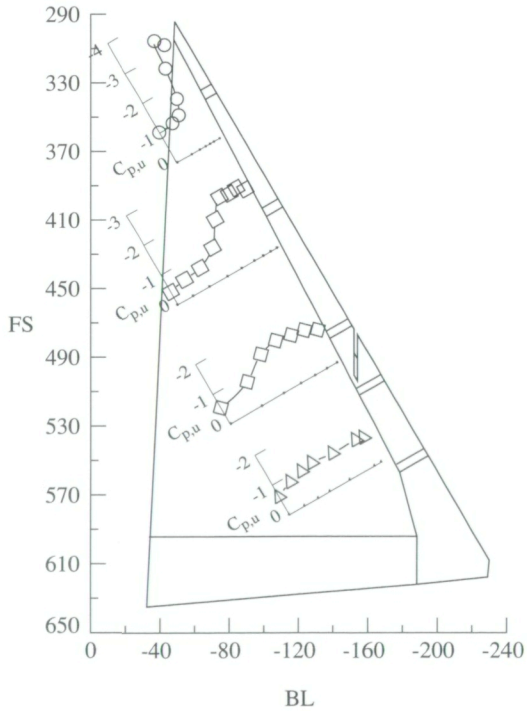

(g) $\alpha = 22.5°$; $M_\infty = 0.32$; $R_n = 26.6 \times 10^6$ (F/S 91-13/09).

Figure 41. Concluded.

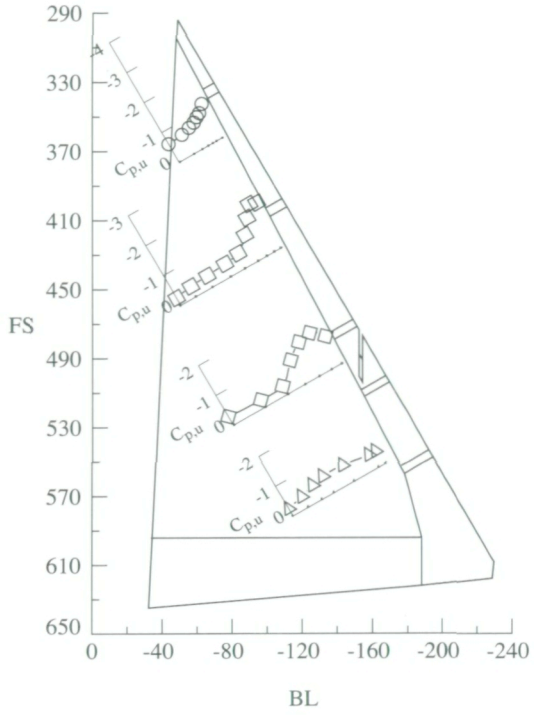

(a) $\alpha = 13.9°$; $M_\infty = 0.54$; $R_n = 30.8 \times 10^6$ (F/S 91-15/06).

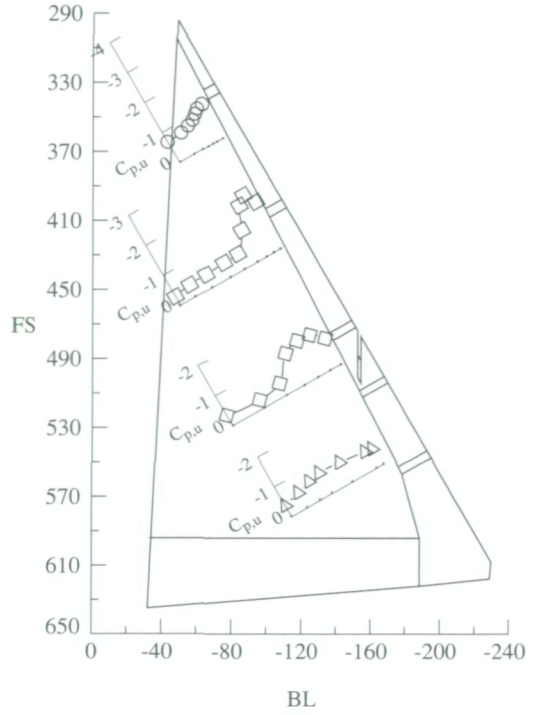

(b) $\alpha = 14.8°$; $M_\infty = 0.53$; $R_n = 29.2 \times 10^6$ (F/S 91-14/07).

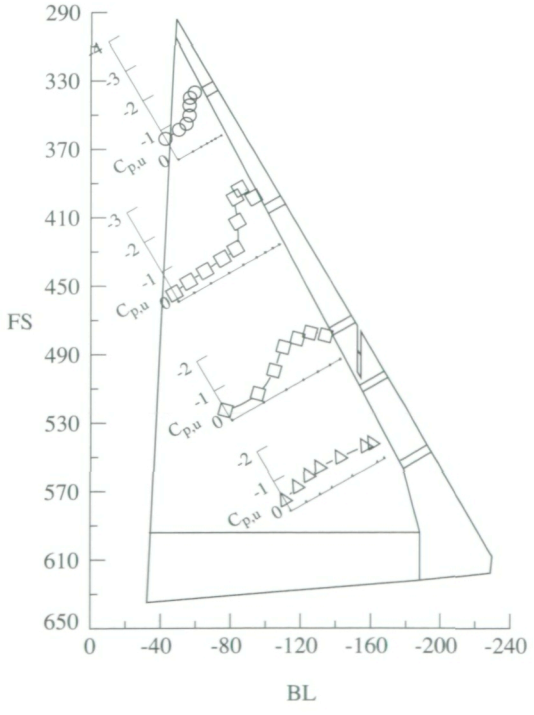

(c) $\alpha = 15.8°$; $M_\infty = 0.50$; $R_n = 27.6 \times 10^6$ (F/S 91-15/08).

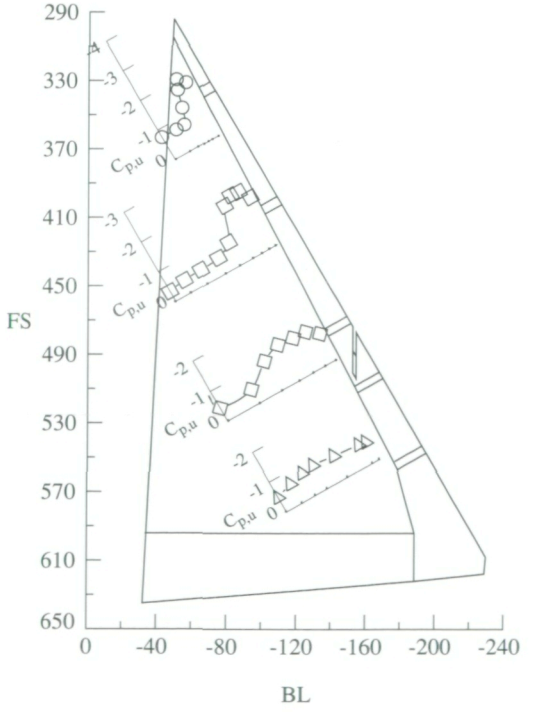

(d) $\alpha = 16.8°$; $M_\infty = 0.49$; $R_n = 26.8 \times 10^6$ (F/S 91-14/08).

Figure 42. Basic upper-surface pressure data for flight/serials at nominal altitude of 35 000 ft and $1g$.

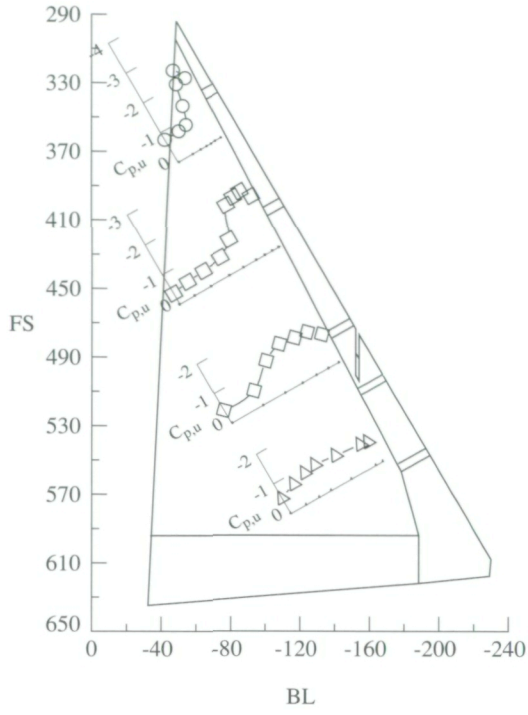

(e) $\alpha = 17.7°$; $M_\infty = 0.47$; $R_n = 25.8 \times 10^6$ (F/S 91-14/09).

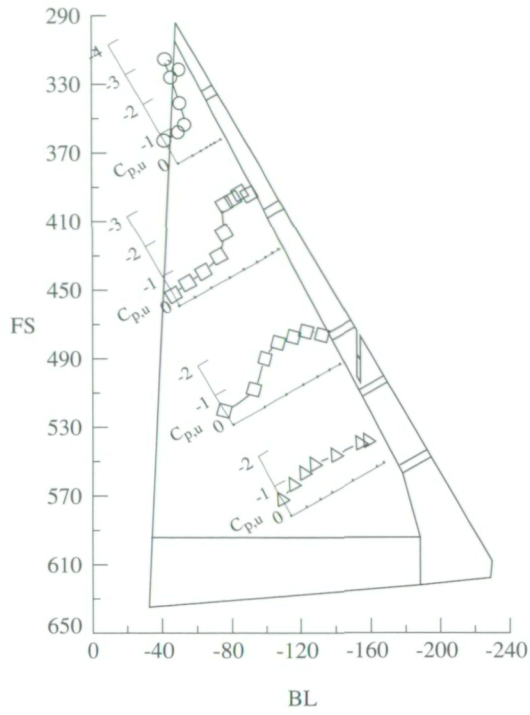

(f) $\alpha = 18.7°$; $M_\infty = 0.45$; $R_n = 24.6 \times 10^6$ (F/S 91-14/10).

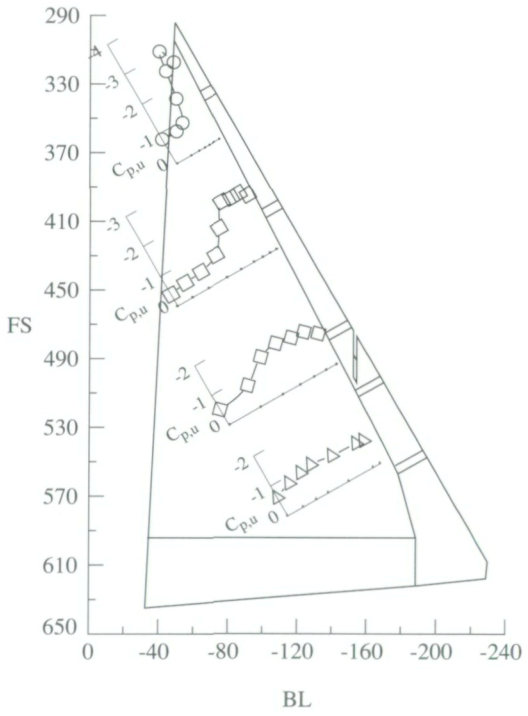

(g) $\alpha = 19.7°$; $M_\infty = 0.44$; $R_n = 23.8 \times 10^6$ (F/S 91-14/11).

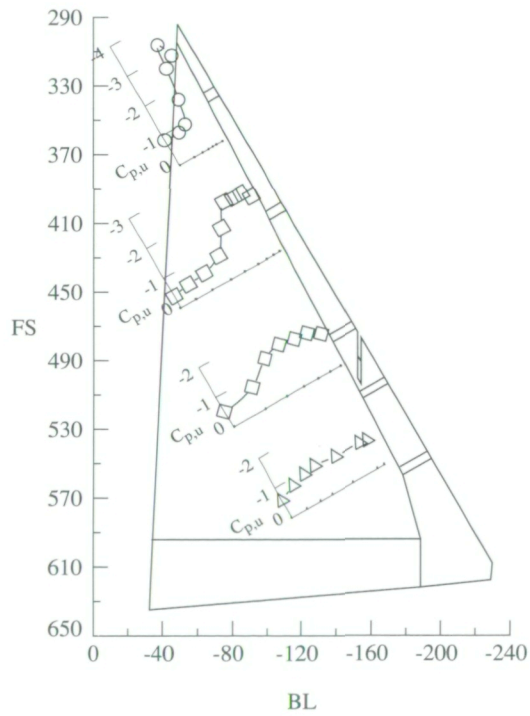

(h) $\alpha = 20.5°$; $M_\infty = 0.42$; $R_n = 23.7 \times 10^6$ (F/S 91-14/12).

Figure 42. Continued.

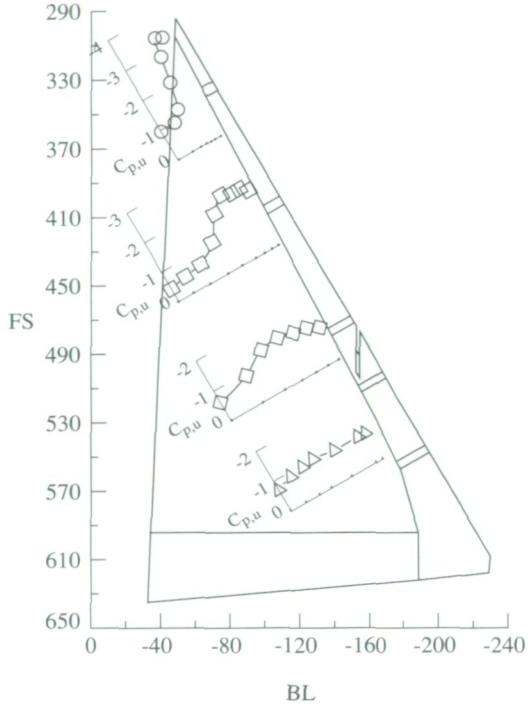

(i) $\alpha = 21.9°$; $M_\infty = 0.40$; $R_n = 22.6 \times 10^6$ (F/S 91-15/10).

Figure 42. Concluded.

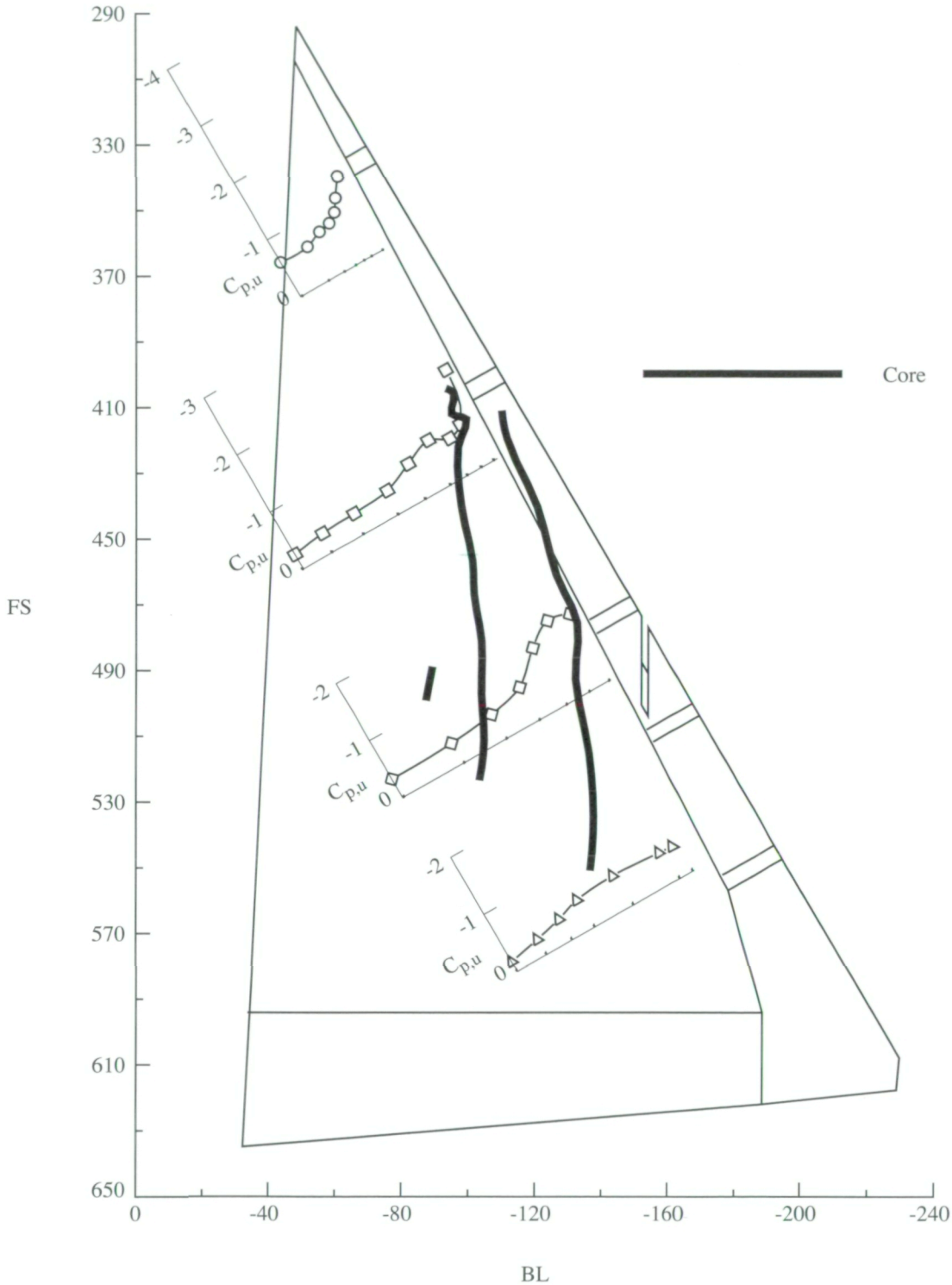

(a) $\alpha = 14.9°$; $M_\infty = 0.41$; $R_n = 34.6 \times 10^6$ (F/S 91-13/05).

Figure 43. Superposition of vapor-screen vortex core tracks on surface pressures at nominal $1g$.

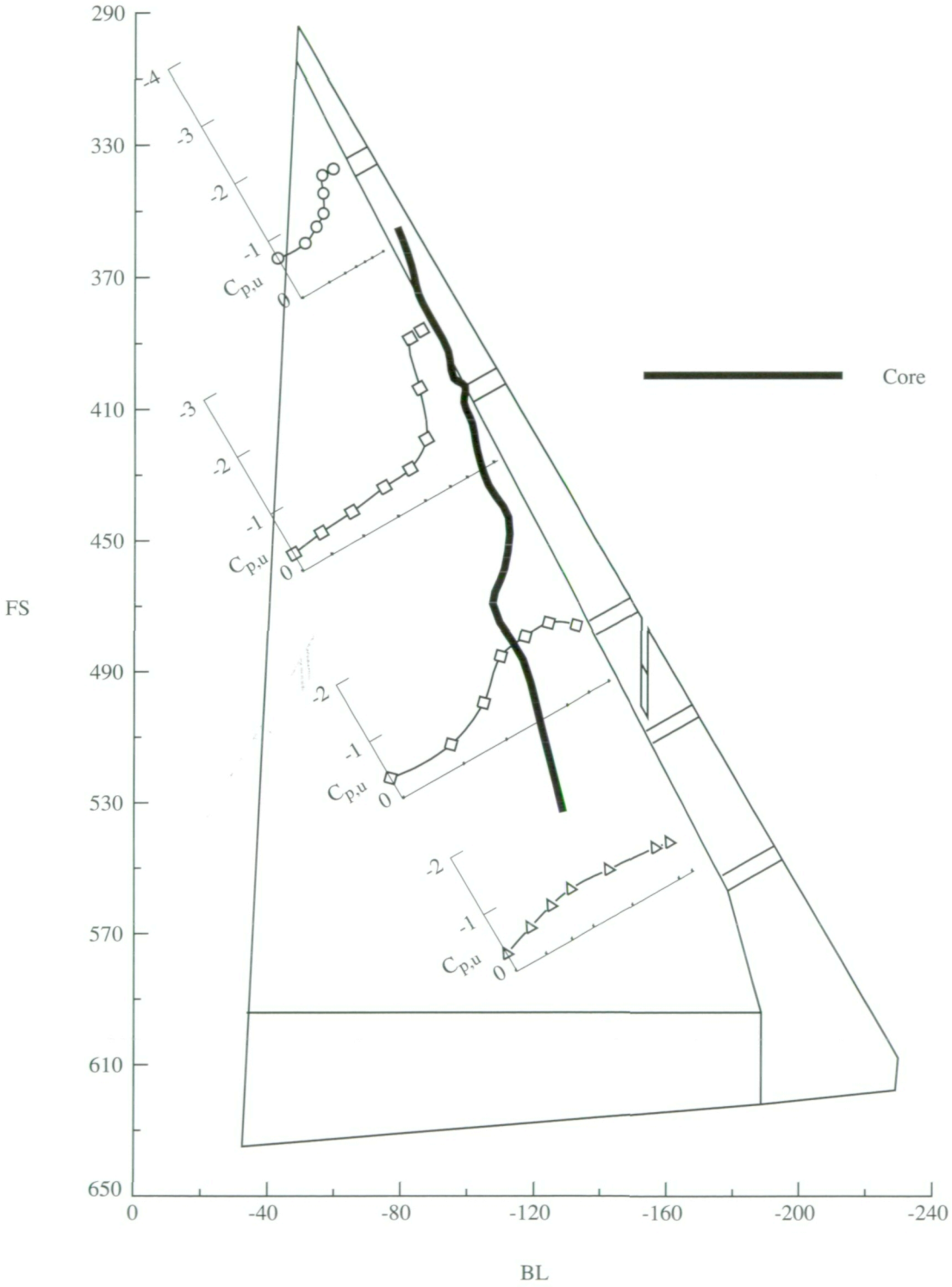

(b) $\alpha = 17.0°$; $M_\infty = 0.38$; $R_n = 32.0 \times 10^6$ (F/S 91-13/06).

Figure 43. Continued.

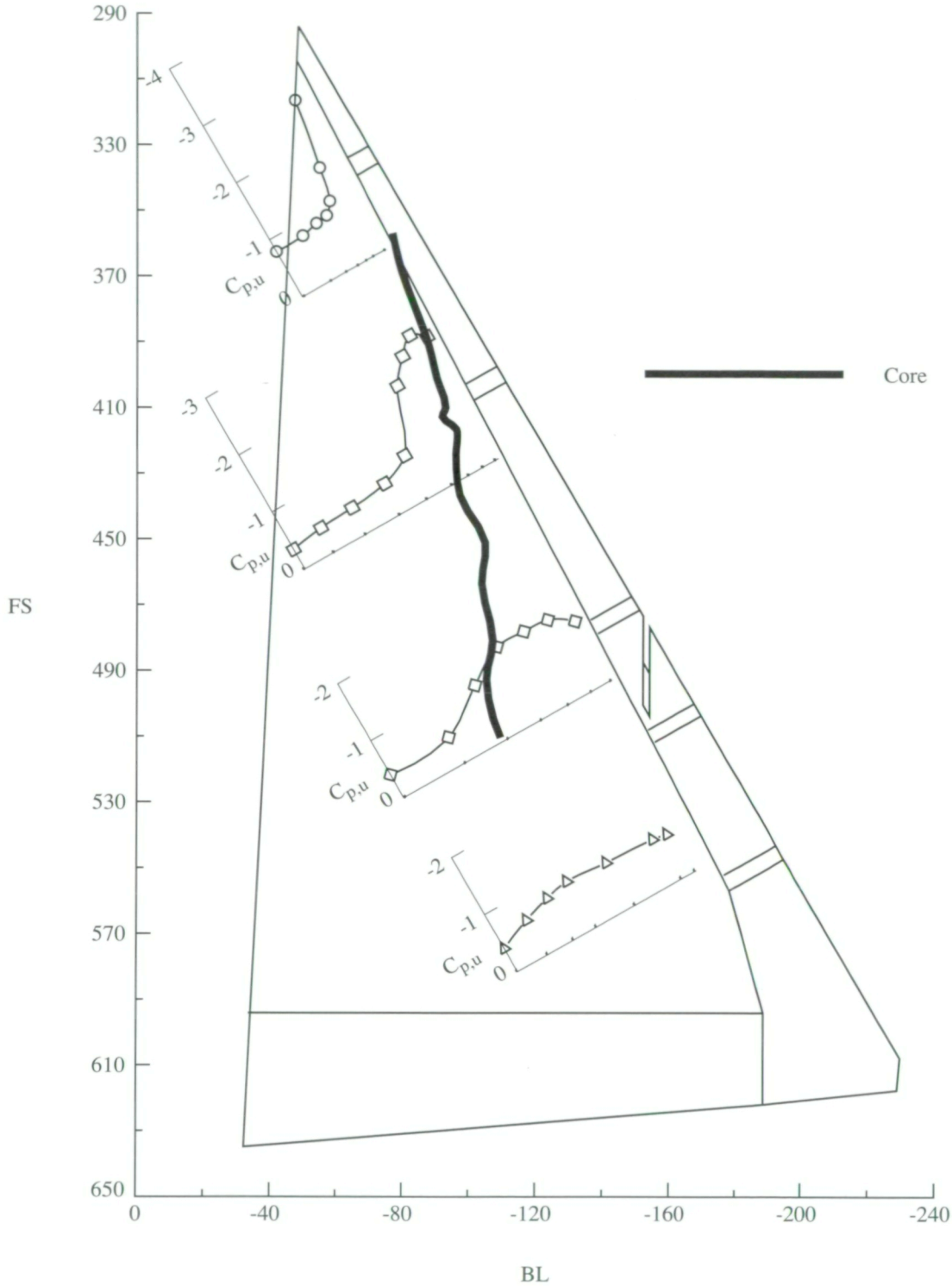

(c) $\alpha = 18.8°$; $M_\infty = 0.35$; $R_n = 29.9 \times 10^6$ (F/S 91-13/07).

Figure 43. Concluded.

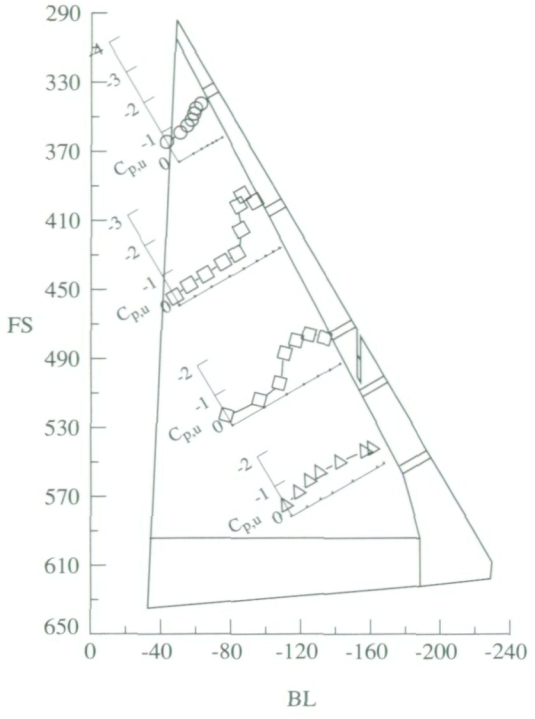

(a) $0.9g$; $M_\infty = 0.53$; $R_n = 29.2 \times 10^6$ (F/S 91-14/07).

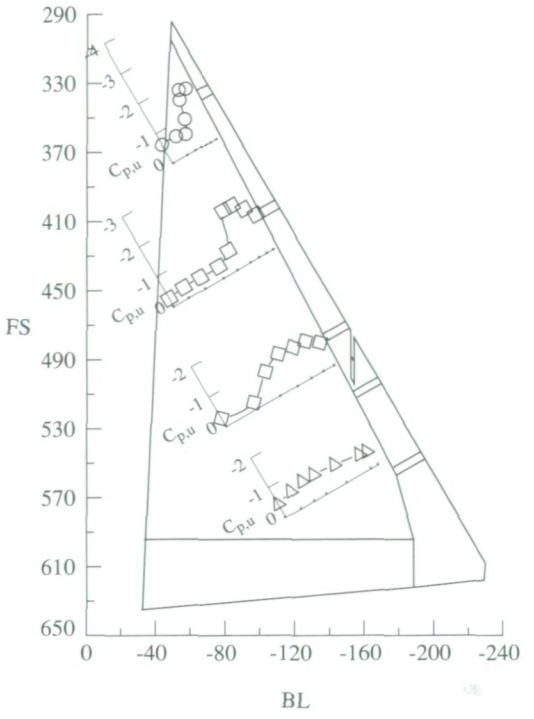

(b) $1.6g$; $M_\infty = 0.68$; $R_n = 35.5 \times 10^6$ (F/S 91-17/05).

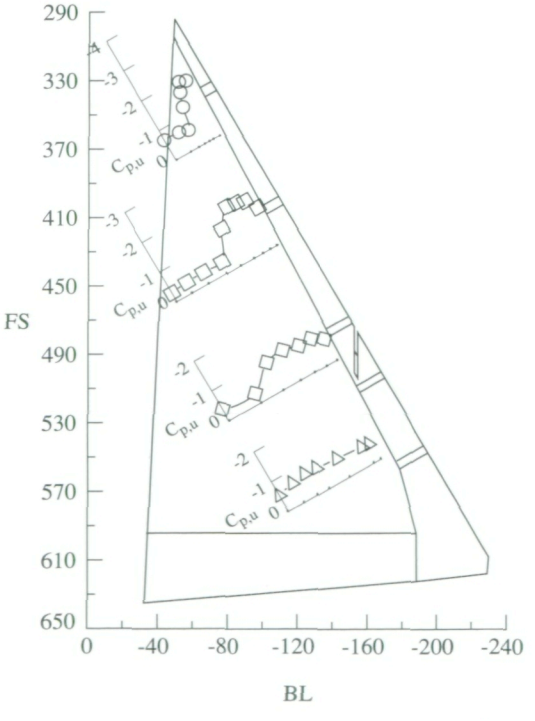

(c) $2.5g$; $M_\infty = 0.73$; $R_n = 45.7 \times 10^6$ (F/S 91-15/11).

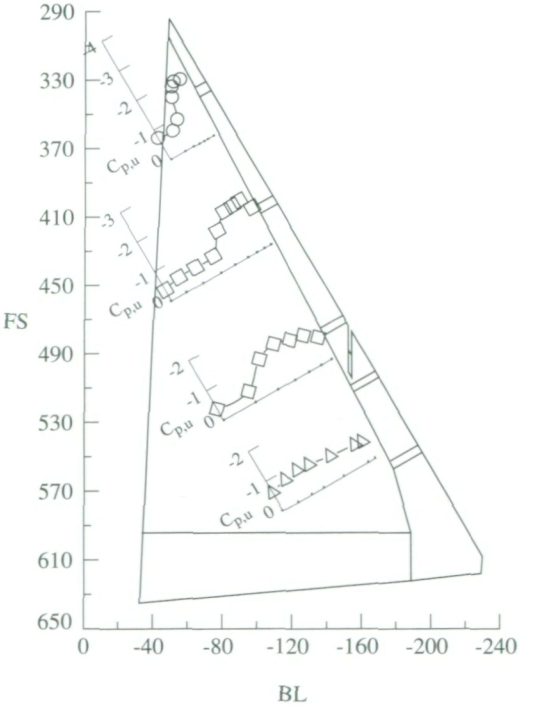

(d) $3.9g$; $M_\infty = 0.80$; $R_n = 57.3 \times 10^6$ (F/S 91-16/07).

Figure 44. Effects of R_n and load factor on upper-surface pressure distributions at nominal altitude of 35 000 ft and $\alpha = 14.8°$.

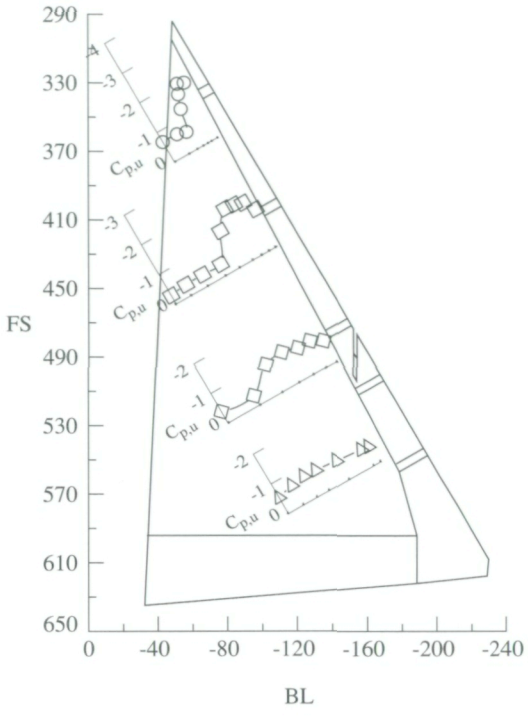

(a) $\alpha = 14.8°$; $M_\infty = 0.73$; $R_n = 45.7 \times 10^6$ (F/S 91-15/11).

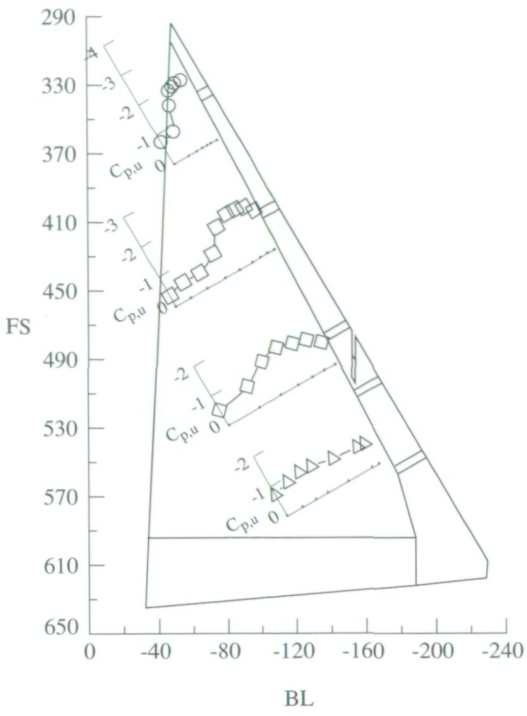

(b) $\alpha = 16.8°$; $M_\infty = 0.78$; $R_n = 44.6 \times 10^6$ (F/S 91-16/05).

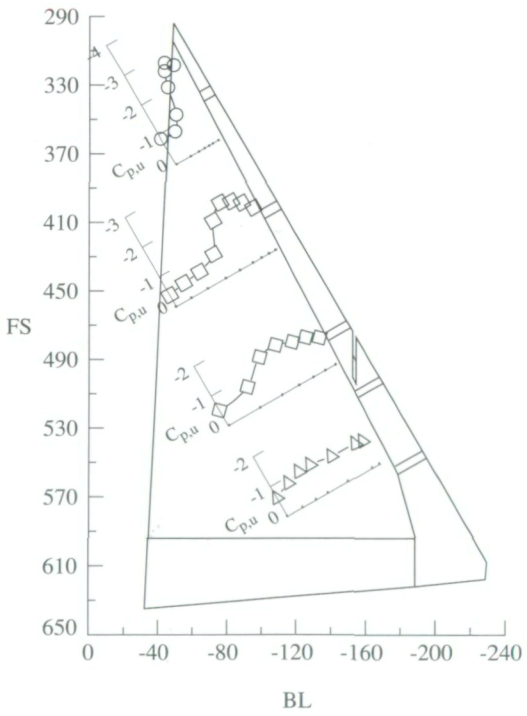

(c) $\alpha = 18.6°$; $M_\infty = 0.67$; $R_n = 35.6 \times 10^6$ (F/S 91-17/06).

Figure 45. Effect of α on upper-surface pressure distributions for loaded spiral descents at nominal altitude of 35 000 ft and 2.6g.

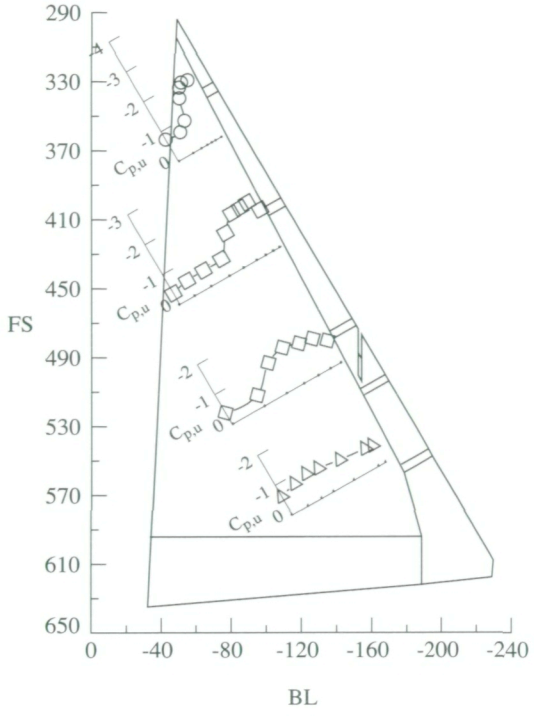

(a) $\alpha = 14.8°$; $M_\infty = 0.80$; $R_n = 57.3 \times 10^6$ (F/S 91-16/07).

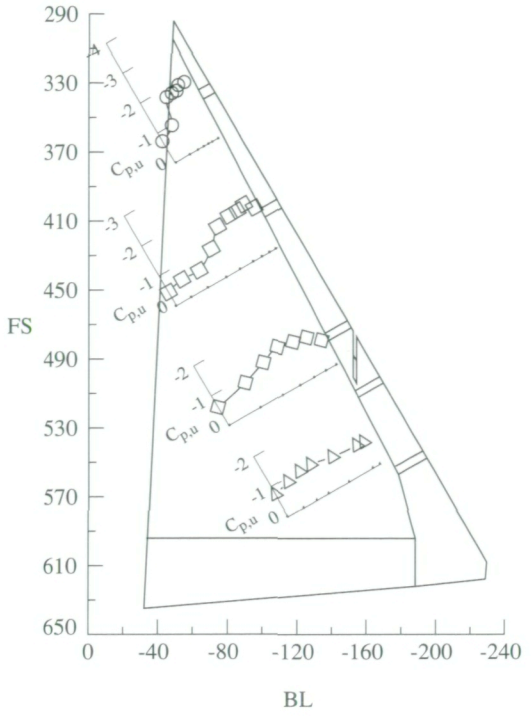

(b) $\alpha = 17.3°$; $M_\infty = 0.81$; $R_n = 48.4 \times 10^6$ (F/S 91-16/08).

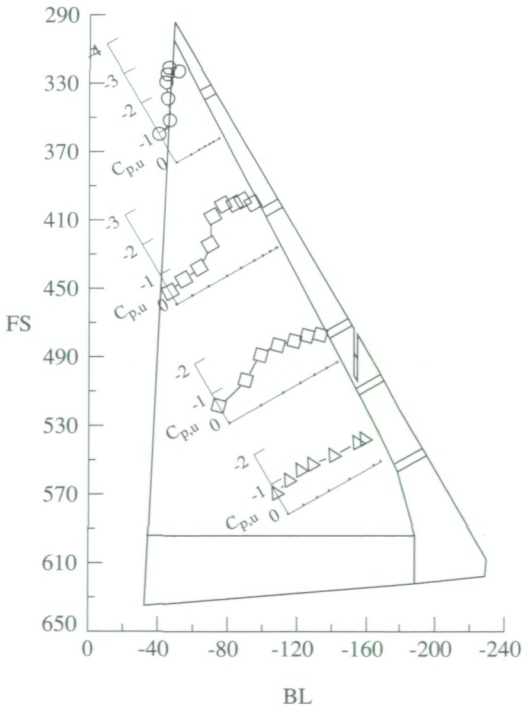

(c) $\alpha = 19.4°$; $M_\infty = 0.69$; $R_n = 46.6 \times 10^6$ (F/S 91-16/06).

Figure 46. Effect of α on upper-surface pressure distributions for loaded spiral descents at nominal altitude of 30 000 ft and $3.7g$.

L-93-37

(a) Photograph from chase airplane.

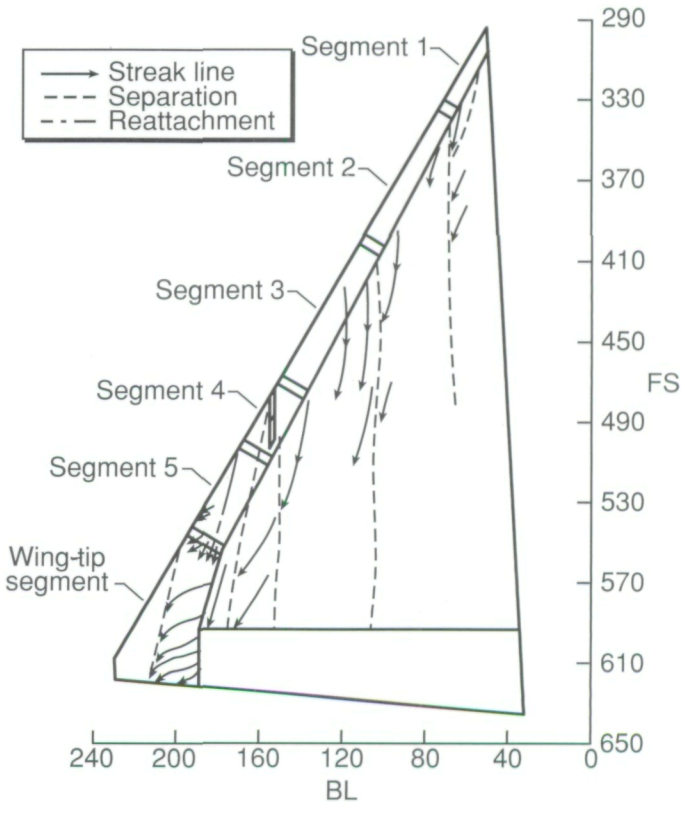

(b) Sketch of flow patterns.

Figure 47. Oil-flow patterns on wing at nominal altitude of 15 000 ft and $\alpha = 13°$.

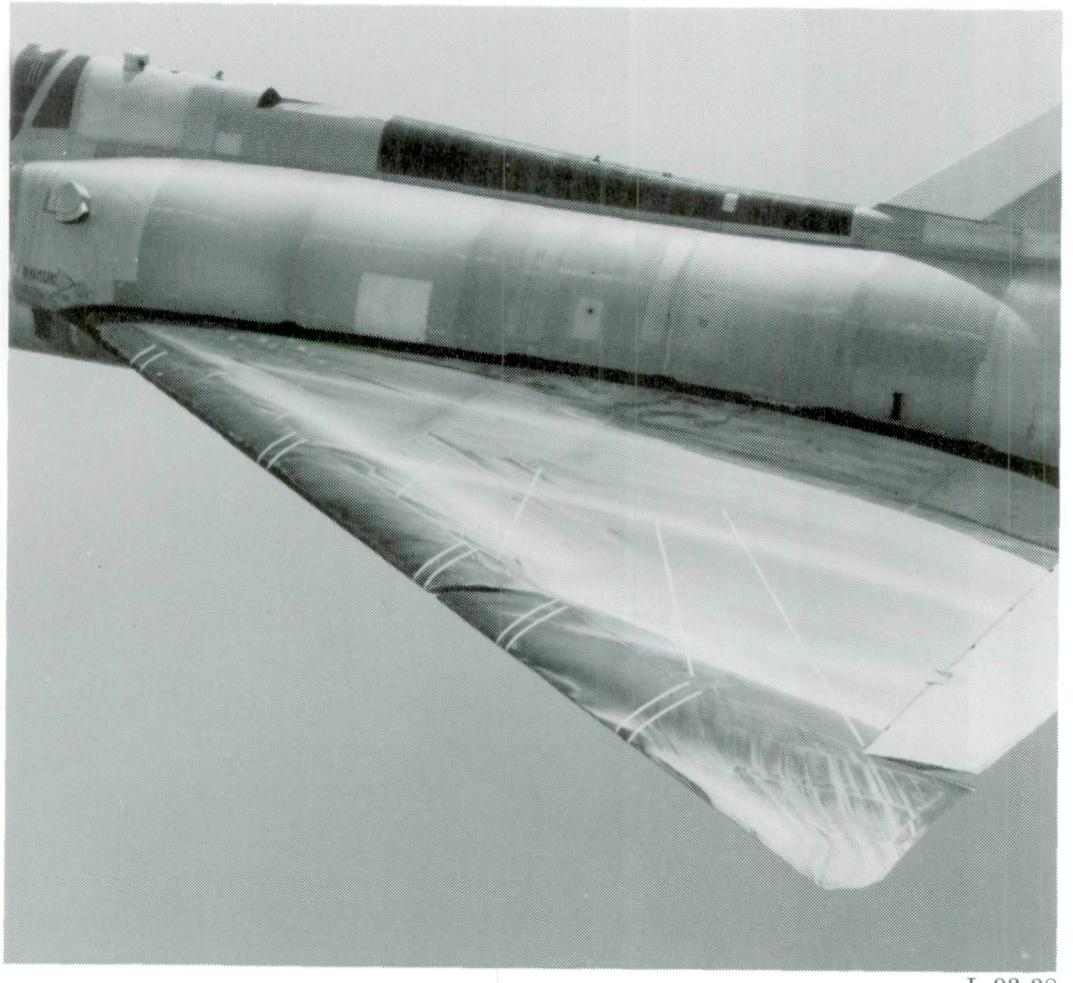

L-93-38

(a) Photograph from chase airplane.

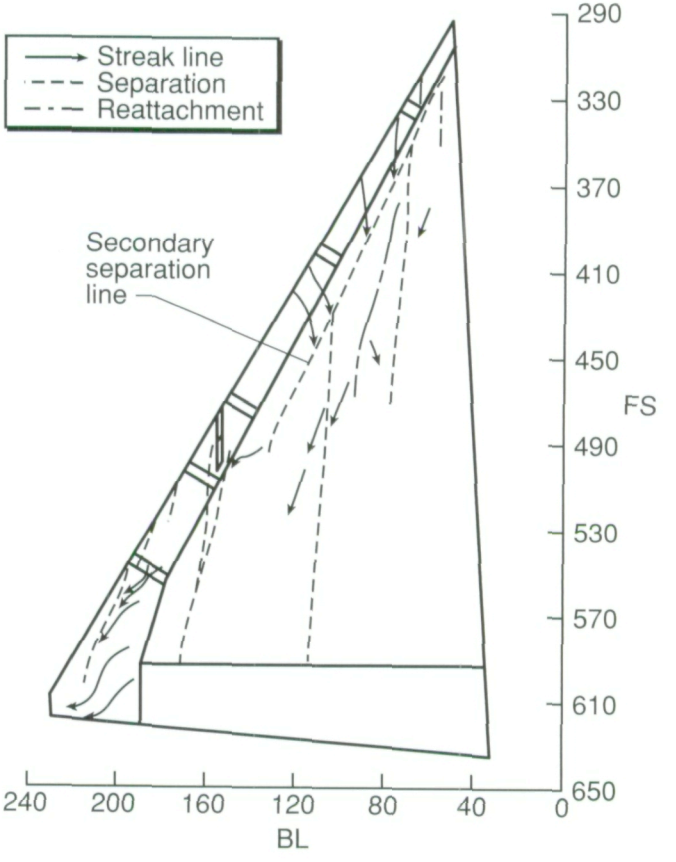

(b) Sketch of flow patterns.

Figure 48. Oil-flow patterns on wing at nominal altitude of 15 000 ft and $\alpha = 15°$.

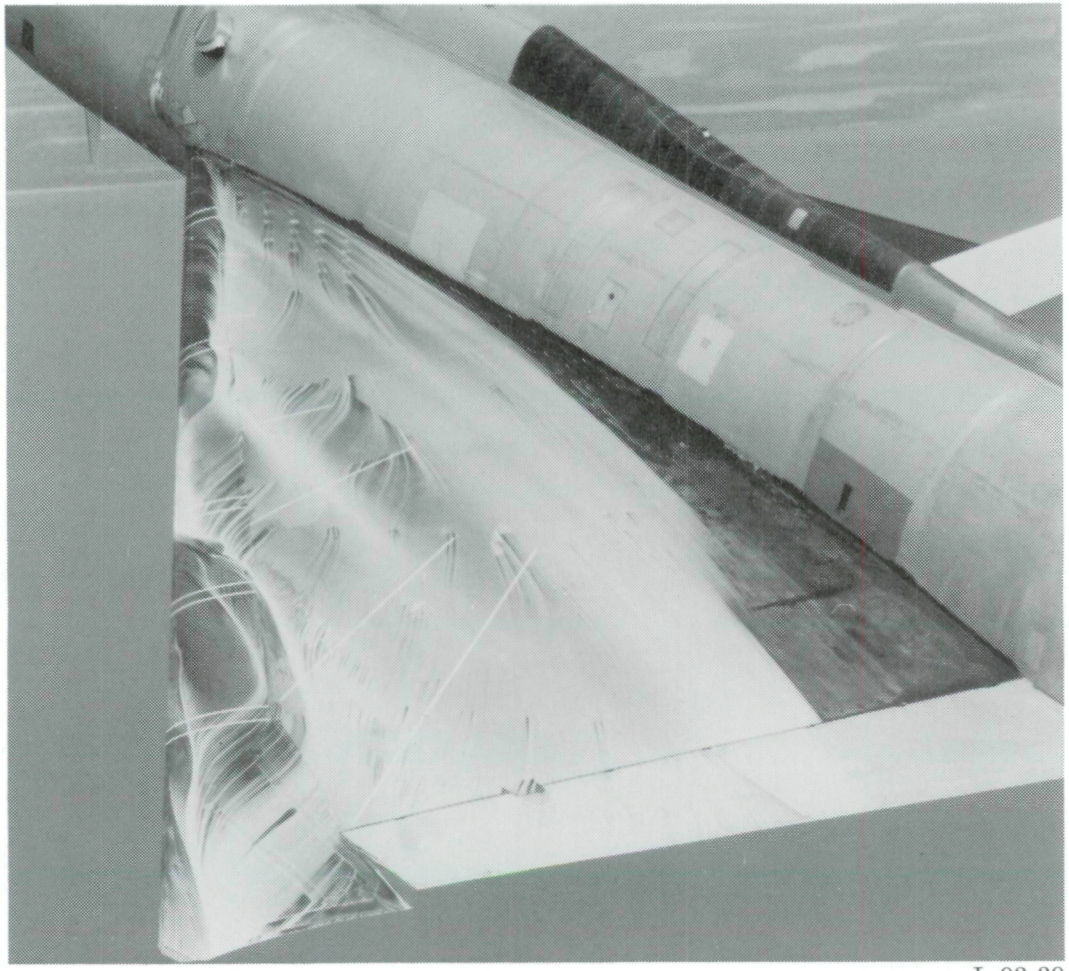

L-93-39

(a) Photograph from chase airplane.

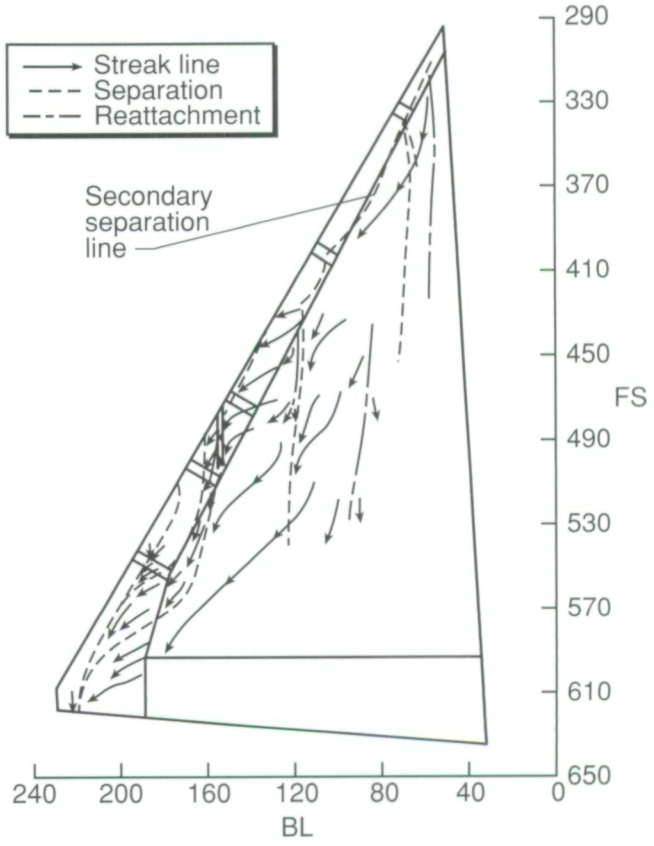

(b) Sketch of flow patterns.

Figure 49. Oil-flow patterns on wing at nominal altitude of 15 000 ft and $\alpha = 17°$.

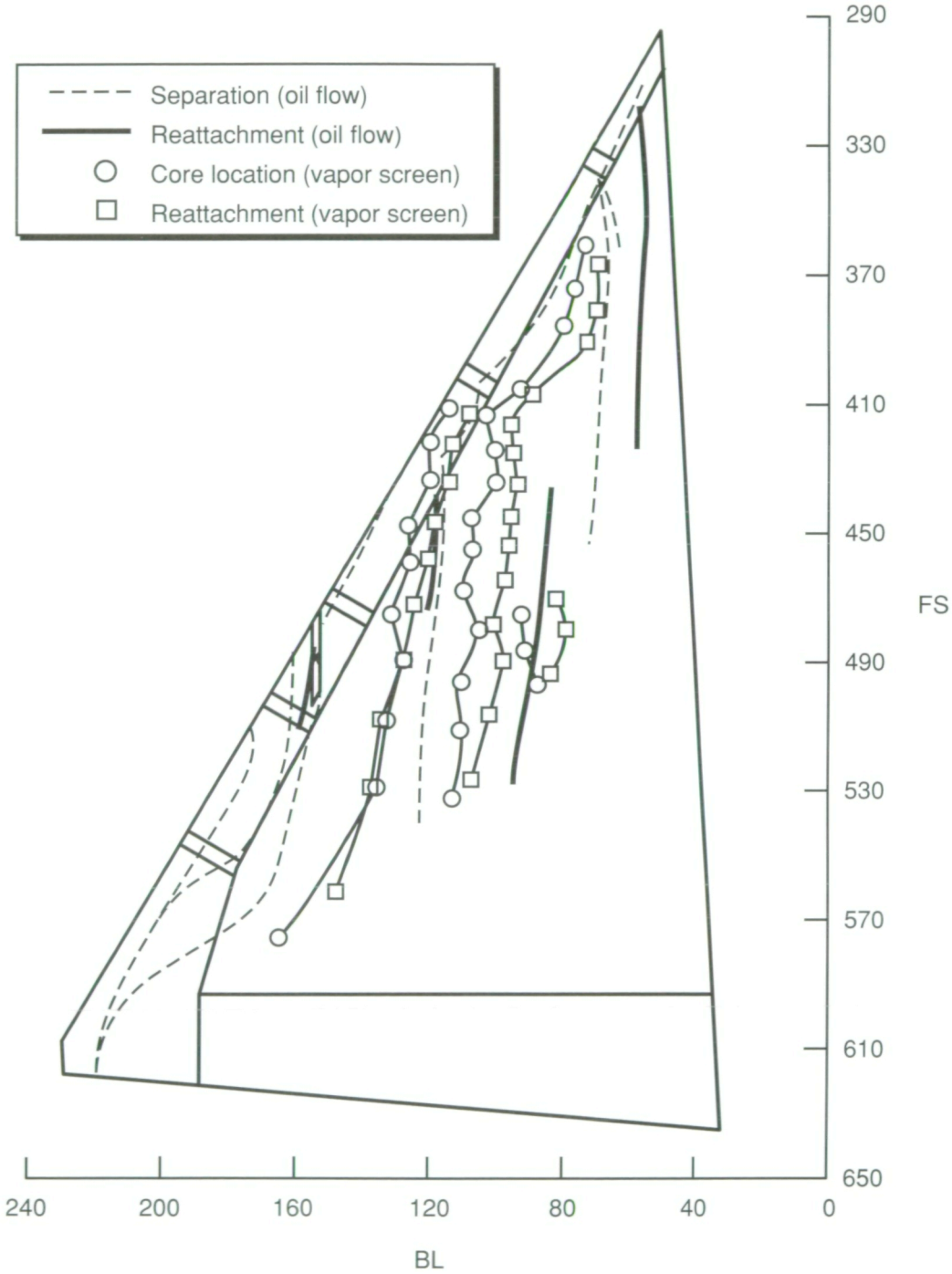

(c) Superposition of vapor-screen vortex-system results on oil-flow patterns.

Figure 49. Concluded.

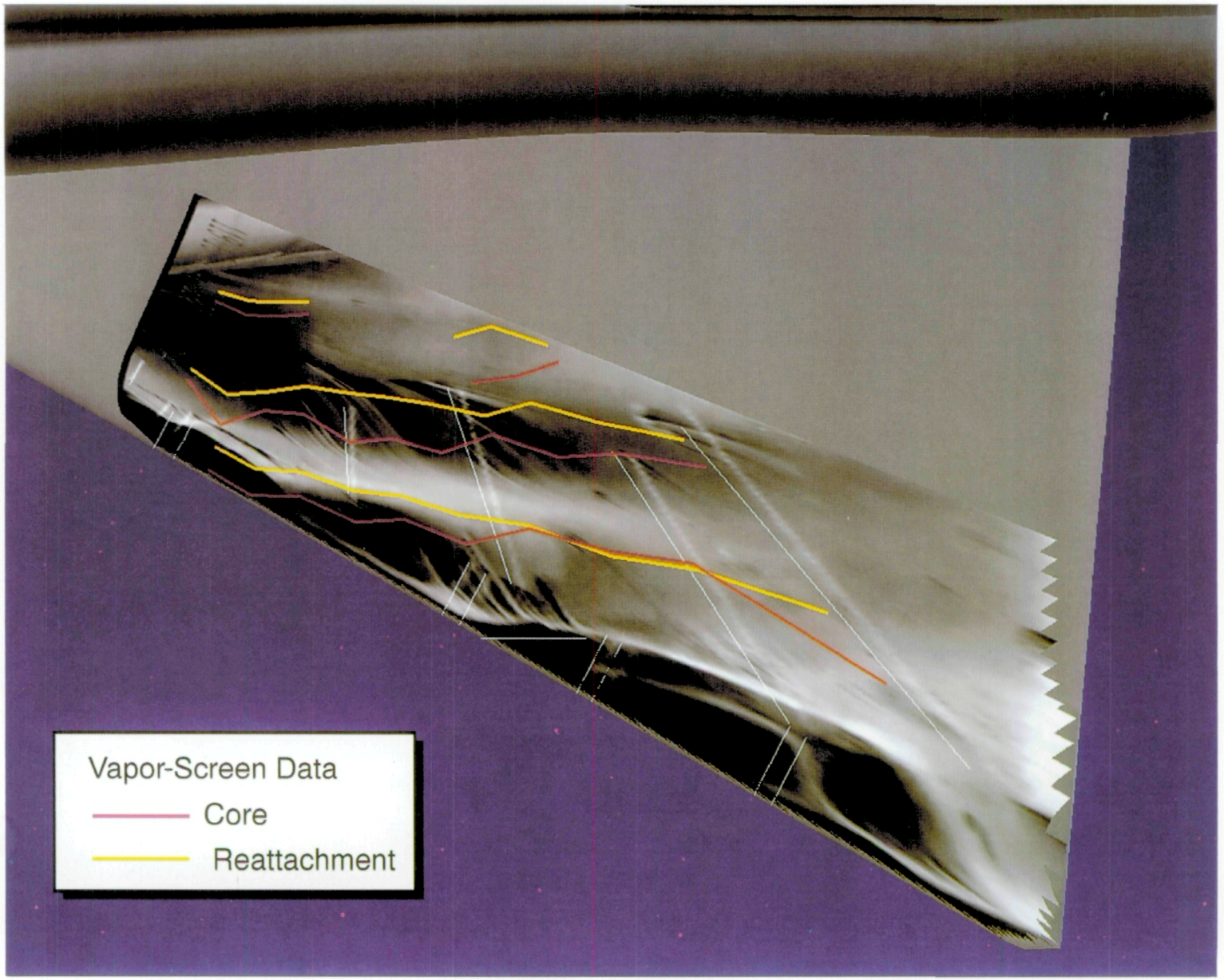

(a) View from above.

Figure 50. Superposition of vapor-screen results on surface oil-flow patterns at nominal altitude of 15 000 ft and $\alpha = 17°$.

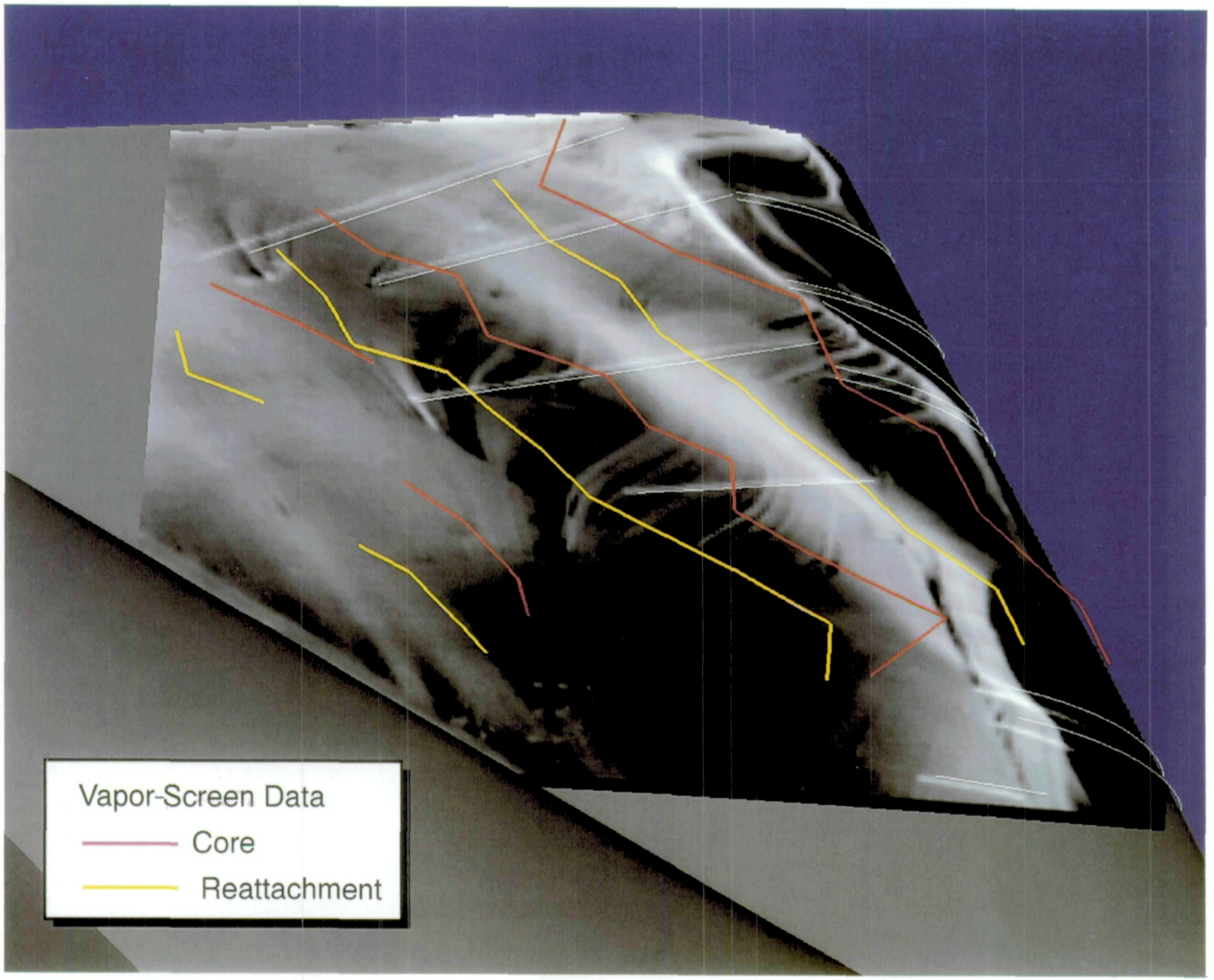

(b) View from top-camera location.

Figure 50. Concluded.

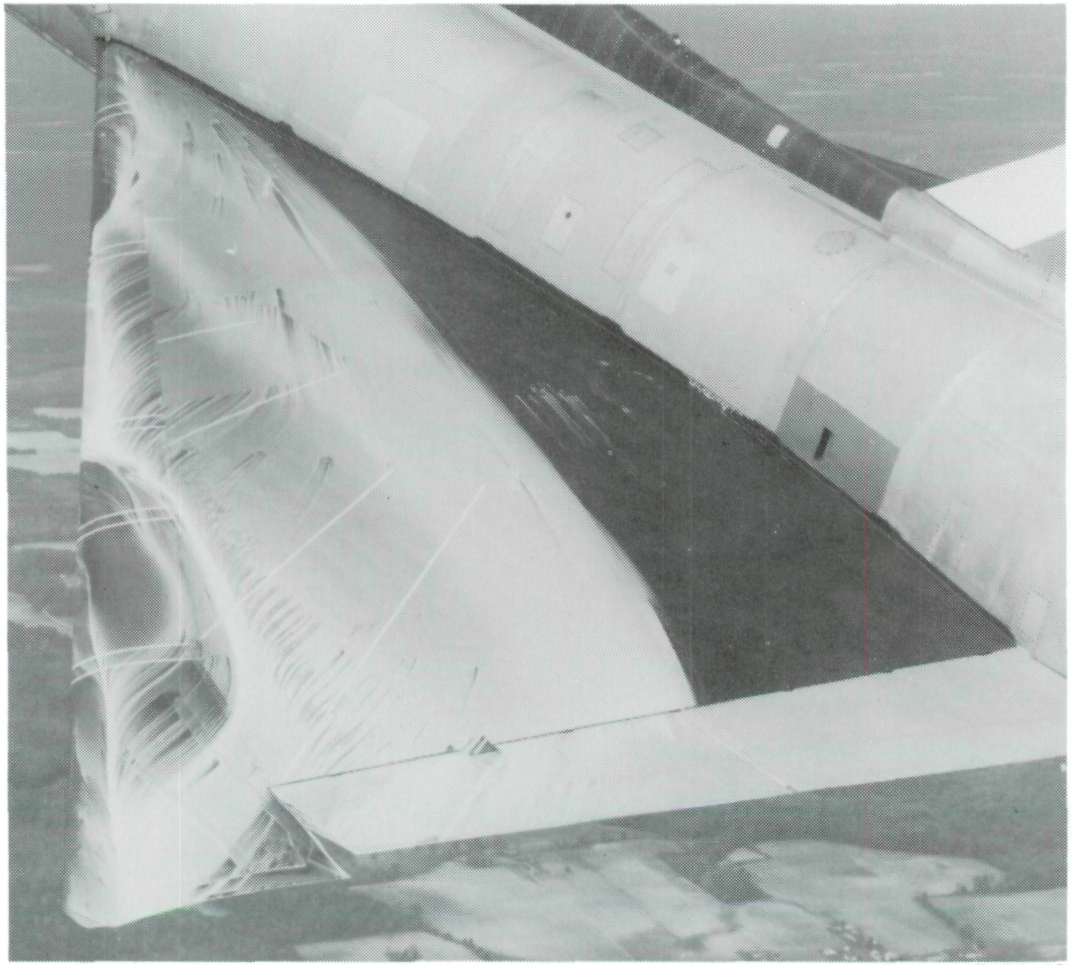

L-93-40

(a) Photograph from chase airplane.

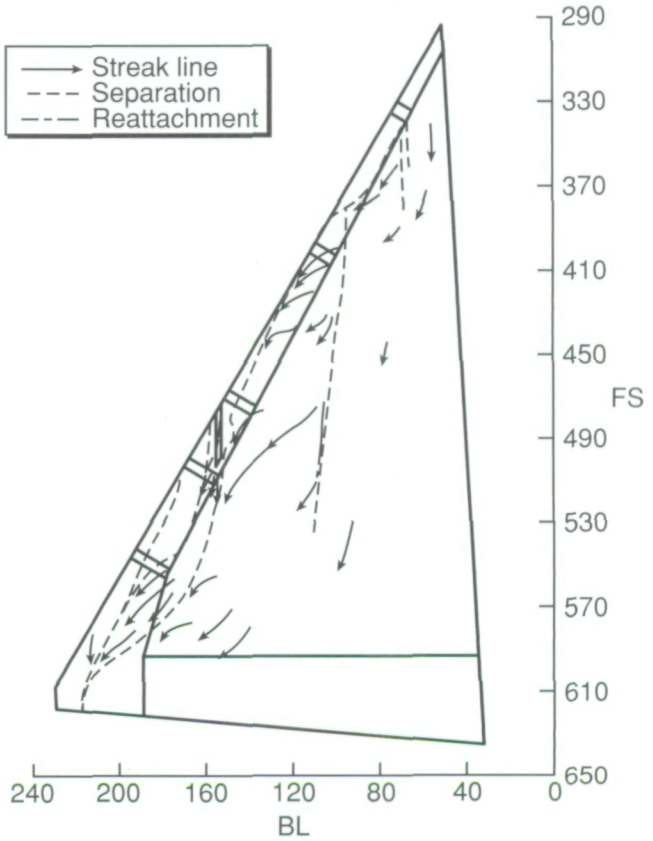

(b) Sketch of flow patterns.

Figure 51. Oil-flow patterns on wing at nominal altitude of 15 000 ft and $\alpha = 19°$.

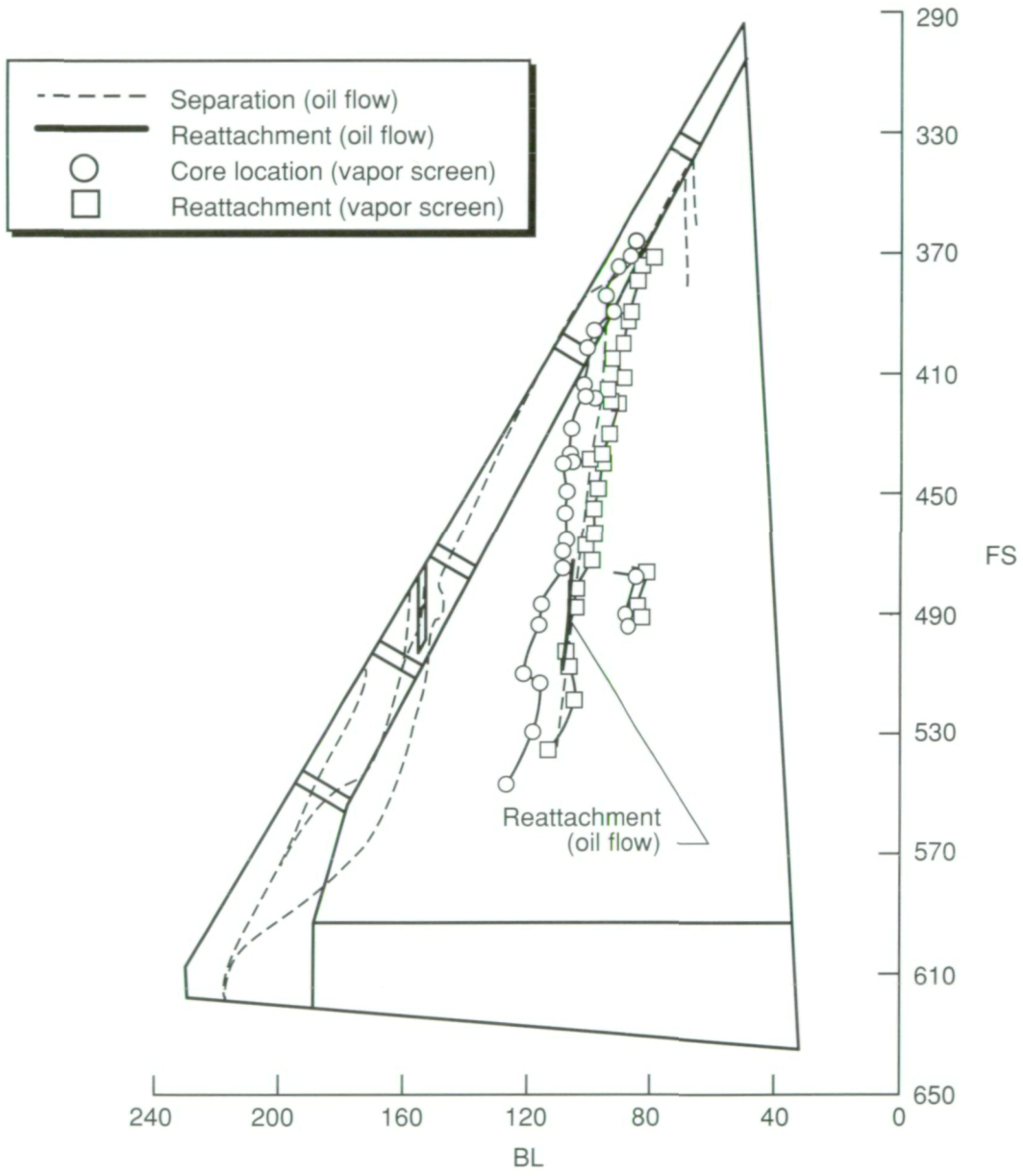

(c) Superposition of vapor-screen vortex-system results on oil-flow patterns without streak lines.

Figure 51. Continued.

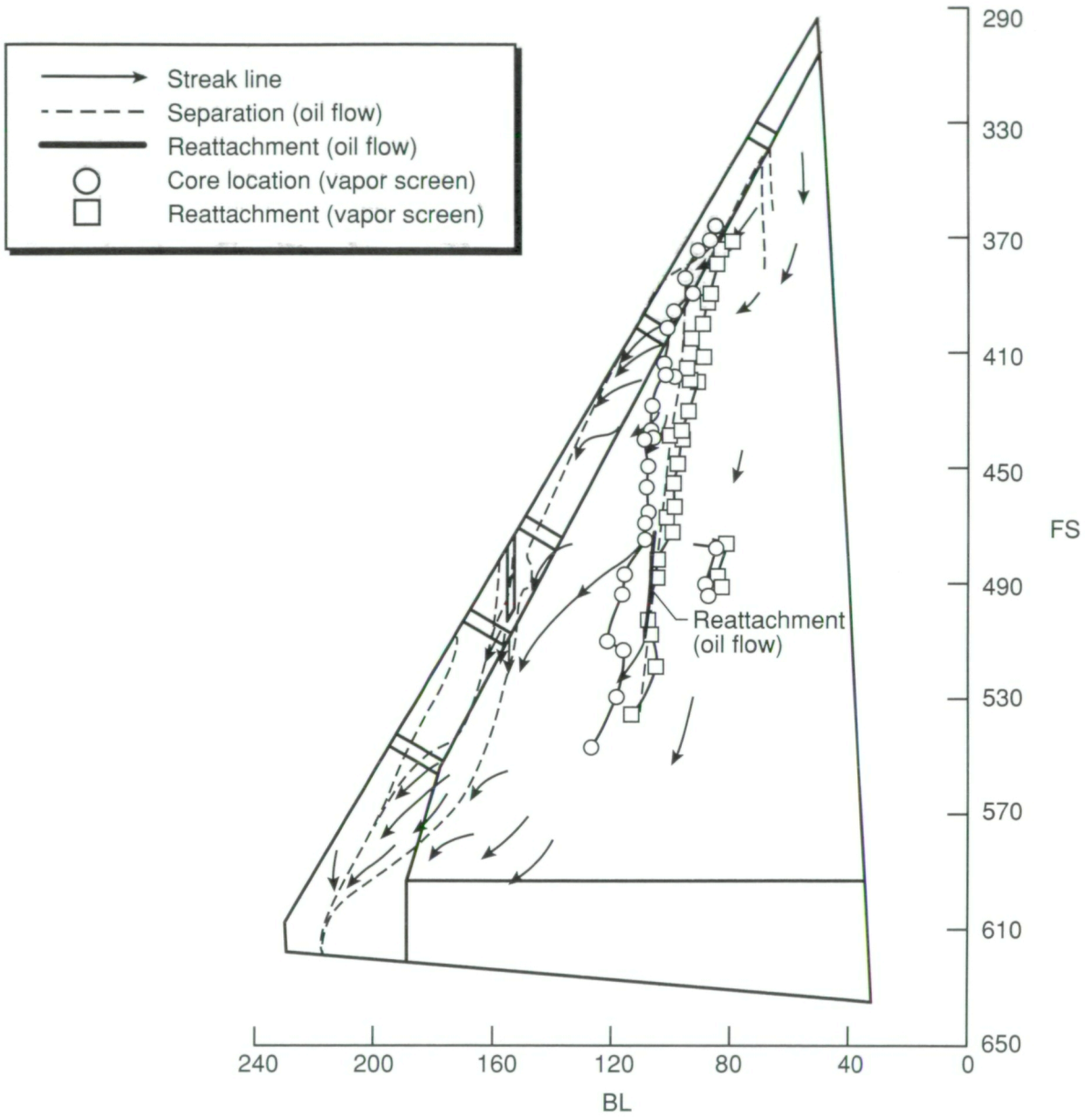

(d) Superposition of vapor-screen vortex-system results on oil-flow patterns with streak lines.

Figure 51. Concluded.

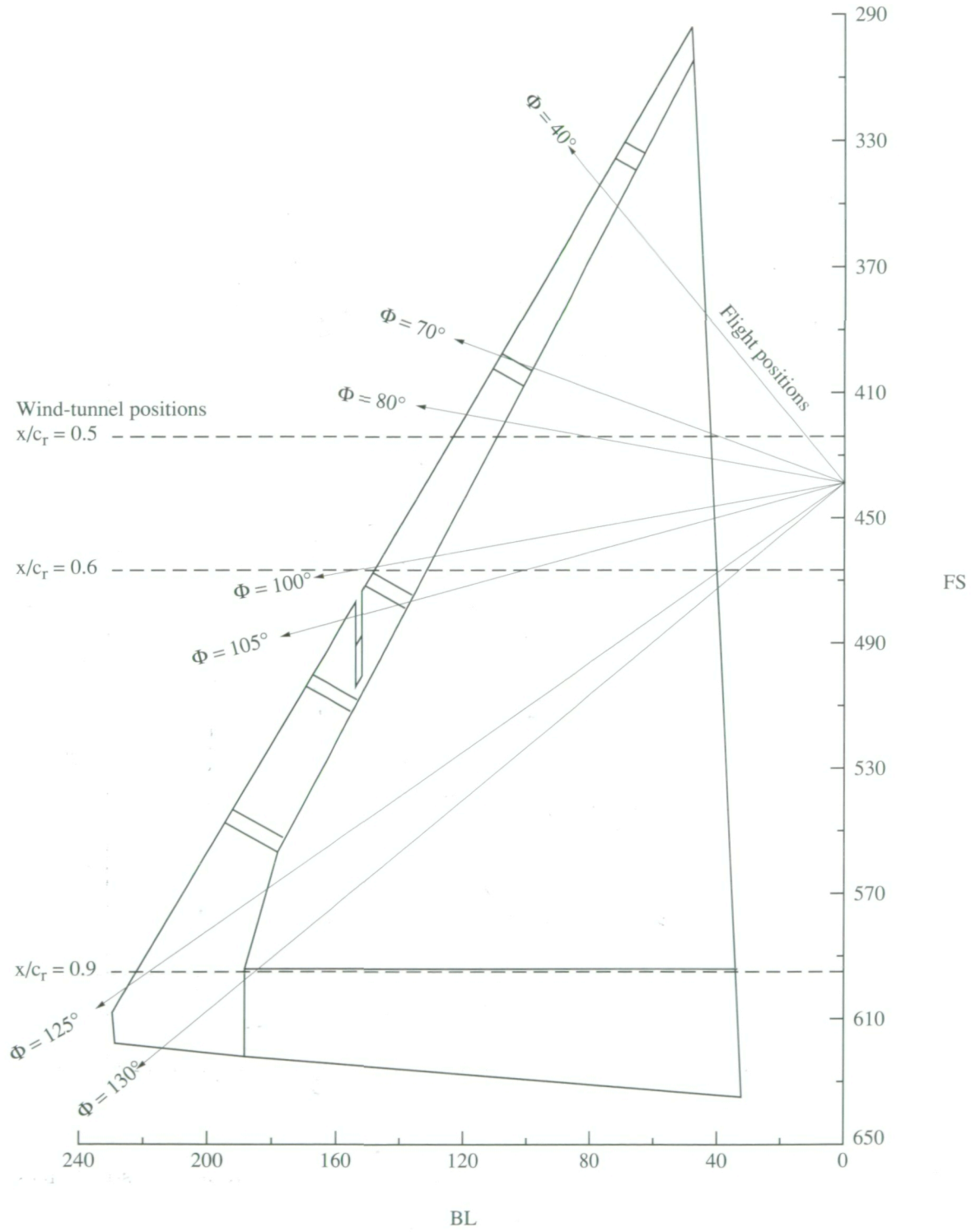

Figure 52. Spatial relationship between light-sheet angles Φ and wind-tunnel longitudinal vapor-screen locations on left wing.

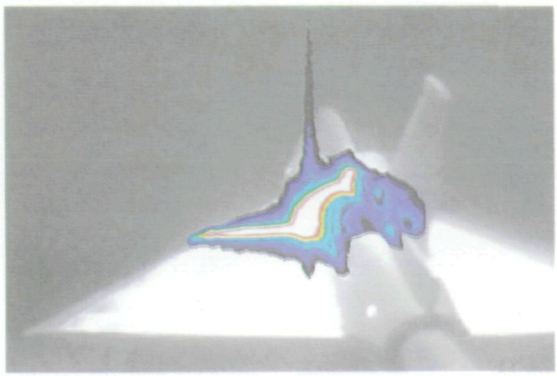

α = 10°

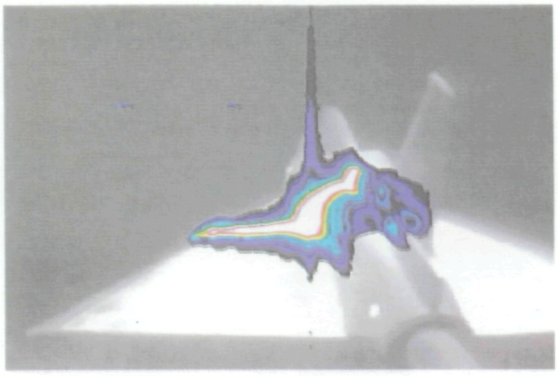

α = 12°

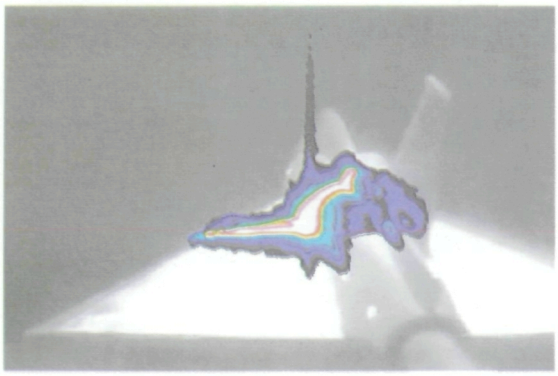

α = 14°

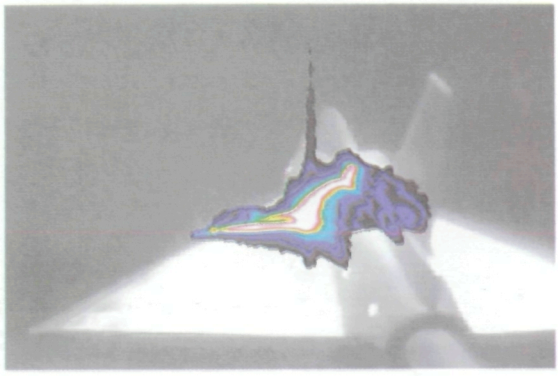

α = 16°

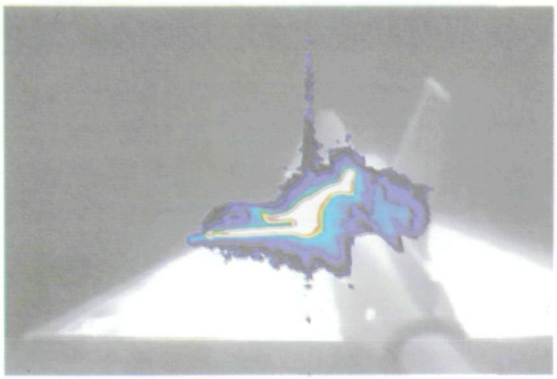

α = 18°

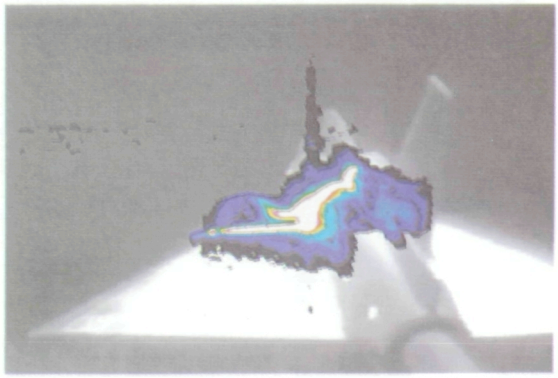

α = 20°

Figure 53. Wind-tunnel vapor-screen images of F-106 model at $M_\infty = 0.6$ and $x/c_r = 0.5$.

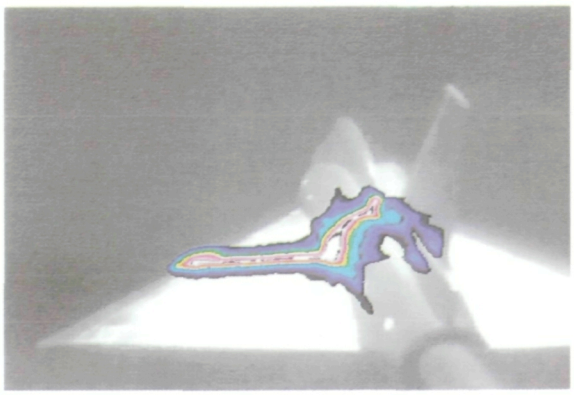

α = 10°

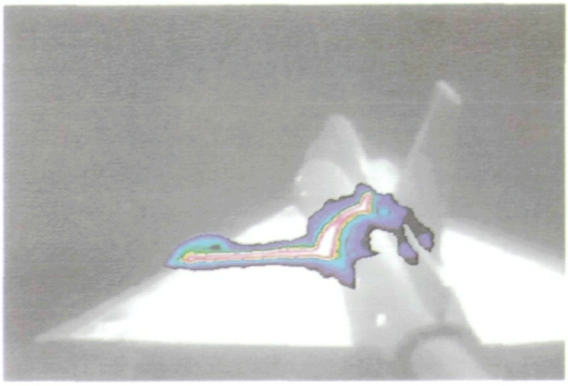

α = 12°

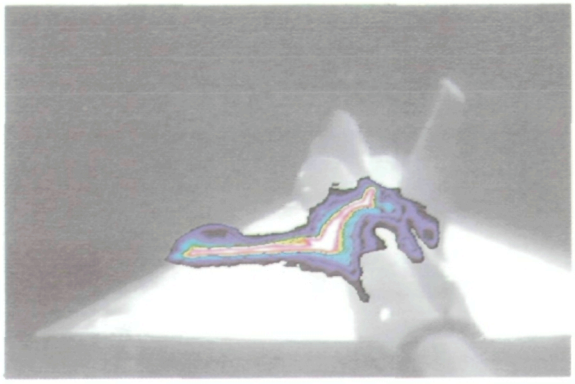

α = 14°

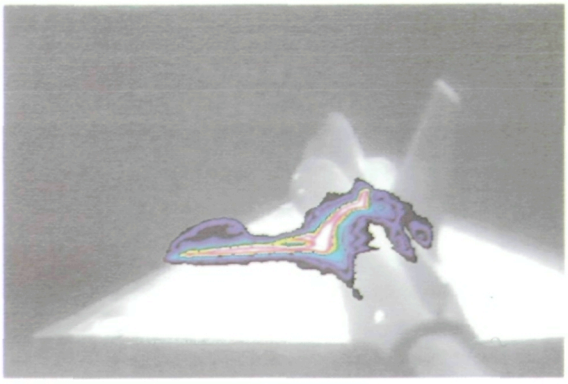

α = 16°

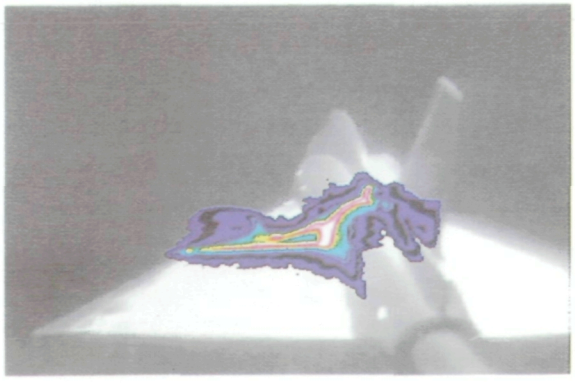

α = 18°

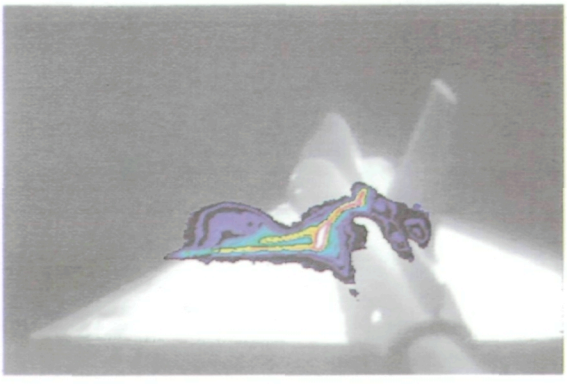

α = 20°

Figure 54. Wind-tunnel vapor-screen images of F-106 model at $M_\infty = 0.6$ and $x/c_r = 0.6$.

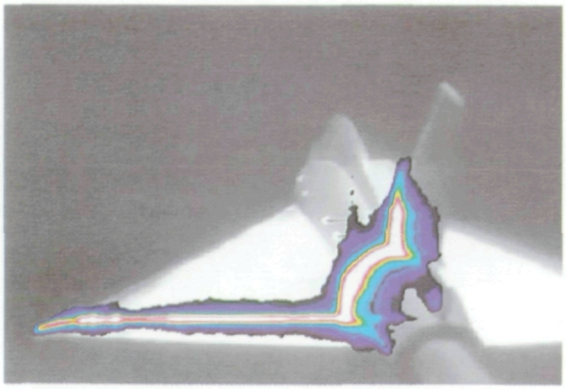

α = 10°

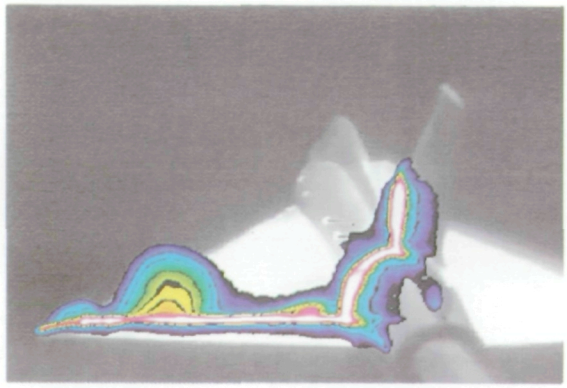

α = 12°

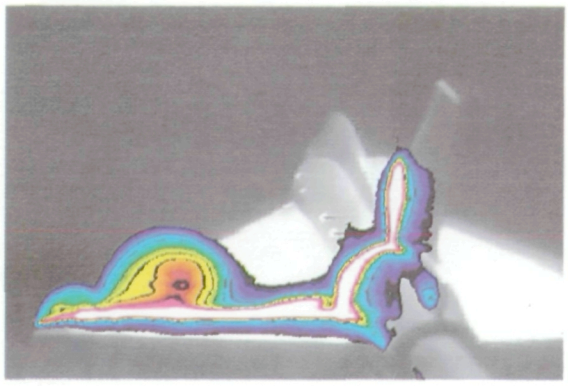

α = 14°

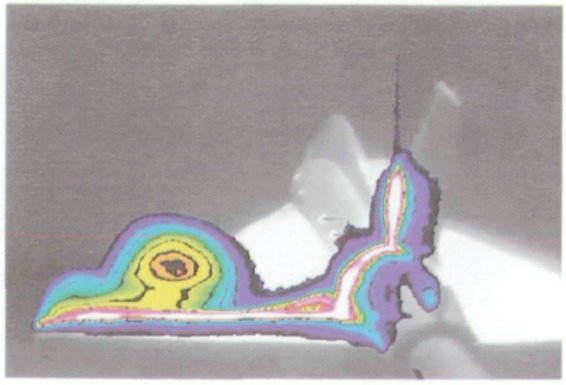

α = 16°

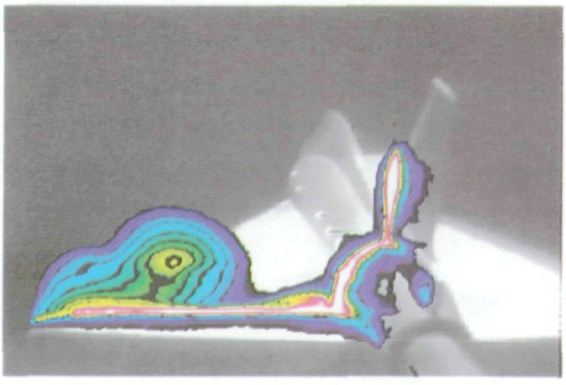

α = 18°

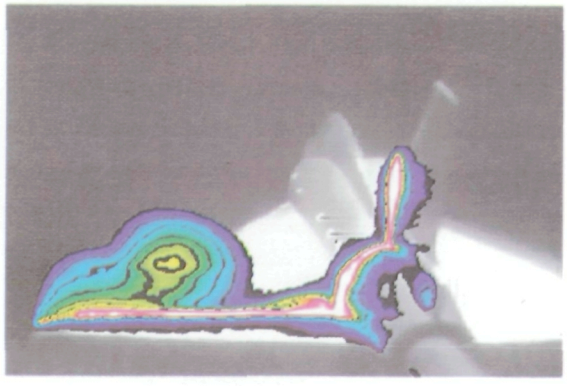

α = 20°

Figure 55. Wind-tunnel vapor-screen images of F-106 model at $M_\infty = 0.6$ and $x/c_r = 0.9$.

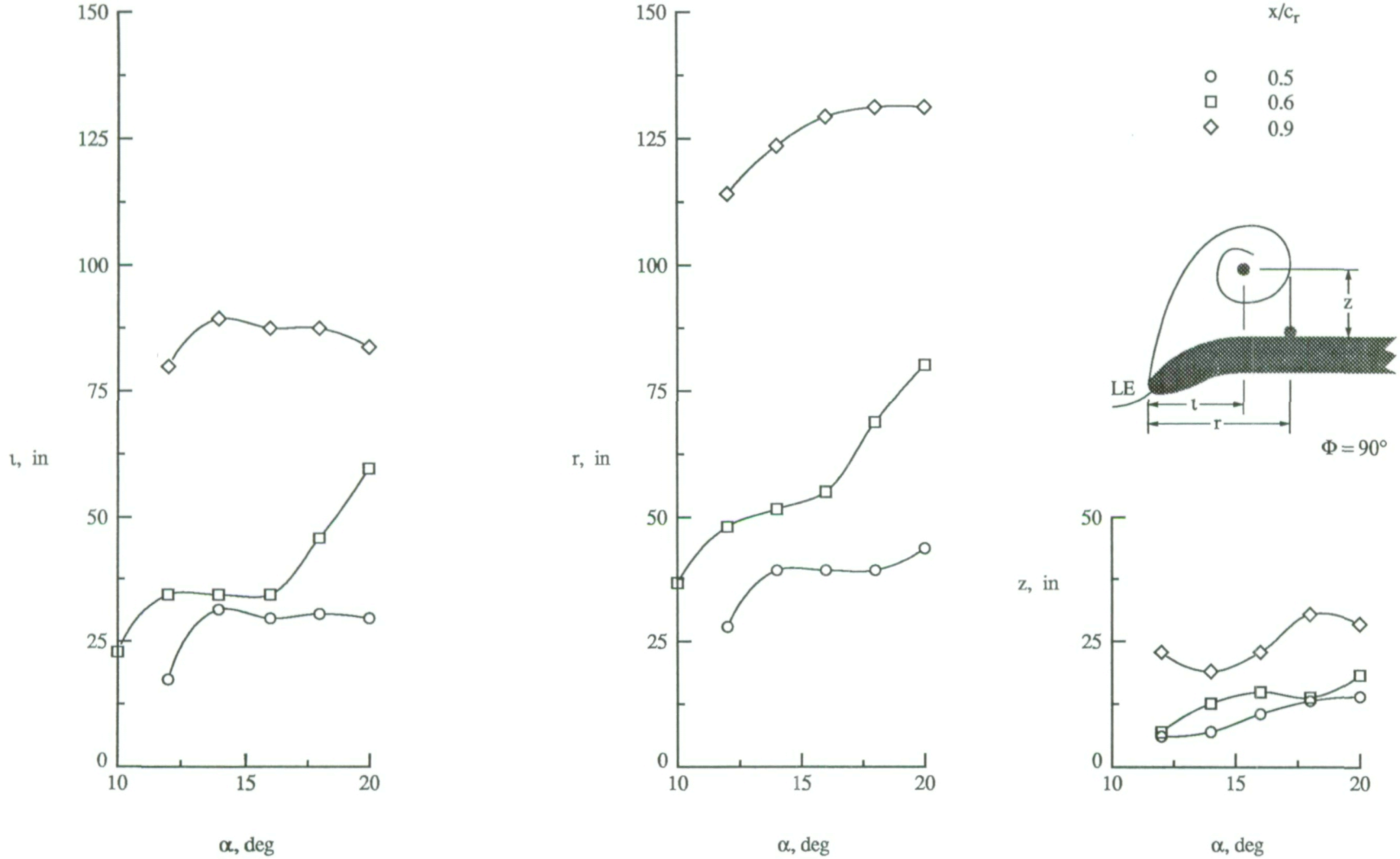

Figure 56. Summary of wind-tunnel vapor-screen vortex-system characteristics. (Reported full scale.)

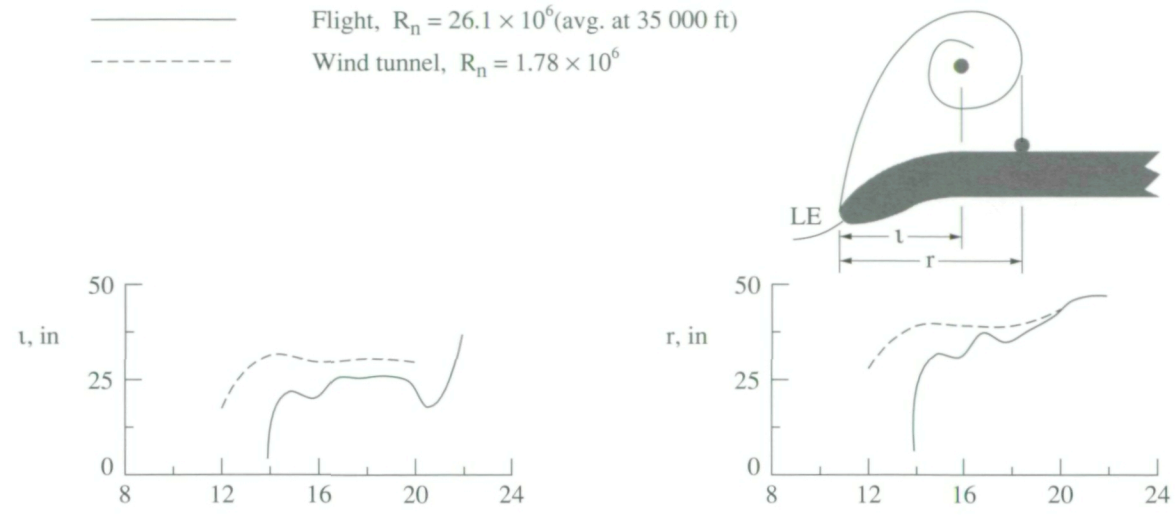

(a) $\Phi = 80°$; $x/c_r = 0.5$.

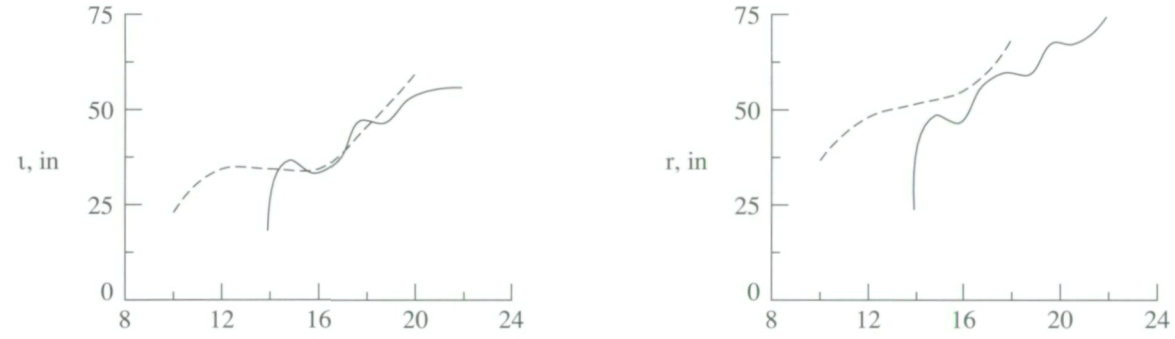

(b) $\Phi = 100°$; $x/c_r = 0.6$.

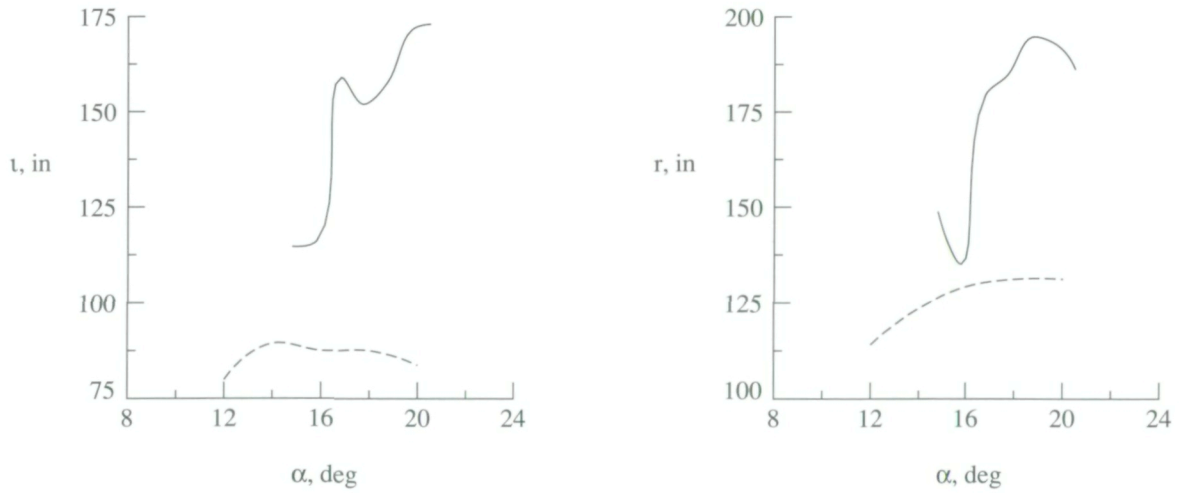

(c) $\Phi = 125°$; $x/c_r = 0.9$.

Figure 57. Vapor-screen vortex-system characteristics based on wind-tunnel (fig. 56) and flight-test results.

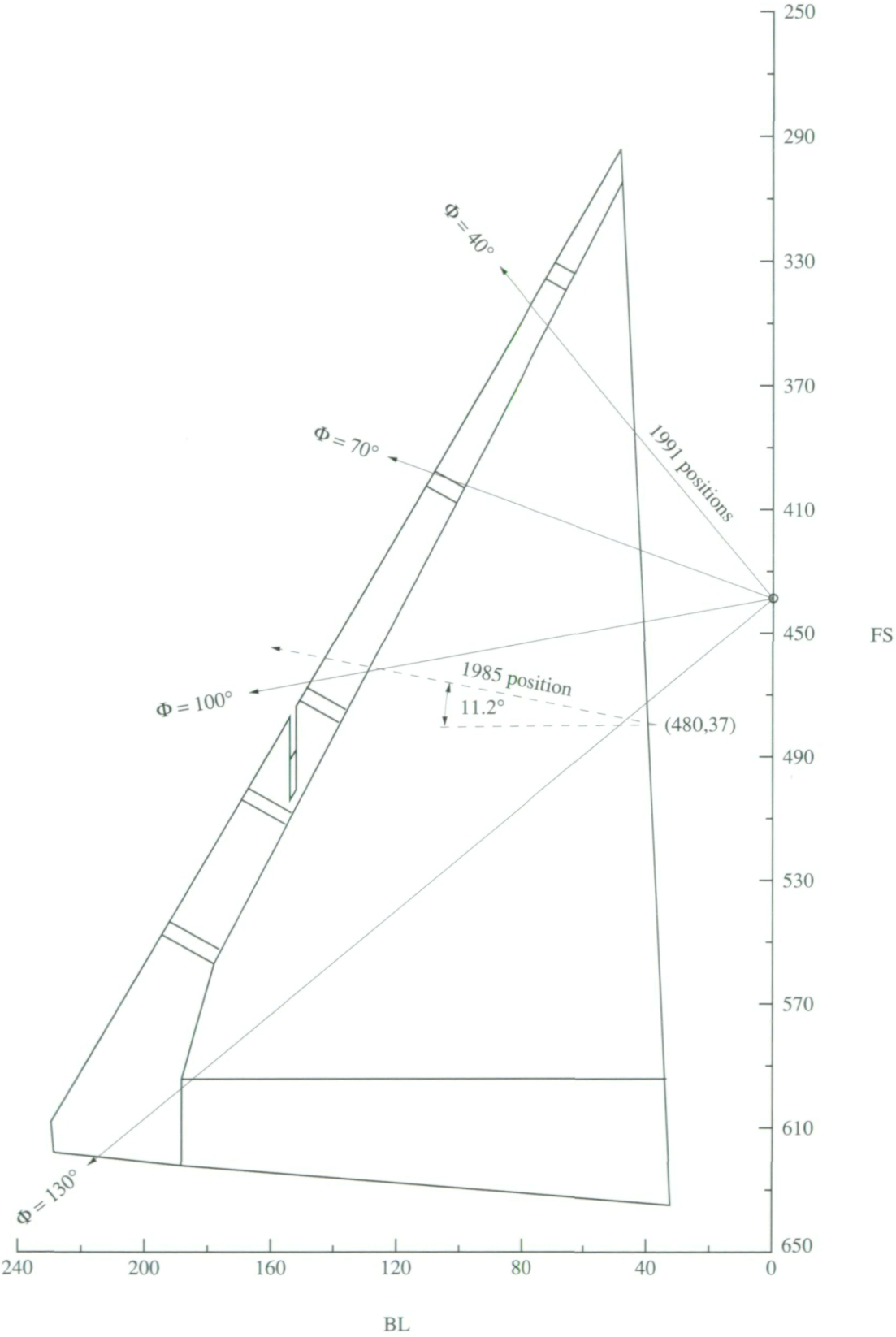

Figure 58. Spatial relationship between light-sheet angles Φ (1991 flights) and previous fixed-light-sheet location (1985 flights) on left wing.

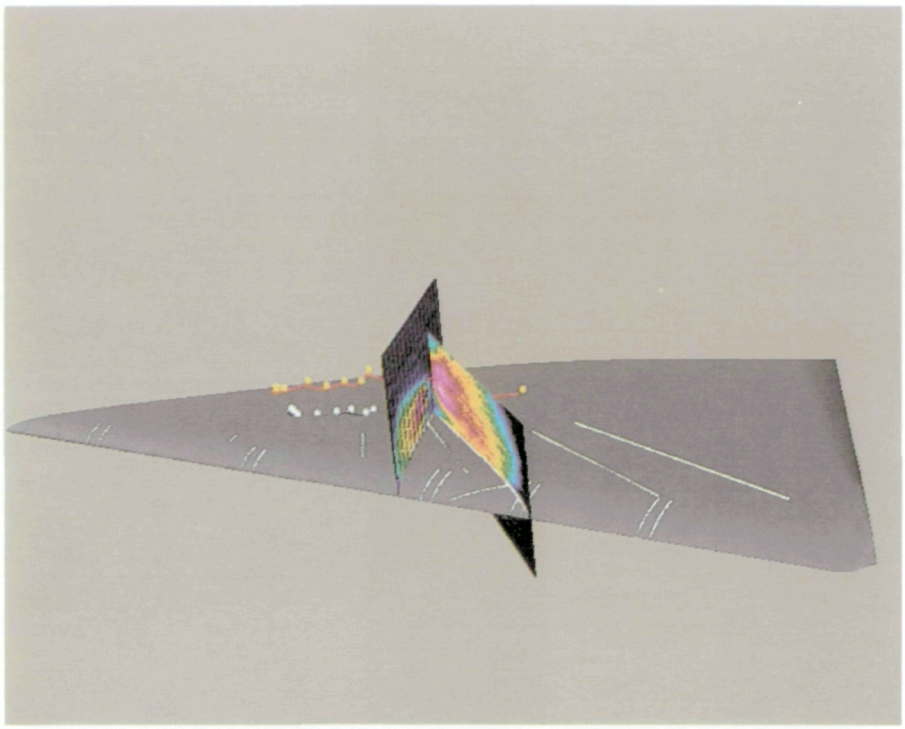

(a) Wing rolled down.

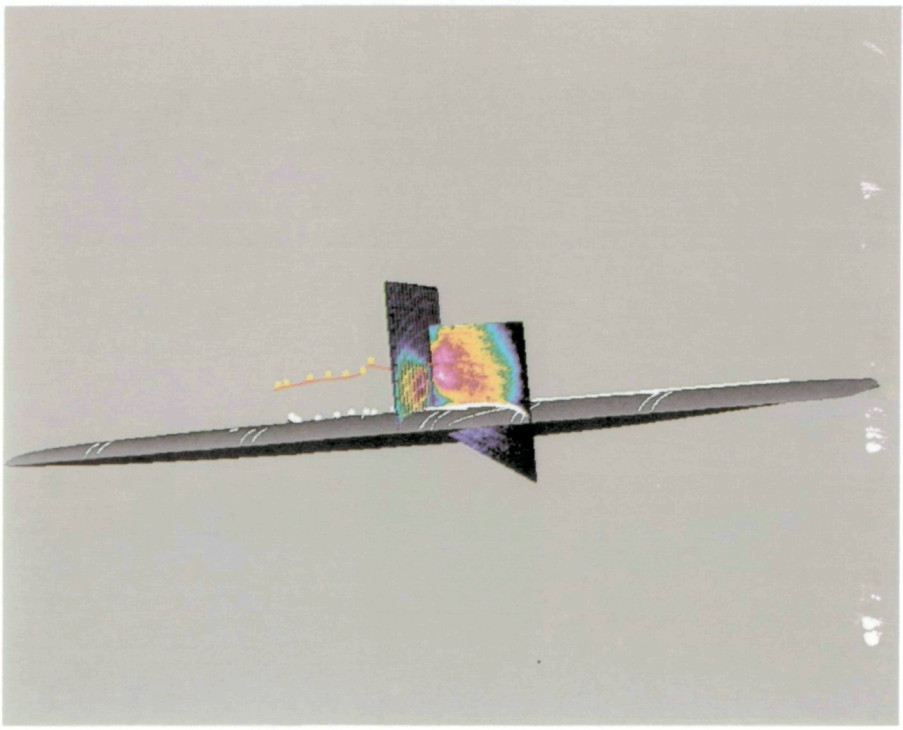

(b) No roll—nominal view used.

Figure 59. Orientation of images from 1985 flight test (left image in gridded plane) and current images on left-wing surface geometry.

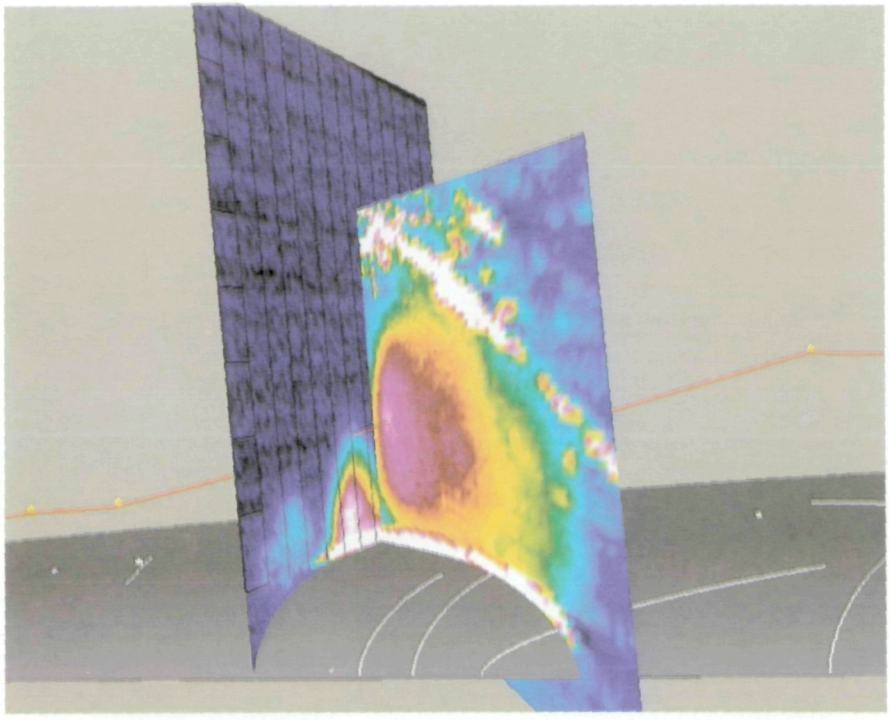

(a) $\alpha \approx 17°$.

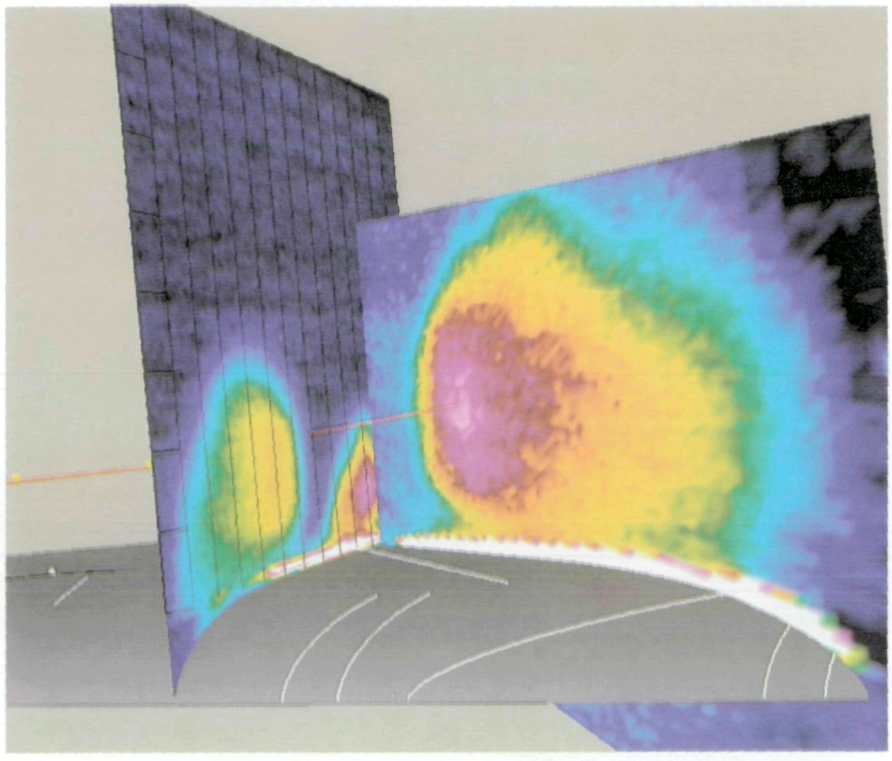

(b) $\alpha \approx 19°$.

Figure 60. Vapor-screen images on left-wing surface geometry from 1985 and current flight tests at same nominal α and $h \approx 25\,000$ ft.

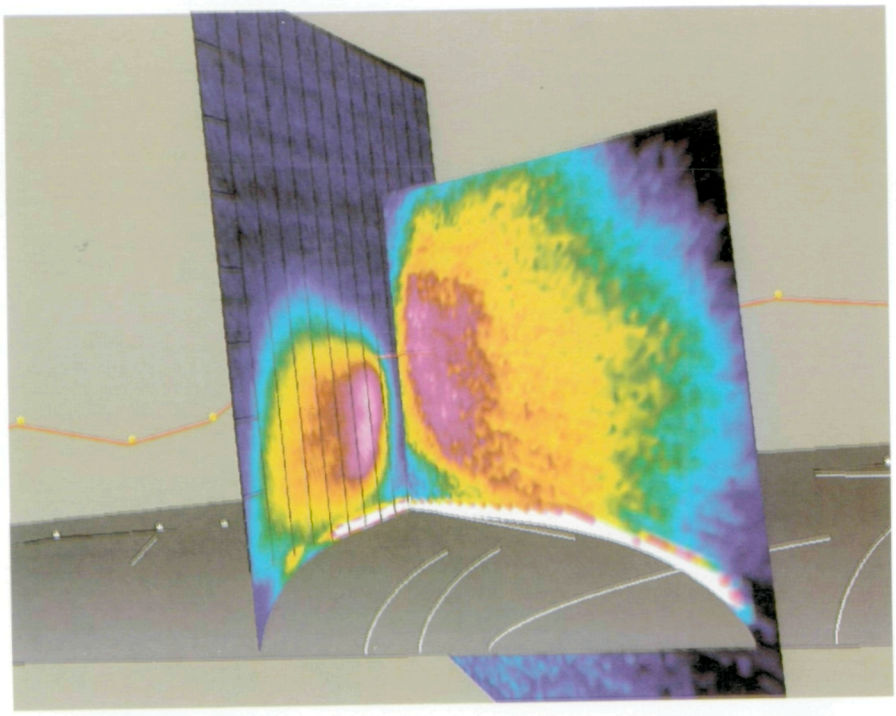

(c) $\alpha \approx 21°$.

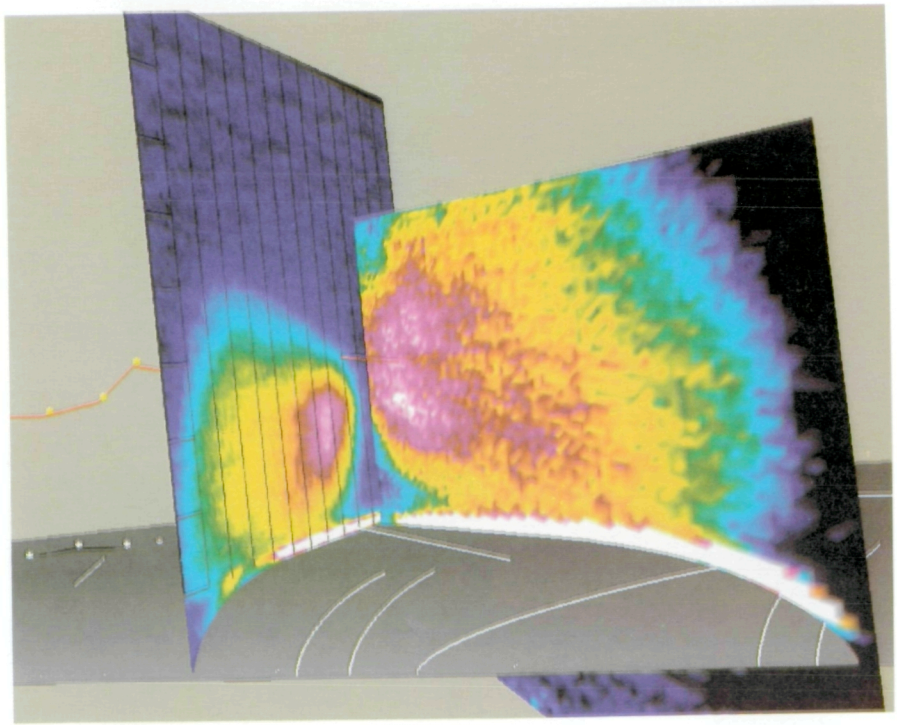

(d) $\alpha \approx 23°$.

Figure 60. Concluded.

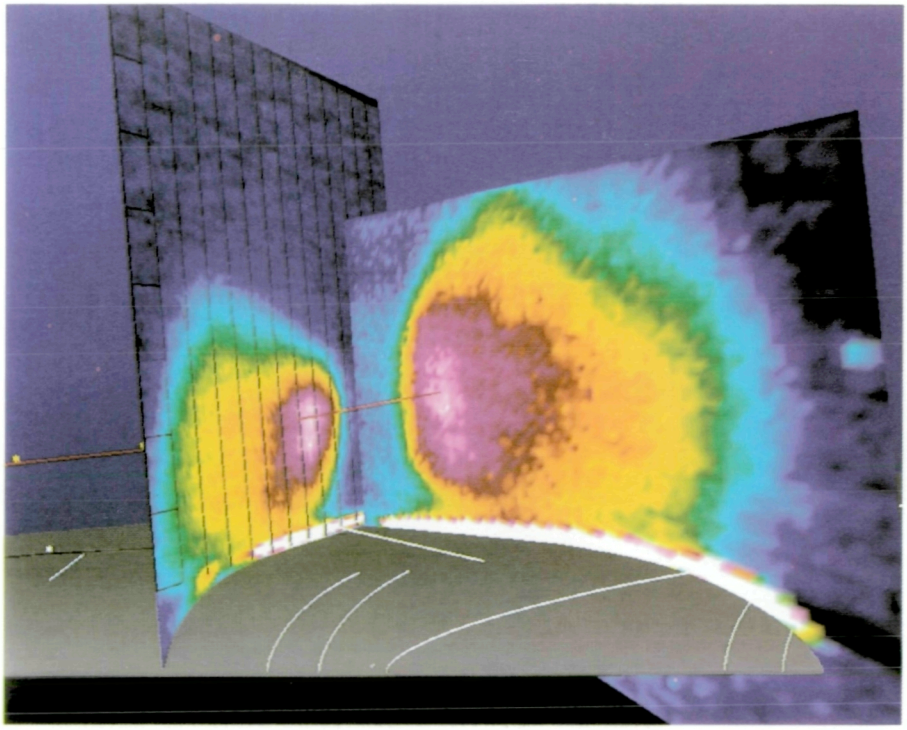

(a) $\alpha = 23°$ and $\alpha = 18.8°$ (F/S 91-13/07).

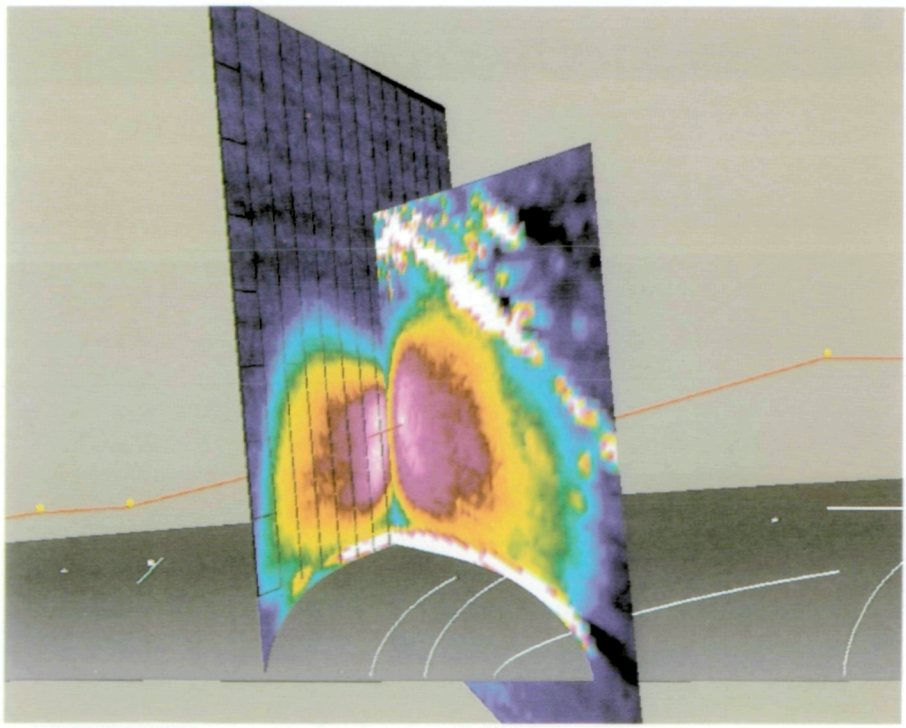

(b) $\alpha = 21°$ and $\alpha = 17.0°$ (F/S 91-13/06).

Figure 61. Vapor-screen images on left-wing surface geometry from 1985 and current flight tests at similar core height and location for nominal altitude of 25 000 ft.

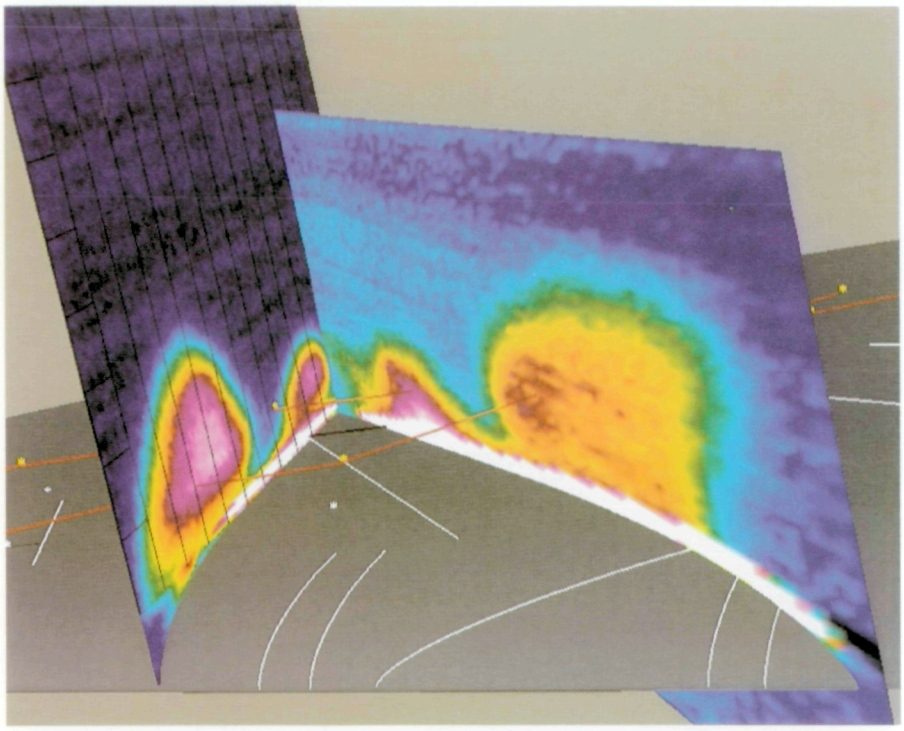

(c) $\alpha = 18°$ and $\alpha = 14.9°$ (F/S 91-13/05).

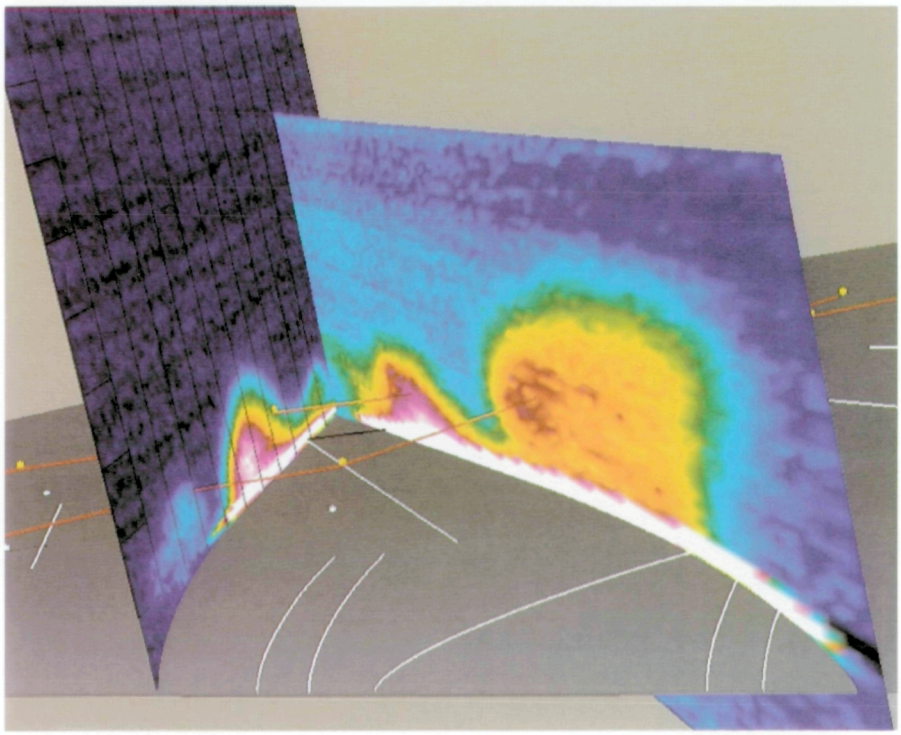

(d) $\alpha = 17°$ and $\alpha = 14.9°$ (F/S 91-13/05).

Figure 61. Continued.

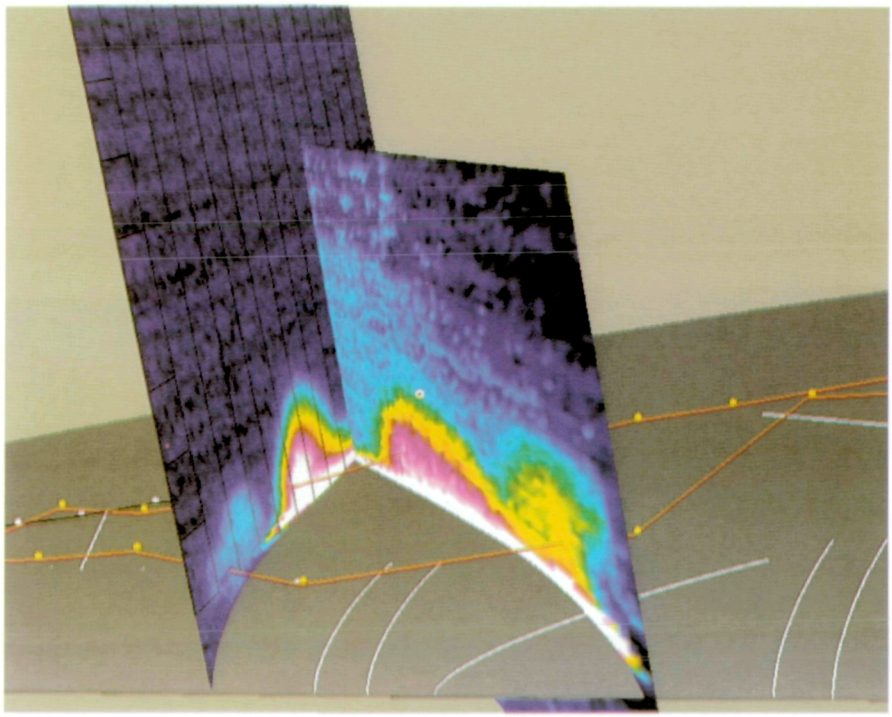

(e) $\alpha = 17°$ and $\alpha = 13.9°$ (F/S 91-13/11).

Figure 61. Concluded.

Video supplement L-0793-127 is available for purchase.

In this video (16 minutes, color, sound, VHS), the following sequences are presented:

Sequence #1. Flight-test operational procedures.

Sequence #2. Animation of post-processing key elements.

Sequence #3. Digitization process of flight video tape.

Sequence #4. **Extractor** procedure demonstration.

Sequence #5. **Reconstructor** procedure demonstration.

Sequence #6. **Reconstructor** used to compare flight results from 1985 with those in 1991.

Sequence #7. **Enhancer** procedure demonstration.

Sequence #8. Mapping of oil-flow photograph onto surface geometry for comparison with vapor-screen-determined vortex characteristics.

To obtain the video, fill out the mail-in card below and return it to

ATTN USER SERVICES
NASA CENTER FOR AEROSPACE INFORMATION
PO BOX 8757
BALTIMORE MD 21240-0757

Cut here ✂ ----------

Please send _____ copies of video supplement L-0793-127 to NASA TP-3374.

Attn: _____
Name

_____
Title

_____
Organization

_____
Street Address

_____
City and State Zip code

REPORT DOCUMENTATION PAGE

Form Approved
OMB No. 0704-0188

1. AGENCY USE ONLY *(Leave blank)*	2. REPORT DATE	3. REPORT TYPE AND DATES COVERED
	November 1993	Technical Paper

4. TITLE AND SUBTITLE
Leading-Edge Vortex-System Details Obtained on F-106B Aircraft Using a Rotating Vapor Screen and Surface Techniques

5. FUNDING NUMBERS
505-59-30-03

6. AUTHOR(S)
John E. Lamar, Jay Brandon, Kathryn Stacy,
Thomas D. Johnson, Jr., Kurt Severance, and Brooks A. Childers

7. PERFORMING ORGANIZATION NAME(S) AND ADDRESS(ES)
NASA Langley Research Center
Hampton, VA 23681-0001

8. PERFORMING ORGANIZATION REPORT NUMBER
L-17150

9. SPONSORING/MONITORING AGENCY NAME(S) AND ADDRESS(ES)
National Aeronautics and Space Administration
Washington, DC 20546-0001

10. SPONSORING/MONITORING AGENCY REPORT NUMBER
NASA TP-3374

11. SUPPLEMENTARY NOTES
Lamar, Brandon, Stacy, Severance, and Childers: Langley Research Center, Hampton, VA; Johnson: Lockheed Engineering & Sciences Company, Hampton, VA.
Video supplement L-0793-127 available for purchase on request.

12a. DISTRIBUTION/AVAILABILITY STATEMENT
Unclassified–Unlimited

Subject Category 02

12b. DISTRIBUTION CODE

13. ABSTRACT *(Maximum 200 words)*

A flight research program to study the flow structure and separated-flow origins over an F-106B aircraft wing is described. The flight parameters presented in this report include Mach numbers from 0.26 to 0.81, angles of attack from 8.5° to 22.5°, Reynolds numbers from 22.6×10^6 to 57.3×10^6, and load factors from 0.9 to 3.9 times the acceleration due to gravity. Techniques for vapor screens, image enhancement, photogrammetry, and computer graphics are integrated to analyze vortex-flow systems. Emphasis is placed on the development and application of the techniques. The spatial location of vortex cores and their tracks over the wing are derived from the analysis. Multiple vortices are observed and are likely attributed to small surface distortions in the wing leading-edge region. A major thrust in this report is to correlate locations of reattachment lines obtained from the off-surface (vapor-screen) observations with those obtained from on-surface oil-flow patterns and pressure-port data. Applying vapor-screen image data to approximate reattachment lines is experimental, but depending on the angle of attack, the agreement with oil-flow results is generally good. Although surface pressure-port data are limited, the vapor-screen data indicate reattachment point occurrences consistent with the available data.

14. SUBJECT TERMS	15. NUMBER OF PAGES
Flight program; Vapor screen; Flow visualization; Pressures; Oil flow; Multiple vortices; Reattachment lines	161
	16. PRICE CODE A08

17. SECURITY CLASSIFICATION OF REPORT	18. SECURITY CLASSIFICATION OF THIS PAGE	19. SECURITY CLASSIFICATION OF ABSTRACT	20. LIMITATION OF ABSTRACT
Unclassified	Unclassified		

National Aeronautics and
Space Administration
Langley Research Center
Mail Code 180
Hampton, VA 23681-00001